Development Of Nickel Hydroxide/Oxyhydroxide Catalysts For The Electrochemical Removal Of Urea In Alkaline Solutions

Anthony Pyka

A dissertation
submitted in partial fulfillment of the
requirements for the degree of

Doctor of Philosophy

University of Washington

2023

Reading Committee:
Eric M. Stuve, Chair
John Berg
David S. Bergsman

Program Authorized to Offer Degree:
Chemical Engineering

University of Washington

Abstract

Development Of Nickel Hydroxide/Oxyhydroxide Catalysts For The Electrochemical Removal Of Urea In Alkaline Solutions

Anthony Pyka

Chair of the Supervisory Committee:
Eric M. Stuve

Urea is a small organic molecule that is continually produced, circulated, and consumed through natural processes. Unfortunately, urea is a common pollutant in waste streams from industrial processes, human excrement, and drug production. High concentrations have been seen to disrupt the natural process of the nitrogen cycle, causing negative environmental impacts. The high concentrations of urea can be removed by several different types of processes, but electrochemical removal poses a double benefit. Electrochemically oxidizing urea allows for urea to removed from the environment with hydrogen as a byproduct.

In first body of work, NiOOH phases were developed using selective electrochemical cycling from 0.9 V_{RHE} to switching potentials between 1.54 and 1.64 V_{RHE} in 0.5 M KOH at 25 °C. Cyclic voltammetry, chronoamperometry, electrochemical impedance spectroscopy (EIS), and scanning electron microscopy (SEM) were used to characterize the surface oxide formed by the cycling procedures. Cycling with a lower switching potential (1.54 V_{RHE}) led to preferential formation of β-NiOOH, while higher switching potentials (1.64 V_{RHE}) favored the formation of γ-NiOOH. Moreover, a high switching potential induced surface roughening through NiOOH lattice expansion and contraction, thereby increasing electrochemical surface area (ECSA) and the number of grain boundaries. Kinetics of the OER were evaluated using Tafel analysis and turnover frequency (TOF). An electrode developed with a switching potential of 1.54 V_{RHE} had TOF values 6–17 times larger than an electrode between 1.56 and

1.66 V developed with a switching potential of 1.64 V_{RHE}, indicating improved OER kinetics of the β-NiOOH phase. Tafel analysis revealed little difference in Tafel slope (38.2–44.2 mV dec^{-1}) between 1.54 and 1.69 V_{RHE}, suggesting β-NiOOH and γ-NiOOH have similar OER mechanisms. The results here show that selective electrochemical cycling can be used to control the formation of NiOOH species can be used for studying the urea oxidation reaction.

In second body of work, urea oxidation is studied to investigate the influence of urea electrooxidation on nickel oxyhydroxide by analyzing nickel phases through detailed electrochemical experiments and mass spectrometry. Urea electrooxidation was studied in KOH electrolytes with and without the presence of incidental iron to understand the UOR activity of the β-NiOOH and γ-NiOOH phases of nickel. Cyclic voltammetry, chronoamperometry and mass spectrometry were used to develop and characterize the urea oxidation and oxygen evolution reaction activities of NiOOH phases. Cycling in urea-free electrolytes with low (1.58 V_{RHE}) and high (1.68 V_{RHE}) switching potentials led to the formation of β-NiOOH and γ-NiOOH (respectfully), while cycling the electrodes in 0.2 M urea lead to a phase of nickel that was more β-NiOOH-like in nature. Window opening experiments in iron-free electrolytes revealed the hysteresis at higher potentials, possibly due to the formation of NiO_2 or a change of UOR reaction pathway. Chronoamperometry, combined with mass spectrometry, showed a drop in current at higher potentials (1.88 V_{RHE}) along with a drop in N_2 faradaic efficiency. The results here show that the surface of nickel is susceptible to change during UOR, which in turn affects the selectivity of reaction products.

Next, high chromium and molybdenum nickel-based alloys and pure Ni were used as electrocatalysts to study the electrochemical urea oxidation reaction with varying concentrations of Ni, Cr, and Mo. Slow cyclic voltammetry (1 mV s^{-1}) and polarization curves were performed with 10, 50, and 100 mM urea in 1 M KOH at 37 °C. The electrochemically active surface area (ECSA) was determined by capacitance measurements at the open circuit poten-

tial. The ECSA tracked the extent of oxide layer growth for all electrodes. Electrodes with mature oxide layers exhibited larger ECSAs compared to those of initial oxide layers. Alloys showed higher reaction rates per geometric area than nickel. However, the alloys showed showed significantly lower urea electrooxidation turnover frequencies (TOF) (0.057–0.1 s^{-1}) when compared to a pure Ni electrode (< 0.30 s^{-1}). Key findings emphasize: the correlation between electrochemical surface area and roughness with urea oxidation active area, the utilization of the Langmuir-Hinshelwood model for determining the urea oxidation mechanism versus potential, and the determination that urea oxidation activity remained constant on a per-site basis through TOF ratio analysis despite the growth of the oxide layer.

The last body of work focuses on developing and characterizing nickel-based catalysts to enhance urea oxidation in a wearable artificial kidney. Various catalysts (Ni, NiMn, NiCr, NiMo, NiFe) are synthesized onto nickel foam to increase the electrochemically active surface area and roughness. Mass transfer limits are observed for urea oxidation at physiological concentrations (10 mM). Urea oxidation kinetics are explored at higher concentrations (200 mM), showing improved performance during polarization but lower currents per active site. A simplified dialysis model is introduced to evaluate mass transfer coefficients' and extent of reactions' impact on flowrates, urea concentrations, and pH levels in streams. A nickel hydroxide catalyst is evaluated with this model and shows a minimum electrode area of 1,314 cm^2 is needed for continuous operation. This research combines experimental data and a computational dialysis model, highlighting the potential of these catalysts and paving the way for future improvements.

The results of these studies suggest that, although the urea oxidation reaction on nickel-based catalysts has been well studied, there is room for improvement for employing nickel-based electrodes in waste water applications. Furthermore, the methodologies developed in this research can be applied to other NiOOH-based systems to investigate and enhance their electrocatalytic performance.

TABLE OF CONTENTS

LIST OF FIGURES

LIST OF TABLES

ACKNOWLEDGMENTS

I would like to thank my advisor Dr. Eric Stuve for making this work possible. His guidance in electrochemistry and writing has guided me from a naive college undergraduate to the scientist I am today. Whether we talk about science, classic rock, or books, I thoroughly enjoy his presence. I also would like to thank Dr. David S. Bergsman for taking the time to sit down and meet with me, no matter how busy his schedule (and still is, I'm assuming). I would also like to thank the members of my committee; Dr. John Berg, and Dr. Bruce Hinds for the conversations and support throughout the years.

I also acknowledge my friends and labmates I've met along the way. To undergraduate friends, Michael Bauer, Blake Bronson, Kyle Chin, Caitlin Ditullio, Evan Komp, Ryan Hanson, Joe Lohmann, Berkley Noble, Maria Politi, Carson Silsby, Brett Stoneman, Marc Wiederhold, Troy Woodard, and many more, you all helped and supported me through undergraduate school in more ways than I can count. To all the friends I met in graduate school: Kelly Carpenter, Brian Gerwe, Isaac Kretzmer, Giang Le, and Jon Witt. And lastly to the fellow ruggers: Brendan Butler, Ben Carney, Jacob Christy, Duncan Reece, and Zach Lilja.

I would also like to special thanks to my parents, Werner and Ellyn, for raising me with love and allowing for my engineering spirit to roam free. Thank you Julie and Heidi for being the best sisters I could have asked for. I thank Scott, Tracy, Blake, and Brittany for accepting me with open arms and for raising an incredible woman that I am proud to call my wife.

DEDICATION

To my wife, Lauren.

Your encouragement and support mean everything.

Chapter 1

INTRODUCTION

Urea, when in high concentration, causes negative environmental responses by disturbing the natural balance of the nitrogen cycle. Nitrogen is normally converted into multiple chemical forms as it circulates through atmospheric, terrestrial, and marine ecosystems. Reactive nitrogen (in the form of ammonia, nitrates, etc.) is created mostly by microbes in soil.[1] Reactive nitrogen is used by organisms, such as plants and animals, to facilitate metabolic processes and is reverted to unusable nitrogen (N_2). A balance between reactive and unusable nitrogen naturally occurs as nitrogen moves through ecosystems. However, the balance of the nitrogen cycle has been disturbed as the demand for food production has increased the total agricultural output by 1.1 % every year since 2000.[2] The excess nitrogen from several major sources, as seen in Figure 1.1, pollutes the environment with urea. The accumulation of urea in the environment, due to runoff from industrial and agricultural sources, causes the balance of reactive and unusable to nitrogen shift, causing negative environmental changes.

Urea is seen in a variety of processes, ranging from the liver's conversion of ammonia to mass production of drugs, adhesives, and fertilizers.[3–5] A typical modern urea production plant will create wastewater in a ratio of 0.3:1 for every unit of urea produced.[6] The heavy use in both biological and industrial settings has caused urea to be a major waste product. The continuous increase in global urea usage has the potential to raise the input of nitrogen into rivers and coastal waters. The ecosystem shifts as nature restores balance when large amounts of urea enters the environment. For instance, the increase in urea in the Florida Keys has shifted the phytoplankton community diversity and nutrient cycling, leading to more phytoplankton blooms, which may include toxic species.[7] A similar situation occurred

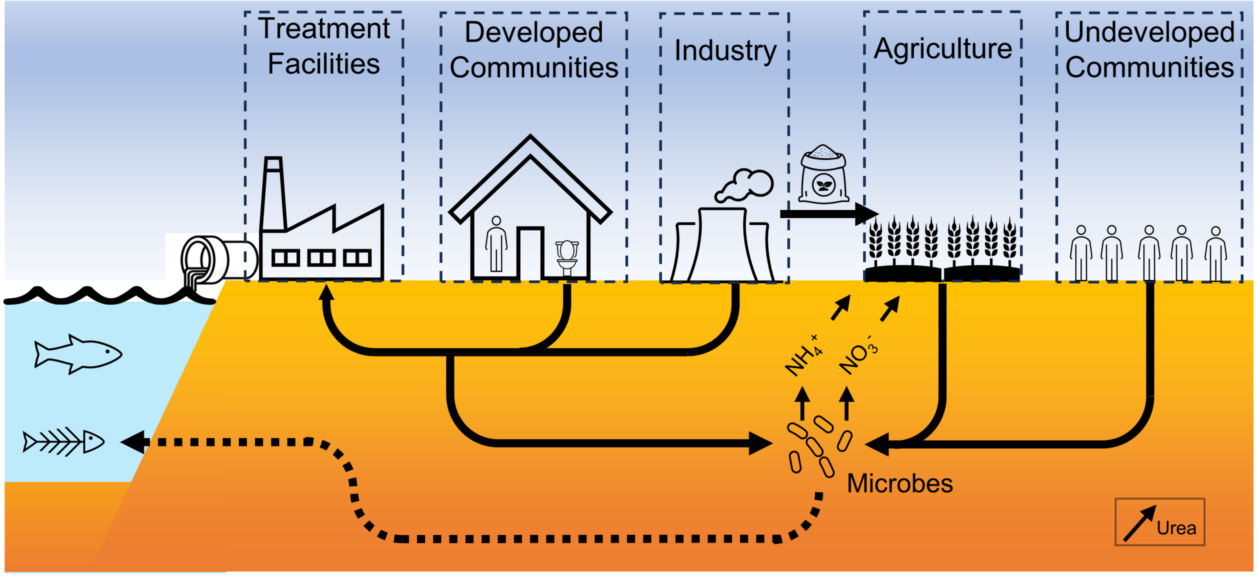

Fig. 1.1 Nitrogen pollution from major sources. Urea is removed by treatment facilities and naturally by microbes, but excess urea can accumulate and will cause negative effects.

in Lake Erie during 2011, where a large algae bloom covered a substantial area of water, as seen in Figure 1.2.

The kidney dialysis industry, in particular, produces large amounts of urea-rich water as a waste product from dialysis treatments. Humans that are unable to filter urea from blood must undergo kidney dialysis, a procedure to remove waste products and excess fluid from the blood. Access to affordable chronic kidney disease treatment has been a major problem as the number of end-stage kidney disease cases has increased by 41.8 % from 2000 to 2019.[8] The approximate cost of kidney-related treatment exceeded \$48 billion in 2015, meaning 6.7% of the total Medicare budget was used to care for less than 1% of the covered population.[9] Patients diagnosed with end-stage renal failure suffer from high burdens and have high rates of mortality.[10] The high burden, on top of co-existing diseases, depression, and symptoms, leads to a poor health-related quality of life.[11–13] There is evidence suggesting more frequent treatments, like daily home dialysis, would benefit patients by improving metabolic parameters.[10]

Fig. 1.2 Satellite imagery of Detroit and Lake Erie during June 1st, 2011 (left) and October 9th, 2011 (right). The bright green color represents the area occupied during an algae bloom. Images taken by the National Oceanic and Atmospheric Administration Centers for Coastal Ocean Science.

The bottlenecks for converting patients from traditional dialysis to home dialysis are storage, cost, and disposal of fresh dialysate. Traditional hemodialysis is an expensive process that exposes patients to 300-600 liters of dialysate during a typical week.[14] The composition of the fresh dialysate is important as it influences the exchange of ions between the blood and the dialyzer, restores acid-base equilibrium, and strongly affects cardiovascular stability.[15] Patients of different ages, sizes, gender, and other external factors will have varying compositions of dialysate, making a "one size fits all" fluid difficult to achieve.[16]

Portable dialysis, as seen in Figure 1.3, relies on a small amount of dialysate and a regenerator to eliminate urea and recycle dialysate back to the dialyzer. The urea reacts quickly on the spot, instead of being sent to a treatment facility along with with 300-600 L of dialysate. This poses advantages of cleaning wastewater outside of dialysis as well, allowing for water-challenged areas of the world to recycle water without a large treatment facility.

Water-challenged areas of the world need to remove urea to recycle wastewater into usable water. Ingestion of urea-contaminated water causes irritation of the gastrointestinal tract that may result in nausea, vomiting, headaches, confusion, and electrolyte depletion. Reusing wastewater may also cause environmental risk due to increased nitrogen, phosphorus, and endocrine fluids into the groundwater.[17] When found in high concentrations in aqueous media, urea will decompose into cyanate and ammonium. The cyanate then readily converts to CO_2 and ammonia.[18] Ammonia is a highly toxic substance that, when left untreated, negatively affects the biodiversity of sensitive ecosystems through soil acidification and direct toxic damage. Ammonia is also a nutrient for phytoplankton, the organism responsibly for the algae bloom seen in Fig. 1.2.

An easy, low cost method is needed to remove urea from waste streams before any environ-

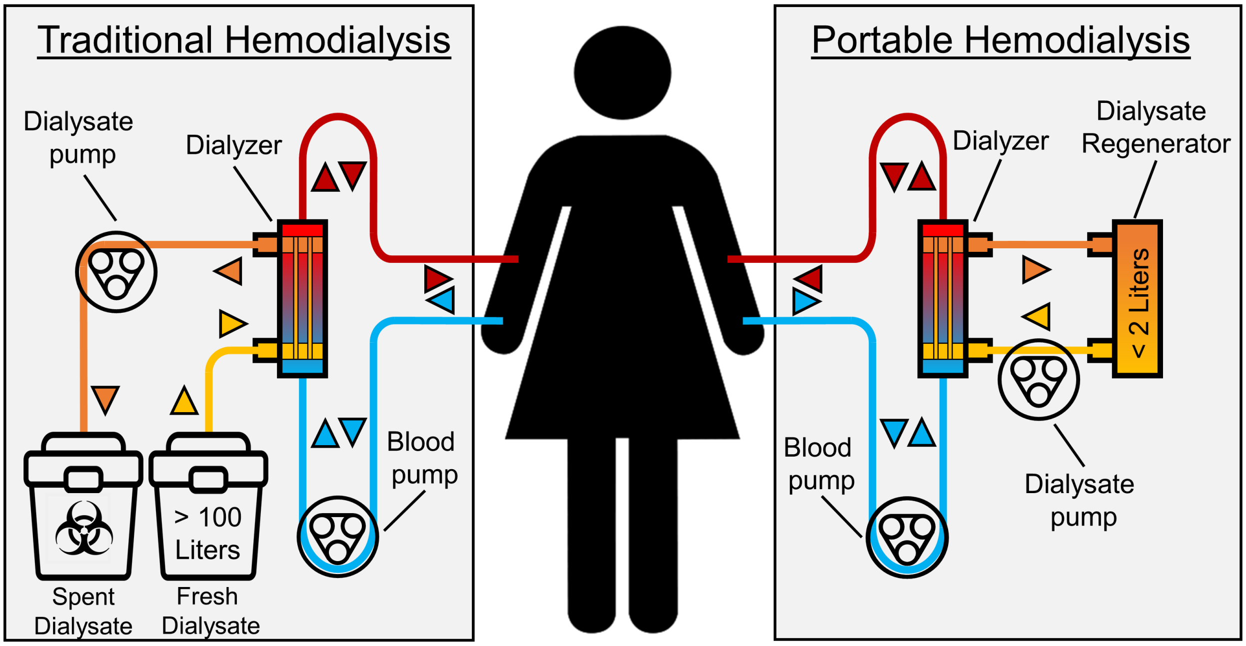

Fig. 1.3 Depiction of traditional (left) and portable (right) hemodialysis. Traditional dialysis relies on a large amount of fresh dialysate composed of electrolytes and water to remove blood toxins in a single-pass configuration. Portable dialysis relies on a small amount of recycled dialysate to make the operation small enough to be comfortably carried. Adopted from National Institute of Diabetes and Digestive and Kidney Diseases, National Institutes of Health.

mental damage becomes irreversible. The three major technologies for efficiently removing urea are: physisorption and chemisorption, enzymatic hydrolysis, and reactive decomposition.[19] Physisorption and chemisorption *via* sorbent materials are ideal as there are no byproducts of a reaction, but the sorbents are highly selective and need to be replaced frequently.[20,21] Enzymatic hydrolysis utilizes urease to remove urea at near-neutral pH. The urea is converted to ammonium, which is far more toxic than urea; thus extensive filters are required for implementation.[22]

Electrochemical oxidation, a form of reactive decomposition, has been shown to be an efficient method for urea removal from wastewater.[23,24] Electrochemical urea oxidation can be tuned accordingly by adjusting catalyst area, composition, and properties to fit specifications necessary for operation. For example, portable kidney dialyzers needs to be small and lightweight, thus requiring a small amount of catalyst in order to achieve a lower form factor. Industrial treatment plants have looser size requirements and can have larger electrocatalyst sizes, but may need catalysts to treat a wide variety of molecules. Electrochemical urea oxidation also poses a double benefit, as the the process can be used to generate energy or hydrogen during times of an energy demand or surplus, respectively.

In order to generate electricity, a half-cell reaction with a higher reduction potential than urea reduction must occur on the cathode. The oxygen reduction reaction (ORR), seen in Table 1.1, has a standard reduction potential of 1.23 V_{RHE}, which is greater than the urea reduction reaction (URR) potential of 0.08 V_{RHE}. With ORR on the cathode, the urea will oxidize (the opposite of reduction) on the anode, causing the overall theoretical cell voltage to

Table 1.1 Hydrogen evolution (HER), urea reduction (URR), and oxygen reduction (ORR) standard reduction equations and potentials.[25]

Label	Reaction	V_{RHE}
HER	$2\,H_2O_{(l)} + 2\,e^- \longrightarrow H_{2,\,(g)} + 2\,OH^-$	0.00 V
URR	$CO_{2,\,(g)} + N_{2,\,(g)} + 5\,H_2O_{(l)} + 6\,e^- \longrightarrow CO(NH_2)_{2,(aq)} + 6\,OH^-_{(aq)}$	0.08 V
ORR	$O_{2,\,(g)} + H_2O_{(l)} + 4\,e^- \longrightarrow 4\,OH^-_{(aq)}$	1.23 V

be 1.15 V at 25 °C. The coupled reactions produce power indicated by the positive potential and can be implemented into a fuel cell configuration, as seen in Figure 1.4b.

Instead of producing energy by ORR, urea oxidation can use energy to produce hydrogen through water splitting. The hydrogen evolution reaction (HER), seen in Table 1.1, has a lower standard reduction potential than URR. Therefore, a minimum of 0.08 V must be applied to oxidize urea on the anode. This potential is the theoretical minimum and requires overpotentials greater than 0.08 V to overcome kinetic, ohmic, charge transfer, and concentration losses.[26] The HER and urea oxidation reactions can be used to generate hydrogen at scale with an electrolyzer configuration, as seen in Figure 1.4c. The electrochemical production of hydrogen is useful for achieving a green economy and moving away from the current carbon-based economy of today.

Hydrogen is a highly sought-after commodity as it is an alternative energy source to avoid greenhouse gasses. Typically, hydrogen is produced by splitting water, where HER is facilitated on the cathode and the oxygen is produced on the anode. The rate of hydrogen production is usually governed by the sluggish oxygen evolution reaction (OER), the reverse reaction of ORR.[27] Noble metals, such as iridium and ruthenium oxides, can accelerate the OER kinetics at all pH values.[28,29] However, these materials are scarce and costly, limiting their use in an expanded industrial setting.

The urea oxidation reaction can be used as the anodic half-cell reaction in an alkaline stack for a more energy-effective method of hydrogen production than OER. While platinum and rhodium show some activity towards urea oxidation, they are costly and are easily poisoned by adsorbed NH* species, a surface intermediate in the reaction.[30] Therefore, a non-precious metal that can oxidize urea with low overpotentials and low selectivity to toxic products is desired for producing hydrogen at scale.

Considerable research in the last several decades has presented a myriad of non-precious metal alternatives for urea oxidation such as: carbon-based materials (graphite, graphene, graphene oxide), oxide/hydroxide earth abundant materials (nickel, cobalt, manganese, molybdenum, iron, etc.), and mixtures of compounds to form ternary-plus composi-

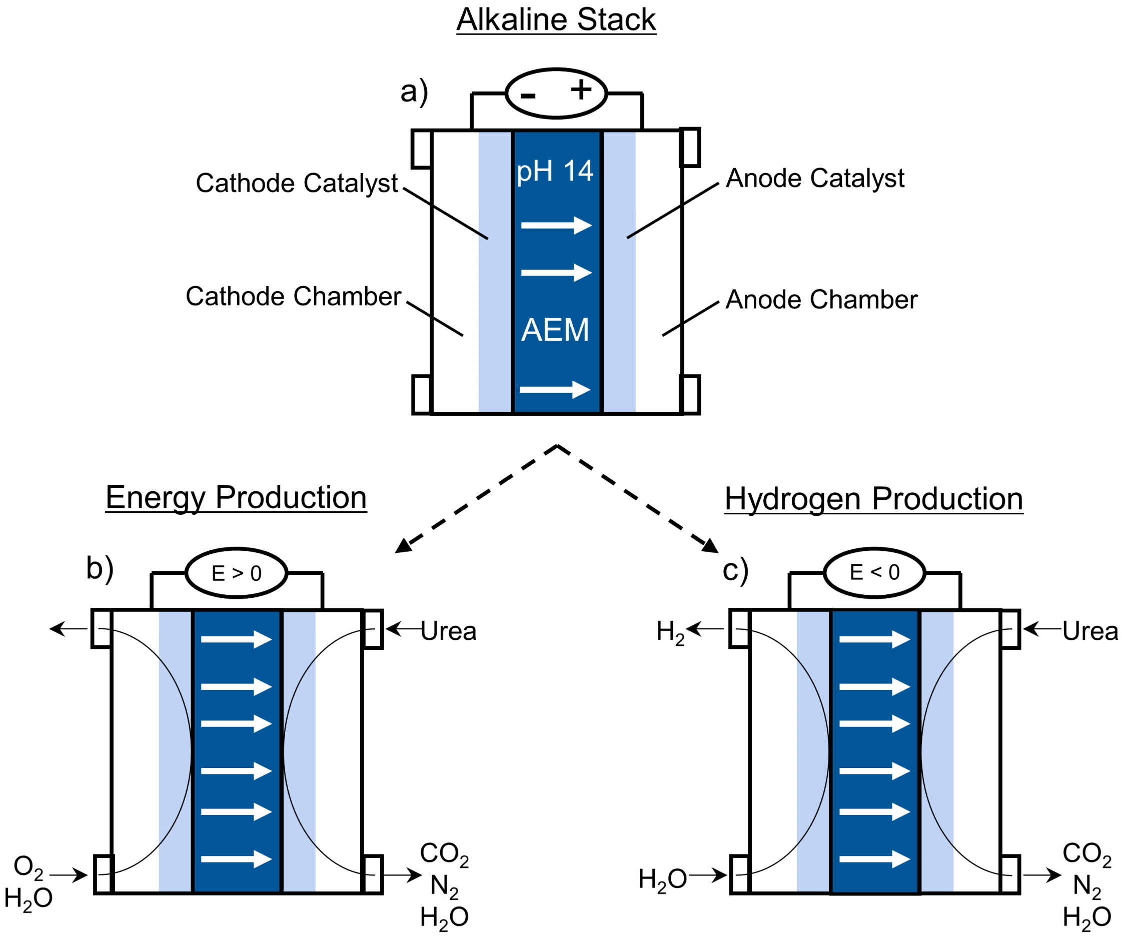

Fig. 1.4 Configuration for an alkaline membrane electrolyzer for removal of urea at the anode. The pH in the anion exchange membrane (AEM) is high due to immobilized cations in the membrane. White arrows show the direction of anions flowing from cathode to anode through the AEM.

tions.[28,31–36] Earth abundant metals are viable candidates for facilitating the urea oxidation reaction in an alkaline electrolyzer device. The focus of this research is to advance the current understanding of the electrochemical urea oxidation reaction on nickel and nickel-based catalysts. Applications such as dialysis and wastewater remediation will benefit from a material that oxidizes urea for the remediation of fluids. Additionally, the electrochemical removal of urea can be used to generate hydrogen by water-splitting or generate power by oxygen reduction. These reactions, as mentioned in Table 1.1, can be used in an alkaline stack for scalable electrolyzer or fuel cell operations, respectively. Before such a device can be fashioned, an anodic catalyst material must be chosen to facilitate the urea half-reaction. Chapter 2 reviews the current understanding of nickel and nickel-based catalysts for their applications of urea removal in alkaline environments. This knowledge gives a foundation necessary to understand the properties and mechanisms of nickel associated with the urea oxidation reaction.

Chapter 2

LITERATURE REVIEW

2.1 Overview

Removal of urea via oxidation has been of interest since the 1970s to recover potable water from urine for extended space travel.[37] These studies aimed to improve the activity of an electrode without considering the oxidation products. Selectivity is an important factor, as a catalyst that oxidizes urea into toxic compounds is undesirable. Additionally, the stability of the catalyst is necessary for long lifetime of operation without corrosion or deactivation. Figure 2.1 is a Venn diagram that shows a catalyst with desired traits of high selectivity, stability, and activity. If one of the categories is not satisfied, then the catalyst is not suitable for industrial applications.

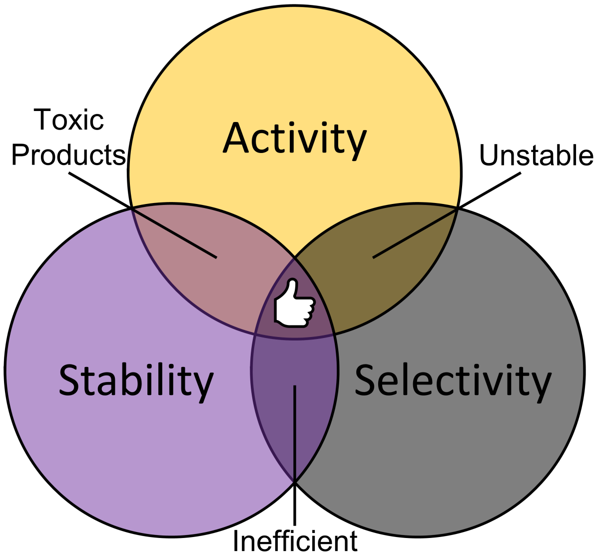

Fig. 2.1 Venn Diagram of a perfect catalyst based on stability, selectivity, and activity.

Platinum electrodes exhibit good urea oxidation characteristics and small dissolution rates in alkaline solutions, but ammonia is the primary product.[38–40] Nickel electrodes show affinity for urea oxidation with lower selectivity for ammonia-type compounds, but easily corrode in chloride-containing environments.[41–44] Nickel-based alloys show promise for stability in alkaline applications and have been studied as catalysts for urea electrooxidation.[45–48] The reactions and mechanisms of urea oxidation on nickel must be understood before diving into binary, ternary, and nickel-based alloy systems.

2.2 Reaction Mechanism

Two mechanisms have been identified for urea electrooxidation in previous works.[49–52] The direct urea oxidation reaction (DUOR) consists of urea reacting on the nickel oxyhydroxide surface, as seen in Reaction 2.1, where x represents the degree of oxidation of urea during reaction. The indirect urea oxidation reaction (IUOR) is the chemical reaction of urea with an electrogenerated active species of NiOOH, in turn reducing $Ni(OH)_2$ to NiOOH, as seen in Reaction 2.2. The electrogenerated species NiOOH is supplied by the nickel transition reaction, as seen in Reaction 2.3. Reaction 2.4, hydrogen evolution, is used to balance the half reactions and occurs on the cathode in an electrolyzer-type configuration.

$$\mathrm{CO(NH_2)_{2,(aq)}} + x\,\mathrm{OH^-_{(aq)}} \longrightarrow \mathrm{products} + x\,\mathrm{e^-} \tag{2.1}$$

$$x\,\mathrm{NiOOH_{(s)}} + \mathrm{CO(NH_2)_{2,(aq)}} + \mathrm{H_2O_{(l)}} \longrightarrow x\,\mathrm{Ni(OH)_{2,(\mathit{s})}} + \mathrm{products} \tag{2.2}$$

$$\mathrm{Ni(OH)_{2,(\mathit{s})}} + \mathrm{OH^-_{(aq)}} \rightleftharpoons \mathrm{NiOOH_{(s)}} + \mathrm{H_2O_{(l)}} + \mathrm{e^-} \tag{2.3}$$

$$2\,\mathrm{H_2O_{(l)}} + 2\,\mathrm{e^-} \longrightarrow \mathrm{H_{2,(\mathit{g})}} + 2\,\mathrm{OH^-} \tag{2.4}$$

$$\mathrm{CO(NH_2)_{2,(aq)}} + x\,\mathrm{H_2O_{(l)}} \longrightarrow \mathrm{products} + \mathrm{H_{2,(\mathit{g})}} \tag{2.5}$$

The overall urea oxidation reaction (UOR), Reaction 2.5, is used to express the process in an electrolysis cell. Both direct and indirect mechanisms rely on the presence of NiOOH on the surface. Thus, UOR is mediated through an electrochemical activation of nickel from $Ni(OH)_2$ to NiOOH, which occurs at 1.35 V_{RHE}.[41,53] OER also occurs at the NiOOH surface as Reaction 2.6:

$$4\,\mathrm{OH^-_{(aq)}} \longrightarrow \mathrm{O_{2,(\mathit{g})}} + 2\,\mathrm{H_2O_{(l)}} + 4\,\mathrm{e^-} \tag{2.6}$$

OER is a sluggish process that requires 4 electrons to proceed and is a competitor to UOR at high anodic potentials. Nickel-based catalysts have been researched considerably for applications of OER, but these studies can be used to study UOR as well. For instance, the synthesis of nickel double-layer hydroxides and nickel single-crystals have been reported, and can be used for UOR exploration.[28,54–58] However, improvement of OER may lead to decreased efficiency towards UOR, as they both occur on the anode.

2.3 Urea Oxidation Density Functional Theory

The electrochemical removal of urea on nickel can yield under-oxidized ($x < 6$) products of NH_3 and HNCO, neutral-oxidized ($x = 6$) products of N_2 and CO_2, and over-oxidized ($x > 6$) products of NCO^-, ${NO_2}^-$, and ${NO_3}^-$.The elementary step mechanisms by which urea dissociates on the surface give insight to pathways leading to respective products.[60–63] Density functional theory (DFT) has been performed to computationally predict the products, mechanisms, and rate-determining steps of urea oxidation on a NiOOH surface.[64,65] The product distribution is split into categories of under-, neutral-, and over-oxidation of the product nitrogen, as seen in Figure 2.2. For instance, the oxidation state of nitrogen in ammonia is -3 and is a result of the underoxidation of urea.

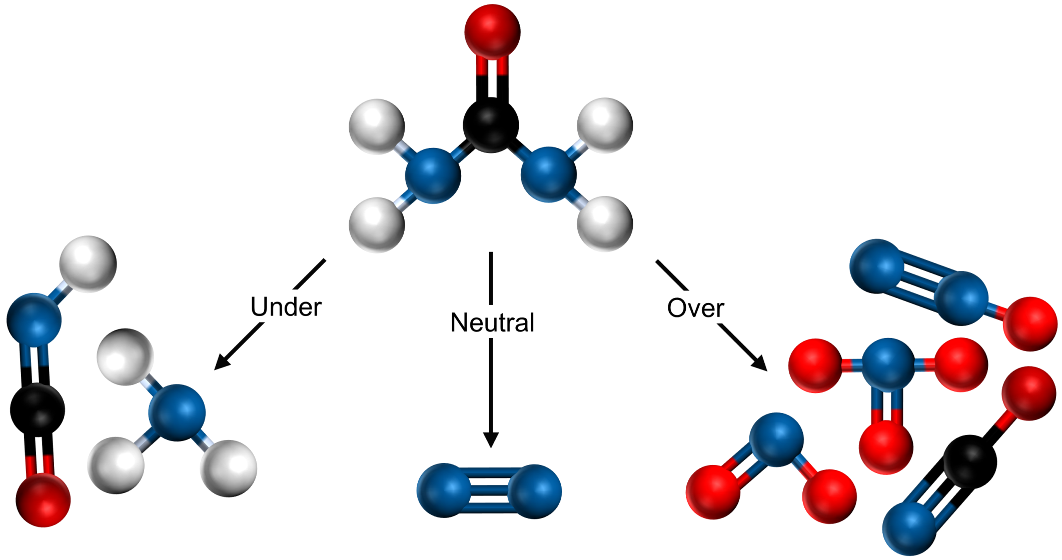

Fig. 2.2 Under, neutral, and overoxidation pathways of urea. Colors in the Figure: Red balls are O; blue balls are N; black balls are C; white balls are H.

Daramola *et al.* concluded that ammonia forms as a result of a non-electrochemical reaction with NiOOH. The group also concluded that neutral oxidation of urea was from an electrochemical interaction with NiOOH through several different OH^--assisted reaction pathways.[64] Li *et al.* identified the N–N coupling pathway, where two nitrogen atoms from one or two urea atoms bond together, favors the production of N_2. Li *et al.* also showed that overoxidation leads to the formation of ${NO_3}^-$, ${NO_2}^-$, and NCO^- species *via* the OH^--assisted cleavage of C–N bond in urea.[59] Both N–N coupling and C–N cleavage pathways, along with their respective free energy diagrams, are seen in Figure 2.3. The under- and over-oxidized species are undesirable as they are the molecules for negative environmental effects. The C–N cleavage, identified as the overoxidation mechanism, occurs less frequently when the surface has adjacent defects or vacancies. Tatarchuk *et al.* found that introducing copper into nickel doubled the N_2 selectivity from ${NO_2}^-$ of undoped nickel by altering the electronic structure and creating defects.[65]

A further improvement to selectivity includes the stabilization of the γ-NiOOH phase.[66]

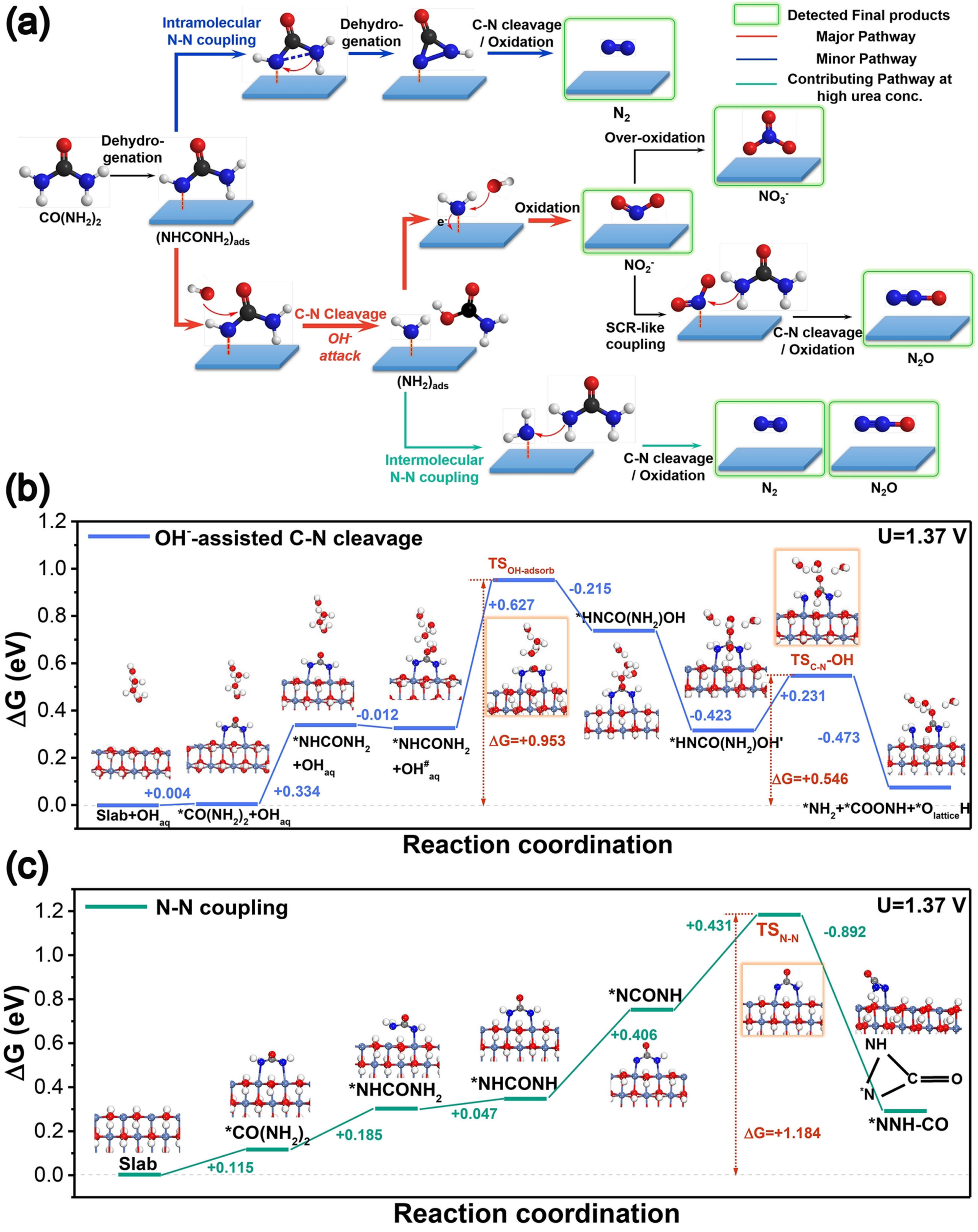

Fig. 2.3 a) Schematic illustration of the proposed UOR pathways. b,c) Gibbs free energy profiles calculated along the OH^--assisted C–N cleavage and N–N coupling pathways at 1.37 V_{RHE}. The numbers between two adjacent states in the profiles represent the free energy change (in eV) of each elemental step. Colors in the Figure: Cyan balls are Ni; red balls are O; blue balls are N; gray balls are C; white balls are H. Reprinted with permission from Li *et al.*. Copyright 2021 Angewandte Chemie International Edition.[59]

Nickel can occupy three distinct phases that have different physical and electronic properties. γ-NiOOH, the most disordered and active phase, naturally stabilizes into well-structured β-NiOOH with aging and electrochemical processing. The phase composition of the electrode has been shown to dictate the selectivity of products and must be well understood while performing electrochemical experiments.[66]

2.4 Nickel Morphology

Nickel, when exposed to oxygen, naturally oxidizes to nickel oxide on the surface as a thin film. Four unique phases of nickel oxide have been identified; the formation of each phase depends on the state of the electrode during oxidation. The nickel oxide phases form with increasing temperature by $\alpha \ll \beta < \gamma < \delta$.[67] A diagram of nickel oxide phases forming from nickel, with respective temperatures, is seen in Figure 2.4a. Low temperature, electrochemical applications of nickel do not require temperatures higher than 60°C, suggesting most air-grown oxides are α-NiO.[68]

The nickel oxide film transforms into a $Ni(OH)_2$ film when placed into an alkaline solution. The oxyhydroxide film on nickel is comprised of a complex structure of crystalline phases. The oxyhydroxide phases are formed through a combination of structural and electrochemical transformations, first identified by H. Bode *etal.*. The Bode diagram, presented in Figure 2.4b, is expanded to include polymorphs of both the hydroxide and oxyhydroxide phases along with the respective nickel oxidation states.[70,71] α-$Ni(OH)_2$ and β-$Ni(OH)_2$ are the two fundamental configurations of nickel hydroxide.[72]

The α-$Ni(OH)_2$ polymorph consists of turbostratic β-$Ni(OH)_2$ layers held together by intercalar water molecules.[71] The intercalated water adds a parameter of mobility within sheets, allowing adjacent layers to have little to no orientation relative to each other.[73] The α-$Ni(OH)_2$ phase can transform into β-$Ni(OH)_2$ phase by an aging or by an dehydration process as seen by the reaction:[70,74]

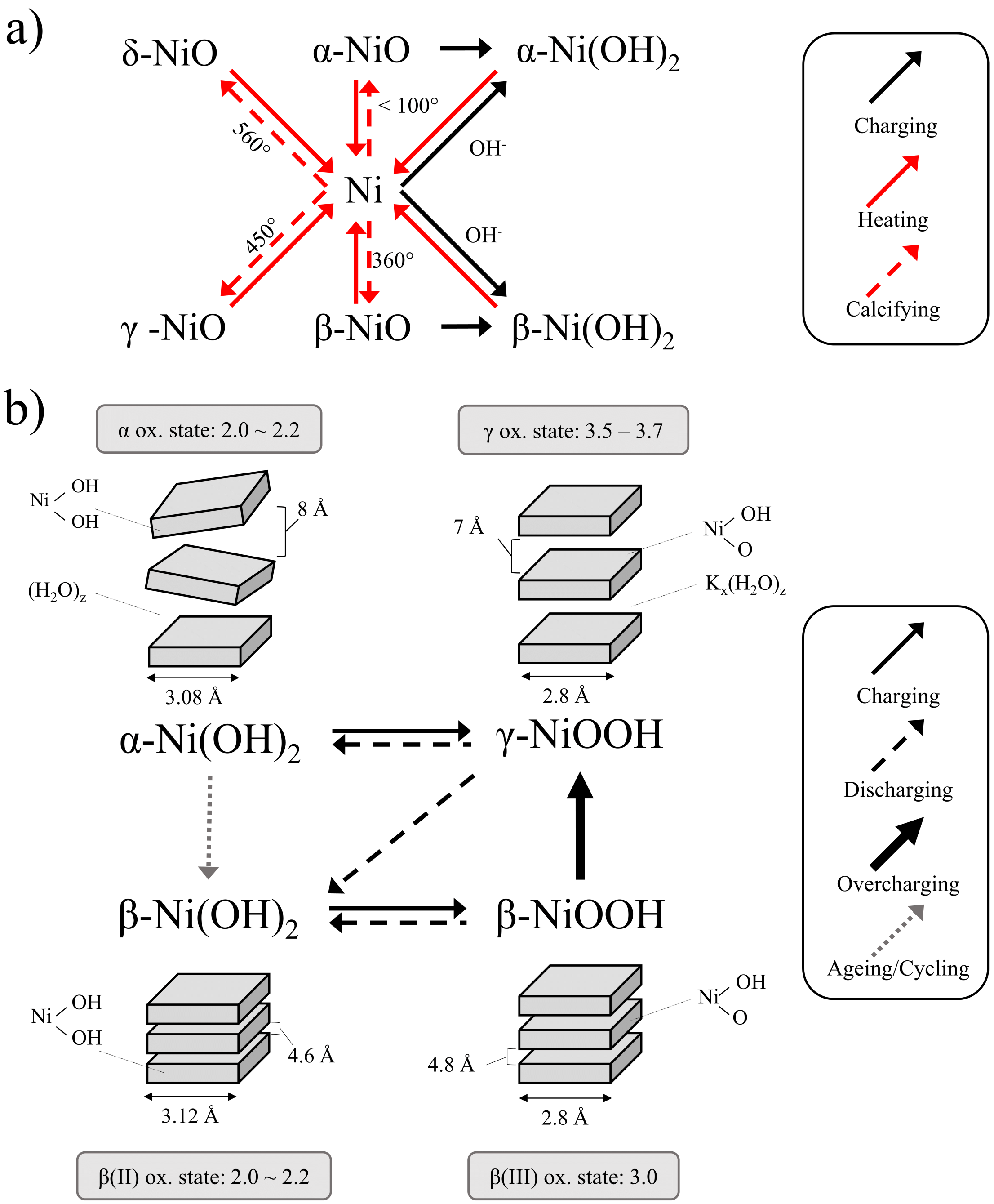

Fig. 2.4 A) Web of nickel oxide phases and b) of nickel hydroxide phases. Nickel oxidizes to nickel oxide and $Ni(OH)_2$ with different calcination temperatures (°C) and with hydroxide ions, respectively. $Ni(OH)_2$ oxidizes to NiOOH *via* different types of processes. Adapted from Van der Ven *et al.*.[69]

$$\alpha[3\,\mathrm{Ni(OH)_2}\ \cdot\ 2\,\mathrm{H_2O}\,] \longrightarrow \beta[3\,\mathrm{Ni(OH)_2}] + 2\,\mathrm{H_2O} \tag{2.7}$$

When a moderate bias is applied (> 1.35 V_{RHE}), α-$Ni(OH)_2$ and β-$Ni(OH)_2$ convert to their oxyhydroxide equivalents, γ-NiOOH and β-NiOOH, respectively. The γ-NiOOH phase also develops from β-NiOOH during overcharge, the application of a large overpotential that induces OER. The γ-Ni family exhibits varying intersheet distances like α-Ni species, with the space between layers commonly occupied by cations partially solvated with water.[71] The oxyhydroxide phases discharge to their respective hydroxide phases once a reducing potential is reached, although γ-NiOOH will also form β-$Ni(OH)_2$, leading to a complex web of Ni phases.[69,75,76]

The two active phases, β-NiOOH and γ-NiOOH, have been extensively studied for their differing OER properties. At high potentials, NiOOH layers may grow up to 1.4 μm, altering the the charge transport properties of the compact oxide layers.[77–81] The loss in activity at high potentials of nickel electrodes is assigned to the formation of inert Ni^{4+} centers on the surface.[78,82,83] The higher oxidation state (3.5–3.7) of γ-NiOOH supports a mixture of $Ni^{2/3/4+}$ centers on the surface, with the inert Ni^{2+} and Ni^{4+} species lowering the total activity of the electrode.[75,84] β-NiOOH, on the other hand, has an oxidation state of 3, suggesting that all electrochemically-active surface sites participate in reactions.[71] A consensus has emerged that the β-NiOOH surface is more catalytically active towards OER than γ-NiOOH.[85]

The expanded Bode diagram provides a high-level framework for the relationship between Ni polymorphs and practical electrochemical control of these surface species have been extensively studied. Pissinis *et al.* devised special potential-scan techniques to increase the growth of γ-NiOOH species, while Dose *et al.* used targeted electrochemical aging protocols to control capacity loss in nickel-lithium batteries.[86,87] Overcharge is a common descriptor for explaining the conversion of β-NiOOH to γ-NiOOH.[53,71,73,75,82,88–90] However, the addition of other metal atoms into the electrode causes nickel to change phases without the need for overcharge. Binary metals systems (nickel + metal) have improved electrochemical properties over pure nickel, allowing them to have better catalytic properties.[9,14,35,54,71]

2.5 Binary Metal Systems

Incorporating different metals into nickel alters electrochemical properties, such as charge transfer resistance, conductivity, charge capacitance, charge capacity, *etc.*, to tailor a nickel electrode to a specific application. Here, a select number of dopants are reviewed for their improvements to urea oxidation from pure nickel. Select dopants were used to synthesize catalysts seen in this report.

The intentional addition of iron into nickel creates a distribution of α and γ phases. The interlayer distances showed a split peak at 4.8 (α) and 7.7(γ) Å *via* wide-angle XRD.[54] Inclusion of iron, even in concentrations as low as 40 ppb, positively shifts the $Ni(OH)_2/NiOOH$ onset potential by 50 mV and decreases the OER onset potential by almost 200 mV.[57,63] Corrigan theorized the increased OER activity of iron-doped nickel was the result of a change of the rate determining step or from the increased conductivity from iron incorporated surface sites due to barrier effects.[91] Spanos *et al.* concluded that the increase in activity could not be solely explained by enhanced conductivity, meaning that iron impurities alter the surface and act as active sites.[92] Tafel slopes, the amount of additional applied potential required to observe a logarithmic increase in current, were used to determine the electrode characteristic of exchange current and rate constants. Tafel slopes for nickel iron hydroxide (57 mV dec^{-1}) were also reported to be lower than pure nickel (102 mV dec^{-1}), indicating that iron enhances the potential dependence of UOR.[93]

Introducing chromium into nickel changes the composition and the protective properties of the oxide layer. Incorporation of Cr has been shown to form double-layered oxide films, where Cr-based oxides [Cr_2O_3 or $Cr(OH)_3$] are seen at the metal/film interface, and Ni-based oxides are found at the electrolyte interface.[94] In terms of urea oxidation, the inclusion of chromium oxide into nickel has shown to depress the density of states at the Fermi level of the d-band of nickel, thereby weakening the $Ni\text{-}O_{urea}$ bond and decreasing the energy for adsorption.[95] Thus, including Cr has been shown to improve the UOR activity by altering the electronic structure of nickel hydroxide.

Introducing molybdenum into nickel also changes the nature of the oxide film. Mo is unevenly distributed within the passivated film, with Mo^{4+} residing at the metal/oxide interface and Mo^{6+} present at the electrolyte interface.[96] Mo does not form a phase-separated oxide species (Mo_xO_y) within the film. The proposed role of Mo oxide films is to inhibit localized breakdown by stabilizing cation vacancies.[97] Electrochemically, the inclusion of Mo causes nickel to complete the $Ni(OH)_2$/NiOOH transition at lower onset potentials.[98] The onset potential for UOR is also lowered from the addition of Mo into Ni, as UOR is dependent on the presence of NiOOH. Doping of Mo promotes coupling of the N—N bond on the intramolecular level as well as the fracture of the C=O in urea, promoting the selectivity of N_2 and CO_2 products.[99]

The inclusion of sulfides during hydrothermal growth produces NiS nanotubes composed of tight vertical nanosheets that lead to improved redox performance and ion transport properties. These structures also increase the electrochemical surface area by the high surface area of nanotubes and facilitate transport of reactants and products to and from the bulk electrolyte.[100] The increased transport helps prevent the limitation of mass transfer from the electrolyte to the electrode, thus allowing higher concentrations of urea to be utilized. However, the oxidation of urea in high concentration (300 mM) leads to an increased coverage of CO, which block active NiOOH sites on the nickel sulfide catalyst.[101]

Adding tin to nickel enhances the adsorption of urea by forming $Sn\text{-}O_{urea}$ and $Ni\text{-}N_{urea}$ bonds on the surface, as seen in Figure 2.5. This is beneficial for accelerating the oxidation of intermediates, effectively alleviating catalyst poisoning. Additionally, Ji *et al.* observed that the addition of tin into nickel altered the electronic structure of the hydroxide. The change in electronic structure has been shown to generate more interfaces, expose more active sites, and induce atomic distortions, thereby changing the oxidation state and increasing the conductivity of the surface.[90,102]

Hydrothermally incorporating borate into nickel modifies the electronic properties as well

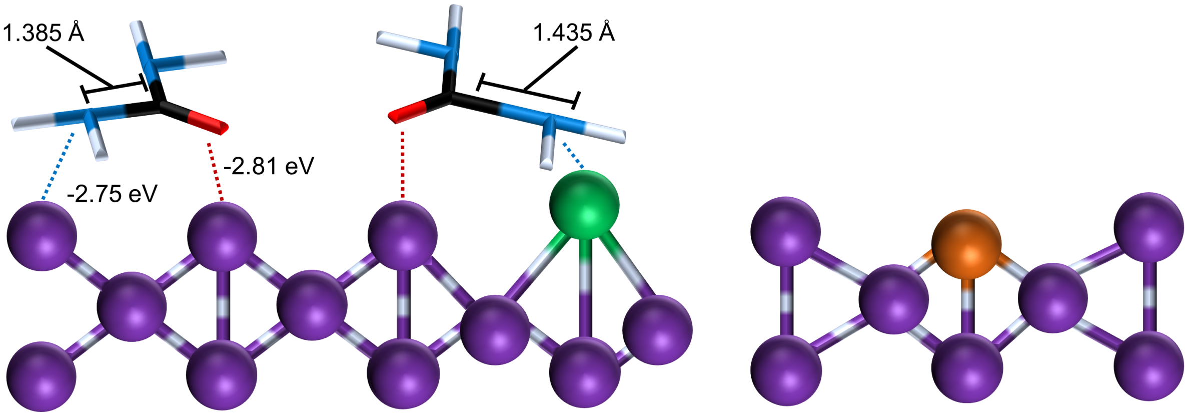

Fig. 2.5 Urea adsorption on nickel (purple) and tin (green) and boron (orange). The incorporation of tin (IV) weakens the adsorption energy of urea and stretches the C–N bond (from 1.385 to 1.435 Å).[64,102] The incorporation of boron forms a nucleophilic borate network with nickel, improving the deprotonation of urea with higher activities.[102–104]

as the adsorption/desorption properties of urea and surface intermediates. The nucleophilic borate network enhances the deprotonation ability of nickel.[99] The altered structure of nickel is seen in Fig. 2.5. The deprotonation of urea is believed to be a possible rate-determining step for UOR. Thus, it is believed that borate, along other nucleophilic heteroatoms, can improve the activity of nickel catalysts by lowering the energy needed for deprotonation.[102–104]

When cobalt is introduced, the nickel atoms reach a higher oxidation state during UOR, which promotes the electrons transfer and increases the conductivity of the surface. Wu *et al.* proposed the lowering the onset potential for nickel transition would also decrease the onset potential for urea oxidation, as both direct and indirect mechanisms rely on the formation of NiOOH. However, the cobalt atoms are themselves inactive, and decrease the number of electrochemically active nickel sites when added in excess. The benefit of integrating cobalt into the nickel hydroxide film was maximized at 20 wt%, before the total activity decreased with additional cobalt.[103]

2.6 Incidental Iron

2.6.1 Impact On Oxygen Evolution

Recently, the role of incidental iron impurities within an electrolyte has been studied in the context of improving the oxygen evolution reaction on nickel hydroxide catalysts.[57,106] Iron, once incorporated into the nickel hydroxide layer, has been seen to increase the oxidizing power of $Ni(OH)_2$, making Ni^{2+} require higher overpotentials to oxidize into $Ni^{3+/4+}$, as seen in Figure. 2.6.[54,91,107] This is seen by the increase of nickel transition onset potential during cyclic voltammetry in alkaline solutions. Additionally, the inclusion of iron has been shown to reduce the onset of the oxygen evolution reaction, also seen in Fig. 2.6.[57,108]

Incidental iron has been seen to increase the catalytic activity of $Ni(OH)_2$/NiOOH for OER through several mechanisms. Trotochaud *et al.* reported that the Fe-containing films showed a lower oxide thickness-dependence than to Fe-free films. This claim is consistent with iron affecting the charge-transfer mechanism, allowing more nickel centers to be active throughout the film.[57] The film also increased in crystallinity with aging, with Fe-containing films showing an increase in OER activity. Trotochaud *et al.*, Klaus *et al.* attributed the increase in OER activity to iron serving as the active site, with Dionigi *et al.* observing that nickel incorporates a γ-like structure wit the presence of iron.[54,57,106]

The role of incidental iron in crystalline structures of nickel hydroxide was investigated by Klaus *et al.*. Characterization techniques, such as Raman spectroscopy and quart crystal microbalance, allowed for the identification of phases during electrochemical oxidation of $Ni(OH)_2$ to NiOOH with and without iron-containing electrolytes. They reported that the addition of incidental iron shifts the main oxidation waves to more anodic potentials, which is congruent with other works.[35,91] They also identified phase transformations were observed with nickel after aging and overcharging with iron-free electrolytes, as seen by Figure 2.7. Therefore, the relationships of the Bode diagram (Fig. 2.4) are appropriate for iron-containing and iron-free electrolytes for the nickel hydroxide electrode.

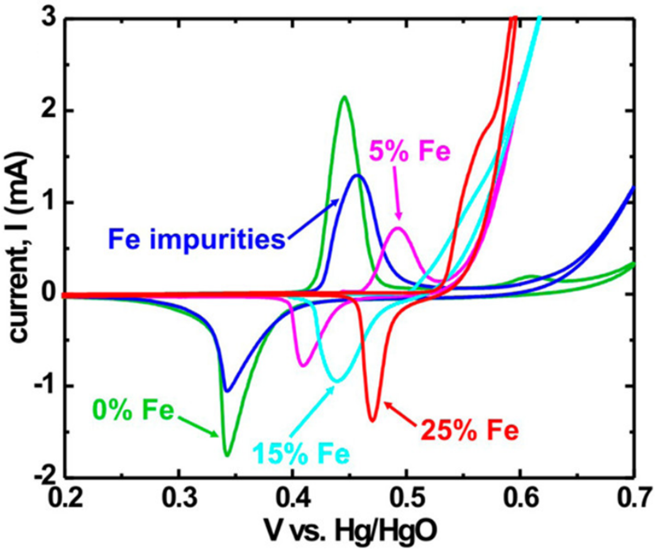

Fig. 2.6 Cyclic Voltammetry scans (10 mV s^{-1} for iron-containing nickel hydroxide films in 1 M KOH. Percentages represent deliberate integration of iron into the film, while the term impurities represent electrodes that were cycled in electrolytes containing <36 ppb Fe. Reprinted (adapted) with permission from Trotochaud *et al.*. Copyright 2014 American Chemical Society.[57]

2.6.2 Impact On Urea Oxidation

While several groups have identified the impact of incidental iron on oxygen evolution, Zemtsova *et al.* focused on unveiling the role of iron in the nickel-catalyzed urea oxidation reaction (UOR).[109] They report that urea oxidation occurs at a lower onset potential for an iron-free electrolyte than an iron-containing electrolyte, as UOR is dependent on the nickel transition onset potential. They observed a decrease in UOR activity in an iron-containing electrolyte due to the lowered OER onset potential.[65,110,111] Additionally, iron-free electrolytes were used to study the urea oxidation pathway at higher potentials for the formation of N_2 and nitrite/nitrate products without the presence of OER.

Chakrabarty *et al.*, although they did not purify the electrolyte from iron, focused on the activity of α/γ-Ni and β-Ni catalysts towards urea oxidation. α/γ-Ni were reported to have a lower nickel transition onset potential than β-Ni catalysts, which match the observations

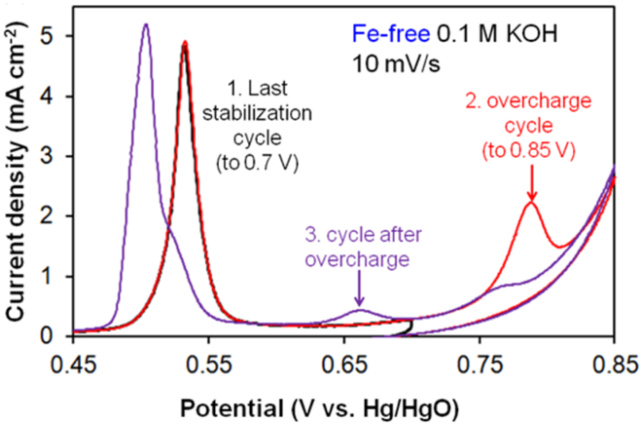

Fig. 2.7 Cyclic voltammogram of an aged $Ni(OH)_2$ film in 0.1 M Fe-free KOH (after 6 days of aging in 1 M Fe-free KOH) with a 10 mV s^{-1} scan rate. The electrodes were stabilized to 0.7 V_{RHE} before overcharge scan to 0.85 V_{RHE}. Reprinted (adapted) with permission from Klaus *et al.*. Copyright 2015 American Chemical Society.[106]

in literature.[76,86,91,106] The lower onset potential allows for urea to oxidize at lower potentials than β-Ni, which is congruent with UOR requiring NiOOH on the surface.[64,66]

These reports have studied the impact of iron incorporation and phase composition towards the urea oxidation reaction. Although extensive, they do not report the long term effects of urea oxidation on the nickel hydroxide electrode, particularly the role of urea during the reduction of $Ni^{3+/4+}$ to Ni^{2+}.

2.7 Ternary-Plus Metal Systems

Binary metal systems show an improvement for electrocatalysis beyond that of pure nickel. The doping of a heteroatom is intended to create more interfaces and atomic distortions to change the electronic structure of a reactive nickel.[102] Tweaking these parameters changes the adsorption and reaction coordinate of the reactants, intermediates, and products. Adjusting these parameters to reduce the energy of adsorption, reaction, and desorption provides insight to construct better catalysts for UOR. Adding more than one metal into nickel, thus forming a ternary-plus metal, has been seen to further improve oxidation of urea.

The addition of vanadium and cobalt into nickel has been shown to act as a catalytic promoter and stabilizer, respectively.[102] The cobalt increases the conductivity of the surface and prevents CO poisoning of the surface during oxidation.[112] Vanadium receives electrons from surrounding metal ions, increasing the carrier concentration and electronic conduction.[113] The benefits of adding Co and V combine, resulting with a ternary catalyst that has higher UOR activity and stability than of its NiCo and NiV constituents. Nickel-cobalt-molybdenum (NiCoMo) has been also seen to be a good UOR catalysts with high catalytic activity, fast kinetics, low onset potentials, and high stability. The molybdenum forms a complex where Mo^{6+} and Mo^{4+} coexist, leading molybdenum to stabilize the Ni and Co arrangement.[96] Molybdenum can stabilize nickel with other metals as well, as seen in Xu *et al.*'s synthesized $FeNi_3$-MoO_2 heterostructures.[114]

Additionally, incorporation of other metals aids to the stability of nickel by further passivating the surface and preventing corrosion. The role of Mo in NiCr films has been seen to promote the film growth of Cr_xO_y oxides. The proposed role of incorporated Mo stability arises from Mo^{6+} replacing Cr^{3+} vacancies, thus reducing the number of accessible point defects susceptible to corrosion.[115] The increased concentration of Mo in corrosion pits and crevices shows the ability for Mo to prevent further corrosion, re-passivating the surface and allowing the oxide layer to self-heal. While these corrosion mechanisms are useful for extending the lifetime of the electrode, an understanding of UOR on these NiCrMo surfaces is necessary for deployment in an application-based setting.

Stainless steel is an attractive class of alloys because of its passivity in chloride, high activity, and commercial availability. Stainless steel 316 (SS-316) and 304 (SS-304) are two common alloys used in water desalination, marine environments, ship hulls, super heaters, pharmaceutical industries, turbine blades, and petrochemical industry.[116–118] Along with there superb corrosion properties, SS-304 and SS-316 are able to conduct OER at as low as 450 mV and 470 mV overpotentials at 10 mA cm^{-2} and pH 13.[58,116] Stainless steels show catalytic properties and corrosion-resistance for OER, and can potentially be used for increased urea oxidation capabilities as well. Additionally, these commercially available alloys serve as reproducible electrodes amongst different laboratories, enabling more consistent measurements for Ni electrodes.

2.8 Research Hypotheses

This literature review presents up-to-date information of nickel and nickel-based catalysts for use in urea oxidation. Several hypotheses are drawn from this information, aiding to the progression of the field. These hypotheses are presented as:

1. The effect of γ-NiOOH and β-NiOOH on the urea oxidation reaction can be studied by developing the phases with extended potential cycling and characterizing the resulting surface according to oxygen evolution kinetics.
2. The urea oxidation reaction can be studied on the phases of NiOOH phases within short time scales, since urea can affect the composition of nickel phases over time scales longer than UOR.
3. Alloying Cr and Mo with nickel improves the urea electrooxdiation properties of pure nickel within an alkaline media.
4. Nickel foams with hydrothermally-grown mixed-metal crystals improve the overall urea removal current to pure nickel foams, allowing for smaller geometric areas to be used within a portable dialysis device.

Chapter 3

METHODOLOGY

3.1 Overview

An explanation of the electrochemical and non-electrochemical methods are included, as these techniques are used for characterizing the surface, oxygen evolution reaction, and urea oxidation reaction on nickel-based electrocatalysts. The phase, facet, oxide layer, roughness, electrode composition, and solution composition must be controlled to obtain a well-defined, reproducible surface of nickel hydroxide. The results generated within this report are based on the electrochemical setup, electrode preparation, and electrochemical procedures found below.

3.2 Electrochemical Setup

A three-electrode cell was used to perform all electrochemical experiments. The three-electrode cell housed a counter, reference, and working electrode, as seen in Figure 3.1. The working electrode, the electrode of interest, was examined by adjusting the applied voltage or current measured with respect to an Hg/HgO reference electrode. The counter electrode, a high-surface area platinum electrode (~ 5 cm^2), was responsible for supplying current to the working electrode. All electrodes were controlled and monitored by a Solartron 1287A potentiostat coupled with a Solartron 1252A frequency response analyzer. Together, the system was able to perform the electrochemical measurements of cyclic voltammetry, potentiostatic holds, and electrochemical impedance spectroscopy.

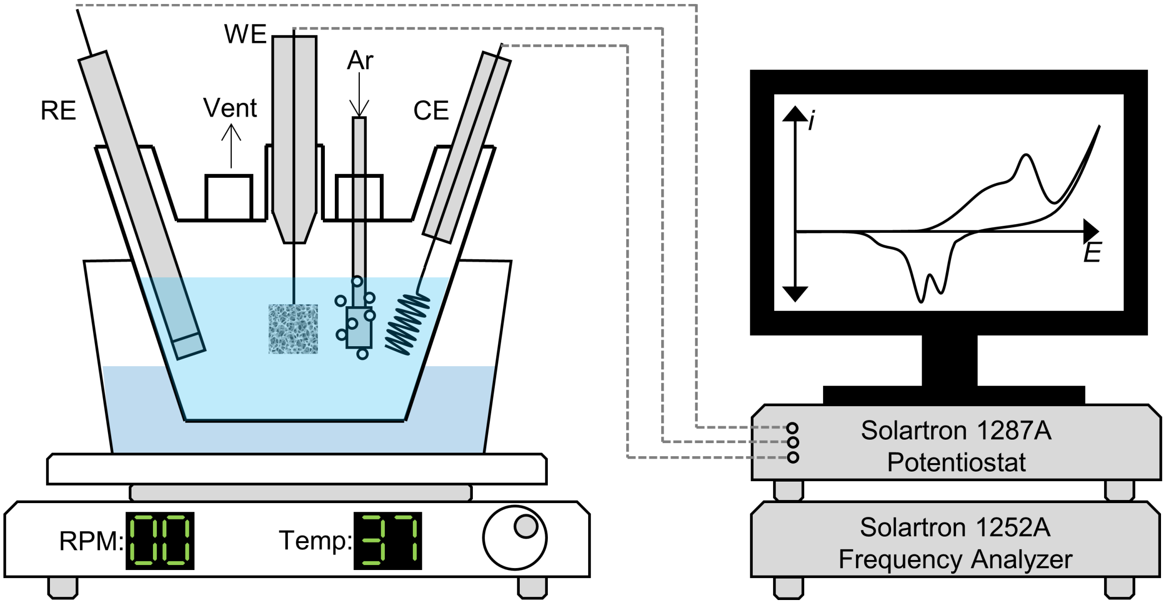

Fig. 3.1 Diagram of three-electrode cell with reference electrode (RE), working electrode (WE), and counter electrode (CE). The electrodes connect to a potentiostat and a frequency response analyzer that interact with a computer to perform electrochemical experiments. The three electrode is submersed in a temperature-controlled water bath.

3.3 Electrolyte

3.3.1 Overall

A supporting electrolyte within the three electrode cell allowed for reactants to move to the working and counter electrodes during electrochemical reactions while allowing ions to migrate to balance the movement of charge. In this study, the supporting electrolyte contains potassium hydroxide (KOH) with varying concentrations (0.5 - 1 M KOH) to ensure high conductivity. For urea oxidation studies, urea was added into the supporting electrolyte to simulate dialysate-relevant concentrations (10 mM) or prevent mass transfer limitations on the electrode ($>$ 50 mM) to determine reaction kinetics. Prior to each experiment, the electrolyte was sparged with of argon to remove dissolved oxygen and to prevent CO_2 absorption from the atmosphere.

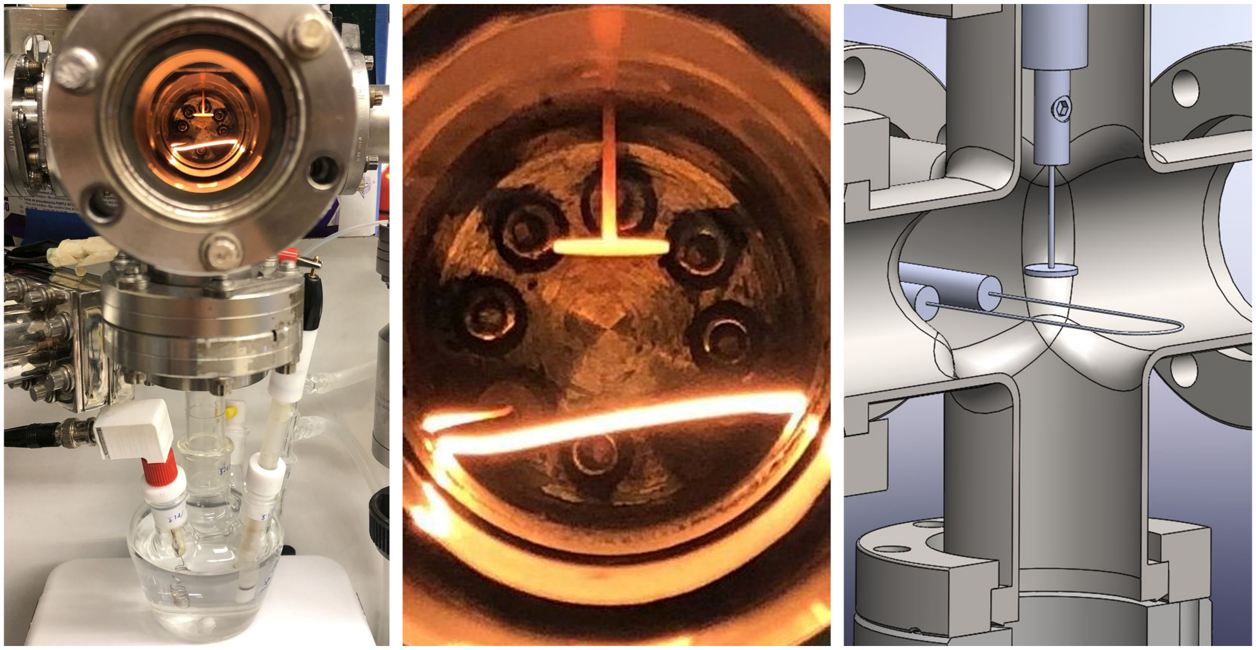

Fig. 3.2 Left: vacuum chamber and three electrode cell. Center: close-up of the vacuum chamber where the working electrode was heated to thermally desorb oxides. Right: 3D-rendered cross section of vacuum system showing the filament and electrode position during heating

3.3.2 Iron Removal

The procedure for removing incidental iron from alkaline solutions was adopted from Trotochaud *et al.* and Zemtsova *et al.*. In a H_2SO_4-cleaned 50 mL polypropylene centrifuge tube, ∼2 g of 99.999% $Ni(NO_3)_2 \cdot 6\ H_2O$ were dissolved in ∼4 mL of DI water. 20 mL of 0.5 M KOH were added to precipitate high-purity $Ni(OH)_2$. The lot ana The mixture was shaken and centrifuged, and the supernatant was decanted. The $Ni(OH)_2$ then underwent three washing cycles by adding ∼20 mL of DI water and ∼2 mL of 0.5 M KOH to the tube, redispersing the solid, centrifuging, and decanting the supernatant. Finally, the tube was filled with 30 mL of 0.5 M KOH for purification. The solid was redispersed and mechanically agitated until there were no large particles. 20 mL of 0.5 M KOH was added and agitated for at least 10 min, followed by at least 48 h of resting. The mixture was centrifuged, and the purified KOH supernatant was added to the three electrode cell immediately and used for electrochemical experiments. This procedure has been seen to lower the concentration of incidental iron from 60.6 to 9.4 ppb from 1 M KOH solutions.[108] Figure 9.1 in Appendix shows a graphical representation of the electrolyte cleaning process.[57,108]

3.4 Electrode Preparation

A nickel electrode can be single or multiple phases, be smooth or rough, or have thin or thick oxide layers, each exhibiting a different electrochemical behavior. Therefore, the best practice is to reset the surface by removing roughness, removing oxides, and having only one phase. Here, preparation of metallic, alloyed, and hydrothermal nickel forms are explained to obtain a consistent electrochemical response in alkaline solution.

3.4.1 Metallic Nickel Preparation

Metallic electrodes (flat, planar geometries) were used to finely control the surface. The electrodes were polished to a mirror surface to smooth any roughness that may have occurred from the previous experiments or from the growth of oxides from the atmosphere. The oxide layers were removed and the phase was reset by heating the nickel electrode to above 600 °C in vacuum by electron bombardment[67] The vacuum chamber, as seen in Figure 3.2, was connected to an electrochemical cell through a gate valve and a 2.75" ConFlat to 14/20 glass connection. The ConFlat connection had a gas port and was used to replace the cell headspace with argon. Once heated and cooled under vacuum, the electrode was lowered into the three electrode cell under argon flow to prevent oxygen exposure. When the electrolyte's surface tension was broken, the electrode was raised to form a meniscus on the surface. The meniscus prevented reactions from occurring on the sides and top of the electrode and improved the removal of gaseous products from the electrolyte.

3.4.2 Alloyed Nickel Preparation

Nickel alloys cannot be heated up to high temperatures due to the annealing properties of the metal. Stainless steels, which are high in nickel content, will form different material phases at varying temperatures. For example, carbon steel can adopt austenite, ledeburite, and pearlite at the same wt. % carbon with increasing temperature.[119] Thus, nickel alloys were polished to a mirror finish to remove any roughness and sonicated sequentially in DI water and ethanol for 10 minutes each to remove any leftover polish. The electrodes were then electrochemically reduced at -0.48 V_{RHE} in alkaline solution to remove any nascent oxides.

3.4.3 Hydrothermal Nickel Preparation

Nickel, when fashioned into a high-porosity foam, allowed for fluid to occupy space throughout the electrode, thus allowing for a higher reaction rates for a given geometric area than planar nickel and alloys. The electrochemically active area was of nickel foam was further increased by hydrothermally growing nickel-metal hydroxides. Nickel foam (99.5 wt %, 95% porosity) was laser cut to 1 cm^2 pieces and used as a substrate for hydrothermal growth. The nickel foam (NiF) was sequentially sonicated in deionized water (DI, Millipore-Q water system), ethanol (95 wt.%), and 3 M HCl for 10 minutes each before being placed in the hydrothermal growth chamber. The percentage of metal grown on the working electrode was targeted to be 1 mol%, with the remainder as nickel. The metallic salts of 1.00 mg of $Cr(NO_3)_3 \cdot 9H_2O$ (99.9 wt.%), 1.01 mg of $Fe(NO_3)_3 \cdot 9H_2O$ (99.95 wt.%), 0.39 mg of $KMnO_4$ (>99 wt.%), and 1.75 mg of $(NH_4)_6Mo_7O_{24} \cdot 4H_2O$ (99.97 wt.%) were added and mixed with 20 mL DI water in separate vials. Then, 72 mg $Ni(NO_3)_2 \cdot 6H_2O$ (99.9 wt.%) and 150 mg urea (99.6 wt. %) were added and mixed into each vial. The solutions were individually transferred into a 25 mL Teflon-lined stainless-steel hydrothermal vessel. Four pieces of NiF are placed vertically into the solution in the vessel. The vessel was sealed and placed in a 105 °C oven for 12 hours. The vessels were cooled to room temperature before opening. The hydrothermally grown NiF pieces were sonicated sequentially in DI water and ethanol for 10 minutes each to remove loose particulates. The NiF electrodes did undergo reduction, as thermally reducing or electrochemically reducing destroys the hydrothermally grown crystals.

3.5 Electrochemical Experiments

3.5.1 Cyclic Voltammetry

Cyclic voltammetry (CV) is a useful electrochemical technique capable of probing redox processes of an electrode surface. During this technique, a potential was increasingly applied to an electrode with a scan rate ν until the switching potential E_λ was reached, and the potential was decreased with ν to the starting potential. The time, potential, and current were collected during the cycle by the potentiostat. Figure 3.3a shows a sample CV along with the locations of commonly defined potential terms. The half-wave potential $E_{1/2}$ was defined as the average potential between the anodic E_A and cathodic E_C peaks while the onset potential E_{OS} was defined as the location where the extrapolated current of a reaction reaches zero. These terms are useful for comparing characteristics between electrode catalysts.

Figure. 3.3b shows a sample CV of a nickel hydroxide electrode in alkaline solution. Two reactions take place during this CV: the $Ni(OH)_2/NiOOH$ transition and the oxygen evolution (OER) reaction. Starting from E_1, no current passes as there is no reaction taking place. Nickel starts to oxidize as the potential reaches the onset potential. The amount of nickel atoms participating in $Ni(OH)_2/NiOOH$ is limited by the number of electrochemically accessible $Ni(OH)_2$ sites. The current increases until a maximum is reached. The current decreases as the number of reactions decreases as NiOOH replaces $Ni(OH)_2$. At higher potentials, hydroxide ions react on the surface to produce oxygen *via* 2.6. OER is not reversible and only exists in the anodic region, as it does not form hydroxide ions on the reverse sweep. OER does not have an easily discernible $E_{1/2}$, thus E_{OS} is the only viable parameter for comparison between electrodes. The nickel transition is a reversible reaction, therefore the existence of anode peak must mean the existence of a cathode peak, assuming no dissolu-

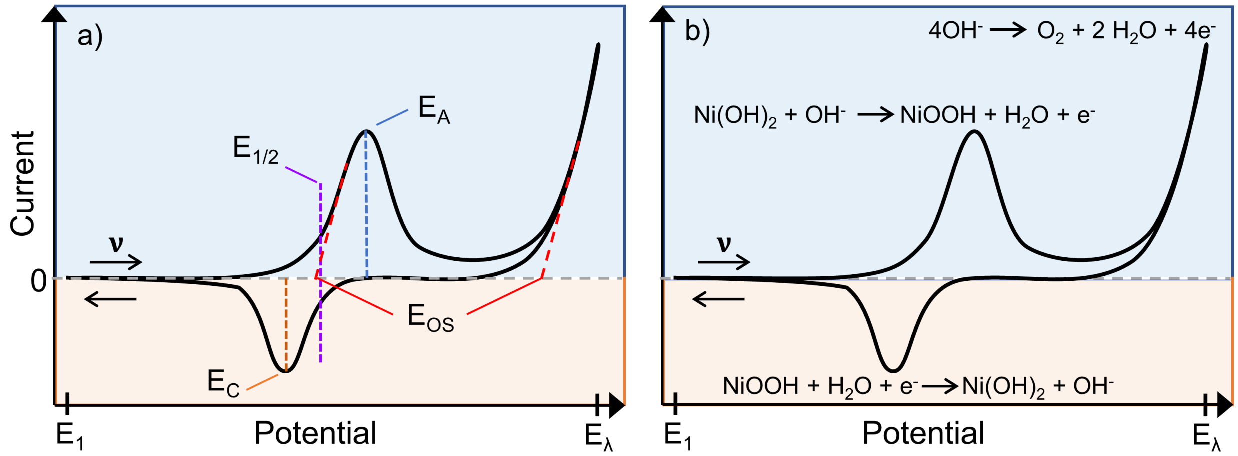

Fig. 3.3 Cyclic voltammetry (CV) of a) nickel transition and oxygen evolution and b) locations of potential definitions. Blue and orange regions indicate anodic and cathodic regions of activity, respectively

tion from the electrode. The peak during reduction occurs from the reduction of NiOOH back to $Ni(OH)_2$. The reverse peak is far enough away from the oxygen evolution curve and, since the nickel transition is reversible, is integrated to find the charge passed during $Ni(OH)_2/NiOOH$. The charge is then correlated to the reduction-based electrochemically active surface area A_{R-ECSA} by Equation 3.1:

$$A_{R-ECSA} = \frac{Q_{\mathrm{r}} N_A}{nF\Gamma} \tag{3.1}$$

where Q_{r} is the NiOOH reduction charge, N_A is Avogadro's number, n is the number of electrons involved in $Ni(OH)_2/NiOOH$ ($1e^-$, Reac. 2.3), F is Faraday's constant, and Γ is the NiOOH site density. A Γ value of 5.7×10^{14} cm^{-2} is calculated by the average unit cell planar density of the (100), (110), and (111) planes of NiOOH (a = b = 0.283 nm, α = 90°).[120] The reduction integration allows for the number of active sites to be calculated for use in turnover frequency analysis. However, the capacitance effects that take place during cyclic voltammetry make the calculated number of sites and electrochemically active surface area (ECSA) a close approximation.

Since the capacitance is surface sensitive, it too is can be used to calculate ECSA. The double layer is comprised of two parallel layers of ions surrounding the surface as seen in Figure 3.4a. The first layer is adsorbed onto the surface while the second layer is attracted to the first layer by opposite charge. The second layer is impacted by non-faradaic reactions and is influenced by ν. The double layer capacitance is found by cycling ± 50 mV around the open circuit potential E_{OCP}, a potential region where no faradaic effects occur, as seen in Fig. 3.4b. The charging current at open circuit potential i_{OCP} is determined by Eq. 3.2 by the average of the anodic i_c and cathodic i_c currents.

$$i_{OCP} = \frac{1}{2}(i_a - i_c)_{OCP} \tag{3.2}$$

The double layer capacitance C_{dl} is found by the slope of linear fits of the charging current *vs.* ν at E_{OCP} through Eq. 3.3 and seen in Fig. 3.4c.

$$C_{dl} = \frac{\Delta i_{OCP}}{\Delta \nu} \tag{3.3}$$

The capacitance electrochemically active surface area, A_{C-ECSA}, is calculated by Eq. 3.4

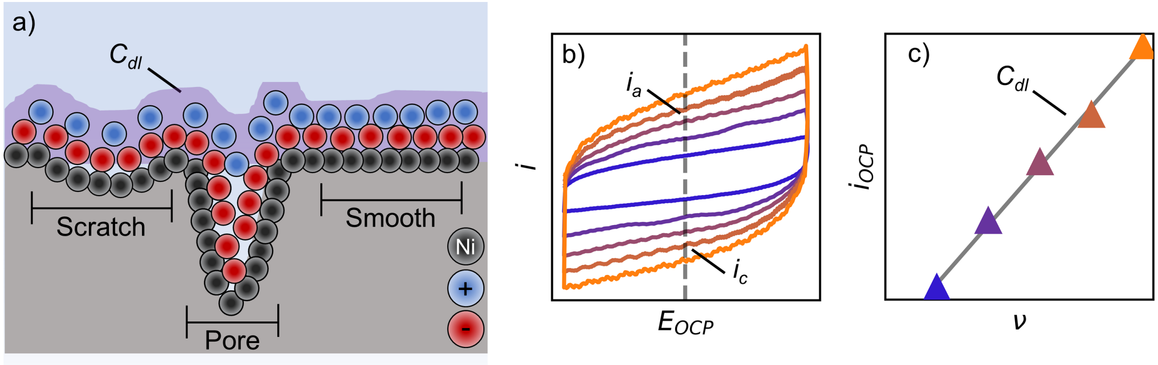

Fig. 3.4 a) Visual representation of a double layer acting on the nickel surface. b) cycling within a non-faradaic region to find the anodic and cathodic currents at open circuit potential. c) finding double layer capacitance as a linear fit to the difference anodic and cathodic currents and scan rate.

on the basis of a reference charge density for nickel of $\hat{C}_{\mathrm{Ni}} = 40$ µF cm^{-2} obtained from literature.[121]

$$A_{C-ECSA} = \frac{C_{dl}}{\hat{C}_{Ni}} \tag{3.4}$$

The reduction and capacitance techniques have conditions that must be met in order to provide accurate values. The reduction method relies on the one-electron exchange during $\mathrm{Ni(OH)_2/NiOOH}$ and cannot be used when another reaction relies on the nickel transition. Organic molecules oxidize on nickel before the reduction transition is complete, effectively dampening the current response read by the potentiostat. The capacitance method is only valid for regions of little to no defects, as seen by the "scratch" and the "smooth" sections of Fig. 3.4a. Pores and pits have a poor representation of the boundary layer, effectively making them invisible during the scanning method used in Fig. 3.4b. Additionally, the reference value of $\hat{C}_{\mathrm{Ni}} = 40$ µF cm^{-2} represents a perfectly flat, smooth piece of nickel and can be used for other surfaces, like nickel-based alloys, with a grain of salt. Both methods applied to a flat, smooth nickel electrolyte in pure alkaline electrolyte result in similar values of $ECSA$.[121]

Although the cyclic voltammetry profiles in Figure 3.3 show a single peak in the reverse sweep, the presence of different nickel phases may give a multi-peak response. An example of a CV for the multiple peaks identified with the respective phases and oxidation state is seen in Figure 3.5a. The oxidation peak has an α-$\mathrm{Ni(OH)_2}$/γ-NiOOH transition as well as a β-$\mathrm{Ni(OH)_2}$/β-NiOOH transition are typically are too close to deconvolute (the peaks are exaggerated in 3.5a for clarity). The reduction curves, however, can be deconvoluted using a generalized lateral interactions model (GLI).[122] Based off the work of Alévêque & Levillain, the GLI model is based on the following assumptions:

- The surface coverage θ is equal to the sum of the coverage of the reduction θ_R and oxidation θ_O species
- The electroactive species on the electrode are distributed with a unimodal statistical dis-

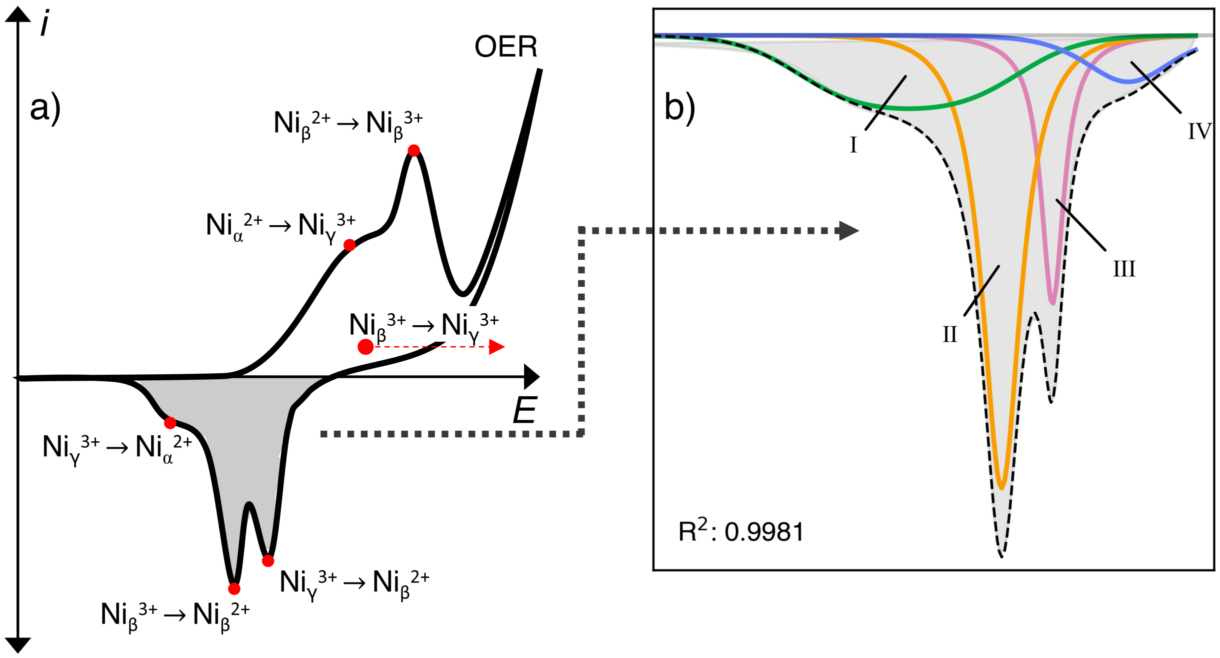

Fig. 3.5 Cyclic voltammetry of nickel with multiple phases on the surface and b) reduction peak fitting with a generalized lateral interactions model.

tribution

- The electrochemical rate constant of the redox reactions are independent of coverage
- The number of electrons transferred between the oxidizing and reducing species is one

These assumptions, combined with the Butler-Volmer equation (Eq. 3.5) and the Nernst equation (Eq. 3.6), give an electrochemical basis for deriving the model.

$$i = i_O[e^{\frac{\alpha nF}{RT}(E-E_{eq})} - e^{\frac{(-1-\alpha)nF}{RT}(E-E_{eq})}] \tag{3.5}$$

$$E = E_{eq} - \frac{RT}{nF} ln(Q_{RXN}) \tag{3.6}$$

Where i_o is the exchange current, α is the transfer coefficient, and E_{eq} is the equilibrium potential. Q_{RXN} is defined as the ratio of products over reactants. The derivation using these two equations with surface coverage leads to a function recursion, where determining the value of i requires i to be defined. Alévêque & Levillain circumvented this by incorporating a generalized sigmoid function with additional fitting parameters B and T. The GLI function is complete as shown:

$$\begin{aligned} i(E) =& \frac{n^2F^2A\nu}{RT}\frac{Te^X}{(1+e^X)^2-2Be^X} \\ \text{where} & \left\{ \begin{array}{l} X = \dfrac{nF}{RT}(E-E_{eq}) + \dfrac{2B}{1+e^{\left(-\frac{nF}{RT}\frac{(E-E_{eq})}{(1-\gamma B)}\right)}} \\ \gamma = 0.4 \\ |B| < 2 \end{array} \right\} \end{aligned} \tag{3.7}$$

where E_{eq}, B, and T are fitting parameters based on experimental data i and E obtained from cyclic voltammetry. The GLI model is used to deconvolute the reduction current of a nickel hydroxide electrode in alkaline solution, as seen in Figure 3.5b. While the Bode diagram (Fig. 2.4b) contains 3 reduction reactions (dashed arrows), four peaks are fitted to improve the accuracy of the major peaks. The extracted parameters, E_{eq}, B, and T, provide information for quantitatively finding the amount of a phase of nickel for a provided set of reaction conditions. Furthermore, this information can provide the relative activities of β-Ni$(OH)_2$ and α-Ni$(OH)_2$ towards UOR and OER, respectively.

3.5.2 Polarization Curve

A polarization curve is a fundamental technique for assessing the performance of an electrode catalyst for a desired application. For instance, the operating conditions for an electrolyzer are determined by the current-potential relationship found in the respective polarization curve for the device. A polarization curve is generated by staircase potentiostatic steps, where a potential is held until a steady state current is reached and incrementally increased, as seen in Figure. 3.6a. The steady state current is plotted against the respective potential, as seen in Figure 3.6b.

While the steady state current response can be estimated with the Butler-Volmer equation, the measured current response changes over time when a particular potential is applied to an electrode. Most of the current change occurs at the beginning of the potential switch at $t = 0$ due to a change of equilibrium of the system. Here, a general system is defined as the working electrode surface with an aqueous reactant in the the electrolyte, as seen in Figure 3.7a. Near $t = 0$, the system has the highest equilibrium imbalance, as there is a relatively high amount of oxidizeable molecules on the surface. The slow speed oxidized products moving from the electrode pose a diffusion-limited current. If the applied potential is sufficiently high, the current follows a diffusion-limited current response noted by the Cottrell equation as seen as

$$i_d(t) = \frac{nFAD_O^{1/2}C_{O,B}}{\pi^{1/2}t^{1/2}} \tag{3.8}$$

where $i_d(t)$ is diffusion-limited current, D_O is the diffusion coefficient of oxidized products

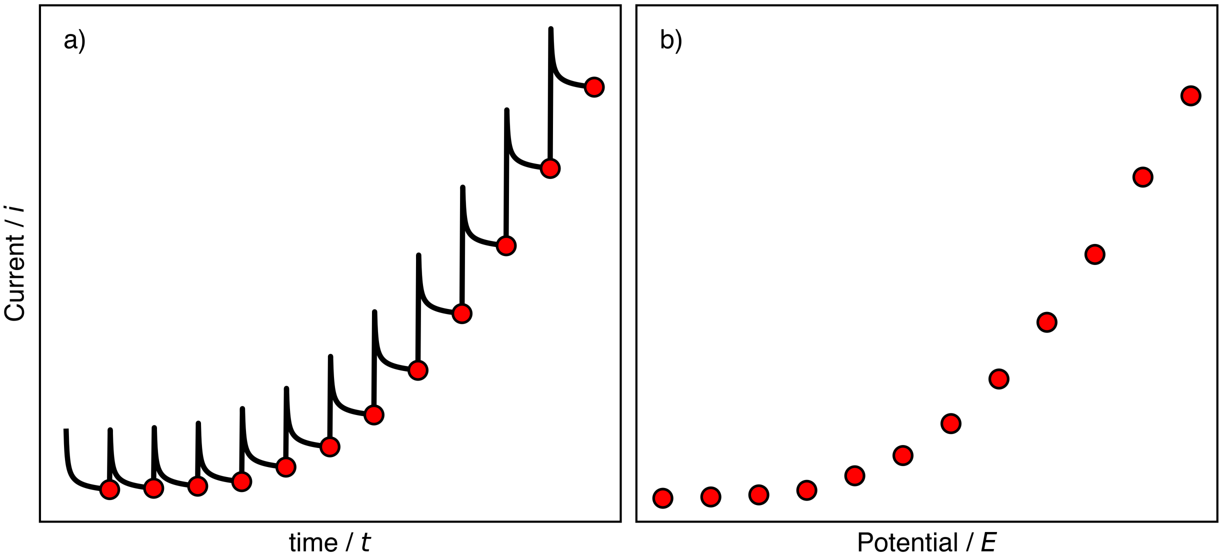

Fig. 3.6 a) Sample staircase potentiostatic steps, where the steady state current is plotted as b) a polarization curve.

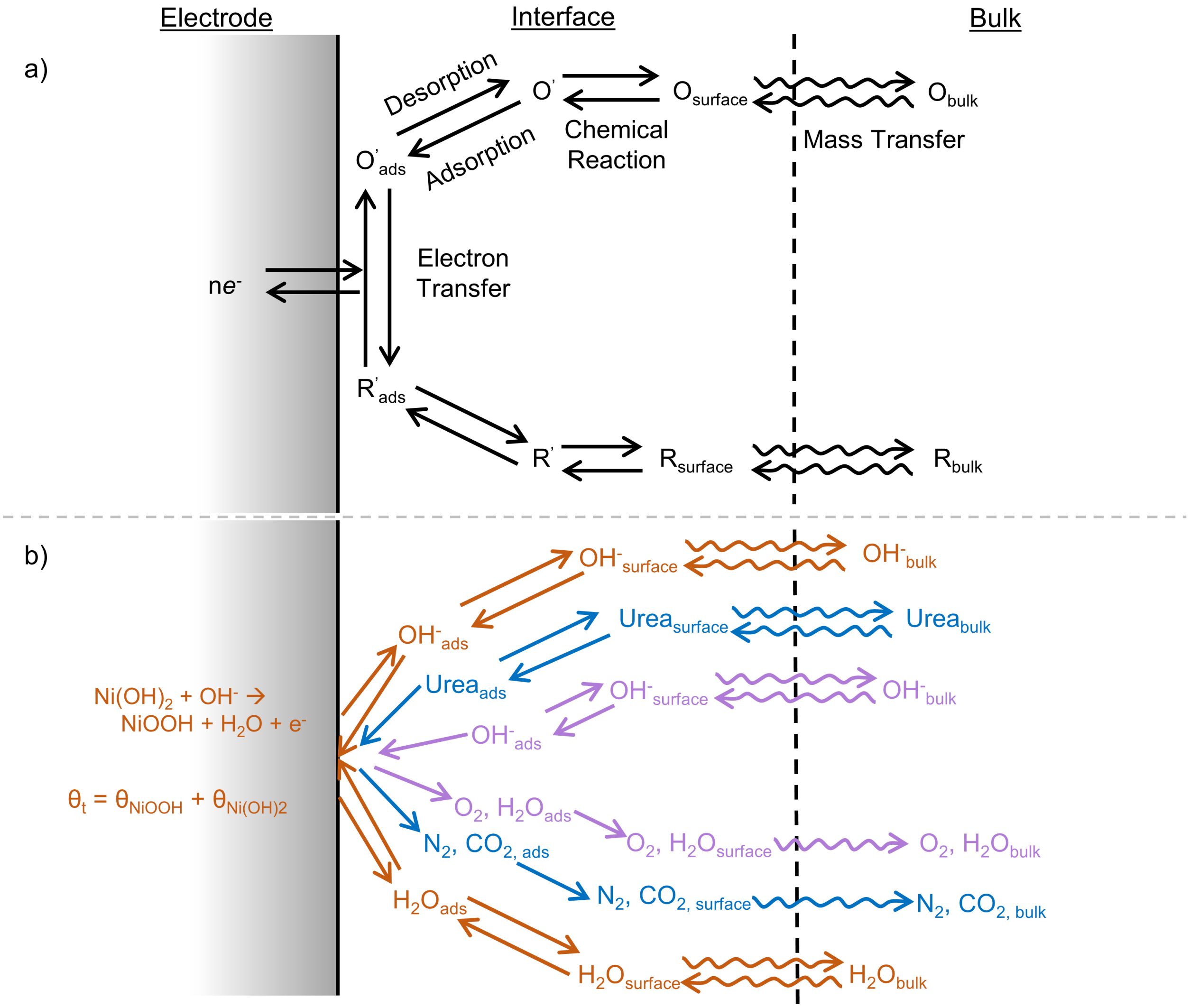

Fig. 3.7 a) Pathway of a general electrode system. B) Pathways of nickel transition (orange), urea oxidation (blue), and oxygen evolution (pink). The number of NiOOH sites (θ_{NiOOH}) is limited to the number of available Ni(OH)$_2$ sites ($\theta_{Ni(OH)_2}$). Note the urea oxidation pathway does not include the underoxidation and overoxidation pathways.

into the bulk, $C_{O,B}$ is the bulk concentration of oxidized products, and t is time. However, the system in this study is more complicated than the general system in Fig. 3.7a. A more-representative scheme of the nickel electrode is seen in Fig. 3.7b, where the nickel transition, urea oxidation, and oxygen evolution pathways are included.

OER follows the general reaction scheme since the reactants are in the aqueous phase and produces a steady state current. UOR presents a steady state current at potentials above the nickel transition onset potential, as urea is theorized to consume electrons or NiOOH sites through Reac. 2.1 or Reac. 2.2, respectively. The diffusion coefficient in Eq. 3.8 can be determined by applying a sufficiently high potential and recording the current decay *vs.* time. Additionally, the time required for the current to decay to steady state marks the minimum testing time for generating a polarization curve (per potential step). The potential hold time is generally extended much further than the time frame for a Cottrell response, typically up to 10-30 minutes per step, to ensure the current has reached steady state.

The steady state current for UOR, as well as OER, is useful for determining turnover frequencies (TOF). TOF analysis allows for the comparison of catalysts on a per-site basis instead of comparing current densities across the entire electrode. TOF is given by

$$\mathrm{TOF} = \frac{i_{SCP} N_A}{F n \Gamma} \tag{3.9}$$

where i_{SCP} is the staircase polarization current, n is number of electrons involved in the reaction (6 e^- for neutral-oxidation UOR, 4 e^- for OER), and Γ is the number of NiOOH sites. The TOF is a metric to compare the intrinsic activity among different electrodes. The activity based on TOF derived from Eq. 3.9 looks at the rate of reaction based on current, but does not take into consideration the range of oxidation products. Therefore, TOF is useful for only comparing the rate of urea removal or oxygen production on a per-site basis, but not for comparing the relative distributions of products.

3.5.3 Electrochemical Impedance Spectroscopy

Electrochemical Impedance Spectroscopy (EIS) is a technique useful for probing electrical, electrochemical, and physical processes occurring in an electrochemical system. EIS is performed by applying a set potential and perturbing an electrode with an additional sinusoidal potential and recording the sinusoidal response. The perturbation is swept from high to low frequencies to measure the fast and slow system responses. The current response is a sinusoidal signal similar to the potential signal, but shifted in phase and amplitude as seen in Figure 3.8a. Here, the input potential and output current are defined as:

$$\begin{aligned} E(t) &= E_o cos(\omega t) \\ i(t) &= i_o cos(\omega t - \phi) \end{aligned} \tag{3.10}$$

where E_o and i_o are magnitudes of potential and current, ω is angular frequency, and ϕ is the phase angle shift. The sinusoidal signals are broken into real and imaginary components using Euler's formula:

$$\begin{aligned} e^{jx} &= cos(x) + j\ sin(x) \\ Me^{j(\omega t+\phi)} &= Mcos(\omega t + \phi) + Mj\ sin(\omega t + \phi) \end{aligned} \tag{3.11}$$

where M is any given amplitude. Continuing the derivation gives:

$$Re[Me^{j(\omega t+\phi)}] = Re[Mcos(\omega t + \phi) + Mj\ sin(\omega t + \phi)] \tag{3.12}$$

where the real Re[ ] portions give:

$$Me^{j(\omega t+\phi)} = Re[Mcos(\omega t + \phi)]Me^{j(\omega t+\phi)} = Re[\hat{X}cos(\omega t + \phi)] \tag{3.13}$$

where $\hat{X}$ is the time independent expression $\hat{X} = Me^{j\phi}$ Using Eq. 3.10 the sinusoidal wave forms are rewritten as:

$$E(t) = Re[E_o e^{j\omega t}] \tag{3.14}$$

$$i(t) = Re[i_o e^{-j\phi} e^{j\omega t}] \tag{3.15}$$

Lastly, the definition of impedance Z is the effective resistance (the combination of ohmic resistance and reactance) from an alternating current at steady state and is taken as:

$$Z = \frac{\hat{E}}{\hat{i}} = \frac{Re[E_o e^{j\omega t}]}{Re[i_o e^{-j\phi} e^{j\omega t}]} = |Z| e^{j\phi} \tag{3.16}$$

where $|Z|$ is the magnitude of the impedance. Using Euler's formula again (Eq.3.11), the impedance magnitude is represented by real Z_r and imaginary Z_i parts:

$$Z = Z_r + jZ_i \tag{3.17}$$

and is useful for determining processes occurring on the electrode.[123–127] A Nyquist plot (Fig. 3.8b.) allows relationships between real and imaginary impedance of a system to be visually observed. In order to extract electrochemical parameters, an equivalent circuit with a similar impedance response is fitted to the real and imaginary components, as seen in Fig. 3.8b.[128]

The Randles Circuit is used to fit a metallic nickel electrode impedance response.[129] The circuit is seen in Fig. 3.8b and is comprised of a constant phase element (CPE) and a resistor (R_{ct}) in parallel with a resistor (R_s) in series. The CPE represents a capacitor with adjusted terms to achieve a lower error of the impedance fit. The capacitance C is derived from the CPE as

$$C_{\text{eff}} = Q^{1/\alpha} \left(\frac{R_{\text{e}} R_{\text{ct}}}{R_{\text{e}} + R_{\text{ct}}} \right)^{(1-\alpha)/\alpha} \tag{3.18}$$

where α is the degree of ideality.[130] When $\alpha = 1$, the CPE resembles a capacitor. The CPE correlates to the double layer capacitance and the faradaic capacitance of the electrode surface and solution. The R_s resistor identifies the solution resistance of the three-electrode cell and is the ohmic drop between the working and counter electrode. The R_{ct} resistor represents the charge transfer resistance, the resistance an electron needs to overcome to participate in a reaction on the electrode surface. The charge transfer resistance has been seen to be inversely related to the kinetic rate constant.[123] These parameters allow for the characterizing and benchmarking of catalysts across different solutions, potentials, and electrode types.

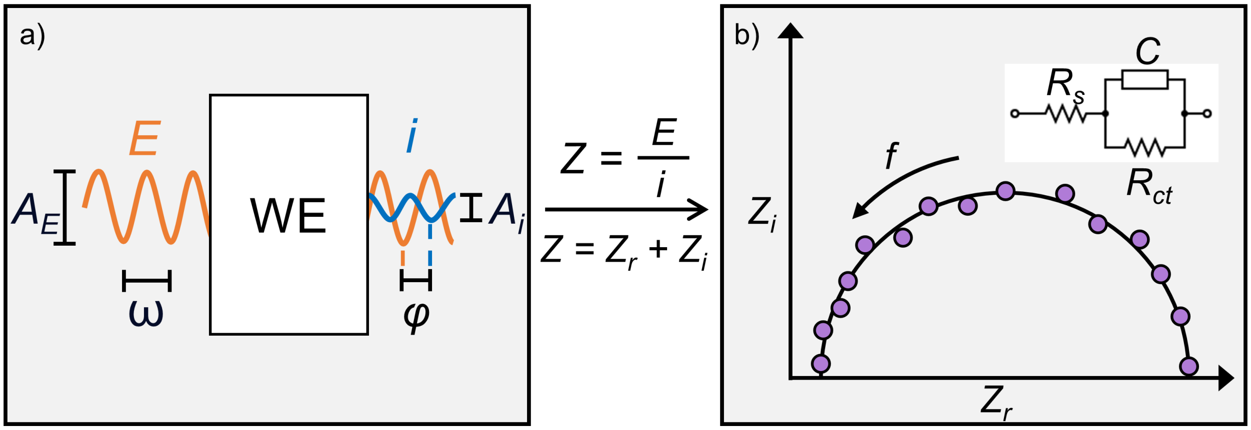

Fig. 3.8 a) Voltage perturbation with amplitude (A_E) and frequency (ω) applied to a working electrode (WE). The current response has a shift in phase angle (ϕ) and amplitude (A_i). The impedance (Z) is calculated from the voltage perturbation and current response and contains real (Z_r) and imaginary (Z_i) parts. b) The Nyquist Plot of Z_i *vs.* Z_r is fitted with a Randles Circuit to find solution resistance (R_s), capacitance (C), and charge transfer resistance (R_{ct}).

3.6 Non-electrochemical Methods

3.6.1 Scanning Electron Microscopy And Electron Dispersive Spectroscopy

Scanning electron microscopy (SEM) is a technique that images a surface by using a focused beam of electrons. The electrons interact with the atoms on the sample that produce signals that depend on the atoms environment. The electron response carries information about the surface topography and composition of the sample. SEM is typically performed under high vacuum, allowing for magnifications to reach up to 1,000,000x under the correct conditions.[131] SEM is used in this context to observe the size and roughness of facets and the density of grain boundaries on a metallic nickel surface. Additionally, SEM is used to observe the structures of crystals formed on hydrothermally-grown nickel hydroxide on nickel foam.

Typically, SEM is paired with electron dispersive spectroscopy (EDS). EDS is a technique used for elemental analysis of a sample by X-ray excitation. Each type of atom has an X-ray excitation footprint due to a unique electromagnetic emission spectrum. For example, a chromium-doped nickel crystal will exhibit unique peaks for both chromium and nickel,

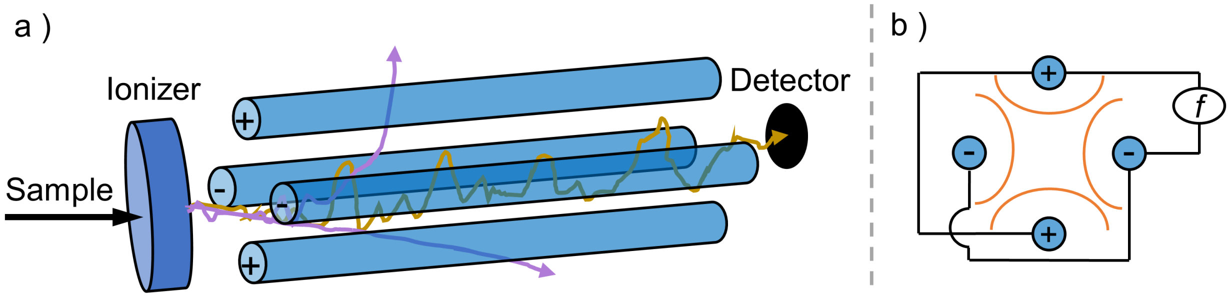

Fig. 3.9 a) Basic components of a quadrupole with example paths of ions. b) The electrical control of positive and negative poles with radio frequency (f) and respective fields (orange).

which then are deconvoluted to obtain the relative amount of chromium and nickel in the sample.

3.6.2 Mass Spectrometry

Performed under vacuum ($< 5\text{x}10^{-5}$ torr), mass spectrometry takes advantage of the ion-to-mass ratio of the samples to identify the composition of a sample. A sample is ionized by an electron beam and accelerated by an electric or magnetic field to separate the ions by their respective mass. The masses are filtered, typically by magnetic sector or by radio-frequency (RF) quadrupole. An RF quadrupole is comprised of four equally-spaced rods from a central axis, as seen in Figure 3.9. The two pairs of positively and negatively charged rods are held with a direct voltage field at a particular frequency, forming a high- and low-pass filter. The filter allows ions of a particular mass range to go through a large number of stable, periodic oscillations while traveling towards the detector.[132] The detector is typically a Faraday cup (for low vacuum and high sample concentration) or an electron multiplier (for high vacuum and low sample concentration). The mass spectrometer is used in this context to qualitatively compare the rate of oxygen production between β-NiOOH and γ-NiOOH with and without urea in the electrolyte.

The mass spectrometry system used to determine the product distribution for nickel foam catalysts was a 50 L vacuum chamber pumped down with a Balzers 330 turbomolecular

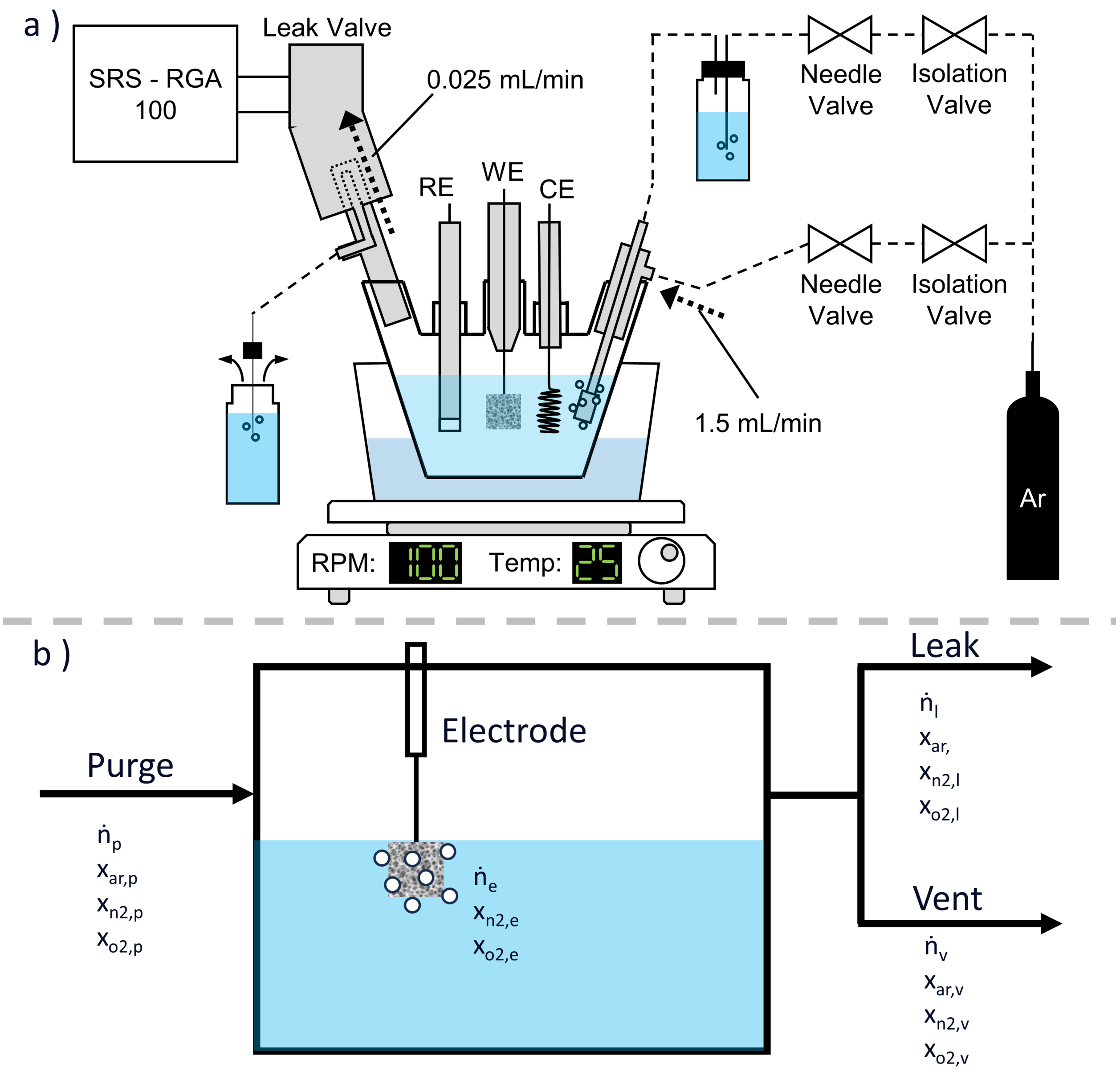

Fig. 3.10 a) Depiction of the three electrode cell, gas handling, and mass spectrometry system. Dashed lines represent the flow path of argon gas, where 1.5 mL min^{-1} was continuously entering the cell. As the gasses flowed out of the cell, a mass spectrometer (SRS-RGA 100) analyzes the composition through a leak valve. b) Depiction of in and out streams used to close the mass balance measured by electrochemical current and mass spectrometry.

pump (330 L s^{-1}). The vacuum chamber housed an Stanford Research Systems Residual Gas Analyzer 100 (RGA-100) for analysis and a Nude ion gauge for pressure measurement. The base pressure of the unbaked vacuum chamber was 1.5x10^{-9} torr. The system was not baked out as water vapor was introduced into the vacuum chamber from the headspace through a leak valve during experimentation, as seen in Figure 3.10a. The flowrate of the carrier gas, Ar, was measured by average displacement of volume in the venting vial over period of 10 seconds. The flowrate of gas entering the vent valve was found by measuring the volume lost in the vial venting over a period of 1 hour while the three electrode cell was sealed and the carrier gas flowrate was zero. The gasses, once through the leak valve, passed through a 1.33" ID Conflat pipe before reaching the detector.

The partial pressures of N_2, O_2, and Ar measured by the mass spectrometry were used to close the overall mass balance. Fig. 3.10a is simplified into Fig. 3.10b for a better understanding of the system. The mass spectrometry was used to find composition of the purge ($\dot{n}_p$), leak ($\dot{n}_l$), and vent ($\dot{n}_v$) streams.

$$x_{ar,p} = \frac{P_{ar,background}/S_{ar}}{P_{n2,background}/S_{n2} + P_{o2,background}/S_{o2} + P_{ar,background}/S_{ar}}$$

$$x_{n2,p} = \frac{P_{n2,background}/S_{n2}}{P_{n2,background}/S_{n2} + P_{o2,background}/S_{o2} + P_{ar,background}/S_{ar}}$$

$$x_{o2,p} = \frac{P_{o2,background}/S_{o2}}{P_{n2,background}/S_{n2} + P_{o2,background}/S_{o2} + P_{ar,background}/S_{ar}}$$

$$x_{ar,p} = x_{ar,l} = \frac{P_{ar,5hr}/S_{ar}}{P_{n2,5hr}/S_{n2} + P_{o2,5hr}/S_{o2} + P_{ar,5hr}/S_{ar}}$$

$$x_{n2,p} = x_{n2,l} = \frac{P_{n2,5hr}/S_{n2}}{P_{n2,5hr}/S_{n2} + P_{o2,5hr}/S_{o2} + P_{ar,5hr}/S_{ar}}$$

$$x_{o2,p} = x_{o2,l} = \frac{P_{o2,5hr}/S_{o2}}{P_{n2,5hr}/S_{n2} + P_{o2,5hr}/S_{o2} + P_{ar,5hr}/S_{ar}}$$

Where the sensitivity factors of nitrogen (S_{n2}), oxygen (S_{o2}), and argon (S_{ar}) are a function of the mass spectrometer and are 1, 0.85, and 1.35 respectively. The value of $\dot{n}_p$ and $\dot{n}_l$ are found by using the molar volume of argon at 25°C and 1 atm (0.0409 $\frac{mole}{L}$, obtained from NIST).

$$\dot{n}_p = \frac{1.5\ mL}{min} \cdot \frac{1\ L}{1000\ mL} \cdot \frac{1\ min}{60\ s} \cdot \frac{0.0409\ mole}{L} = 1.11x10^{-6}\frac{mol}{s}$$

$$\dot{n}_l = \frac{0.025\ mL}{min} \cdot \frac{1\ L}{1000\ mL} \cdot \frac{1\ min}{60\ s} \cdot \frac{0.0409\ mole}{L} = 1.75x10^{-8}\frac{mol}{s}$$

The mass balance is closed around Ar to find the value of $\dot{n}_v$.

$$\dot{n}_v = \frac{\dot{n}_p x_{ar,p} - \dot{n}_l x_{ar,l}}{x_{ar,v}}$$

The overall mass balance is used to find the molar flow of gasses produced by the electrode ($\dot{n}_e$).

$$\dot{n}_e = \dot{n}_l + \dot{n}_v - \dot{n}_p$$

The mass balance is closed around N_2 to find the composition of $\dot{n}_e$.

$$x_{n2,e} = \frac{\dot{n}_l x_{n2,l} + \dot{n}_v x_{n2,v} - \dot{n}_p x_{n2,p}}{\dot{n}_e}$$

$$x_{o2,e} = 1 - x_{n2,e}$$

Lastly, the molar flow and composition of gasses produced by the electrode are used to find the an equivalent current measured by mass spectrometry (i_{ms}).

$$i_{ms} = \dot{n}_e x_{o2,e} F n_{OER} + \dot{n}_e x_{n2,e} F n_{UOR}$$

where n_{OER} is 4 and n_{UOR} is 6. Faradaic efficiency of the urea oxidation reaction for complete oxidation to N_2 is the percentage of current used to generate N_2 seen by mass spectrometry versus by the potentiostat:

$$F.E. = \frac{\dot{n}_e x_{n2,e} F n_{UOR}}{i_e - \dot{n}_e x_{o2,e} F n_{OER}} * 100$$

where i_e is electrochemical current over the last 45 minutes of the potential hold.

Chapter 4

SELECTIVE NICKEL-OXYHYDROXIDE PHASE GROWTH THROUGH CONTROLLED ELECTROCHEMICAL CYCLING PROCEDURES FOR IMPROVED OXYGEN EVOLUTION

4.1 Introduction

Developing efficient and affordable electricity storage methods is a critical step in adopting widespread renewable energy production. Furthermore, replacing the use of greenhouse gas-emitting energy sources is a necessity for developing a low-carbon economy.[133] A promising energy carrier that fulfills these requirements is hydrogen gas, a clean-burning fuel that can be produced through alkaline water electrolysis.[134–137] In many cases, however, the rate of hydrogen production is governed by the sluggish anodic process, whether the oxygen evolution reaction (OER, Eq. 2.6) when H_2 is obtained from H_2O or electrolysis of a hydrogen containing organic substance such as urea or glucose.[49,75,89,138–140]

Currently, noble-metal catalysts such as ruthenium oxide (RuO_2) and iridium oxide (IrO_2) are considered the best electrocatalysts for alkaline OER, but their high cost makes widespread use a challenge.[28] As a result, the development of inexpensive and efficient oxidation electrocatalysts is crucial for improving the performance and viability of alkaline water electrolysis systems.

Nickel is a promising transition metal electrocatalyst due to its high electrical conductivity, surface area, and stability in alkaline media.[141] Nickel, when coupled with hetero-metal atoms, shows improved OER activity by lowering activation energies, shifting nickel to more-active phases, lowering ohmic resistances, and enhancing stability of the oxide film.[142–147] The catalytic activity of Ni arises from formation of highly active oxyhydroxide phases upon positive electrochemical bias ($1.27 - 1.34\ V_{RHE}$ in 0.5 M KOH), as indicated by Eq. 2.3.[53]

The oxyhydroxide phases are formed through a combination of structural and electrochemical transformations, first identified by Bode *et al.*.[88] The Bode diagram - presented in Fig. 2.4 - is expanded to include both the hydroxide and oxyhydroxide phases. The two fundamental hydroxide phases, α-$Ni(OH)_2$ and β-$Ni(OH)_2$, form from metallic Ni and NiO at open-circuit potential (OCP) in alkaline conditions. The α-$Ni(OH)_2$ phase consists of turbostratic β-$Ni(OH)_2$ layers held together by intercalated water molecules.[71] When a moderate bias is applied (1.32 V_{RHE} in 0.5 M KOH), α-$Ni(OH)_2$ and β-$Ni(OH)_2$ convert to their respective oxyhydroxide equivalents, γ-NiOOH and β-NiOOH. The γ-NiOOH phase also develops from β-NiOOH during overcharge, the application of a large overpotential that induces OER. Upon reduction, both β-NiOOH and γ-NiOOH convert to β-$Ni(OH)_2$.[69,75,76] There is some discrepancy in the literature, however, of whether γ-NiOOH also reduces to α-$Ni(OH)_2$; several studies support conversion to α-$Ni(OH)_2$, while others consider this unlikely.[86,148–151] Lyons *et al.* report that α-$Ni(OH)_2$ is formed, although they also note that α-$Ni(OH)_2$ can dehydrate and convert to β-$Ni(OH)_2$ without charge transfer.[150] Thus, α-$Ni(OH)_2$ could form as a transient species and subsequently convert to the more stable β-$Ni(OH)_2$ phase.

The two active phases, β-NiOOH and γ-NiOOH, have been extensively studied for their difference in OER properties. A consensus has emerged that the β-NiOOH surface is more catalytically active towards OER than is γ-NiOOH.[85] At high overpotentials, electrocatalytic activity decreases, which has been attributed to a thick layer of NiOOH (up to 1.4 μm)[78–81] that reduces charge transport or to formation of inactive Ni^{4+} on the surface.[78,82,83] That the oxidation state of γ-NiOOH is in the range of 3.5–3.7, is evidence of a mixture of $Ni^{2/3/4+}$ centers on the surface, resulting in a decrease in activity.[75,84,152,153] β-NiOOH, on the other hand, has an oxidation state of 3, suggesting that all electrochemically-active surface sites are able to participate in OER.[71]

The relative amounts of β-NiOOH and γ-NiOOH can be controlled with potential cycling. Potential cycling is a common procedure in preparing anodes for Ni-based batteries in order to increase the potential where overcharge begins. Overcharge converts γ-NiOOH to β-NiOOH, which subsequently decreases the overcharge potential.[53,71,73,75,82,88,89,154] Lyons, Brandon, and co-workers[150] conducted cycling over a wide potential range, from hydrogen evolution reaction (HER) to OER potentials (–0.5 to 1.59 V_{RHE}), at 350 mV s^{-1} and reported that hydrous oxide accumulation over a number of cycles is facilitated by the lower potential limit, which partially reduces the hydrous oxide within each cycle. They also modeled the hydrous oxide layer as a porous assembly within which oxidation occurs by proton diffusion. Godwin and Lyons[155] examined the effect of ageing induced by potential cycling of Ni electrons on OER. Ageing was performed by 150 cycles at 10 mV s^{-1} between 1.04 V_{RHE}, where $Ni(OH)_2$ is stable, to 1.54 V_{RHE} in the OER region. This ageing protocol produced significant enhancement of OER, with a reported turnover frequency of 1.16 s^{-1} when the number of sites is based on the oxide reduction charge. Pissinis *et al.* employed potential cycling for varying upper and lower limits from 1.0 to 1.6 V_{RHE} at 50 mV s^{-1} and for up to 600 cycles to control the relative amounts of β-NiOOH and γ-NiOOH.[86] Formation of β-NiOOH was favored for an upper limit of 1.5 V_{RHE}, whereas γ-NiOOH was favored for an upper limit of 1.6 V_{RHE}. Varying the lower limit potential from 1.0 to 1.1 V_{RHE} favored the β-$Ni(OH)_2$ phase.

Molecular level aspects of OER on Ni catalysts have recently received attention in the literature. Rajan *et al.* examined OER on three low index facets of β-NiOOH by density functional theory (DFT).[156] They found that all three facets exhibit high OER activity, though each with a distinct reaction mechanism. They note that metal-ion oxidation states, which include oxidation of Ni(III) to Ni(IV), and lattice oxygen stabilization are critical in describing low overpotential OER pathways. The effect of four-coordinate cation vacancies produced by leaching of Ni ions in borate electrolyte at pH 7–9 was studied with DFT by Li *et al.*[157] A self-healing process involving re-deposition of Ni ions yields 2–3 nm particles of γ-NiOOH that exhibit high OER activity. The authors report that this mechanism will not work at high pH, however. Peng *et al.* found that co-doping CoS_2 catalysts with Fe and Ni yielded enhanced OER activity due to easier formation of the oxyhydroxide surface species.[158] An interesting point of this study is that codoping suppressed formation of $Ni(OH)_2$, leading to improved catalyst stability. The nature of the surface intermediate in OER on NiOOH was examined with *in-situ* surface enhanced Raman spectroscopy (SERS) by Diaz-Morales *et al.*[159] This study found the active surface intermediate to be a superoxo (Ni–OO$^-$) species and that OER proceeds by deprotonation of the surface at high pH, which has the implication that NiOOH would not be a good catalyst at intermediate pH even if it were stable at this condition.

The role of incidental iron in solution has received recent attention in the context of oxygen evolution reaction on nickel hydroxide. The inclusion of iron is-well known to improve the oxygen capabilities of nickel as low as 36 ppm.[57] Several groups have employed extensive electrolyte cleaning procedures to remove the incidental iron from solutions.[35,85,106] In this study, the electrolyte was not purified to remove the incidental iron (0.28 ppm max, Table S1), as the potential cycling procedure has been seen to change the distribution of nickel phases with and without iron.[108] Therefore, the electrode catalysts in this study may be assumed to contain iron impurities from the electrolyte, but the phases that form on the surface can still be controlled with switching potential within a reasonable degree.

Nickel electrocatalysts are also effective for electrooxidation of urea, methanol, glycerol, and glucose.[52,66,109,160–170] These reactions proceed at the onset of NiOOH formation, in contrast to OER, which occurs at potentials where the conversion of $Ni(OH)_2$ to NiOOH is complete. The relative catalytic activities of the γ-NiOOH and β-NiOOH phases towards electrooxidation of small molecules are likely to be different than for OER. This study was motivated by the need to prepare NiOOH oxide surfaces with varying amounts of γ-NiOOH and β-NiOOH to examine the catalytic properties of these phases in urea electrooxidation, which is ongoing in our laboratory. The relative amounts of γ-NiOOH and β-NiOOH are controlled by the upper limit cycling potential, which takes the electrode into the OER region, where γ-NiOOH production occurs on overcharge.

This study examines the influence of the upper limit switching potential on the formation of NiOOH phases on Ni electrodes following prolonged cycling at low sweep rates (10 mV s^{-1}). Cyclic voltammetry, chronoamperometry, electrochemical impedance spectroscopy (EIS), and scanning electron microscopy (SEM) were employed to explore this relationship.

Our aim is to quantify how electrochemical cycling and switching potential (extent of overcharge) affect the relative concentrations of NiOOH phases on the catalyst surface and to correlate these changes with OER kinetics. Here, we characterize kinetics in terms of turnover frequency, which has not been widely reported for electrocatalysts aged by potential cycling.

4.2 Experimental

4.2.1 Electrodes

The working electrode was prepared by sanding a 99.995% Ni disk (ESPI Metals) using 240 and 600 grit sandpaper until planar, followed by polishing with 9, 3, and 1 micron diamond suspensions (Buehler) until a mirror surface was obtained. The geometric surface area of the polished region was calculated to be 0.71 $\mathrm{cm}^2_{\mathrm{geo}}$. After polishing, the working electrodes were sonicated in deionized water (DI, Millipore-Q water system) and dichloromethane (99.5 wt.%, Fisher Scientific) for 15 minutes each to remove remaining surface contaminants. A Pt coil (ca. 5 cm^2) was used as the counter electrode. The reference electrode was a double junction Hg/HgO electrode (Pine Instruments) with 4.24 M KOH solution. Since measurements were made in 0.5 M KOH, the reference electrode potential was adjusted for the liquid junction potential of –25.1 mV between 4.24 M KOH and 0.5 M KOH calculated with the stationary Nernst–Planck equation using LJPcalc software (`https://swharden.com/LJPcalc`).[171] This adjustment yielded very good agreement with the half-wave potential of the β-$\mathrm{Ni(OH)_2}$ to β-NiOOH transition reported by Alsabet *et al.*[76] All reported voltages are with respect to the reversible hydrogen electrode (RHE), calculated using the equation:

$$E_{\mathrm{RHE}} = E_{\mathrm{Hg/HgO}} + (0.059)\,\mathrm{pH} + E^{\ominus}_{\mathrm{Hg/HgO}} - E_{\mathrm{LJP}} \tag{4.1}$$

where $E^{\ominus}_{\mathrm{Hg/HgO}}$ is the standard potential of the mercury oxide reference electrode, 0.098 V *vs.* the normal hydrogen electrode for 4.24 M KOH at 25 °C, and E_{LJP} is the liquid junction potential of –25.1 mV.[171] Equation 4.1 is based on the use of liquid junction potentials for adjusting Hg/HgO reference electrodes reported by Kawashima *et al.*[172]

4.2.2 Electrochemical Apparatus

All electrochemical experiments were performed in a glass 150 mL, three-electrode cell (Pine electrochemistry). The cell was filled with concentrated H_2SO_4 ($>$ 51 wt.% , Mallinckrodt Chemicals) for at least an hour prior to experimentation to remove trace amounts of iron and other metal solutes in the glass. The electrolyte was an unstirred, 0.5 M potassium hydroxide (KOH) solution created using KOH pellets (87.4 wt.%, Fisher Scientific) and DI water (0.04 μS cm^{-1}). A 0.5 M KOH solution was used to limit the amount of impurities into the electrolyte while trying to maximize the activity of OH^-. The presence of iron (as low as 40 ppb) has been seen to affect nickel transition and oxygen evolution properties of a nickel electrode. However, other groups have identified that nickel undergoes transformations seen in the Bode diagram with or without the presence of incidental iron in the electrolyte.[57,106] The concentration of iron was not monitored within this study, as the phases of nickel can be controlled without extensive cleaning of the electrolyte. A 25 °C water bath (Fisher Scientific) was used to maintain a constant cell temperature. A Solartron 1287 potentiostat paired with a Solartron 1252A frequency response analyzer was used to collect electrochemical data..

The working electrode was first heated by electron bombardment in vacuum to temperatures greater than 600 °C to remove any previously formed oxides.[67] As seen in Fig. 3.2, the vacuum chamber was connected to the electrochemical cell through a gate valve and a ConFlat-to-glass connection. The ConFlat connection had a gas port used to replace the cell headspace with argon gas (Linde, 99.998 %). Once heated and cooled under vacuum, the working electrode was lowered into the three electrode cell under argon flow to prevent oxygen exposure. When the electrolyte's surface tension was broken, the electrode was raised to form a meniscus on the surface. This prevented reactions from occurring on the sides and top of the electrode and improved the removal of gaseous products from the electrolyte. Electrochemical experiments were initiated immediately upon exposure of the working electrode to the alkaline electrolyte.

4.2.3 Electrochemical Methods

A 600-cycle oxide development procedure was performed using cyclic voltammetry (CV) for switching potentials (E_λ) between 1.54 and 1.64 V in 0.02 V increments per 600-cycle set. The starting potential was 0.90 V, and the scan rate was 10 mV s^{-1}. Following oxide development, EIS was conducted at a potential hold (Edc) every 10 mV between 1.54 and 1.69 V using an amplitude of 5 mV and a frequency range of 100 kHz to 0.1 Hz. Overpotentials were calculated using the standard equilibrium potential of 1.23 V_{RHE} for OER in 0.5 M KOH at 25 °C.

4.2.4 Scanning Electron Microscopy

The morphology of electrodes after thermal annealing in vacuum and after oxide development for switching potentials of 1.54 and 1.64 V were analyzed by scanning electron microscopy (SEM) with a ThermoFisher Scientific Apreo-Symmetry Ultimax 100 at 2 kV with 65x–25,000x magnification. Electrodes were placed in ethanol (95 wt. %, Fisher-Scientific) post-heating or post-electrochemical treatment and were sampled immediately. Three different locations were imaged along each electrode surface. The surface exhibited similar features and length scales among each location, thus the reported images are proper representations along the entire electrode surface.

4.3 Results

To electrochemically activate Ni electrodes and develop an oxide layer in alkaline medium, potential cycling was conducted up to varying switching potentials, as presented in Fig. 4.1. During the forward (anodic) scan, current response is minimal until an oxidation wave forms at potentials greater than 1.32 V (A^*). The peak potential for this wave is initially between 1.41 and 1.42 V, shifting positively and increasing in magnitude throughout oxide development and stabilizing between 1.43 and 1.47 V (peak A) depending on E_λ. An exponential current response corresponding to the oxygen evolution reaction is observed at potentials

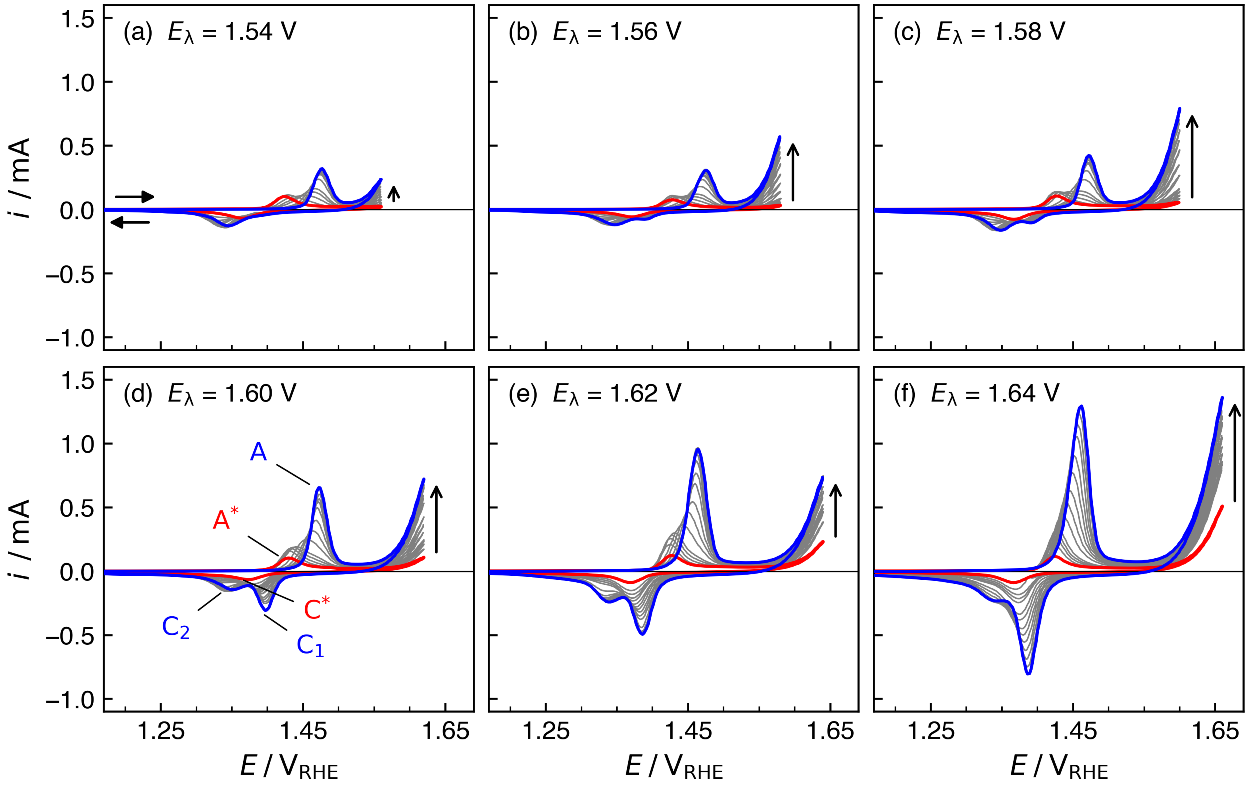

Fig. 4.1 Oxide development cyclic voltammograms for switching potentials of (a) 1.54, (b) 1.56, (c) 1.58, (d) 1.60, (e) 1.62, and (f) 1.64 V_{RHE}. The initial scan is orange, while grey lines indicate every 60th scan up to the final (blue), 600th scan. The scan direction is denoted by the horizontal arrows, while the vertical arrow shows the change in maximum OER current over the course of oxide development

greater than 1.50 V. The magnitude of OER current increases with scan number, denoted by a vertical arrow. During the reverse (cathodic) scan, a single peak between 1.24 and 1.28 V is initially observed (C^*). As the number of cycles increases, this feature either remains a single peak (Fig. 4.1a), splits into multiple peaks (Figs. 4.1b-e), or forms a peak with a shoulder (Fig. 4.1f). Reduction peak and shoulder potentials are between 1.25 and 1.31 V (peaks C_1 and C_2). The reduction current magnitude increases with cycle number, more notably for the higher E_λ values. This increase in current corresponds to a thickening of the Ni oxide layer.

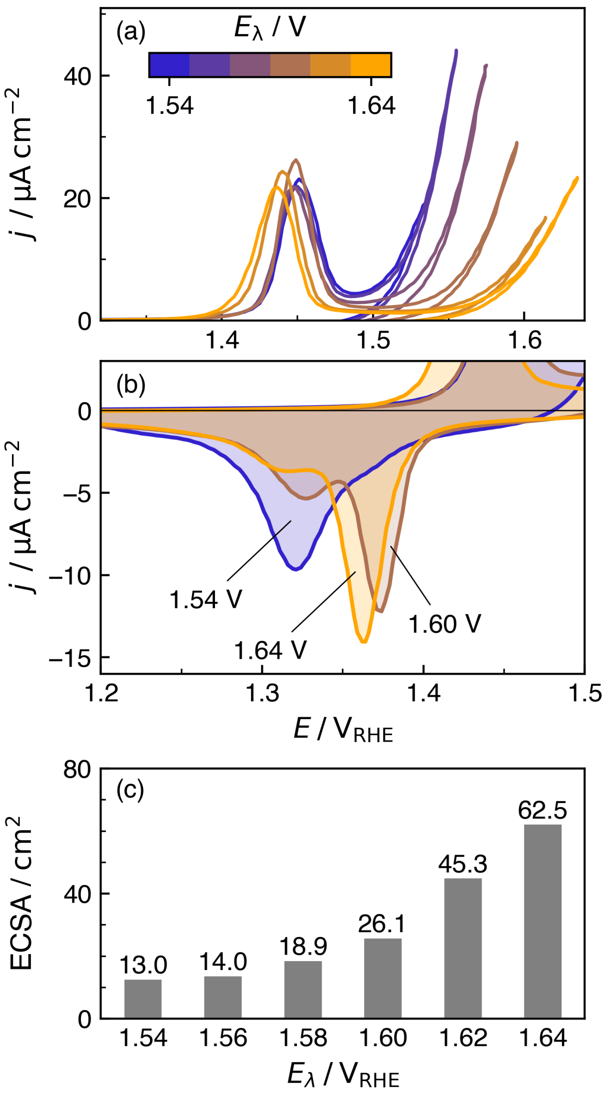

Fig. 4.2 (a) The final (600th), forward oxide development sweep for each E_λ potential on a 0.71 $\mathrm{cm}^2_{\mathrm{geo}}$ electrode, presented as ECSA-normalized current. (b) The corresponding reverse sweep for selected switching potentials. (c) ECSA, calculated using Equation 3.1

Figure 4.2a shows the anodic current normalized by ECSA, calculated using Eq. 3.1. Although the values for ECSA are presented in Fig. 4.2c, these values are taken as an approximation for comparing activities of phases and should not be taken as absolute values for kinetic analysis.

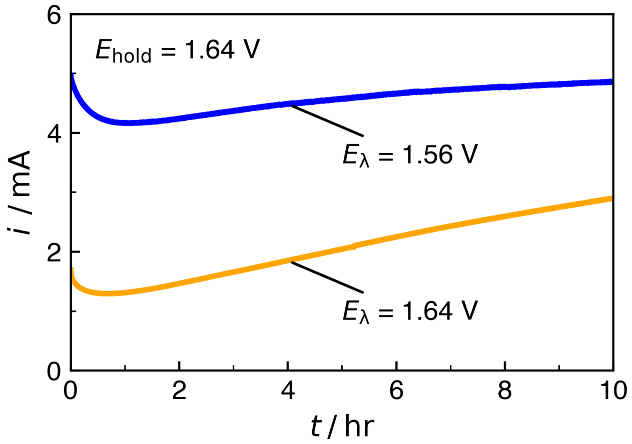

Fig. 4.3 Current response for a 10 hour potentiostatic hold at 1.64 V after 600 cycles up to 1.56 V (blue) and 1.64 V (orange)

The magnitude of the Ni oxidation wave is approximately constant when normalized according to ECSA, while the onset potential undergoes a slight negative shift at the two highest switching potentials. The OER feature at potentials greater than 1.49 V shifts positively with switching potential. The ECSA-normalized reduction waves for switching potentials of 1.54, 1.60, and 1.64 V are shown in Fig. 4.2b. Here, the reduction peak between 1.31 and 1.33 V is the most pronounced for a E_λ of 1.54 V, followed by those at 1.60 V and 1.64 V. The peak between 1.36 and 1.38 V is most pronounced for a E_λ of 1.64 V followed closely by the peak at 1.60 V, while only a small shoulder is visible for a E_λ of 1.54 V.

4.3.1 Potentiostatic Hold

Figure 4.3 shows a 10-hour potential hold at 1.64 V conducted after oxide development for switching potentials of 1.56 and 1.64 V. After the initial step to 1.64 V, the current for the electrode with a switching potential of 1.56 V is approximately 3x higher than that of the electrode developed with a switching potential of 1.64 V. Both currents initially decay, reaching a minimum after $\sim$ 1 hour. Both currents then increase over the remaining 9 hours,

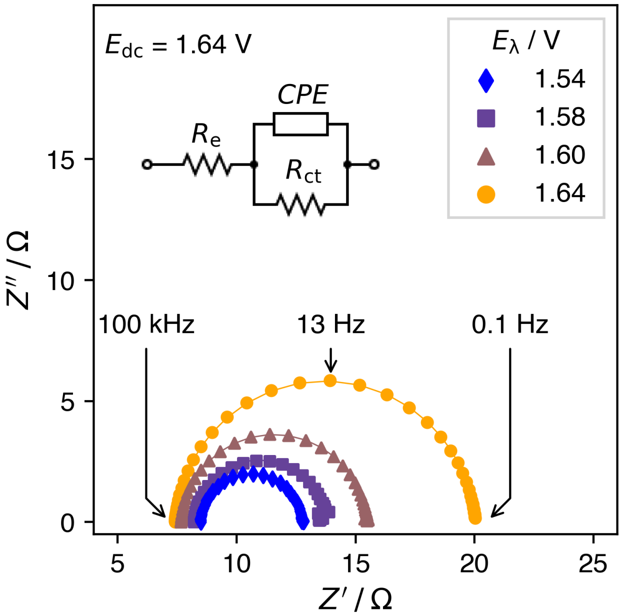

Fig. 4.4 Impedance spectroscopy conducted at a bias of 1.64 V for a series of electrodes developed with different switching potentials. Markers and solid lines represent data points and fits to a simplified Randles circuit, respectively. E_{dc} represents the holding potential during EIS.

with final values of 4.9 and 2.9 mA for switching potentials of 1.56 and 1.64 V, respectively. The nickel oxyhydroxide phase were assumed to be unaffected in cases where potentiostatic hold was higher than E_λ due to the differences in time scales between for the potential hold (10 hours) and for the development of phases (greater than 20 hours).

4.3.2 Electrochemical Impedance Spectroscopy

A Nyquist plot for EIS conducted at 1.64 V for electrodes developed with different switching potentials is shown in Fig. 4.4. A simplified Randles circuit, seen as an inset in Fig. 4.4, is used to fit the data. Other works have been seen to use more-complicated equivalent circuits to model the NiOOH surface to include the adsorption of OER intermediates and to lower the overall fitting error.[173–175] A simplified Randles circuit is used in this work as the OER intermediate contribution to the Nyquist plot is too small to detect, and the highest percent

Table 4.1 Equivalent circuit fitting parameters for EIS data presented in Fig. 4.4. Values from left to right are the switching potential (E_λ), ohmic resistance (R_e), charge-transfer resistance (R_ct), CPE parameter (Q), and CPE exponent (α)

E_λ/ V	R_e / Ω	R_ct / Ω $\mathrm{cm}^{-2}_\mathrm{geo}$	Q/mS $\mathrm{s}^{-\mathrm{n}}$	α
1.54	8.47	6.06	0.762	0.951
1.58	8.24	7.57	0.721	0.972
1.60	7.65	11.1	0.884	0.950
1.64	7.40	17.8	1.21	0.950

error amongst all fitting parameters for all data shown in Fig. 4.4 is 3.4%, which is an acceptable value. The time scale of each EIS experiment is relatively small (near 2 minutes) compared to the time needed to fully develop a particular nickel oxyhydroxide phase (greater than 20 hours). Additionally, the nickel oxyhydroxide phase was assumed to be unaffected in cases where the potentiostatic hold for EIS is higher than E_λ due to the differences in time scales. Thus, the values presented in Fig. 4.4 represent the intended nickel surfaces, within reason.

The parameters calculated from fitting a simplified Randles circuit are tabulated in Table 4.1. Nyquist plots for other biases and switching potentials are shown in Figure 4.5 and Figure. 4.6. With increasing switching potential, both the charge transfer resistance and the constant phase element (CPE) parameter increase. The capacitance C is derived from the CPE in Eq. 3.18. The capacitance was estimated for each curve fit and is presented along with the remaining fitting parameters in Figure 4.7. All CPE fits had α values above 0.92 and closely resembled capacitors. The capacitance is not truly a double layer capacitance, as the double layer is disturbed by the presence of the oxygen evolution reaction. The capacitance values here cannot be used to determine ECSA, as typical conversion units require the electrode to be in a certain set of conditions.[175]

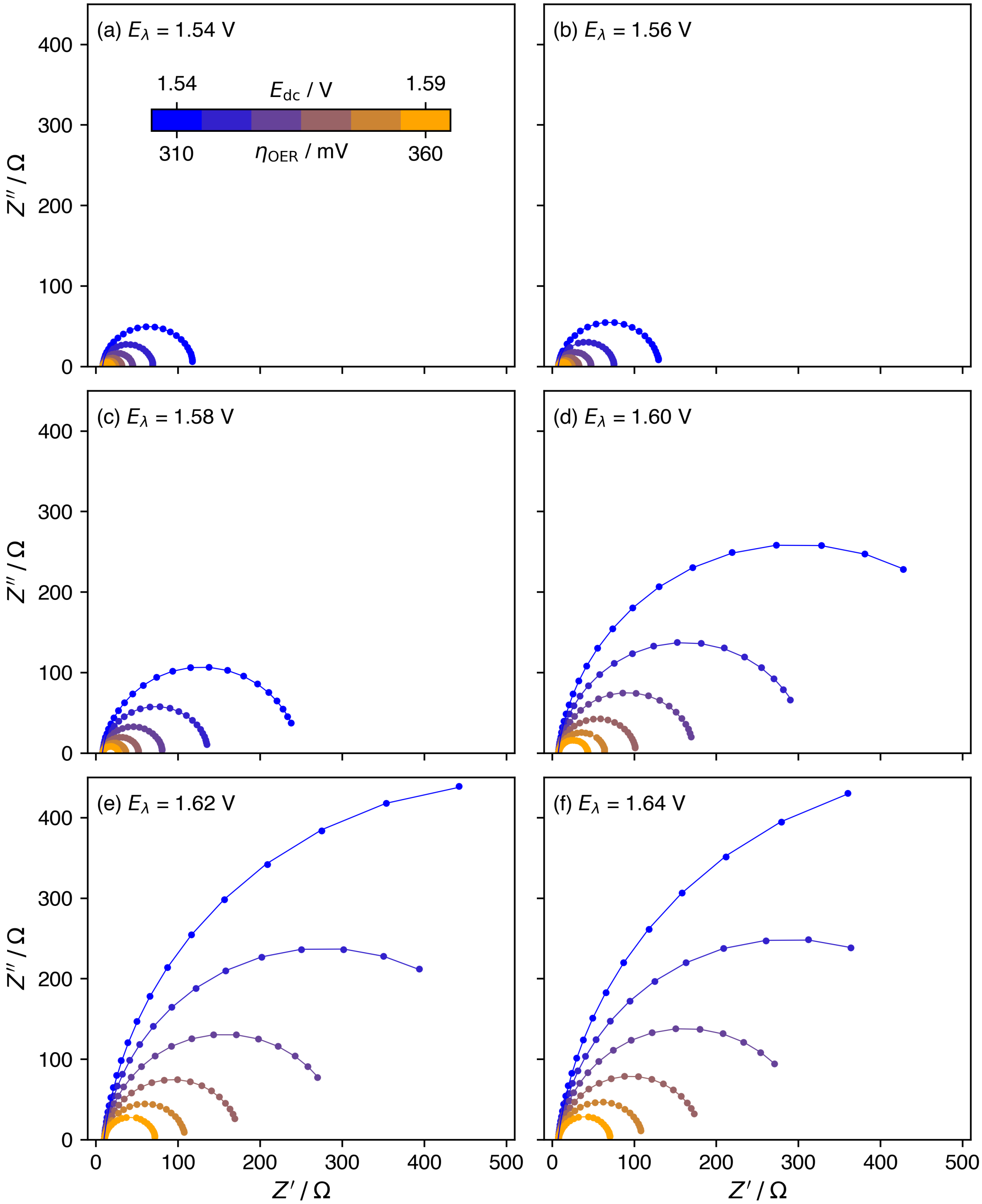

Fig. 4.5 Electrochemical Impedance Spectra conducted at DC biases between 1.54 and 1.59 V_{RHE} for electrodes developed with switching potentials between 1.54 and 1.64 V_{RHE}. E_{dc} represents the holding potential during EIS.

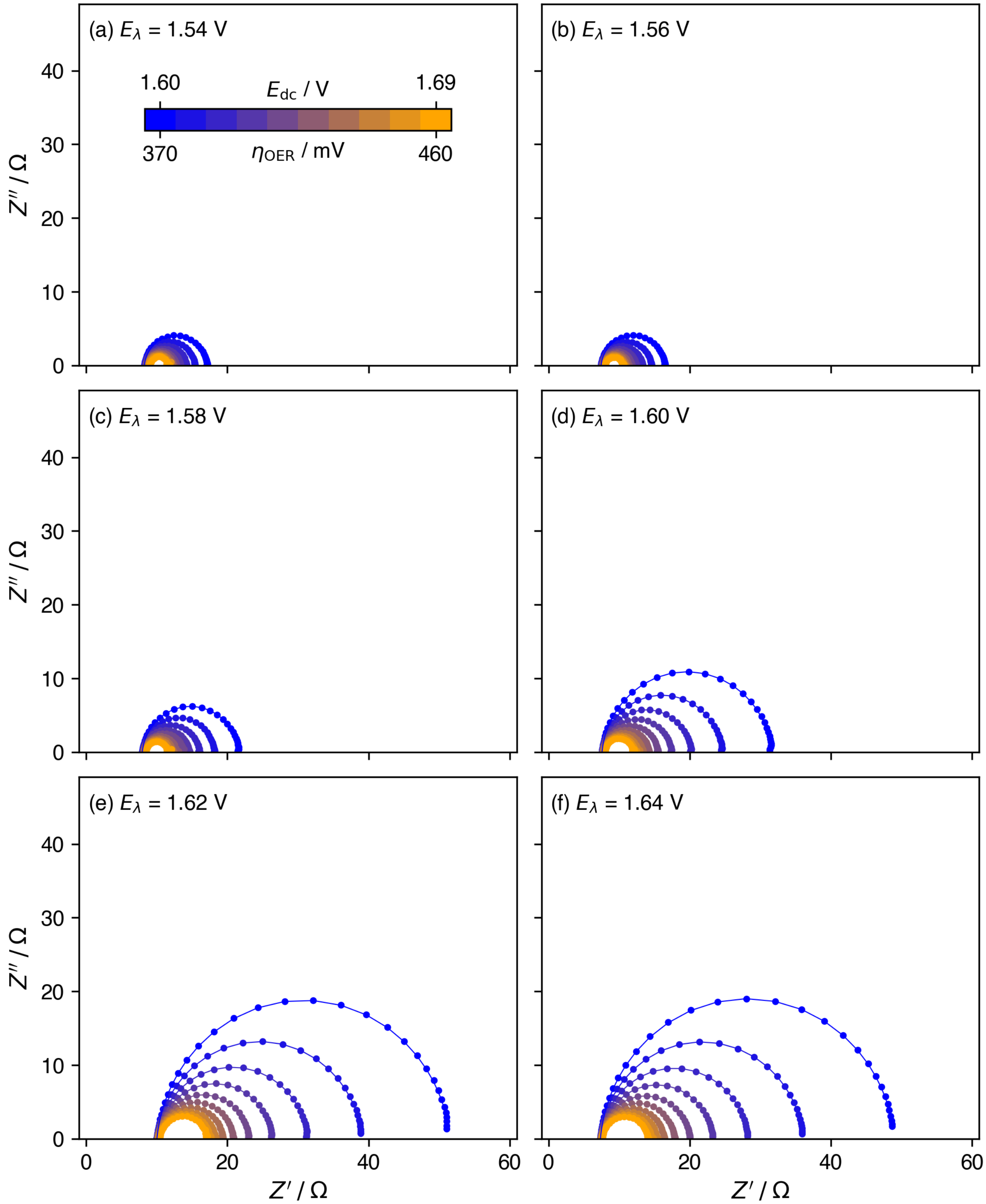

Fig. 4.6 Electrochemical Impedance Spectra conducted at DC biases between 1.60 and 1.69 V_{RHE} for electrodes developed with switching potentials between 1.54 and 1.64 V_{RHE}. E_{dc} represents the holding potential during EIS.

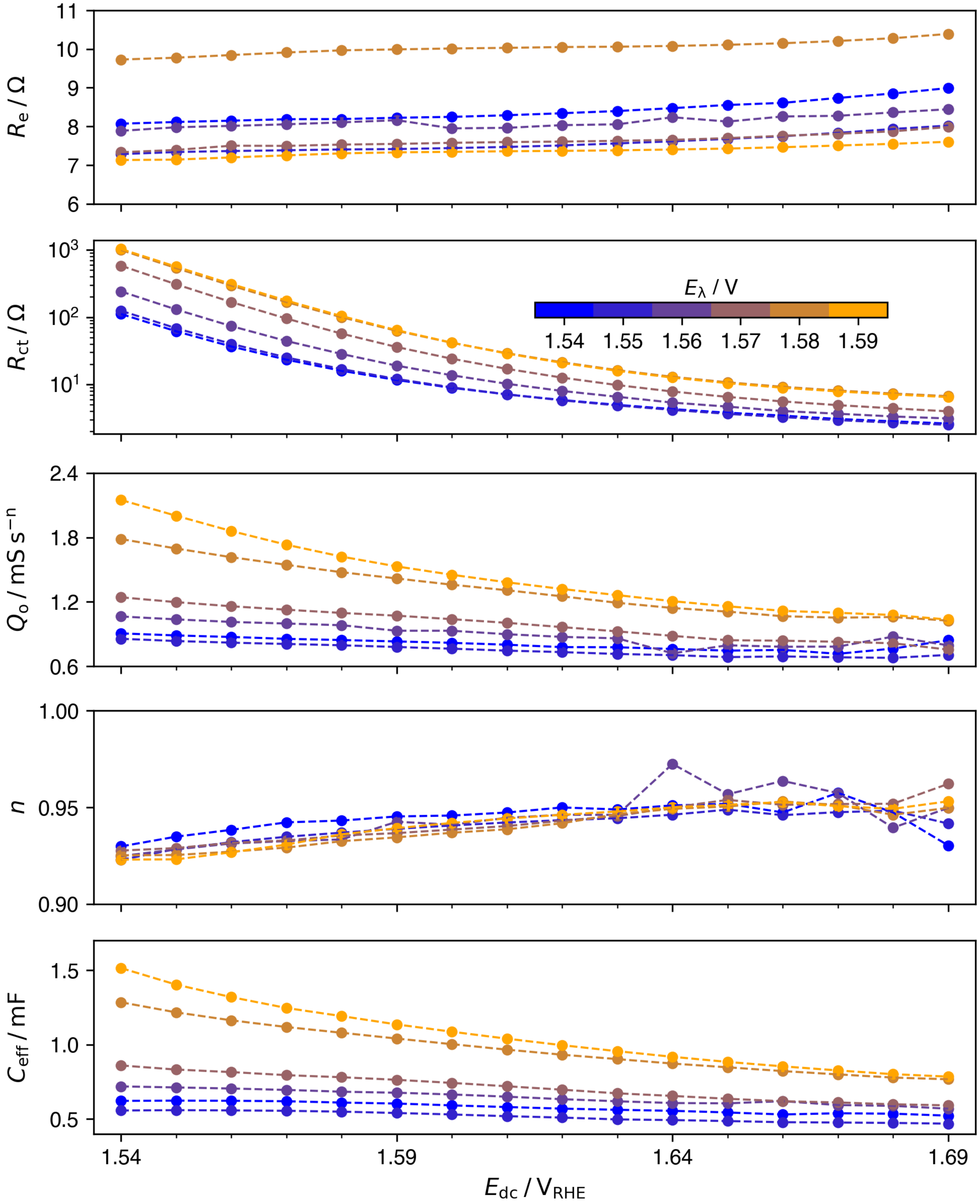

Fig. 4.7 Fitted and estimated parameters for impedance spectra shown in Fig. 4.5 and Fig. 4.6. Values from top to bottom are the ohmic resistance (R_e), charge-transfer resistance (R_{ct}), CPE parameter (Q), CPE exponent (α), and effective capacitance (C). E_{dc} represents the holding potential during EIS.

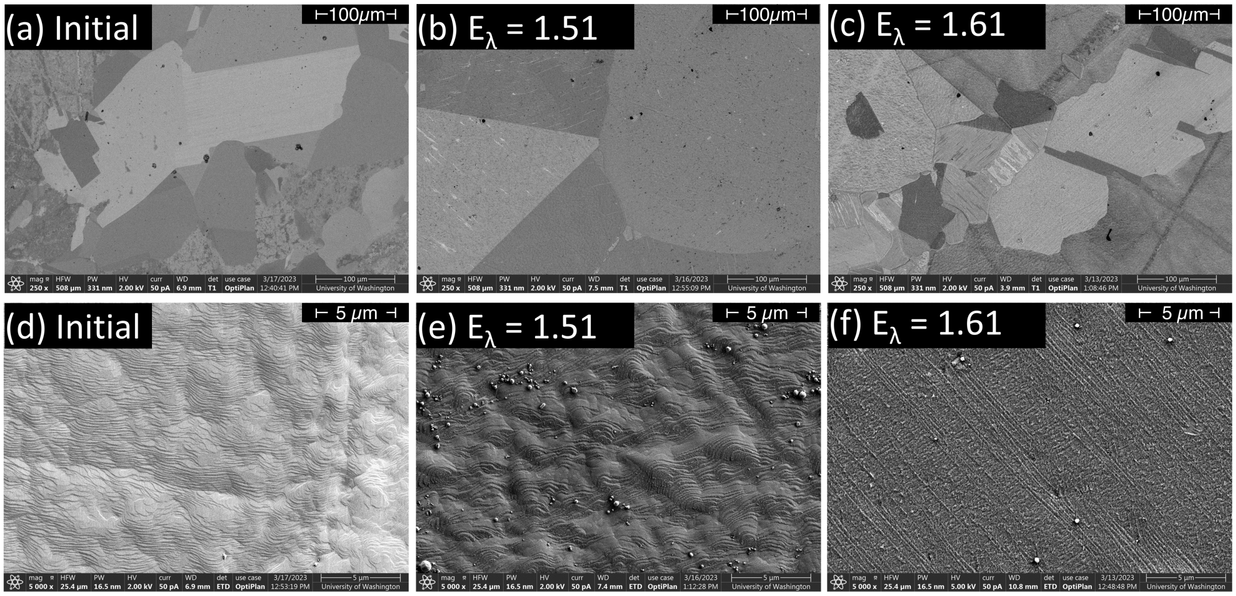

Fig. 4.8 Scanning electron microscopy images of nickel electrodes with 250x and 5000x magnification for (a,d) initial and post-oxide growth procedures for (b,e) 1.54 V and (c,f) 1.64 V switching potentials, respectively.

However, the CPE is useful for fitting the data to obtain the charge transfer resistance. The charge transfer resistance is an indicator of difficulty for an OH^- to transfer from the electrolyte crossing the electrode/electrolyte interface and is used as a metric for OER. The ohmic resistance (R_e) decreases by 12.6% with increasing switching potential, while α stays approximately constant.

4.3.3 SEM

SEM images of electrodes before and after oxide development using switching potentials of 1.54 V and 1.64 V are shown in Fig. 4.8. The images do not contain all necessary information to identify the γ-NiOOH and β-NiOOH phases, but rather show the physical response of overcharge on the electrode surface. The undeveloped electrode (Fig. 4.8a) exhibited grain structures similar to those of electrodes annealed in vacuum as reported in the literature.[176,177] The electrode developed with a switching potential of 1.54 V had larger facet planes and fewer grain boundaries than the electrode developed with a switching potential of 1.64 V. The larger facets showed large, uniform planes with length scales greater than 250 μM, while smaller facets showed broken planes with mottled texture and sizes ranging from 10 - 200 μM, as seen in Fig. 4.8b,c. While the 250x magnifications of the initial and developed electrodes differ, the 5000x magnifications look similar. Fig. 4.8d,e exhibit distinct plateaus across the surface while Fig. 4.8f exhibits parallel lines, possibly due to the alignment of the surface to the detector.

4.4 Discussion

4.4.1 Oxyhydroxide Development

Prior to electrochemical cycling, the Ni working electrode was subjected to a thermal desorption preparation procedure at temperatures greater than 600°C to remove surface oxides and contaminants. According to Alsabet *et al.*, α-Ni(OH)$_2$ is the predominant Ni phase to form after high temperature annealing and exposure to alkaline media, which is attributed to the low standard equilibrium potential of the Ni to α-Ni(OH)$_2$ reaction (0.256 V_{RHE}).[178]

A primarily α-Ni(OH)$_2$ surface will oxidize to both β-Ni(OH)$_2$ and γ-NiOOH, forming a high concentration of the latter. In Fig. 4.1, the anodic peak near 1.42 V (A^*) corresponds to the α-Ni(OH)$_2$ to γ-NiOOH oxidation reaction, with a matching reduction peak near 1.37 V (C^*). As the electrode is cycled, peak A^* shrinks while a new, larger anodic peak forms (A) with a peak potential of 1.45 V. Peak A is almost universally attributed to the β-Ni(OH)$_2$ to β-NiOOH oxidation reaction.[175,178,179]

During the cathodic sweep, the reduction of γ-NiOOH appears as a peak near 1.30 V (C_1), while the reduction of β-NiOOH to β-Ni(OH)$_2$ appears as a peak near 1.25 V (C_2).[86] Considering β-Ni(OH)$_2$ the more thermodynamically stable phase, the reduction of γ-NiOOH to β-Ni(OH)$_2$ would seem preferred.[71] The β-redox pair is the dominant surface process for electrodes with a low switching potential (1.54, 1.56, and 1.58 V).[71] When the switching potential is raised to 1.60 V or higher, the C_2 peak, which corresponds to γ-NiOOH, develops considerably more than the β-NiOOH peak, indicating that higher switching potentials lead to preferential formation of the γ-phase. The process of overcharging an electrode is proposed to drive the transformation of β-NiOOH to γ-NiOOH, corroborating this claim.[154]

For all switching potentials, a net increase in the maximum OER current (occurring at the switching potential) was seen, as indicated by the vertical arrow in each plot of Fig. 4.1. The improvement in OER current with cycle number can be explained by an increase in ECSA caused by roughening of the surface. The act of cycling a Ni electrode between the various (oxy)hydroxide phases induces lattice expansion and contraction.[71,180–183] The mechanical stress leads to cracks and faults in the oxide layer, exposing fresh, active Ni sites.[87] Moreover, it is suggested that place-exchange processes will occur in parallel with the OER at high potentials, leading to structural rearrangement and surface roughening.[184–186]

In Fig. 4.2a, the onset potential of the Ni oxidation reaction is approximately constant for switching potentials up to 1.60 V. For E_λ of 1.62 and 1.64 V, there is a negative shift in onset potential. The increased formation of γ-NiOOH that occurs at higher switching potentials provides more γ-NiOOH upon reduction, leading to a decrease in onset potential.[53] The area of the oxidation wave is approximately constant, indicating that system reversibility is similar for for all switching potentials.

In Fig. 4.2b, two major peaks are identified: the reduction of β-NiOOH to β-$Ni(OH)_2$ at 1.26 V and the reduction of γ-NiOOH to β-$Ni(OH)_2$ near 1.31 V. The ratio of γ-NiOOH to β-NiOOH increases with switching potential, consistent with electrode overcharge.

4.4.2 Oxygen Evolution

To examine the effect of switching potential on electrocatalytic properties, oxygen evolution kinetics were measured using three benchmark parameters: Tafel slope (b), overpotential (η), and turnover frequency (TOF). The first benchmark, Tafel slopes, were evaluated using EIS data, along with the following equation:[123]

$$\log\left(\frac{1}{R_{\mathrm{ct}}}\right) = \frac{\eta}{b} + \log\left(\frac{2.303 i_0}{b}\right) \tag{4.2}$$

A plot of the inverse log of charge-transfer resistance vs. overpotential yields a slope equal to the inverse of the Tafel slope. In Fig. 4.9, Nyquist plots for a range of biases along with a Tafel plot are presented for an electrode developed with a switching potential of 1.54 V. The dashed line represents the Tafel slope fitted to the first four points, with all fits having an R^2 value of at least 0.996. The Tafel slopes for all switching potentials are also tabulated. The Tafel slope remains approximately constant, although decreasing slightly from 44.2 to 39.1 mV dec^{-1} with increasing switching potential, indicating that a change in mechanistic rate-determining step is unlikely.[55,187] According to Shinagawa *et al.*, an OER Tafel slope of $\sim$ 40 mV dec^{-1} can arise from one of two possible rate-determining steps:[188]

$$\mathrm{MO} + \mathrm{OH}^- \rightleftharpoons \mathrm{MOOH} + \mathrm{e}^- \tag{4.3}$$

$$\mathrm{MOO}^- \rightleftharpoons \mathrm{M} + \mathrm{O}_2 + \mathrm{e}^- \tag{4.4}$$

While identification of the exact step is outside the scope of this work, the results presented here show good agreement with Tafel slopes estimated in the microkinetics analysis.[188]

To further quantify the OER kinetics as a function of switching potential, overpotentials were calculated for two conditions and are presented in Fig. 4.10a; the first, η_{ons}, corresponds to the onset overpotential of OER, measured at 0.5 mA cm$_{geo}^{-2}$. The second, η_{10}, is the overpotential required to generate 10 mA cm$_{geo}^{-2}$ of OER current, an often-used metric for water splitting devices.[189] The value of η_{10} was extrapolated using the Butler-Volmer equation and charge-transfer coefficients estimated from impedance data.[190] Both overpotentials generally increase with switching potential; the value of η_{ons} increases from 256 to 286 mV, while η_{10} trends from 360 to 427 mV.

Turnover frequency (TOF) is presented for each switching potential in Fig. 4.10b. The TOF values were calculated at potentials of 1.59 and 1.69 V after a hold of 3.5 minutes using

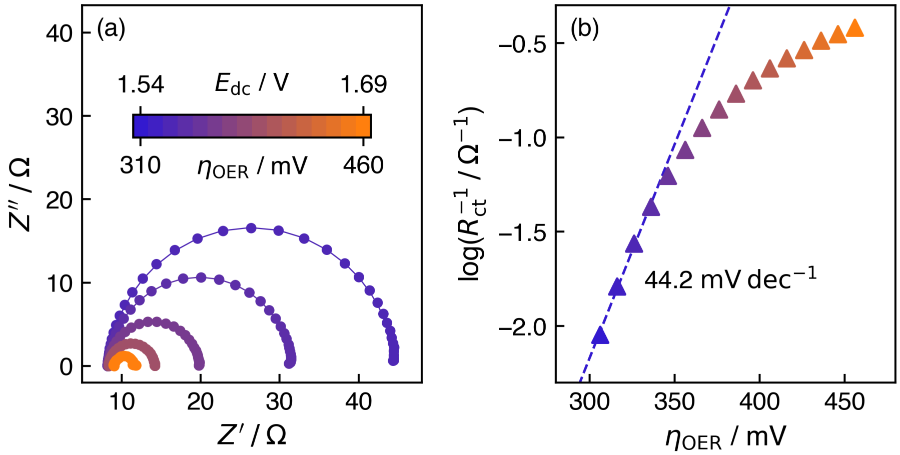

E_λ/ V	b / mV dec^{-1}
1.54	44.2
1.56	43.2
1.58	40.7
1.60	38.2
1.62	38.7
1.64	39.1

Fig. 4.9 (a) Nyquist plots for EIS conducted between 1.54 and 1.64 V (select plots shown) and (b) Tafel plot constructed using R_{ct} from equivalent circuit fits. Markers and solid lines represent data points and fits to a simplified Randles circuit, respectively. E_{dc} represents the holding potential during EIS. The electrode was developed using a switching potential of 1.54 V, and Tafel slopes for the other switching potentials are tabulated.

equation:[191]

$$\mathrm{TOF} = \frac{jN_A}{nF\Gamma} \tag{4.5}$$

where j is the current density, N_A is Avogadro's number, n is the number of electrons exchanged during OER (4), F is Faraday's constant, and Γ is the number of sites, estimated using the reduction-peak integration method as described by Anantharaj *et al.*.[191] In the values of the low switching potential range (1.54–1.56 V), TOF values were high, ranging between 10–18 s^{-1}. As the switching potential increased, TOF values decreased. At switching potentials of 1.62 and 1.64 V, the TOF values were only between 0.57–3.5 s^{-1}.

In conjunction with the potentiostatic hold data of Fig. 4.3, the TOF values indicate that the OER occurs at much shorter time scales compared with the duration of the poteniostatic hold data. For example, the initial decay in current in Fig. 4.3 has a time constant of approximately 10 minutes, while the long-term rise in time constant occurs on a time scale of 4 hours or longer. With OER turnover frequencies of 9.2–19 s^{-1} for $E_\lambda = 1.56$ V and 0.57–3.7 s^{-1} for $E_\lambda = 1.64$ V, it is clear that, for even the lowest TOF, OER active sites are

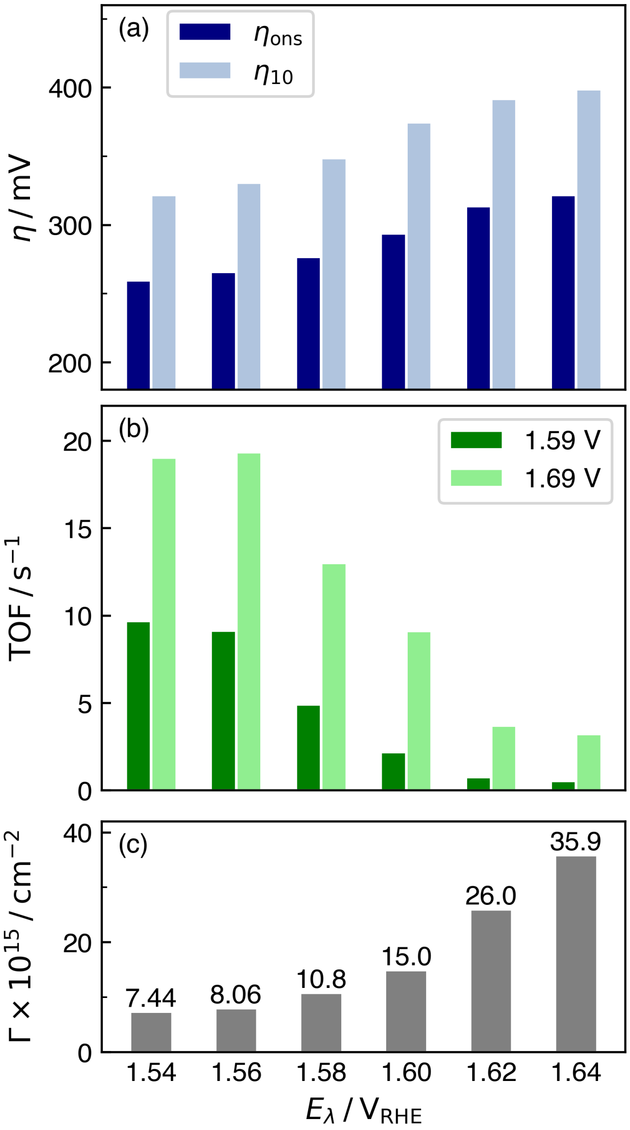

Fig. 4.10 (a) The OER onset overpotential and theoretical overpotential required to reach 10 mA cm$^{-2}_{geo}$ of OER current as a function of E_λ. (b) TOF evaluated at 1.59 and 1.69 V as a function of E_λ using Eq. 4.5. (c) number of sites of NiOOH.

turned over at least 600 times during the 10 min time constant for the short-term decrease and at least 10,000 times for the time constant of the long-term increase. The interpretation here is that OER kinetics are much faster than those for the processes responsible for the potentiostatic hold features in Fig. 4.3. We conclude, therefore, that changes in surface structure brought about by potential cycling remain in the OER region, by which OER current can serve as a measure of the activity of these surfaces. Thus, the higher OER current in Fig. 4.3 for the β-NiOOH surface formed at $E_\lambda = 1.56$ V reflects a higher OER activity than that of the γ-NiOOH surface formed at $E_\lambda = 1.64$ V. The ratio of β-NiOOH: γ-NiOOH for the surface developed at 1.56 V was higher than the surface developed at 1.64 V, which matches the trend for the increased activity.[106,155,192]

4.4.3 Morphology

The distribution of facet sizes and number of grain boundaries changed between the initial and developed oxide layers, as seen in Fig. 4.8. A mixture of roughened (jagged) and faceted (straight) boundaries was observed prior to oxide development (Fig. 4.8a).[176,193] The oxide growth procedure altered the surface *via* growth of dominant facets and formation of grain boundaries. However, the oxide-growth procedure introduced roughening as indicated by the increase in ECSA (Fig. 4.2) of the surface by forming more grain boundaries at a higher switching potential, as seen by the differences between Fig. 4.8b and c. The increase in grain boundaries may also explain the increase in sites participating in $Ni(OH)_2$/NiOOH during oxide growth among different E_λ, as seen in Fig. 4.1. Thus, the oxide growth procedure was able to decrease or increase roughness by allowing the surface to minimize its surface energy or by increasing the number of grain boundaries, respectively.

4.5 Conclusions

The electrochemical development of NiOOH species through potential cycling in alkaline media was studied as a function of switching potential. The influence of switching potential on oxide composition and oxygen evolution kinetics was quantified using CV, EIS, and Tafel analysis, while the surface morphology was studied using SEM. From these results, the following conclusions were drawn:

- Cycling at different switching potentials influences the extent of overcharge applied to the nickel electrode, allowing control of β-NiOOH (low E_λ) and γ-NiOOH (high E_λ) formation and enabling their effect on OER to be probed, respectively.

- At high switching potentials, increased overcharge and surface roughening leads to an increase in electrochemical surface area and number of NiOOH sites.
- The β-NiOOH phase has improved OER kinetics compared to the γ-NiOOH phase, as the overpotentials are lower and turnover frequencies are higher. Furthermore, the improved kinetics last over time periods much longer than required for conversion of β-NiOOH to γ-NiOOH.
- Increasing the switching potential from 1.54 to 1.64 V_{RHE} decreases facet size and increases the number of grain boundaries.

4.6 Incidental Iron Investigation

The role of incidental iron has been previously been discovered to affect the phases and oxygen evolution reaction properties of nickel hydroxide. The solutions used to collect the data in Fig. 4.1 were not purified from iron, and resulted with nickel hydroxide electrodes with Tafel slopes similar to iron-containing hydroxides.[57,106] The control of the nickel phases has been seen to be obtained with iron-free and iron-containing electrolytes, thus the conclusions made about the β-NiOOH and γ-NiOOH surfaces are valid within the context of the oxygen evolution reaction.

To resolve any concerns between the iron affecting the hydroxide, an iron-free electrolyte was created using a procedure developed by Márquez *et al.*, and was used to test the formation of a γ-NiOOH-like catalysts.[108] Figure 4.11 shows the development of hydroxides with and

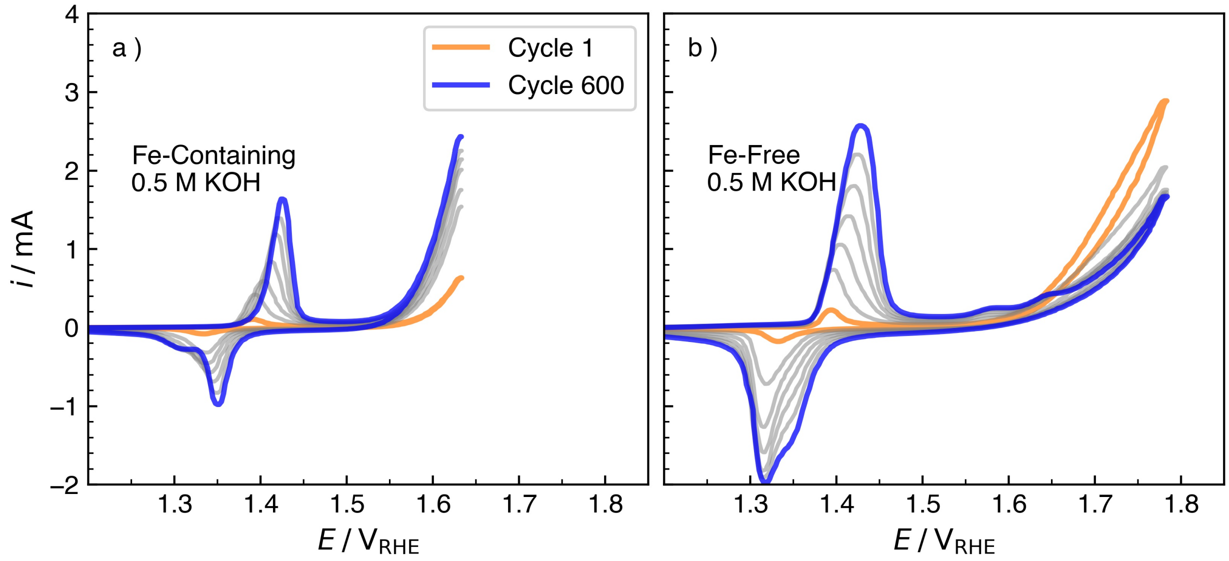

Fig. 4.11 Oxide development cyclic voltammograms for iron-containing (a) and iron-free (b) electrolytes . The initial scan is orange, while grey lines indicate every 60th scan up to the final (blue), 600th scan. The scan direction is denoted by the horizontal arrows, while the vertical arrow shows the change in maximum OER current over the course of oxide development

without iron in the electrolyte. The switching potential for the iron-free solution needed to be increased to drive the oxygen evolution reaction for the formation of a γ-NiOOH on the surface. The shape of cyclic voltammetry profile for the iron-free electrode was similar to γ-NiOOH-surfaces in other works; particularly, the formation of the two bumps at 1.57 and 1.65 V_{RHE} has been seen in profiles for γ-NiOOH by Fig. 2.7.[108]

Additionally, an iron-free solution was created with the presence of urea. Figure 4.12 shows the development of hydroxides with and without iron in the electrolyte containing 200 mM urea. An important feature arose in the insets of Fig. 4.11, where the onset potential of the urea oxidation reaction (as well as the nickel transition reaction) shifted positively in the presence of urea, with and without the presence of incidental iron. Another feature arose during the forward scans of Fig. 4.11b, where the current reached a local maximum. Zemtsova *et al.* attributed the decrease in current after the maximum as a shift

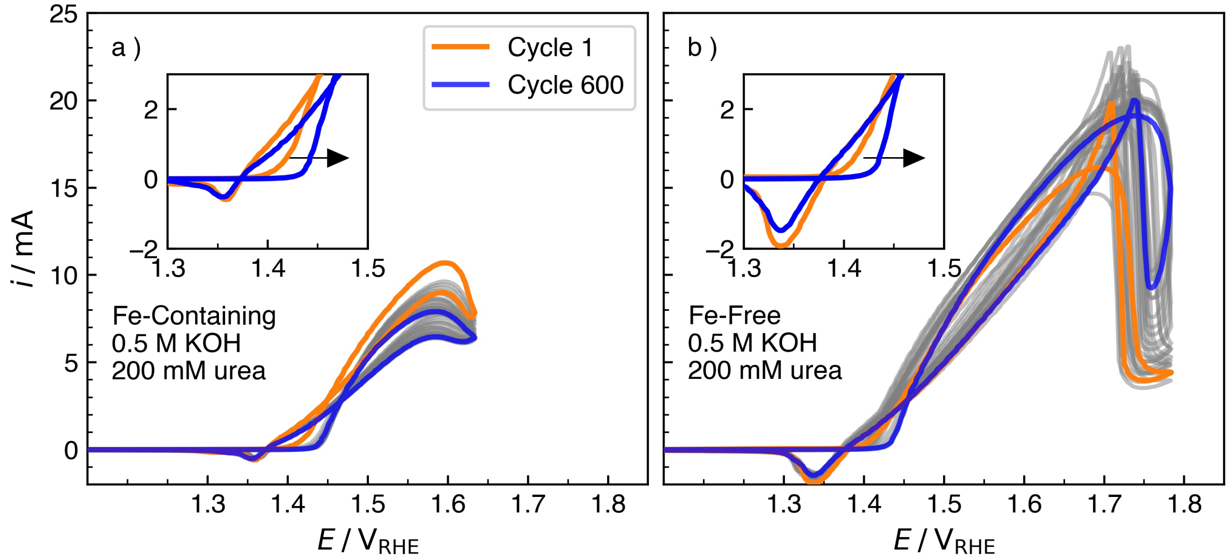

Fig. 4.12 Oxide development cyclic voltammograms for iron-containing (a) and iron-free (b) electrolytes with urea. The initial scan is orange, while grey lines indicate every 60th scan up to the final (blue), 600th scan. The scan direction is denoted by the horizontal arrows, while the vertical arrow shows the change in maximum OER current over the course of oxide development

in reaction pathway, where the isocyanate starts to form on the surface. However, this potential location could also be attributed the formation of inert Ni^{4+}.[194] This is explained by the sharp increase of current on the reverse scan, where Ni^{4+} reduced back to Ni^{3+} and urea oxidation takes place on centers that were previously inactive. Further study with spectroscopic methods is suggested to identify the phases and oxidation state of nickel hydroxide during electrochemical cycling with urea.

4.7 Acknowledgements

Part of this work was conducted at the Molecular Analysis Facility, a National Nanotechnology Coordinated Infrastructure (NNCI) site at the University of Washington, which is supported in part by funds from the National Science Foundation (awards NNCI-2025489, NNCI-1542101), the Molecular Engineering & Sciences Institute, and the Clean Energy Institute. The authors thank Prof. Gregory Jerkiewicz and Dr. Derek Essau for advice on apparatus construction and guidance of electrochemical topics. The authors thank Prof. Peter Strasser for the opportunity to visit his laboratory and Dr. Fabio Dionigi for advice on performance and preparation procedure of nickel hydroxide catalysts.

Chapter 5

THE IMPACT OF UREA ELECTROOXIDATION ON NICKEL OXYHYDROXIDE CATALYSTS

5.1 Introduction

Nickel-based catalysts have gained popularity over the last several decades for their catalytic activity towards oxygen evolution and oxidation of small organic molecules, such as urea, for the production of hydrogen.[41–44,49,75,89,138–140,166,195–197] The attractiveness of nickel stems from its wide-spread availability and stability in alkaline conditions.[198–201] The catalytic activity of Ni arises from its formation of highly active oxyhydroxide phases at a positive electrochemical bias ($1.31 - 1.38$ V_{RHE}), as indicated by Reaction 2.3:[53,70,150]

The presence of NiOOH is necessary for the electrochemical oxidation of urea. Early studies have reported that the electrochemical oxidation of urea on nickel yielded products solely comprised of N_2, CO_2, H_2O.[41,49,93] Recent works have shown that electrochemical oxidation of urea on nickel, depending on the experimental conditions, can form under-oxidized products of ammonia (NH_3) and cyanate (NCO^-) and over-oxidized products of nitrites (${NO_2}^-$), nitrates (${NO_3}^-$), and nitrous oxide (N_2O).[52,64,66] Although these studies report an in-depth analysis of reaction products, they do not report the long term effects of urea oxidation on the phases of the nickel hydroxide electrode, particularly the role of urea during the reduction of NiOOH to $Ni(OH)_2$.

Two mechanisms have been identified for electrooxidation of urea on nickel oxyhydroxide.[64,126,127] The direct urea oxidation reaction consists of urea reacting on the nickel oxyhydroxide surface, as seen in Reaction 2.1. The indirect urea oxidation reaction (IUOR) is the chemical reaction of urea with an electrogenerated active species of NiOOH, which in turn reduces NiOOH to $Ni(OH)_2$, as seen in Reaction 2.2.[49] The overall urea oxidation reaction

(UOR), Reaction 2.5, is used to express the process in an electrolysis cell. Both direct and indirect mechanisms rely on the presence of NiOOH on the surface. Thus, UOR is mediated through an electrochemical activation of nickel from $Ni(OH)_2$ to NiOOH near 1.35 V_{RHE}.[53] Determination of the mechanism of UOR on nickel is difficult based on electrochemical data due to the required presence of NiOOH. Additionally, the urea oxidation mechanism may rely on the reaction conditions (potential, temperature, urea concentration, pH), and the two mechanisms may occur at the same time on different regions of the surface. For simplicity, the indirect mechanism is the primary focus of this report, as it is the mechanism most relevant near the $Ni(OH)_2$/NiOOH onset potential.[64,160]

Physical transformations arise along with the electrochemical transformation of nickel (Eq. 2.3), first identified by Bode *et al.*. The Bode diagram, seen in Figure 2.4, identifies three distinct physical forms (α, β, γ) that can occur during the electrochemical transition of $Ni(OH)_2$/NiOOH. Nickel, when exposed to alkaline conditions, forms the α-$Ni(OH)_2$ hydroxide phase instantly as a passivated layer.[71,72,202] The α-$Ni(OH)_2$ is able to transform into β-$Ni(OH)_2$ through aging and electrochemical cycling. The α-$Ni(OH)_2$ and β-$Ni(OH)_2$ hydroxide phases have been seen to be non-conductive and non-catalytic.[71,121,203]

The catalytically active phases, γ-NiOOH and β-NiOOH, form from α-$Ni(OH)_2$ and β-$Ni(OH)_2$, respectively, through Reac. 2.3 once a moderate bias is applied. Additionally, β-NiOOH can convert to γ-NiOOH through an overcharging process.[53,71,73,75,82,88,89,154] The oxyhydroxide phases return to their respective states by electrochemical reduction when a reducing potential is applied. However, γ-NiOOH is able to convert to β-$Ni(OH)_2$ through a dehydration process along with reduction.[70,74,150]

The Bode diagram is useful for understanding changes during nickel transition and oxygen evolution, but does not incorporate the possible physical and chemical changes during reactions with small organic molecules. Barakat *et al.* identified that oxidizing methanol on a developed nickel oxyhydroxide layer consumes NiOOH sites and the mechanism of oxidation changes over time.[204] Hall *et al.* identified that the incorporation of oxalate ions ($C_2O_4{}^{2-}$) in the electrolyte drives the formation of α-$Ni(OH)_2$ on the surface at high potential scan rates.[71,205] The effect of urea oxidation on the nickel hydroxide phases, especially over long time scales, has not been thoroughly investigated with regard to changes in the electrode surface. Since NiOOH relies on urea to reduce to $Ni(OH)_2$ within the indirect mechanism, the presence of urea may have an impact on the phase distributions of nickel hydroxide.

The aim of this study is to investigate the influence of urea oxidation on the reduction of nickel oxyhydroxide by analyzing the nickel phases through detailed electrochemical experiments and mass spectrometry. Electrodes were developed at different switching potentials, allowing the maintenance of stable ratios of β-NiOOH and γ-NiOOH phases on their surfaces. These stable ratios were held at a potential sufficient to induce urea oxidation and oxygen evolution, with the resulting gases analyzed through mass spectrometry. Additionally, window opening experiments paired with mass spectrometry allowed for the determination of faradaic efficiency of N_2 production over a wide potential range. These methods facilitated the detection of changes in the catalyst surface during electrochemical cycling and varying switching potentials, as well as the assessment of selectivity towards the oxygen evolution and urea oxidation reactions.

5.2 Experimental

5.2.1 Electrodes

Nickel foam (99.5 wt %, 95% porosity, Goodfellow) was cut to 2 cm^2 pieces and were sequentially sonicated in ethanol (95 wt.%, Fisher-Scientific) and deionized water (DI, 0.04 µS cm^{-1}, Millipore-Q water system) for ten minutes each and was used as the working electrode. A Pt coil (ca. 5 cm^2) was used as the counter electrode, and a calibrated, double-junction mercury oxide electrode (Hg/HgO, 4.24 M KOH, Pine electrochemistry) was used as the reference electrode. The reference electrode was calibrated by bubbling H_2 gas (99.998%, Linde) over a platinum electrode and was taken to be (0.927 V_{RHE})

5.2.2 Electrochemical Apparatus

All electrochemical experiments were performed in a glass 150 mL, three-electrode cell (Pine electrochemistry), seen in Figure 3.10. The cell was filled with concentrated H_2SO_4 ($>$ 51 wt.% , Mallinckrodt Chemicals)for at least an hour prior to experimentation to remove trace amounts of iron and other metal solutes in the glass. The electrolyte was a stirred, 0.5 M potassium hydroxide (KOH) solution made with KOH pellets (87.4 wt.%, Fisher Scientific) and DI water. A 0.5 M KOH solution was used to limit the amount of impurities into the electrolyte (in comparison with 1 M KOH), while maintaining a high activity of OH^-. The redox properties of nickel hydroxide have been seen to be affected by the presence of incidental iron (as low as 40 ppb) in the electrolyte. However, other groups have identified that nickel undergoes transformations with or without the presence of incidental iron in the electrolyte.[35,57,106] Iron was removed from electrolytes by the iron-cleaning procedure described by Zemtsova *et al.*; these electrolytes were labeled as "purified".[109] Electrolytes that were not subject to an iron-cleaning procedure were labeled as "unpurified". For experiments containing urea, the electrolyte was comprised of a 0.5 M KOH solution with 0.2 M urea (99.6 wt.%, Fisher Scientific). A 25 °C water bath (Fisher Scientific) was used to maintain a constant cell temperature. A Solartron 1287 potentiostat was used to collect electrochemical data. The lot analysis of chemicals is seen in Appendix A.

5.2.3 Electrochemical Methods

Immediately after sonification, the working electrodes were sprayed with excess amounts of 0.5 M KOH to remove any remaining ethanol and placed into the three electrode cell. A potential hold of -0.47 V_{RHE} was applied to the working electrode for 30 minutes to remove any native oxides. A 600-cycle oxide development procedure was performed using cyclic voltammetry (CV) for upper limits (E_λ) of 1.58 and 1.68 V_{RHE} per 600-cycle set. The starting potential was 0.93 V, and the scan rate was 10 mV s^{-1}. Immediately after oxide development of 600 scans, a potential was held for product gas analysis with mass

Table 5.1 The electrochemical procedure for oxide development and gas analysis at different switching potentials (E_λ). Red text represents electrolytes containing 0.5 M KOH, while blue text represents electrolytes containing 0.5 M KOH and 0.2 M urea.

S_B H_B:
1. 600 Scans at E_λ
2. 5 hour Hold at 1.63 V_{RHE}
3. 5 scans at 1.58 V_{RHE}
4. 5 hour Hold at OCP

S_B H_U:
1. 600 Scans at E_λ
2. 5 hour Hold at 1.63 V_{RHE}
3. 5 scans at 1.58 V_{RHE}
4. 5 hour Hold at OCP

S_U H_U:
1. 600 Scans at E_λ
2. 600 Scans at E_λ
3. 5 scans at 1.58 V_{RHE}
4. 5 hour Hold at 1.63 V_{RHE}
5. 5 scans at 1.58 V_{RHE}
6. 5 hour Hold at OCP

spectrometry. The electrodes were then held for five additional hours at zero current to obtain a background mass spectrometer signal. After gas analysis, the electrodes were cycled in 0.5 M KOH solution to 1.58 E_λ to analyze the change in redox behavior of the $Ni(OH)_2/NiOOH$ transition. The electrochemical procedure is described in Table 5.1. For naming conventions, S and H represent electrodes scanned and held, respectively, in blank ($_B$) electrolyte and urea-containing electrolyte ($_U$). For example, an electrode that was cycled without urea and underwent a potential hold with urea is labeled $S_B H_U$.

Electrodes, once sonicated and reduced, underwent a window opening procedure with cyclic voltammetry, staircase polarization, and mass spectrometry. Electrodes were developed in respective electrolytes (0.5 M KOH and 0.5 M KOH + 0.2 M urea) and underwent window opening, starting with 1.78 V_{RHE} and increasing by 0.05 V until 2.18 V_{RHE} was reached. Five scans of cyclic voltammetry and three hours of a potentiostatic hold were performed during each window opening step. Mass spectrometry was collected during each potentiostatic hold step.

5.2.4 Mass Spectrometry

The gasses within the headspace of the three electrode cell were analyzed using mass spectrometry with a Stanford Research Systems Residual Gas Analyzer 100 (SRS-RGA 100) installed in an ultrahigh vacuum chamber with base pressure of 10^{-9} torr. The three electrode cell was sealed using Apiezon M grease and parafilm wax in and around all joints. Prior to the potentiostatic hold, the electrolyte was sparged for 15 minutes with argon (Linde, 99.998 %) to remove any dissolved gases within the solution and to flush out the headspace. Argon was flowed at $\sim$1.5 mL min^{-1} to continuously flush out the headspace as products were being made and to prevent a vacuum from occurring within the cell during a background measurement. The leak valve was adjusted to allow $\sim$0.025 mL min^{-1} (throughput of 3.1x10^{-4} torr L s^{-1}) into the vacuum chamber to maintain a pressure of 5x10^{-6} torr. Mass Spectra were obtained at a scan rate of 5 AMU s^{-1} from 1 to 46 atomic mass units (AMU) using a Faraday Cup detector.

5.3 Results

5.3.1 Unpurified Electrolytes

Oxyhydroxide Development

Potential cycling was conducted to electrochemically activate and develop a stable ratio of oxyhydroxide phases on the nickel surface, as seen in Figure 5.1. Little to no current was

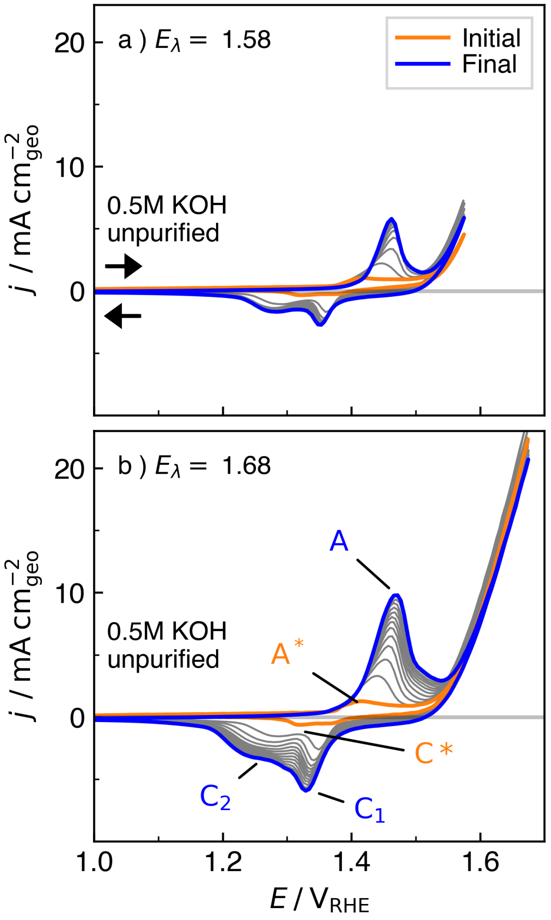

Fig. 5.1 Oxide development cyclic voltammograms for switching potentials of a) 1.58, and b) 1.68 V_{RHE} in 0.5 M KOH with 10 mVs^{-1}. The initial scan is orange, while grey lines indicate every 50th scan up to the final (blue), 600th scan. The scan direction is denoted by the horizontal arrows.

observed during the forward (anodic) scan until the nickel transition onset potential was reached above 1.37 V_{RHE} for initial scans. The onset of the nickel transition increased to 1.42 for final scans for all switching potentials. The peak potential for the initial surface wave was 1.43 V_{RHE} (peak A*) for initial scans, shifting positively and increasing in magnitude throughout development and stabilizing near 1.46 V_{RHE} (peak A) depending on E_λ. The current increased sharply at potentials above 1.54 V_{RHE} as a result of oxygen evolution. The

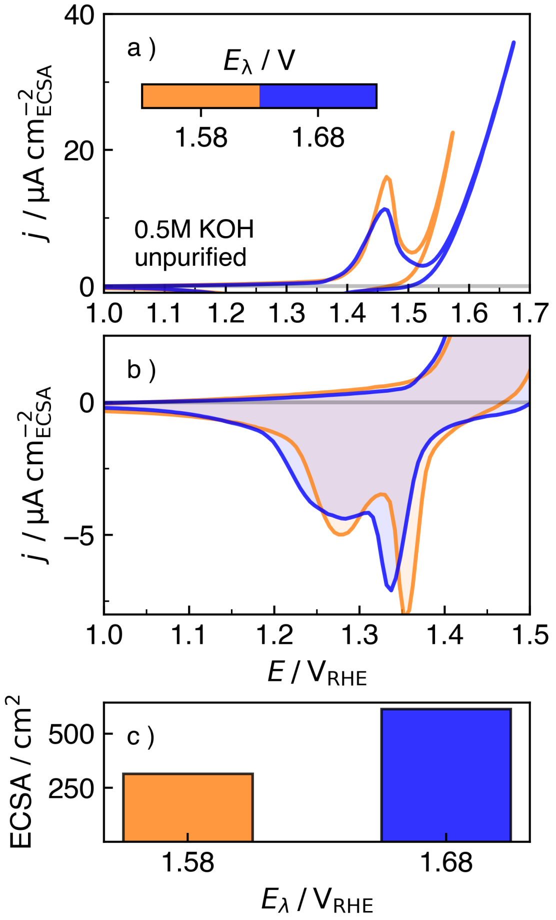

Fig. 5.2 a) Steady state cyclic voltammograms, scaled by the electrochemically active surface area (ECSA) for electrodes developed for each E_λ in 0.5 M KOH over a course of 600 scans. b) The respective reverse sweep. c) ECSA, calculated with Equation 3.1.

reduction wave exhibited a single peak (C*) for initial scans and exhibited double peaks (C_1, C_2) as the number of scans increased.

Electrochemically active surface area (ECSA) is used to compare the activity of catalysts on an equivalent per-site basis. Figure 5.2 shows the 600th scan for each electrode developed in 0.5 M KOH, normalized by the ECSA using the equation Eq. 3.1 Values for ECSA are presented in Fig. 5.2c. The ECSA increased with switching potential, indicating that increasing the extent of overcharge increases the number of sites on the surface.[175,206]

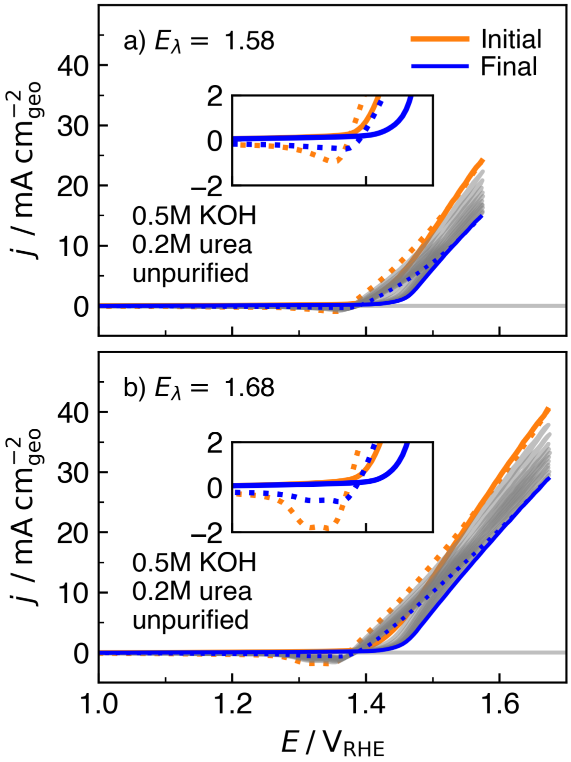

Fig. 5.3 Oxide development cyclic voltammograms (10 mV s^{-1}) for switching potentials of a) 1.58 and b) 1.58 V$_{RHE}$ in 0.5 M KOH and 0.2 M urea, after development in 0.5 M KOH. The initial scan is orange, while grey lines indicate every 50th scan up to the final (blue), 600th scan. Solid lines represent the forward scan, while dotted lines represent the reverse scan. The inset shows the zoomed reduction current.

While the onset potential for the nickel transition was relatively unchanged among all E_λ, the OER onset potential increased with switching potential, as seen in Fig. 5.2a. The OER current a useful feature for comparing OER activities between different phases, where β-NiOOH is known to be a better OER catalyst than γ-NiOOH.[57,85,150] The distribution of phases was observed by the reduction peaks seen in Fig. 5.2b. The surface developed at the lower switching potential, 1.58 V$_{RHE}$, had a clear separation of peaks and a peak with greater magnitude at 1.28 V$_{RHE}$ than the surface developed at 1.68 E_λ.

Electrodes with a previously developed oxide layer in 0.5 M KOH were cycled with urea (0.2 M) to similar switching potentials to examine the effect of urea during reduction, as

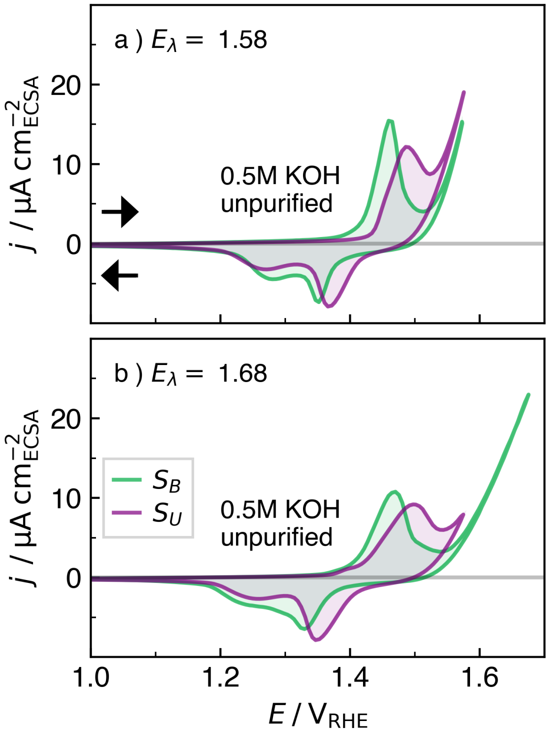

Fig. 5.4 Cyclic voltammograms (10 mV s^{-1}) for switching potentials of a) 1.58 and b) 1.68 V_{RHE} in 0.5 M KOH for nickel electrodes cycled without (green) and with urea (purple). The scan direction is denoted by the horizontal arrows. S represents electrodes scanned in blank ($_B$) electrolyte and urea-containing electrolyte ($_U$).

seen in Figure 5.3. The UOR onset potential shifted positively from 1.42 to 1.46 V_{RHE}. The current density at the highest potential in the scan, E_λ, decreased over each scan. The reverse scan exhibited a crossover, where the current was higher than the current of the forward scan. This hysteresis indicates that NiOOH continues to form on the surface during potentials lower than $Ni(OH)_2$/NiOOH redox potential, assuming that UOR follows the indirect mechanism. The current crossed over again at 1.39 for all E_λ. The reduction peaks in the presence of 0.2 M urea are small due to urea consuming nickel sites, assuming the indirect mechanism occurred during reduction-relevant potentials.

Electrodes that were cycled in urea were once again cycled without urea in 0.5 M KOH to observe changes in the cyclic voltammetry profile. Each electrode was only cycled five

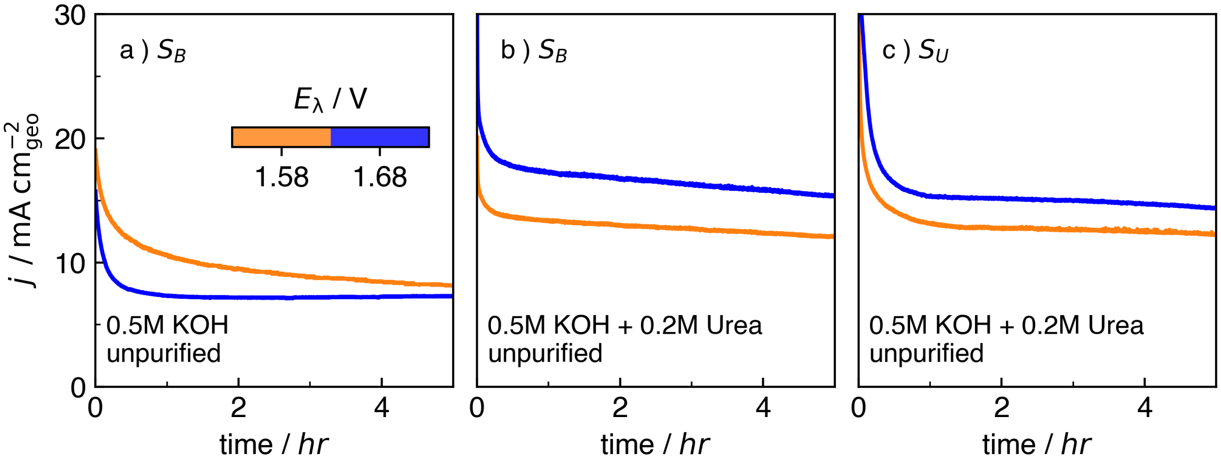

Fig. 5.5 0.70 V_{RHE} potentiostatic hold for a electrodes cycled without urea (S_B) and cycled with urea (S_B) in 0.5 M KOH and 0.2 M urea.

times with a switching potential of 1.58 V_{RHE}. The third scan of electrodes cycled in urea are seen in Fig. 5.4. For all cases, the onset evolution for electrodes cycled with urea have a lower oxygen evolution onset potential. On the reverse sweep, all electrodes exhibited a peak near 1.37 V_{RHE} and a broad peak near 1.32 V_{RHE}.

Once a steady state voltammogram for a particular E_λ potential and electrolyte was obtained, each electrode was subjected to a five hour potentiostatic hold in the presence of 0.5 M KOH with and without urea, seen in Figure. 5.5. All curves exhibit an initial decay similar to a Cottrell response. The current density increased from Fig. 5.5a to b due to the presence of urea within the electrolyte. The current density remained relatively unchanged between Fig. 5.5b and c. The phase and the ECSA of the electrode was unaffected over the course of the 5 hour potentiostatic hold, based on the similar shape of the cyclic voltammetry curve in Figure 5.6.

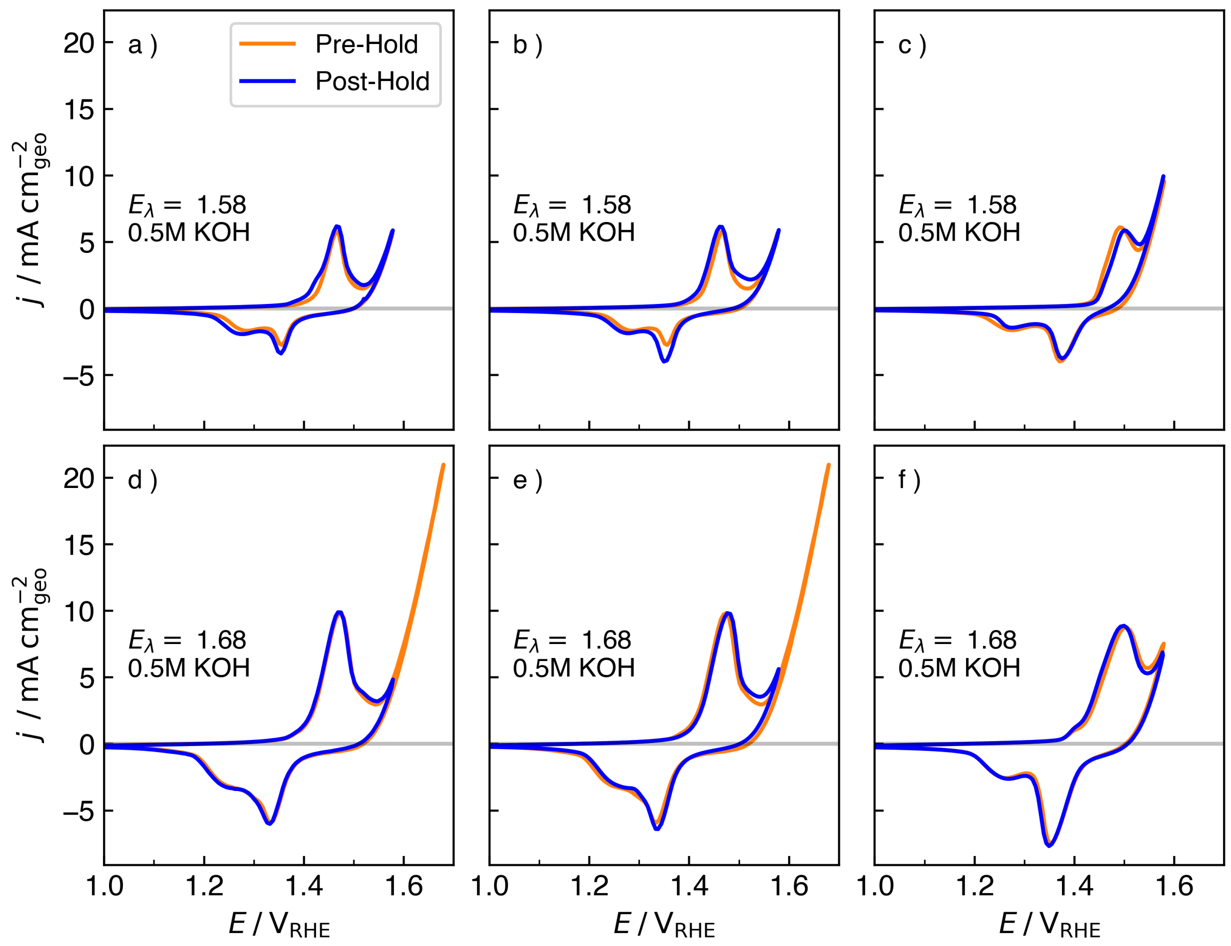

Fig. 5.6 Cyclic voltammetry (10 mV s^{-1}) of nickel foam electrodes before and after a five-hour potential hold at 1.63 V$_{\text{RHE}}$.

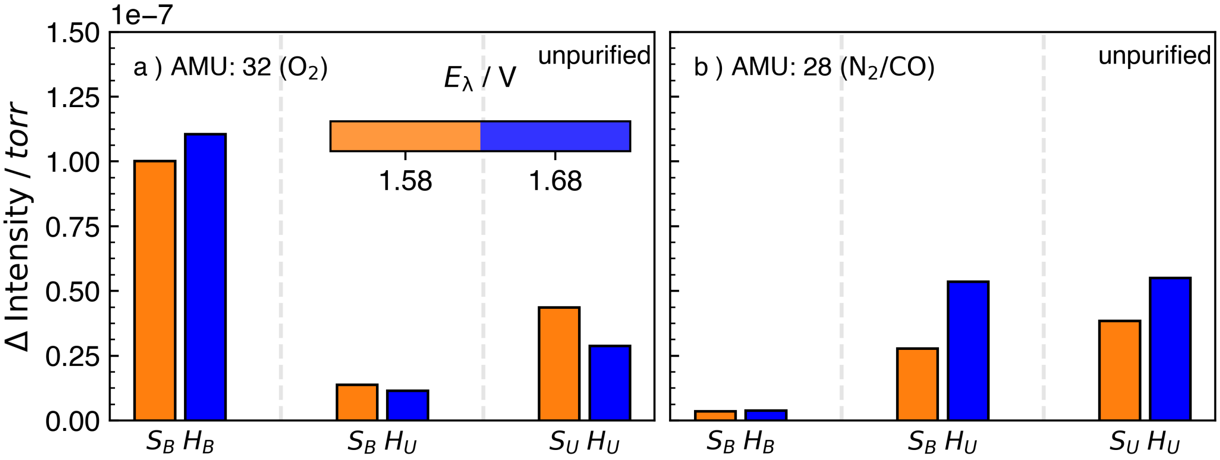

Fig. 5.7 Mass spectrometry change in intensity from background signal for electrodes developed at 1.58 and 1.68 E_λ V_{RHE}. Scan Without and Scan With represent electrodes developed without and with urea up to E_λ, respectively. Hold Without and Hold With represent 5 hour-$1.68V_{RHE}$ potentiostatic holds without and with urea, respectively

Mass Spectrometry

Mass spectrometry was performed during each potentiostatic hold to determine the partial pressure of product gasses. The change of intensity from background spectra for mass 32 (O_2) and mass 28 (N_2/CO) for electrodes developed with an E_λ of 1.58 and 1.68 V_{RHE} are presented in Figure 5.7. The mass spectrometry signal was collected from 2 to 46 AMU, and is seen in Figures 5.8 and 5.9.The working electrode produced oxygen and nitrogen (if urea was present) and the counter electrode produced hydrogen during the potentiostatic hold. Argon was continually introduced into the cell (Fig. 3.10) to aid in movement of gasses to the leak valve.

There was noticeable signal for mass 32 (O_2) for electrolytes only containing 0.5 M KOH in Fig. 5.7, while there was a small mass 28 (N_2/CO) signal was due to lack of urea in the solution. Once urea was added to solution, an increase in signal was observed at mass 28 (N_2/CO) for in Fig. 5.7b. For an electrode cycled without urea, the mass 32 (O_2) decreased from when there was only 0.5 M KOH in the electrolyte. However, for an electrode cycled

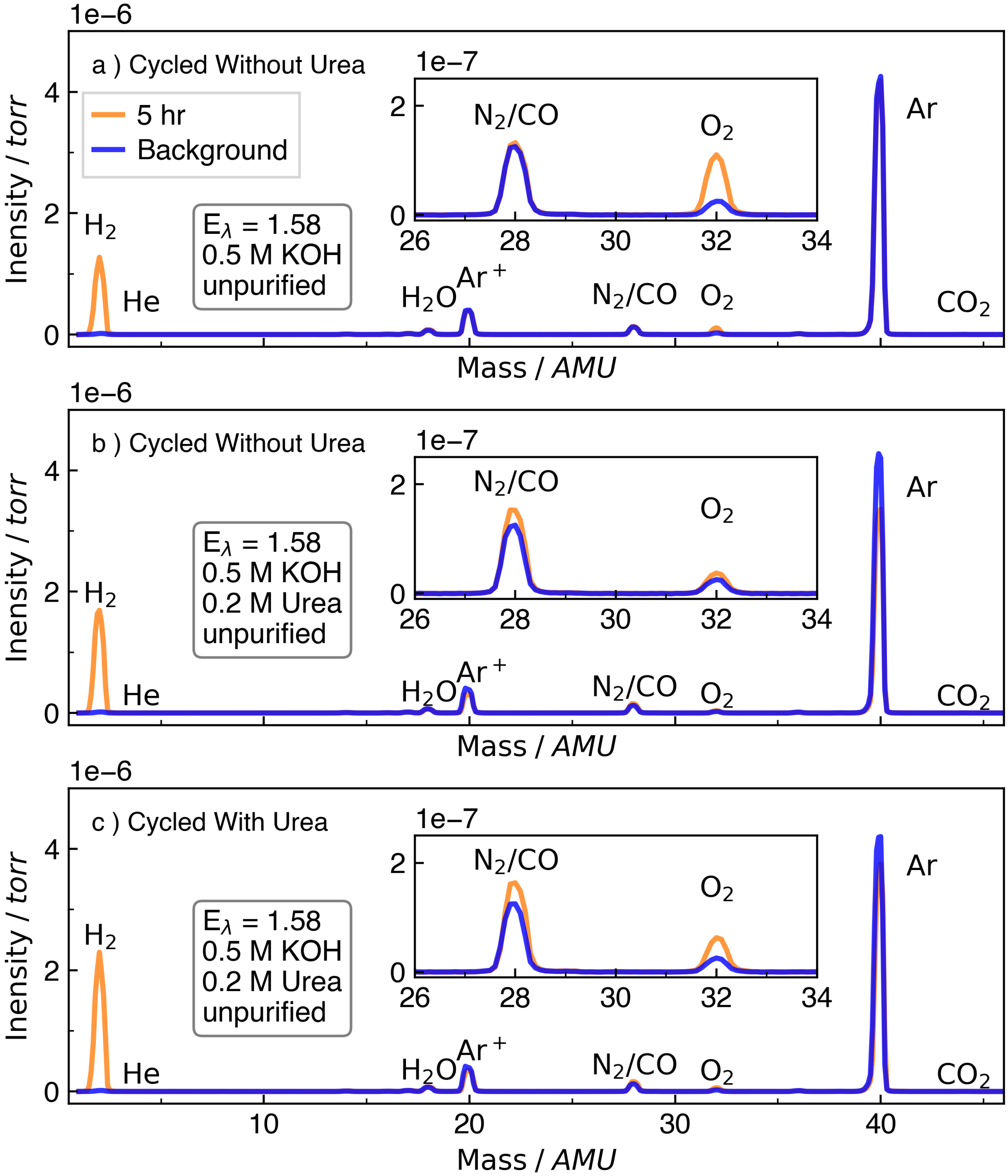

Fig. 5.8 Mass spectrometry for an electrode developed at 1.58 E_λ during a 1.63 $V_{Hg/HgO}$ photostatic hold.

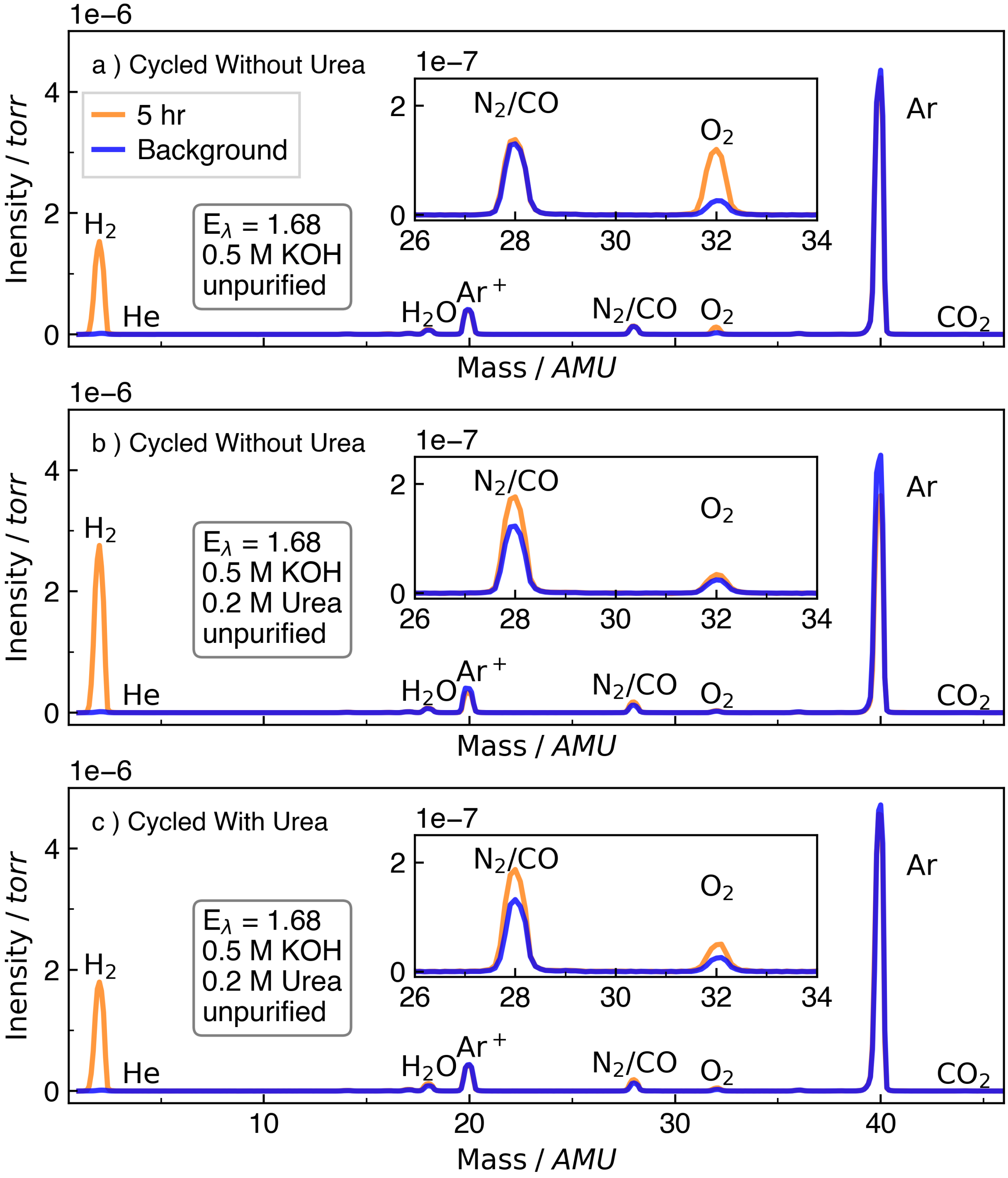

Fig. 5.9 Mass spectrometry for an electrode developed at 1.68 E_λ during a 1.63 $V_{Hg/HgO}$ photostatic hold.

with urea, there is a noticeable increase in signal for mass 32 (O_2), suggesting that more OER occurred on the nickel surface. This phenomenon was observed for all switching potentials. There was no change in peak height for (CO_2) for all scans, consistent with the dissolution of CO_2 into solution immediately after production.[207,208]

The product distribution shifted from primarily OER to UOR when urea was added to the cell, as seen by the decrease in mass 32 intensity in Fig. 5.7a and the increase in mass 28 intensity in Fig. 5.7b between S_BH_B and S_BH_U. When an electrode is cycled with the presence of urea, the mass 28 intensity remained relatively constant, while the mass 32 intensity increased significantly. This increase in mass 32 intensity is ascribed to the change of the electrode surface during electrochemical cycling with the presence of urea in the electrolyte.

5.3.2 Purified Electrolytes

Oxyhydroxide Development With and Without Urea

The role of incidental iron has been previously found to affect the phases and oxygen evolution reaction properties of nickel hydroxide. To resolve any concerns about iron affecting the hydroxide, a purified electrolyte was prepared using a procedure developed by Zemtsova *et al.*, and was used to test the formation of a γ-NiOOH-like catalysts.[109] Figure 5.10 shows the oxide development in an purified electrolyte without and with urea. The switching potential, when compared to Fig. 5.1, for the purified solution was increased to drive the oxygen evolution reaction for the formation of a γ-NiOOH on the surface. The UOR onset potential increased with scan number in Fig. 5.10b for purified solutions, supporting the idea that urea affects the nickel oxyhydroxide surface with and without the presence of iron.

Window-opening

The window-opening experiments in a purified, 0.5 M KOH solutions without and with urea are seen in Figure 5.11. In Fig. 5.11a and b, the onset potential for nickel transition, OER,

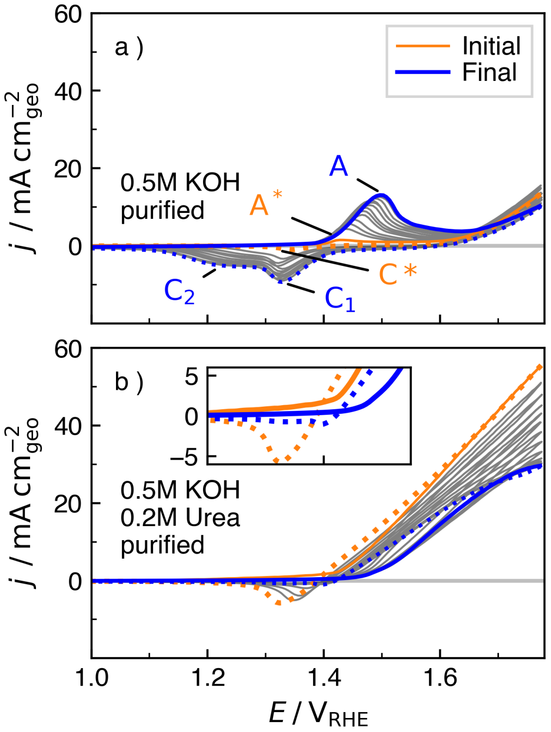

Fig. 5.10 Oxide development cyclic voltammograms (10 mVs^{-1}) for a purified 0.5 M KOH solution containing a) 0 M and b) 0.2 M urea. The initial scan is orange, while grey lines indicate every 50th scan up to the final (blue), 600th scan. Solid lines represent the forward scan, while dotted lines represent the reverse scan. The inset shows the zoomed reduction current.

and UOR remain relatively similar for all switching potentials, indicating the surface did not substantially change during experimentation. The forward scan seen in Fig. 5.11b drops in current at potentials above 2.04 V_{RHE}. The return scan shows an initial drop in current, indicating a hysteresis of the electrode. The reverse scan continues to drop until a sharp increase, as seen by the sharp peaks near 1.96 V_{RHE}. The reverse scan current after the sharp peak is higher than the current observed in the forward scan, until reduction currents are reached near 1.40 V_{RHE}.

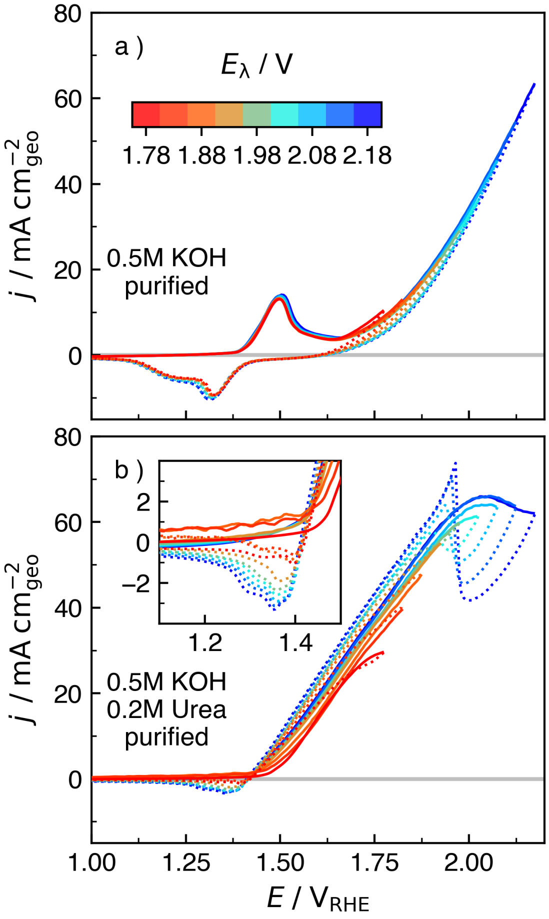

Fig. 5.11 Window-opening cyclic voltammograms (10 mVs^{-1}) for a purified 0.5 M KOH solution containing a) 0 M and b) 0.2 M urea. Solid lines represent the forward scan, while dotted lines represent the reverse scan. The inset shows the zoomed reduction current.

Polarization And Mass Spectrometry

Immediately after the window-opening experiments, each electrode was subjected to a three hour potentiostatic hold in the presence of a purified, 0.5 M KOH electrolyte with and without urea, seen in Figure 5.12. For a solution without urea, increasing the holding voltage resulted in an exponential response in current, as seen in the polarization curve in Fig. 5.12b. The current responses for 1.78 and 1.83 V_{RHE} for a urea-containing solution were near 35 mA cm^{-2} and exhibited large oscillations that ceased at 1.88 V_{RHE} and above. The current

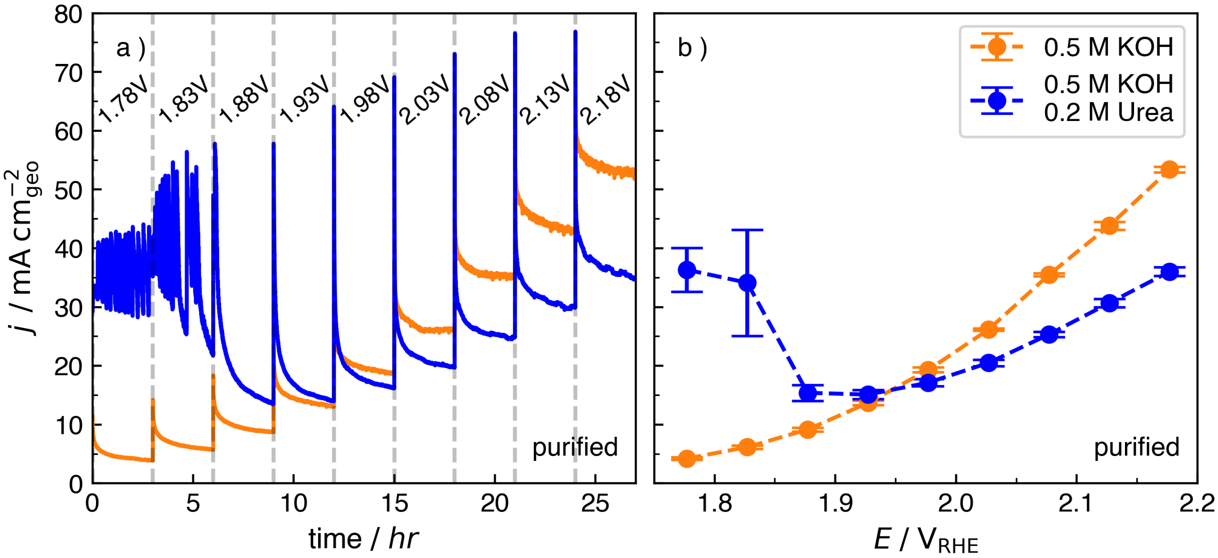

Fig. 5.12 a) staircase polarization curves and b) the resulting polarization curve for purified electrolytes with and without urea. The error bars represent the standard deviation of the current response over the last two hours of each hold.

density after 1.83 V_{RHE} dropped suddenly, and then slowly increased with potential. The drop in current density is most likely to a switch in reaction mechanism or possible further oxidation to NiO_2.[109] Additionally, there may be a site competition between OER and UOR, with OER becoming more dominant with increasing switching potential.

Mass spectrometry was collected during the staircase polarization holds to determine the partial pressure of product gasses for each step and is seen in Figure 5.13. Mass spectra over the range of 2 to 46 AMU is presented in Figure 5.14. The mass 32 (O_2) signal in Fig. 5.13a increased in potential as more OER was occurring on the surface, while the mass 28 (N_2 /CO) signal was too low to detect as there was no urea in the electrolyte. A peak at mass 28 (N_2 /CO) was observed when urea was present in the solution, but diminished as the holding potential increased (Fig. 5.13b). The height of the mass 32 (O_2) peak increased Fig. 5.13b with holding potential. The increase in O_2 and decrease in N_2 /CO with increasing holding potential indicates that the OER dominated the surface at higher potentials.

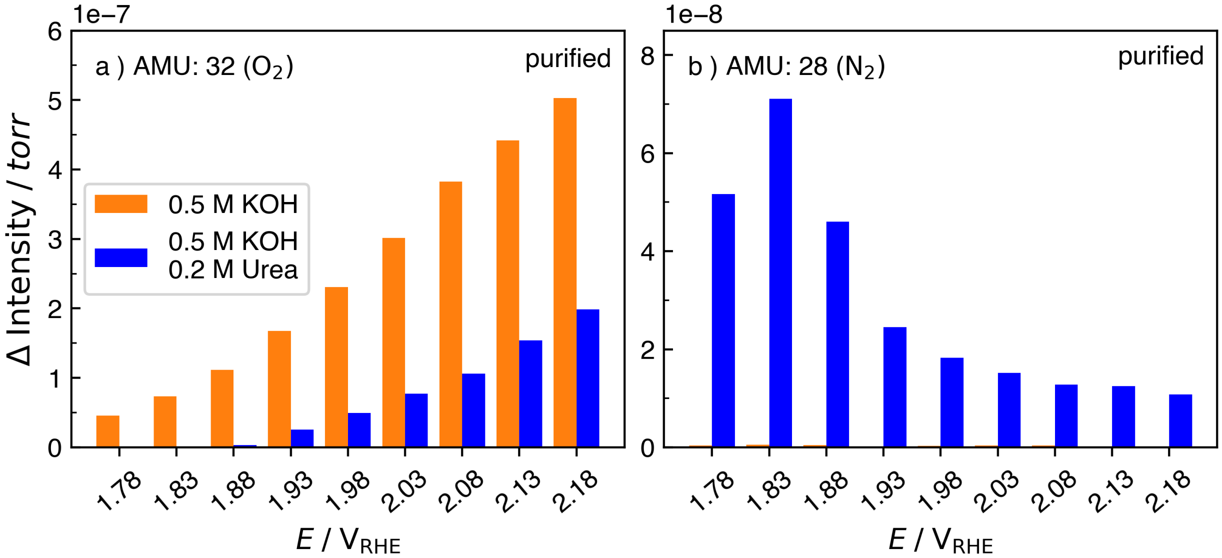

Fig. 5.13 Mass spectrometry change in intensity from background signal for electrodes in purified electrolytes containing a) 0.5 M KOH and b) 0.2 M urea. Background signal is represented by black, while potentials are represented by the color bar.

5.4 Discussion

5.4.1 Oxyhydroxide Development Without Urea

Prior to development, hydroxides were removed from surface by applying a large reducing potential, allowing for a near-metallic nickel surface to be obtained.[148,178,209,210] Initially, the nickel surface forms a primarily α-Ni(OH)$_2$-type surface by exposure to an alkaline environment above 0.28 V$_{\mathrm{RHE}}$, due to the low standard equilibrium potential of Ni to α-Ni(OH)$_2$ reaction.[178,205,211,212] A surface comprised of α-Ni(OH)$_2$ will electrochemically oxidize to γ-NiOOH when a moderate potential is applied. In Fig. 5.1 and Fig. 5.10a, the anodic peak (A*) corresponds to the α-Ni(OH)$_2$ to γ-NiOOH oxidation reaction, with a matching reduction peak (C*). As the electrode cycles, the A* peak diminishes while peak A forms. The formation of β-Ni(OH)$_2$ is expected, as β-Ni(OH)$_2$ is thermodynamically more stable than α-Ni(OH)$_2$.[71] Peak A is widely accepted as the β-Ni(OH)$_2$ to β-NiOOH oxidation reaction.[76,121,148,192,210,213]

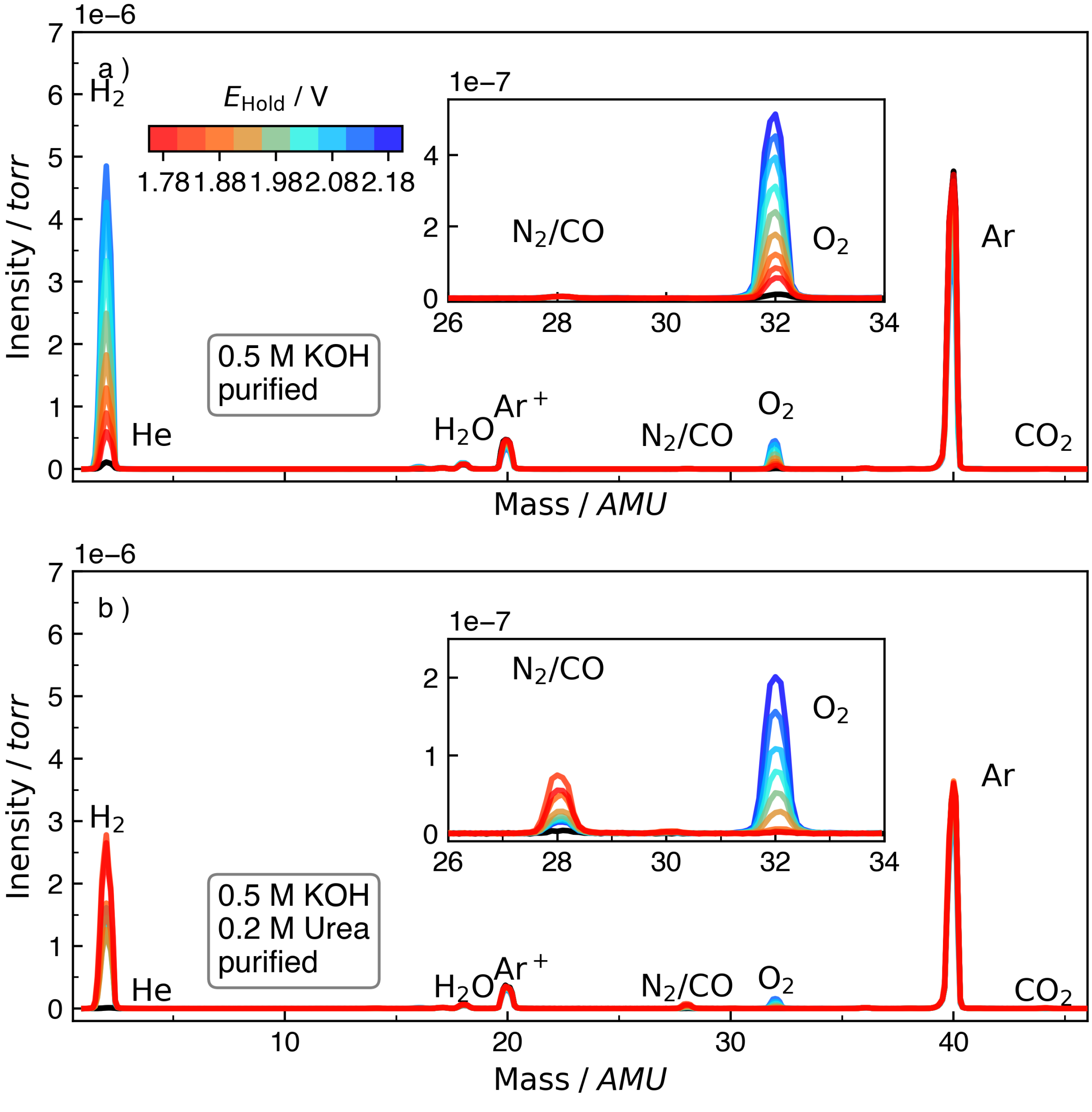

Fig. 5.14 Mass spectrometry for an electrode developed at 1.68 E_λ during a 1.63 $V_{\mathrm{Hg/HgO}}$ photostatic hold.

The final oxidation wave is accompanied by two reduction peaks, where C_1 and C_2 are associated with the reduction of γ-NiOOH and β-NiOOH, respectively. The distribution of the C_1 and C_2 peaks is correlated to the extent of overcharge applied to the surface. The process of overcharging the electrode converts a fraction of β-NiOOH to γ-NiOOH, which is reflected in the size and shape of peaks C_1 and C_2.[86,214] The newly-formed γ-NiOOH can reduce into α-$Ni(OH)_2$ and β-$Ni(OH)_2$, thus allowing a mixture of phases to occupy the surface.[86,106,150]

5.4.2 Oxyhydroxide Development With Urea

Electrodes developed with switching potentials of 1.58 and 1.68 V_{RHE} without urea were scanned in a solution containing 0.5 M KOH and 0.2 M urea to probe the effect of urea during cycling, as seen in Fig. 5.3. Since UOR is assumed to follow the indirect mechanism, the urea oxidation onset potential is theorized to be dependent on the nickel transition onset potential. The indirect mechanism requires urea to bind to readily available NiOOH sites, where the structure of the urea molecule changes shape on the surface and reacts through several intermediate steps, evaluated by Daramola *et al.*.[64] The urea oxidation onset potential of the final scan in Fig. 5.3 showed an increase of 40 mV from the nickel transition onset potential observed in Fig. 5.2. This indicates that an electrode cycled with urea increases the nickel transition onset potential from 1.42 to 1.48 V_{RHE}, which is similar to the onset potential for the β-$Ni(OH)_2$/β-NiOOH transition.[66,215] This phenomenon was observed for the development of oxyhydroxides without the presence of iron, as seen by the increase in UOR onset potential between Fig. 5.10a and 5.10b.

5.4.3 Window-Opening

Electrodes, in a purified electrolyte, underwent potential window-opening experiments to probe the redox properties of OER and UOR, as seen in Fig. 5.11. For cases without urea, the cyclic voltammetry profile remained unchanged with increasing switching potential, with an OER onset potential near 1.8 V_{RHE}, which is similar to the 600 mV overpotentials observed by Klaus *et al.*.[106] The potential window-opening for purified electrolytes containing urea shows a hysteresis effect on the forward scan for switching potentials above 1.98 V_{RHE}, seen by a local maximum near 2 V_{RHE}. The decrease in current on the forward scan was observed Zemtsova *et al.* and was explained by change in UOR mechanism from N_2 to NO_x^- production.[109] Additionally, the decrease in current density can be explained by the transition from NiOOH to NiO_2, where NiO_2 is seen to be inactive towards UOR.[83,194,216] The urea molecules quickly react once the NiO_2 sites reduce back to NiOOH, which appears as a sharp increase in current density, as seen by the inflection point near 1.83 V_{RHE} on the reverse scan for E_λ above 1.98 V_{RHE}.

5.4.4 Potential Holds and Mass Spectrometry

β-NiOOH has been seen in literature to be the better OER catalyst than γ-NiOOH, due to its lower OER onset potential and lower Tafel slope, consistent with results shown in Fig. 5.5a.[84,85,217–219] The most β-like surface (1.58 E_λ) had the highest current density, while the most γ-like surface (1.68 E_λ) had the lowest current density in Fig. 5.5a.

The mass spectrometry reveals the oxygen signal (mass 32) decreases while the N_2/CO signal (mass 28) increases at low potentials when urea is added to the electrolyte, as seen in Fig. 5.7 and 5.13. This is due to UOR dominating the surface at low potentials. The mass 28 signal decreases and the mass 32 increases with increasing potential, indicating that OER is dominant at higher potentials.

5.4.5 Faradaic Efficiency

The mass spectrometry data and potentiostatic hold data can be used in tandem to address the mass balance of the system. The electrochemical current (i_e) was taken as an average over the last two hours of each potential hold and is seen in Table 5.2 and Fig. 5.15. The current necessary to fulfill the compositions seen in the mass spectrometry (i_{ms}) of Fig. 5.7 is seen in Table 5.2 and Fig. 5.15, given the production of N_2 from urea oxidation requires 6 e^- and OER requires 4 e^-. The value of i_{MS} is determined by finding the amount of current

Table 5.2 Electrochemical current (i_e), mass spectrometry-derived current (i_{MS}), and N_2 Faradaic efficiencies (F.E.) for unpurified electrolytes

Regime	i_e	i_{MS}	N_2 F.E.
[-]	[mA]	[mA]	[%]
1.58 V_{RHE}			
$S_B\ H_B$	16.50	13.95	-
$S_B\ H_U$	24.37	15.44	58
$S_U\ H_U$	24.73	13.08	57
1.68 V_{RHE}			
$S_B\ H_B$	14.57	15.47	-
$S_B\ H_U$	31.05	17.28	53
$S_U\ H_U$	29.04	13.26	38

needed to match the N_2 and O_2 signals of each mass spectra for an Ar flowrate of 1.5 mL min^{-1}, by:

$$i_{ms} = i_{N2} + i_{O2} = \dot{n}_e x_{o2} F n_{OER} + \dot{n}_e x_{n2} F n_{UOR} \tag{5.1}$$

where x_{o2} and x_{n2} are the compositions of O_2 and N_2 from mass spectrometry, n_{OER} is the number of electrons involved in OER (4), n_{UOR} is the number of electrons involved in N_2 from UOR (6), and $\dot{n}_e$ is the volumetric amount of gas produced from the electrode. The equations used to determine $\dot{n}_e$ and i_{ms} are seen in Appendix A.

The Faradaic efficiency (F.E.) for the complete oxidation of urea is found by comparing the current necessary to used to generate N_2 seen by mass spectrometry (Fig. 5.7 and 5.15) versus by the potentiostat (Fig. 5.5 and 5.12). An F.E. of 1 indicates that all the current observed by the potentiostat goes towards the production N_2 species by Equation 5.2.

$$6\,\mathrm{NiOOH_{(s)}} + \mathrm{CO(NH_2)_{2,(aq)}} + \mathrm{H_2O_{(l)}} \longrightarrow 6\,\mathrm{Ni(OH)}_{2,(s)} + \mathrm{N}_{2,(g)} + \mathrm{CO}_{2,(g)} \tag{5.2}$$

An F.E. of < 1 indicates that a fraction of the current went to underoxidation or overoxidation (Eq. 5.3) of urea, generating species that enter the electrolyte rather than entering the gas

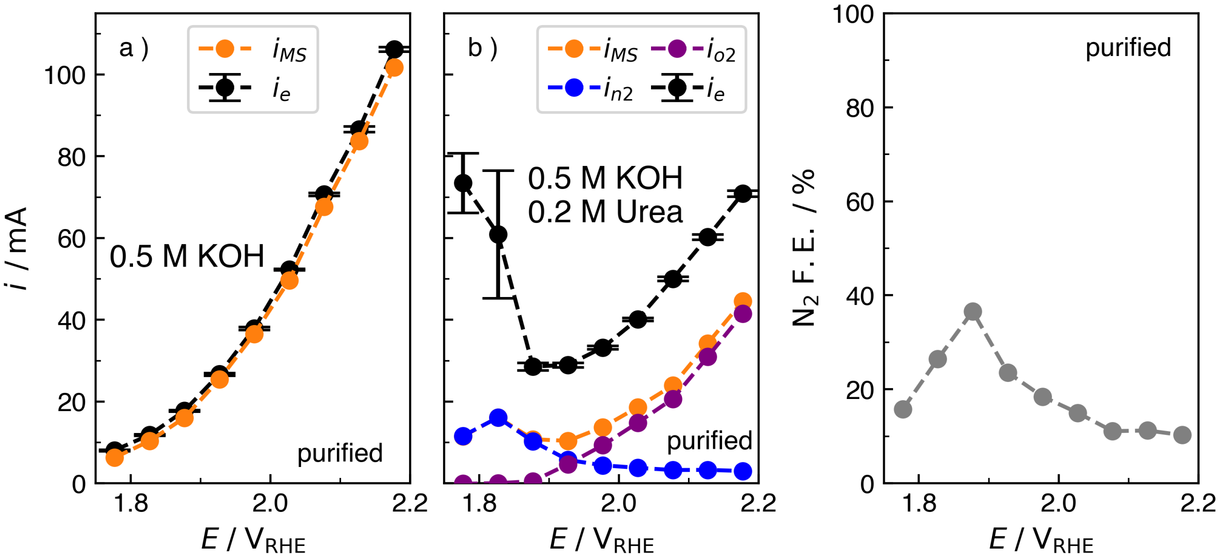

Fig. 5.15 Electrochemical current (i_e) and mass spectrometry-derived current density (i_{MS}) for purified electrolytes with a) 0.5 M KOH and b) 0.2 M urea. c) N_2 Faradaic efficiencies (F.E.) for nickel-oxyhydroxide electrodes in purified electrolytes of 0.5 M KOH and 0.2 M urea.

phase through Equation 5.3.

$$(2\,x + 4)\,OH^-_{(aq)} + CO(NH_2)_{2(aq)} \longrightarrow NCO^-_{(aq)} + NO^-_{x,(aq)} + (4 + x)H_2O_{(l)} + (2\,x + 2)\,e^- \quad (5.3)$$

The Faradaic efficiencies in Table 5.2 and Figure. 5.15 show that urea underwent underoxidation or overoxidation within all studied regimes. These values, although somewhat high, are within range of F.E. seen in other studies.[65,220] The distribution of current for the production of N_2, $NO_2{}^-$, and $NO_3{}^-$ products have been seen to be dependent on experimental conditions and may explain the higher values of F.E. observed here.[59] Additionally, the oxidation of NiOOH to NiO_2 may explain the drop in current and mass 32 signal after 1.83 V_{RHE}, as NiO_2 has UOR poor catalytic properties but is still active towards OER.

5.5 Conclusion

The aim of this study was to investigate the influence of urea oxidation on the reduction of nickel oxyhydroxide by analyzing the nickel phases through detailed electrochemical experiments and mass spectrometry. Electrodes were developed to operate at different switching potentials, allowing a a distribution of β-NiOOH and γ-NiOOH phases to form on their surfaces. These stable ratios are held at a potential sufficient to induce urea oxidation and oxygen evolution, with the resulting gases being analyzed through mass spectrometry. Electrodes cycled with urea, using switching potentials similar to those of electrodes developed without urea, displayed an enhanced propensity for oxygen evolution.

The investigation of purified electrolytes showed a hysteresis during cyclic voltammetry at higher potentials that had a timescale shorter than the duration of the staircase potential experiments. The hysteresis is possibly due to the transitions between $Ni(OH)_2$/NiOOH at low potentials and NiOOH/NiO_2 at high potentials, where nickel can occupy chemical states below the respective redox potential. The existence of different states of nickel during electrochemical experiments convolutes the analysis of whether the drop in current at higher potentials is due to the formation of NiO_2 or a change in UOR reaction mechanism. Therefore, we recommend a comprehensive analysis using spectroscopic methods for in-situ determination of nickel states during anodic urea electrooxidation.

5.6 Acknowledgements

The authors thank Prof. Gregory Jerkiewicz and Dr. Derek Essau for advice on apparatus construction and guidance of electrochemical topics. The authors thank Prof. Peter Strasser for the opportunity to visit his laboratory and Dr. Fabio Dionigi for advice on performance and preparation procedure of nickel hydroxide catalysts.

Chapter 6

ELECTROCATALYTIC UREA OXIDATION ON HIGH CHROMIUM AND MOLYBDENUM NICKEL ALLOYS

6.1 Introduction

6.1.1 Overview

Urea electrolysis as an efficient means to remove urea from urea-rich wastewater and has been a focus of study within the last several decades.[42,44,166,196] Early electrocatalysts were comprised of primarily platinum and ruthenium, but are costly and are capable of producing toxic byproducts.[30,221,222] Nickel-based catalysts are a cheaper alternative to platinum and and ruthenium can produce non-toxic products, such as N_2 and CO_2.[41,43,197] However, nickel catalysts have limited application in wastewater treatment due to the corrosion of nickel from the high concentration of chloride ions. The alloying with chromium and molybdenum into nickel has shown to improve the corrosion resistance in reducing, oxidizing, and brackish water environments.[198–201] These additives have not been studied for their contribution towards improving urea electrooxidation. The transition between $Ni(OH)_2$ and NiOOH is studied here with pure nickel and nickel alloys to understand the role of additives and to identify the reaction mechanism responsible for urea oxidation.

Previous works have identified two possible mechanisms for urea electrooxidation on nickel.[49–52] The direct urea oxidation reaction (DUOR) consists of urea reacting on the nickel oxyhydroxide surface, as seen in Reaction 2.1. The indirect urea oxidation reaction (IUOR) is the chemical reaction of urea with an electrogenerated active species of NiOOH, in turn reducing NiOOH to $Ni(OH)_2$, as seen in Reaction 2.2. The electrogenerated species NiOOH is supplied by the nickel transition reaction, as seen in Reaction 2.3. Reaction 2.4, hydrogen evolution, is used to balance the half reactions that occur on the anode. Urea electrolysis has been seen as an alternative to oxygen evolution for the production of hydrogen within other studies, but is not a main focus of this study.[43,196]

The overall urea oxidation reaction (UOR), Reaction 2.5, is used to express the process in an electrolysis cell. Both direct and indirect mechanisms rely on the presence of NiOOH on the surface. Thus, UOR is mediated through an electrochemical activation of nickel from $Ni(OH)_2$ to NiOOH at 1.35 V_{RHE}.[53] The $Ni(OH)_2$/NiOOH transition redox potential (and the UOR onset potential) is altered by the presence of Cr, Mo, and other metallic additives.

6.1.2 Additives

Haynes® BC-1, C-276, and C-2000 commercial alloys were chosen as electrodes because of their high nickel content ($> 54\%$) and established corrosion resistance.[198–201,223,224] Although these alloys have a variety of other alloying elements, they differ mainly in their relative amounts of Cr and Mo and the inclusion of W in C-276. A list of the alloys and compositions in this study is seen in Table 6.1.

Introducing chromium into nickel changes the composition and the protective properties of the oxide layer. Incorporation of Cr has been shown to form double-layered oxide films, where Cr-based oxides [Cr_2O_3 or $Cr(OH)_3$] are seen at the bulk metal/film interface, and Ni-

Table 6.1 Nominal compositions (wt.%) for three Ni-based alloys. Elements less than 1% for all alloys were excluded.

	BC-1	C-276	C-2000
Ni	60	55	54
Cr	15	16	23
Mo	22	16	16
W	-	4	-
Co	1	2.5	2
Fe	2	5	3
Mn	0.25	1	0.5
Cu	-	0.5	1.6

based oxides are found at the electrolyte interface.[94] In terms of urea oxidation, the inclusion of chromium oxide into nickel has shown to depress the density of states at the Fermi level of the d-band of nickel, thereby weakening the Ni-O_{urea} bond and decreasing the energy for adsorption.[95] Thus, including Cr has shown to improve the UOR activity by altering the electronic structure of nickel hydroxide.

Introducing molybdenum into nickel also changes the nature of the oxide film. Mo is unevenly distributed within the passivated film, with Mo^{4+} residing at the metal/oxide interface and Mo^{6+} present at the electrolyte interface.[96] Mo does not form a phase-separated oxide species (Mo_xO_y) within the film. The proposed role of Mo oxide films is to inhibit localized breakdown by stabilization of the cation vacancies.[97] Electrochemically, the inclusion of Mo causes nickel to complete the $Ni(OH)_2$/NiOOH transition at lower onset potentials.[98] The onset potential for UOR is also lowered from the addition of Mo into Ni, as UOR is dependent on the presence of NiOOH. Doping of Mo promotes coupling of the N—N bond on the intramolecular level as well as the fracture of the C=O bond in urea, promoting the selectivity of N_2 and CO_2 products.[225]

The role of Mo in NiCr films has been seen to promote the film growth of Cr_xO_y oxides. The proposed role of incorporated Mo stability arises from Mo^{6+} replacing Cr^{3+} vacancies, thus reducing the number of accessible point defects susceptible to corrosion.[115] The increased concentration of Mo in corrosion pits and crevices shows the ability for Mo to prevent further corrosion, re-passivating the surface and allowing the oxide layer to self-heal. While these corrosion mechanisms are useful for extending the lifetime of the electrode, an understanding of UOR on these NiCrMo surfaces is necessary for deployment in an application-based setting.

One application that would benefit from a urea-electrooxidative and corrosion-resistant catalyst is kidney dialysis. The use of nickel catalysts in a portable dialysis device has been developed by several groups, however there is a halt in progress possibly due to the generation of chloride species or leaching of metal species.[194,226–229] The corrosive resistance of alloys used in this report has been well-established, but the use of these alloys for urea oxidation has not been previously studied.

This report is an initial study of the UOR performance of the alloys; corrosive environments, such as neutral pH brackish water, were not studied here. As alloys have not been previously studied for UOR, this work focuses on oxide growth and UOR in a high pH environment. These commercially available alloys serve as a reproducible electrodes amongst different laboratories, enabling more consistent measurements for Ni electrodes.

6.2 Experimental

6.2.1 Materials

All alloys were provided by Haynes International as 76 mm x 76 mm x 1.6 mm coupons. Nickel (99.5%) coupons were purchased from Alfa-Aesar. All coupons were cut into 20 mm x 13 mm pieces. A line was physically scored at 11 mm from the bottom of the electrode to serve as a depth marker and ensure a consistent surface area of 3.5 cm^2 (front, back, and edge areas) inserted into solution. The electrodes were polished using 600, 1500, 3000, 5000 silicon carbide grit sandpaper, and 0.3-micron alumina paste to obtain a mirror-like finish. Deionized water was obtained from an in-house Millipore-Q water system. Urea (99.6 wt. %), KOH (87.4 wt. %), and ethanol (95 wt.%) were purchased from Fisher-Scientific and used as received.

6.2.2 Electrochemical Cell

All electrochemical experiments were performed in a Pine Research 150 mL three-electrode cell. The counter electrode was a high surface area ($\sim$ 5 cm^2) Pt coil electrode to prevent mass transfer effects on the cathode. All working electrodes, once sanded and polished, were sonicated in 70% ethanol for removal of non-metal solutes and again in deionized water. Iron contamination of the electrochemical cell and the solution was not monitored. The alloys were not tested for iron contamination since they are known to contain iron. Urea oxidation experiments were conducted in 1 M KOH with concentrations of 10, 50, and 100 mM urea at 37°C. A temperature of 37°C was chosen to mimic the temperature of fluids during dialysis. The reference electrode was an uncalibrated, double-junction Hg/HgO (4.24 M KOH, $E^{\ominus}_{\mathrm{Hg/HgO}} = 0.098$ V) electrode from Pine Research. All voltages are reported with respect to the reversible hydrogen electrode (RHE), calculated using the Eq. 4.1.

6.2.3 Electrochemical Data Collection

The electrochemical experiments were controlled by a Solartron 1287 potentiostat. A potential hold of –0.48 V_{RHE} in 1 M KOH for 30 minutes was performed in the three-electrode cell to reduce the nascent oxide layer that resulted from exposure to atmosphere. This low of potential helps to remove trace amounts of hydroxides on the surface, allowing for a near-metallic nickel surface to be obtained.[148,178,210] Electrodes tested immediately after reduction were labeled initial oxide ($\mathrm{MO}_{\mathrm{x,init}}$). Electrodes that were held at 1.22 V, the highest potential without any observed current, at 37 °C for three hours to facilitate the oxide layer growth were labeled mature oxide ($\mathrm{MO}_{\mathrm{x,mat}}$).

Cyclic voltammetry (CV) and staircase polarization experiments were performed at 37 °C with and without urea. Cyclic voltammetry was performed within a potential window to observe the $\mathrm{Ni(OH)_2/NiOOH}$ transition (Reaction 2.3) and oxygen evolution. Cyclic potential sweeps from 0.92 to 1.57 V_{RHE} were conducted at 1 mV s^{-1} to determine the potentials of the $\mathrm{Ni(OH)_2/NiOOH}$ transition and the UOR at a quasi-steady state time scale. The third CV scan was used for figures and analysis.

Staircase potential step (polarization) experiments were conducted for steady-state analysis of UOR. For the staircase polarization experiments, the potential was stepped from 1.32 to 1.57 V_{RHE} in 10 mV increments at 10 min per step. Staircase polarization curves were generated by plotting the average of the last five minutes of current for a given step vs. the potential of that step. Double layer capacitance measurements were collected at 5, 10, 15, 20, and 25 mV s^{-1} scan rates within a 100 mV range centered at the open circuit potential.

6.3 Results

6.3.1 Nickel Transition and Oxygen Evolution

Staircase polarization current (SPC) and 1 mV s^{-1} CV scans of initial and mature oxide electrodes in 1 M KOH are presented in Figure 6.1. The CV scans (Fig. 6.1a,b) for alloys and nickel show the onset potential for nickel transition of the initial and mature oxide layer near 1.39 V and 1.41 V_{RHE}, respectively. The peak of the CV occurs at 1.41–1.44 V for alloys and 1.43–1.45 V for nickel, depending on the oxide treatment. The current decreases after the peak until about 1.47 V_{RHE} when the Ni transition becomes complete. The current during oxidative peak during the forward scan was assumed to be completely Ni, although Mo can oxidize at these potentials as well.[230] At higher potentials, the current increases sharply due to the oxygen evolution reaction (OER). Currents for the alloys exceed those for Ni.

For the mature oxide layers, the peak of the $Ni(OH)_2$/NiOOH transition shifts to higher potential for BC-1, C-276, and Ni; for BC-1 a two-peak structure is evident. Conversely, there is little shift for C-2000. This implies that the $Ni(OH)_2$/NiOOH transition has an increased overpotential on the mature oxide surface for BC-1, C-276, and Ni, though not for C-2000. The shifted peaks show some deformation on the high potential side due to greater overlap with the OER curve. This is especially evident for Ni. Changes in the OER overpotential are not likely the cause of the peak shifts, however. This is inferred by extrapolation of the OER slope down to zero current; the potentials for the extrapolated "zero-current" OER fall to within 10 mV of 1.49 V_{RHE} for all cases. The current during the reduction of the reverse sweep for mature oxides increased as well, indicating an increase in nickel sites participating in $Ni(OH)_2$/NiOOH for all electrodes.

Being a pseudo-steady state measurement, the SPC data in Fig. 6.1 c,d show essentially zero current in the region of the $Ni(OH)_2$/NiOOH transition, indicating that the system reached equilibrium over the time period of each step hold. Current appears at potentials above 1.47 V_{RHE}, which is ascribed to the onset of OER, consistent with the extrapolated

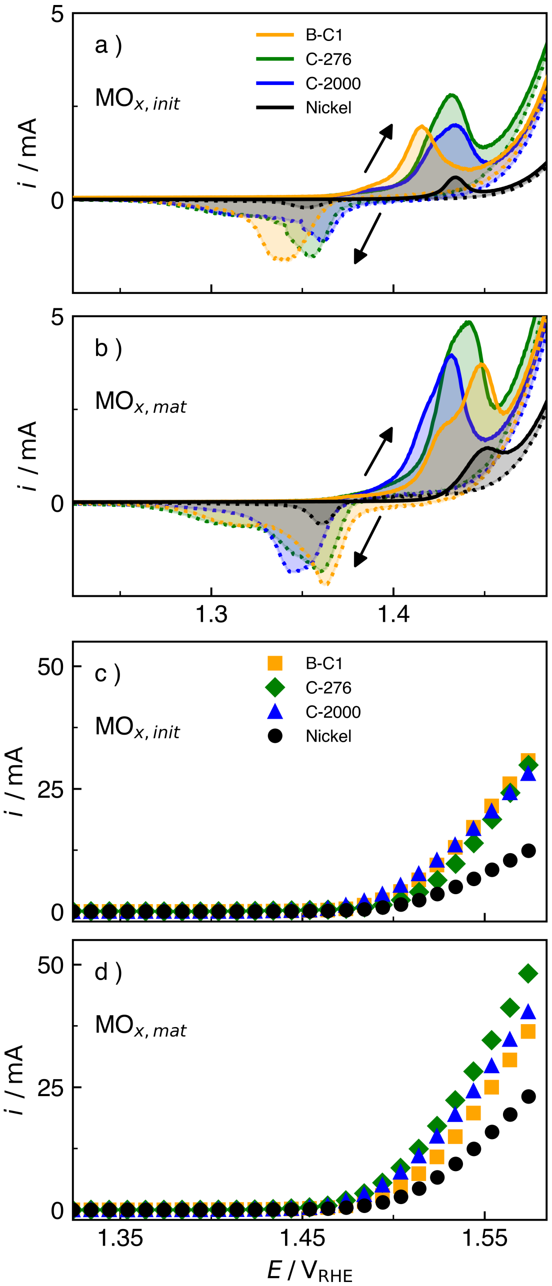

Fig. 6.1 a) 0 mM urea 1 mV s^{-1} CV scans and c) staircase polarization of $MO_{x,init}$. b) 0 mM urea 1 mV s^{-1} CV scans and d) staircase polarization of $MO_{x,mat}$. The solid line on the CV indicates the forward scan while the dotted line indicates the reverse scan.

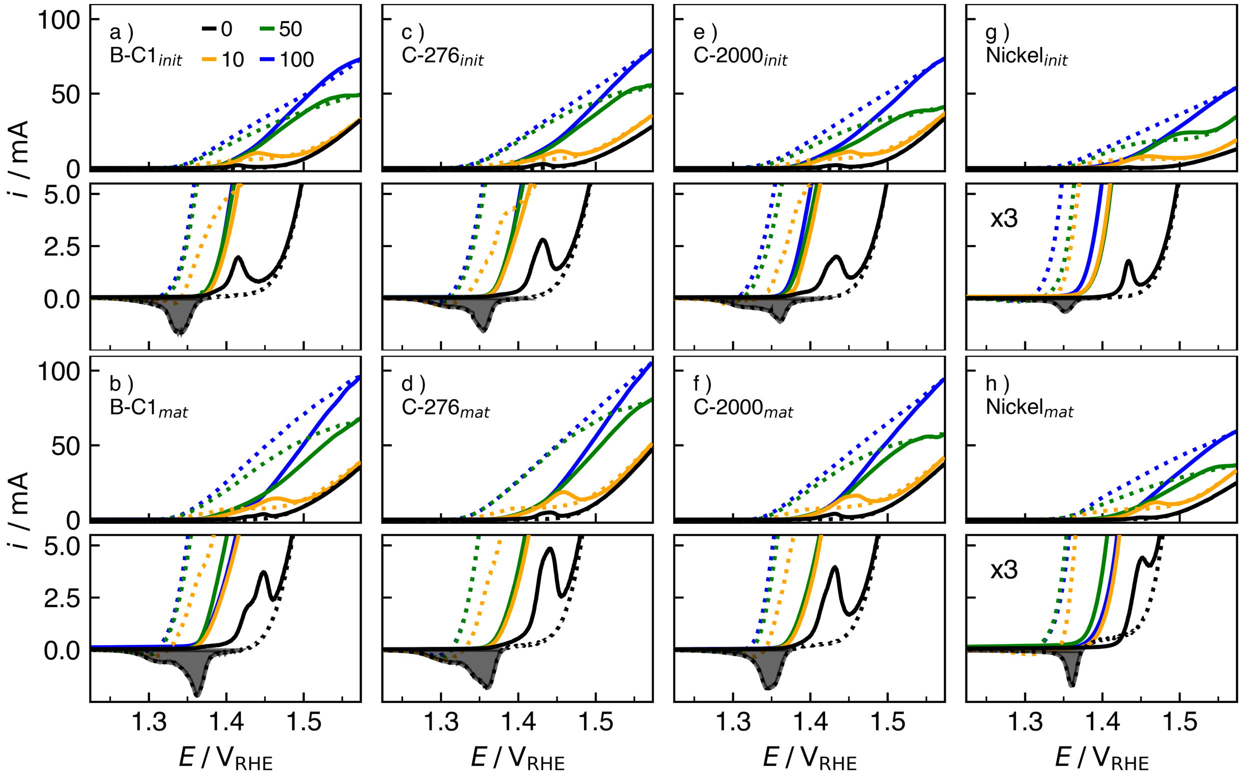

Fig. 6.2 Cyclic voltammetry scans (1 mV s^{-1}) for a,b) BC-1; c,d) C-276; e,f) C-2000; and g,h) nickel for 0 (black), 10 (orange), 50 (blue), and 100 mM urea (green). The zoomed-in feature of each metal and oxide is included to show the $Ni(OH)_2/NiOOH$ transition. The shaded area was used to find the number of nickel atoms participating in $Ni(OH)_2/NiOOH$ transition. The solid line on the CV indicates the forward scan while the dotted line indicates the reverse scan. Note that the zoomed nickel plots are scaled by a factor of 3.

zero-current OER curves as noted above. This implies that there is little change in OER onset potential between the initial and mature oxide layers, although OER currents of the alloys are higher than that of Ni, with C-276 having the highest current.

6.3.2 Urea Oxidation

The urea oxidation reaction was studied for 10 mM urea to understand performance in a realistic application, such as dialysis, and for 50 and 100 mM urea to understand kinetic properties under conditions of reduced mass transfer limitation. Figure 6.2 shows cyclic voltammograms for the alloys and Ni in both initial and mature oxide layer forms. The 0 mM urea CVs (the same as those shown in Fig. 6.1 a,b) show the $Ni(OH)_2$/NiOOH transition for comparison with the UOR data. In all cases, the onset of urea electrooxidation occurs at 1.37 V_{RHE}, which, for many of the electrodes, corresponds to 30 mV lower than the $Ni(OH)_2$/NiOOH transition. For all urea concentrations, the current on the forward scan follows approximately the same curve from onset at 1.37 V up to about 1.42 V.

The higher potential results for 10 mM urea exhibit common behavior for all electrodes. With increasing potential beginning at 1.37 V, electrooxidation goes through a mass-transfer limited peak at about 1.43 and 1.45 V for $MO_{x,init}$ and $MO_{x,mat}$, respectively, followed by the onset of OER. The mass-transfer limited peak is an unsteady-state process whereby the inventory of urea near the surface is depleted due to a concentration gradient at the surface.

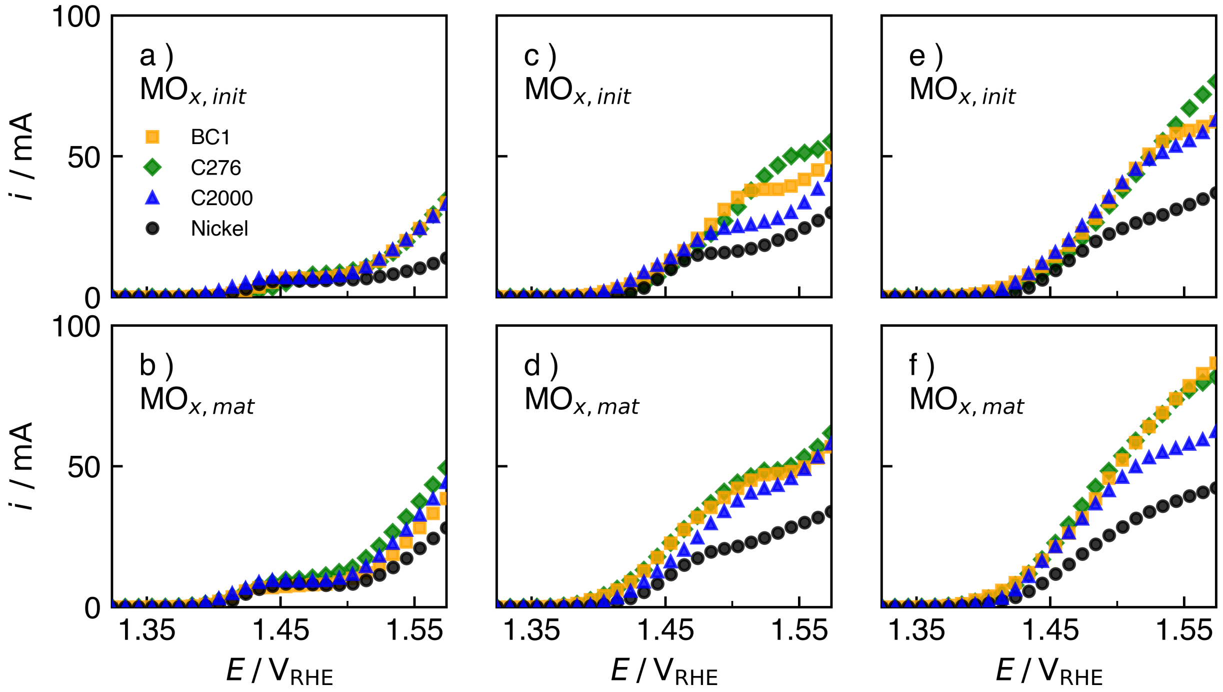

Fig. 6.3 Staircase polarization steps for a,b) 10 mM; c,d) 50 mM; and e,f) 100 mM urea. Each point is the average current from the last five minutes of a ten-minute potential hold per respective step, metal, and urea concentration at 37 °C.

Most curves exhibit a crossover in current between the forward and reverse scans whereby the reverse current exceeds the forward current at lower potentials. With the exceptions of the initial oxide of BC-1, there is no crossover for the 100 mM urea curves. The crossover behavior suggests an inhibition in the reaction during the forward scan that is removed at high potential and does not return on the reverse scan until a much lower potential is reached. Reaction intermediates, such as NCO^- and CO_2, have the ability to poison the surface during urea oxidation.[231,232] Additionally, the crossover affect may occur due to a hysteresis effect of $Ni(OH)_2$/NiOOH; where active NiOOH sites may linger on the surface after being formed at higher potentials.

For the 10 and 50 mM curves, the crossover occurs at potentials above the reversible $Ni(OH)_2$/NiOOH transition. Thus, the reverse current always exceeds the forward current at the potential of the $Ni(OH)_2$/NiOOH transition, here defined as the mid-point potential between the oxidation and reduction peaks in 0 mM urea electrolyte. For all alloys, the reverse current reaches zero at about 1.32 V_{RHE}; for Ni, zero current is attained at about 1.34 V_{RHE}. The reverse current increases between initial and mature oxides, as seen by the increased area of the shaded regions for 0 mM urea in Fig. 6.2.

Staircase polarization curves for the initial and mature oxides in 1 M KOH are presented in Figure 6.3. For all cases, the onset of UOR in the SPC occurs in the range of 1.38–1.41 V_{RHE}, slightly higher than noted for the CV curves (Fig. 6.2). For 10 mM urea (Fig. 6.3 a,b), a mass transfer limited plateau begins at 1.43 V_{RHE} with a current density of 10 ± 2 mA. Figure 6.3c for 50 mM urea shows distinct plateaus or a leveling off of current for the initial oxide layers of BC-1, C-2000, and Ni beginning at 1.47 V, which is the onset of the OER region. The C-276 initial oxide (Fig. 6.3c) does not exhibit a plateau, but rather a small change in slope at 1.52 V. For the mature oxide layers, Fig. 6.3d shows that the alloys have similar behavior with some change of slope at 1.50 V; C-276 and BC-1 have higher kinetics than does C-2000. Figures 6.3 e,f for 100 mM urea show nearly uniform urea oxidation kinetics for the alloys that are much greater than for Ni. Again, a change of slope occurs in the OER region. In the high potential region for mature oxides, the electrocatalytic activity towards OER follows the order C-276 ≈ BC-1 > C-2000 >> Ni.

6.3.3 Electrochemically Activate Surface Area

The oxide layer grows with disorder, which affects the electrochemically active surface area (ECSA) and the roughness of the electrode. The electrochemically active surface area was evaluated by capacitance measurements. Randomly ordered CVs with scan rates of 5, 10, 15, 20, and 25 mV s^{-1} were executed over a potential range of ±50 mV around the open circuit potential (OCP). The charging current at OCP i_{OCP} was determined by Eq. 3.2 by the average of the anodic i_c and cathodic i_c currents. The double layer capacitance C_{dl} for each $MO_{x,init}$ and $MO_{x,mat}$ electrode was found by the slope of linear fits of the charging current vs. scan rate ν at the OCP through Eq. 3.3 and seen in Fig. 6.4.

The electrochemical surface area A_{ECSA} was calculated by Eq. 3.4 on the basis of a reference charge density for nickel of $\hat{C}_{\mathrm{Ni}} = 40$ µF cm^{-2} obtained from literature.[121]

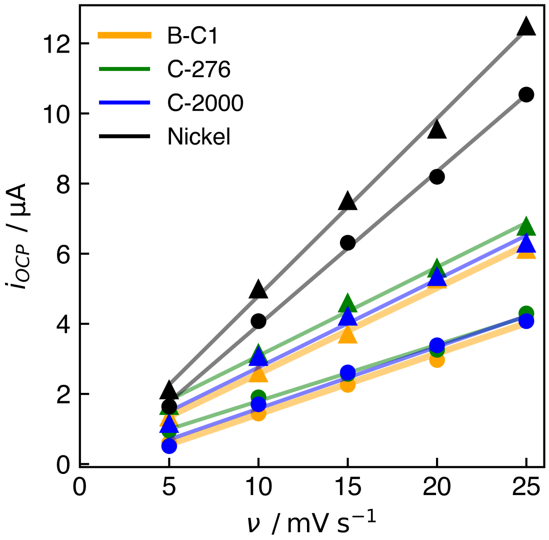

Fig. 6.4 Difference of cathodic and anodic currents while cycling 100 mV around OCP vs. scan rate. Potentials close to OCP are non-faradaic and were used to find the ECSA of initial (circles) and mature (triangles) oxide layers via double layer capacitance.

Table 6.2 Open circuit potential, double layer capacitance (C_{dl}), electrochemical surface area (ECSA), roughness factors (R_f), number of sites, and monolayers (ML) for $\mathrm{MO_{x,init}}$ and $\mathrm{MO_{x,mat}}$ of BC-1, C-276, C-2000, and nickel. Monolayers were found by the dividing the number of sites by the average unit cell site density [5.7 x 10^{14} $\mathrm{cm^{-2}}$ (A_{geo})].

	OCP		$\mathrm{C_{dl}}$		ECSA		$\mathrm{R_f}$		Sites		ML	
	[mV]		[µF]		[$\mathrm{cm^2}$]		[-]		[10^{15} $\mathrm{cm^{-1}}$]		[-]	
	Init	Mat	Init	Mat	Init	Mat	Init	Mat	Init	Mat	Init	Mat
BC-1	779	768	172	272	4.31	6.82	1.21	1.46	82	167	142	290
C-276	800	806	207	305	5.20	7.63	1.46	2.14	103	162	179	282
C-2000	799	781	319	453	8.00	11.34	2.25	3.18	83	126	145	219
Nickel	803	848	520	602	13.02	15.07	3.66	4.23	14	21	24	36

The reference charge density of 40 µF $\mathrm{cm^{-2}}$ was assumed to be equal for all alloys and treatments. Since the emphasis is on trends in surface area as a function of oxide layer growth, the absolute value of the reference is not crucial for the analysis here. An electrochemical roughness factor R_F was estimated from the ratio of the ECSA to the geometric area A_{geo}.

$$R_F = \frac{A_{ECSA}}{A_{geo}} \tag{6.1}$$

Open circuit potential, double layer capacitance, ECSA, and roughness factors are listed in Table 6.2. For the alloy electrodes and the initial oxide layer of Ni, the OCP ranges from 768 to 806 $\mathrm{mV_{RHE}}$, with the mature oxide layer of BC-1 exhibiting the smallest value. The mature oxide layer of Ni shows the largest OCP of 848 $\mathrm{mV_{RHE}}$. The double layer capacitance of the alloys ranges from 172 to 319 µF for the initial oxide layers and from 272 to 453 µF for the mature oxide layers; the percentage increase from initial to mature oxide layer is 42–59%. Nickel shows the highest double layer capacitance in both initial and mature oxide forms (520 and 602 µF, respectively), with only a 15% increase for the mature oxide layer. The ECSA values mirror those for double layer capacitance, since all values have the same reference capacitance. The ECSAs for mature oxide layers exceed those for initial oxide layers. The alloys have substantially lower ECSAs than Ni. The ECSA values follow the order Ni > C-2000 > C276 > BC-1, which is inverse to the wt % of Mo content in the alloys. The capacitance method of determining ECSA relies on the double layer capacitance, which is effectively a "blanket" on the surface that may miss features such as pores and crevices.[233,234] The missed regions may explain the the higher ECSA for nickel from the alloys. The roughness factors show the same trends as for ECSA since the geometric area was the same for all electrodes.

Oxide layer thickness, in monolayers, was estimated from the reduction charge of the $Ni(OH)_2/NiOOH$ transition. The current where reduction was observed ($i < 0$) was integrated vs. time for 0 mM curves, as seen by the shaded regions in Fig. 6.2. The integration yields the charge represented by nickel atoms participating in $Ni(OH)_2/NiOOH$. However, the reduction charge for the alloys may include the reduction of Mo. The number of nickel sites (and also the number of OH^- consumed during $Ni(OH)_2/NiOOH$) is found *via* Eq. 6.2.

$$N_{Sites} = N_{OH^-} = \frac{Q_{\text{red}} N_A n}{F} \tag{6.2}$$

where Q_{red} is the integrated reduction current, N_A is Avogadro's number, n is number of electrons participating in $Ni(OH)_2/NiOOH$, and F is Faraday's constant. For the alloys, these values range from 82 to 103 x 10^{15} OH^- cm^{-1} for the initial oxides and from 126 to 167 x 10^{15} OH^- cm^{-1} for the mature oxides, with C-276 and BC-1 showing the highest values, respectively. For Ni, 14 and 21 x 10^{15} OH^-cm^{-1} were reacted for the initial and mature oxides, respectively. The ratio of OH^- ions consumed for the mature oxide relative to the initial oxide surface density is approximately 1.5 for all electrodes. For monolayer reference, the average unit cell density of the (100), (110), and (111) planes of NiOOH ($a = b = 0.283$ nm, $\alpha = 90°$) 5.7 x 10^{14} cm^{-2} (A_{geo}) was used for all electrodes.[120] With this basis, the number of monolayers of NiOOH was 142 and 179 for the initial oxide alloys, 219 and 290 for the mature oxide alloys, and 24 and 36 for the initial and mature oxides of Ni, respectively. These values are listed in Table 6.2.

However, some amount of charge may contribute to the reduction of Mo with in the alloys and inflating the calculated number of nickel sites. BC-1, the highest in Mo content, had the highest number of N_{Sites} while C-2000, the lowest in Mo content, had the lowest number of N_{Sites} among the alloy mature oxides. Therefore, the integration method for finding the number of active nickel sites is an approximation and is used for determining trends of the alloys.

6.4 Discussion

6.4.1 Mechanism Determination

The deconvolution of direct and indirect mechanisms is difficult based solely on electrochemical data for a set concentration of urea. However, the rate order is used to gain insight on the reaction mechanism by using a Langmuir–Hinshelwood model approach. In some cases, as shown below, it is possible to use urea concentration dependence to distinguish between the IOUR and DOUR mechanisms.

Direct Mechanism

The direct mechanism relies on the presence of catalytic NiOOH sites on the surface to facilitate UOR, given that the sites are not consumed during the reaction. Therefore, Reac. 2.1 is rewritten as

$$\mathrm{CO(NH_2)_2} + 6\,\mathrm{OH^-} + m\,\mathrm{NiOOH} \xrightarrow{k_1} \mathrm{CO_2} + \mathrm{N_2} + 5\,\mathrm{H_2O} + 6\,\mathrm{e^-} + m\,\mathrm{NiOOH} \qquad (6.3)$$

where m is the number of participating nickel sites. Coupled with Reac. 2.3, the reaction rate of UOR *via* Langmuir–Hinshelwood is represented as

$$r_1 = k_1 C_U^n \left(\frac{k_3}{k_3 + k_4}\right)^m \qquad (6.4)$$

where C_U is the concentration of urea, n is the urea rate order dependence, and m is the nickel transition rate order dependence. The activity of KOH and water were taken to be one. The nickel transition rate constants k_3 and k_4 are charge dependent terms related to the Butler-Volmer Equation, but offer no information towards UOR in terms of rate order. Comparing the rate between two different concentrations gives

$$\frac{r_1(C_{U,1})}{r_1(C_{U,2})} = \frac{C_{U,1}^n}{C_{U,2}^n} \tag{6.5}$$

This ratio is non-unity for $C_{U,1} \neq C_{U,2}$ and any non-zero value of n.

Indirect Mechanism

The indirect mechanism relies on the consumption of NiOOH sites during the oxidation of urea, as seen in Reac. 2.2. The rate of UOR is coupled with the nickel transition and is represented as

$$r_2 = \frac{k_2 k_3 C_U^n}{k_3 + k_4 + 6k_2 C_U^n} \tag{6.6}$$

There are no electrons being transferred during Reac. 2.2; thus, k_3 and k_4 are the only potential-dependent terms (Reac. 2.3). Since the electron transfer rate is dependent on potential, the indirect mechanism can be probed through examining the rate order dependence on urea concentration at different applied potentials to an electrode. Thus, two limits are considered: small k_3 and large k_3 (with respect to $6k_2C_U^n$). For potentials above the nickel transition, the value of forward rate constant k_3 is assumed to be larger than k_4 to drive the formation of NiOOH. For small k_3, Eq. 6.6 takes the limit

$$r_2 = \frac{1}{6}k_3 \tag{6.7}$$

which is zero-order in urea concentrations. The ratio of reaction rate at two different urea concentrations of $C_{U,1}$ and $C_{U,2}$ is

$$\left.\frac{r_2(C_{U,1})}{r_2(C_{U,2})}\right|_{k_3 \,\rightarrow\, small} = \frac{k_3/6}{k_3/6} = 1 \tag{6.8}$$

which is independent of both potential and urea concentration. For large k_3, the limit is

$$r_2 = k_2 C_U^n, \tag{6.9}$$

which depends on urea concentration, but not on potential. The large k_3 limit is a plateau representing the maximum UOR rate in the absence mass transfer limitations. The ratio of UOR rate for two urea concentrations is

$$\left.\frac{r_2(C_{U,1})}{r_2(C_{U,2})}\right|_{k_3 \,\rightarrow\, large} = \left(\frac{C_{U,1}}{C_{U,2}}\right)^n \tag{6.10}$$

which is independent of potential so long as the potential is sufficiently large to meet the criterion of a large k_3. Eq. 6.5 for the DUOR is identical to Eq. 6.10 for the IOUR for large k_3 (fast nickel transition), so the mechanisms cannot be distinguished. Under conditions where the nickel transitions is slow, which would only occur slightly above the nickel transition potential, then the lack of concentration dependence (Eq. 6.8) suggests that the IOUR mechanism holds, at least for the potential range from 1.42 to 1.46 V_{RHE}.

Reaction Order

The currents in the polarization curves in Fig. 6.3 show concentration-independent and concentration-dependent responses depending on the applied potential. Figure 6.5 shows the ratio of 100 : 50 mM urea for the SPC data over urea oxidation-relevant potentials. A ratio of 1 indicates the surface reaction has a zero-order dependence on urea concentration, where the indirect UOR mechanism is the rate-determining step (RDS) derived from Eq. 6.8. The zero-order dependence of UOR on nickel (1.42–1.45 V_{RHE}), BC-1 (1.42–1.5 V_{RHE}), and C-276 (1.44–1.54 V_{RHE}) in Fig. 6.5 suggest that the nickel transition rate (k_3) is small at the stated potentials. Non-zero order dependence of UOR, as seen on nickel and C-2000

(1.49–1.54 V_{RHE}) in Fig. 6.5, indicates that the UOR is the RDS from the derivation in Eq. 6.10 as long as the potential is large enough to sustain a high (k_3).

6.4.2 Turnover Frequency

The staircase polarization curves of Fig. 6.3 enable the determination of TOFs to provide some insight into per-site kinetics. The values of Γ for each electrode and treatment are found in Table 6.2, and the TOF results are shown in Figure 6.6. The TOF results largely mirror those of the SPC data and achieve values of up to 0.35 s^{-1} (for the initial oxide of Ni) at 1.47 V_{RHE}. Although the SPC data continue to potentials higher than 1.47 V_{RHE}, oxygen evolution current becomes large and can skew the conclusions for UOR kinetics. The 10 mM results show the mass transfer limited plateau, with TOF values of 0.01 - 0.02 s^{-1}.

The ratios of initial and mature oxide TOF is examined to show the improvement of activity *vs.* the increased electrochemically active area of the electrode. Figure 6.7 shows

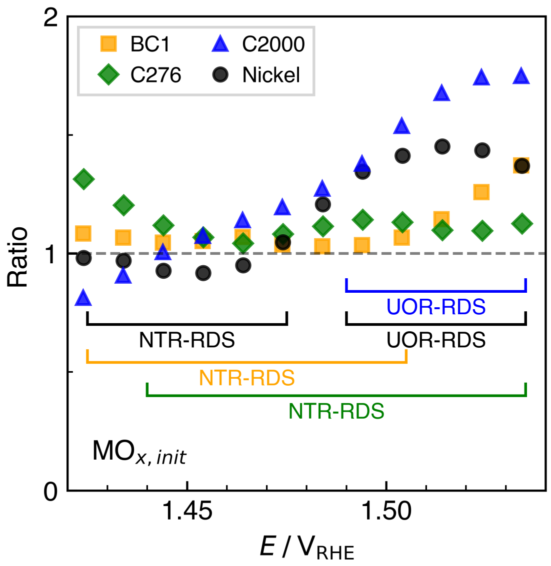

Fig. 6.5 Staircase polarization ratios for initial oxides of 100 : 50 mM urea for BC-1, C-276, C-2000, and Nickel. The nickel transition (NTR) and urea oxidation reaction (UOR) rate determining steps (RDS) are depicted by marked potentials ranges.

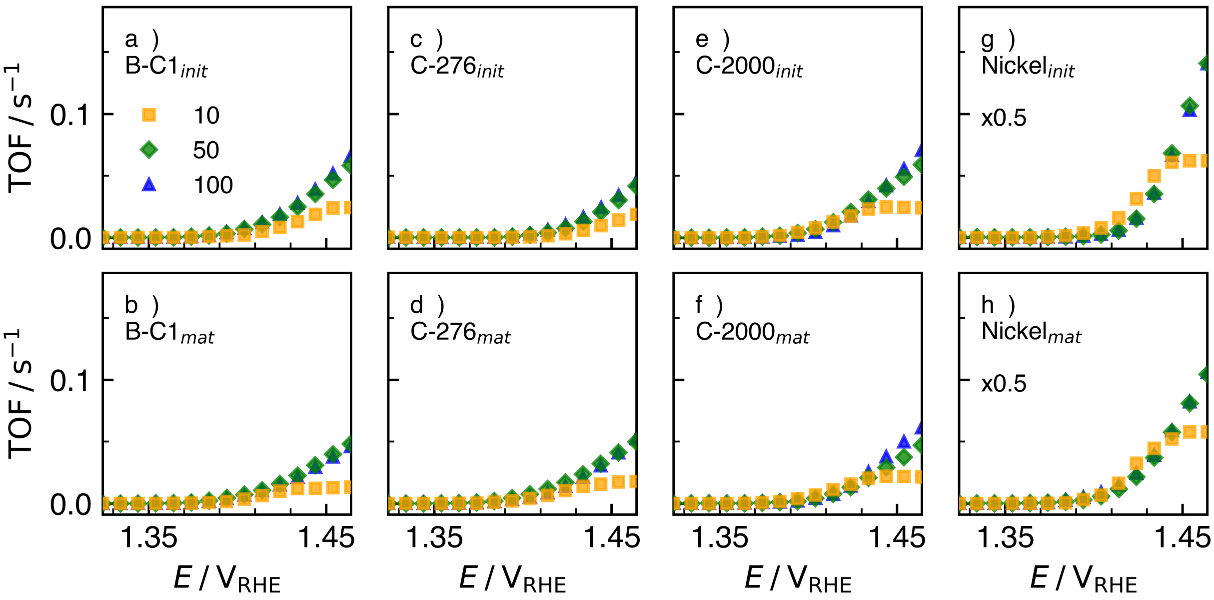

Fig. 6.6 Turnover frequency vs. potential for a,b) BC-1; c,d) C-276; e,f) C-2000; and g,h) nickel in 1M KOH at 37 °C.

the TOF ratios of the mature and initial oxide layers for the alloy and Ni electrodes for 100 mM urea from 1.42 to 1.47 V_{RHE}. The values slowly decrease, but stay relatively consistent. The TOF ratio distribution becomes tighter as potential increases and stays between 0.7 and 1.2. The closer the ratio is to one implies that the change in current in Fig. 6.3 is due to increased number of sites for potentials above the onset. Ratios other than one imply that the mature oxide surface has a different activity than the initial oxide surface on a per-site basis.

The ratio between roughness and number of monolayers between mature and initial oxides is seen in Table 6.3. While the number of monolayers of the mature oxide layer was $\approx$ 1.5 times (except monolayers of nickel and BC-1) those of the initial oxide layers, there is relatively little difference in TOF. The roughness and number of monolayers for mature oxides was $\approx$ 1.5 times those of the initial oxide layers, indicating the change in active area from the growth procedure can be measured by ECSA or reduction current integration.

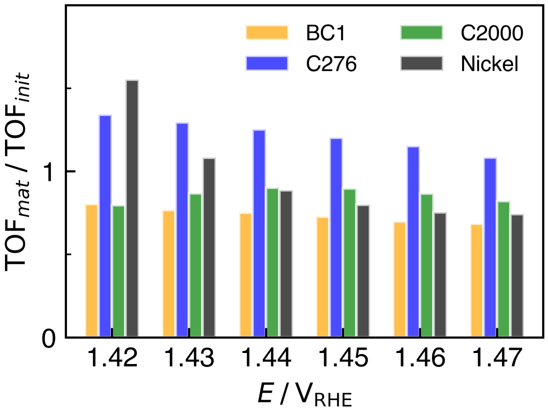

Fig. 6.7 Ratio of initial and mature oxide turnover frequencies (TOF) for alloys and nickel. The Cr : Mo ratios are 0.68, 1, and 1.43 for BC-1, C-276, and C-2000, respectively.

Table 6.3 Ratios of roughness factors (R_f) and number of monolayers (ML) between mature and initial oxide layers

	$R_{F,\text{ mat:init}}$	$ML_{\text{mat:init}}$
BC-1	1.59	2.03
C-276	1.57	1.47
C-2000	1.50	1.41
Ni	1.54	1.16

6.4.3 Influence of Cr and Mo

The role of Cr and Mo in urea oxidation is not well-defined, but trends were observed among the alloys. The Mo content of the alloys is BC-1 > C-2000 = C-276. Based on geometric area, BC-1 had some of the highest UOR current densities in Figs. 6.2 and 6.3. We interpret these results as evidence that Mo improves the performance of these alloy electrodes while Cr degrades the performance (with respect to Mo). The additional metal content, such as the tungsten content of C-276 (4%), may also contribute to UOR performance. Additionally, the iron content in the alloys may have led to improved OER capabilities when compared to Ni, as seen in Figs. 6.2 and 6.3.[106,142,146] Although these electrodes were commercial alloys with a wide range of other alloying elements, we suggest that these results will apply to well-defined NiCrMo alloys in the absence of other additives.

6.5 Conclusion

Nickel-based alloys BC-1, C-276, and C-2000 underwent two different oxide growth development procedures. The cyclic voltammetry and staircase polarization curves indicated that the mature oxides had thicker oxide layers than the initial oxides. The thicker, rougher oxide layers have more electrochemically active sites than as seen from the integration of reduction current of the nickel transition regime and the ECSA from capacitance measurements. The increased oxide layer thickness leads to a higher urea oxidation current, based on the geometric area of the electrode.

Ratios of the TOFs showed that, while the developed oxide layer contributes significantly to the increased number of electrochemically active sites, the UOR activity roughly remains constant on a per-site basis. This work shows that these alloys might be suitable for urea electrooxidation and merit further study in harsh electrochemical environments. From this study, we highlight the key points:

- Nickel-based alloys BC-1, C-276, and C-2000 support urea electrooxidation
- Electrochemical surface area and roughness correlate to urea oxidation active area
- Urea oxidation follows the indirect mechanism by at potentials just above the nickel transition
- The rate determining step changes from nickel transition to urea oxidation at higher potentials and is dependent on alloy composition
- Urea oxidation turnover frequency is similar among site-normalized oxide layers
- Nickel has the highest turnover frequency among the alloys

6.6 Acknowledgements

The authors thank Haynes for providing materials used in this study. The authors also thank Prof. Gregory Jerkiewicz and Dr. Derek Essau for advice on apparatus construction and guidance of electrochemical topics. The authors thank Prof. Peter Strasser for the opportunity to visit his laboratory and Dr. Fabio Dionigi for advice on performance and preparation procedure of nickel hydroxide catalysts.

Chapter 7

CATALYTIC UREA ELECTROOXIDATION ON NICKEL-METAL HYDROXIDE FOAMS FOR USE IN A SIMPLIFIED DIALYSIS DEVICE

7.1 Introduction

Access to affordable chronic kidney disease treatment is a major problem since the increasing number of patients with end-stage kidney disease has outpaced the growth of available treatment options.[8] Patients diagnosed with end-stage renal failure suffer from high burdens and have high rates of mortality.[10] The high burden, coupled with co-morbidity and related mental issues like depression, lead to a poor health-related quality of life.[11–13] There is evidence suggesting more frequent treatments, like daily home dialysis, would benefit patients by improving metabolic parameters.[10] The introduction of more frequent dialysis treatments reduces the magnitude of swings in toxin levels in the blood stream, thereby improving the patient's overall health.

The bottlenecks for converting patients from traditional dialysis to home dialysis are storage, cost, and disposal of fresh dialysate. Traditional hemodialysis is an expensive process requiring 300-600 liters of dialysate per week.[14] The composition of the fresh dialysate is important as it influences the exchange of ions between the blood and the dialyzer, restores acid-base equilibrium, and strongly affects cardiovascular stability.[15] Patients of different ages, sizes, gender, and other external factors will have varying compositions of dialysate, making a "one size fits all" fluid difficult to achieve.[16]

One possible method to overcome the limitations of traditional dialysis is portable dialysis, as seen in Figure 1.3. Portable dialysis, employing a wearable artificial kidney (WAK), relies on a small amount of fluid customized to each individual and that does not need re-placement. The dialysate regenerator in Fig. 1.3 needs to remove major waste components such as urea, creatinine, peptides, and protein-bound toxins, in spent dialysate without appreciable loss of ions.[235] This study focuses on urea removal with a WAK, as urea is the species of high highest concentration in spent dialysate.

The three major technologies for efficiently removing urea from spent dialysate are: physisorption and chemisorption, enzymatic hydrolysis, and reactive decomposition.[236] Physisorption and chemisorption *via* sorbent materials are ideal for a WAK as there are no byproducts of a reaction, but the sorbents are highly selective, requiring many different types to remove all uremic toxins.[20,21] Enzymatic hydrolysis utilizes urease to remove urea at near-neutral pH. The urea is converted to ammonium, which is far more toxic than urea; thus, extensive filters are required for implementation.[22]

Electrochemical removal, a form of reactive decomposition, for dialysate regeneration has been explored by several groups and has been shown to be an efficient method for urea removal for a WAK.[42,195,237–240] However, the method has never been applied in a clinical application with humans.[226–228] The reason a WAK has not been used in a clinical application has not been explicitly stated, but may be due to generation of chloride species, production of ammonia, overoxidation of urea into nitrite and nitrate species, or leaching of metal species.[65,194,226,229,241] Discovery of a catalyst that is stable and efficient, and produces safe reaction products is necessary for application.

Nickel is a promising anode material for electrochemical removal of urea in a WAK. Nickel, although susceptible to chloride corrosion, shows affinity for urea electrooxidation with low selectivity for ammonia-type compounds.[41–44] Addition of other metals into nickel have been shown to improve passivation and minimize corrosion, but their effect on urea oxidation activity has not been well understood.[198,199,201,224]

The urea oxidation reaction (UOR) is catalyzed by the presence of nickel oxyhydroxide (NiOOH), as seen by Reaction 5.2.[126,127] There is debate whether or not the nickel hydroxide sites are consumed during UOR, since UOR is mediated through the electrochemical activation of nickel from $Ni(OH)_2$ to NiOOH at 1.35 V_{RHE}, as seen by Reaction 2.3.[49,160] A catalyst regeneration mechanism has been identified as the mechanism most relevant near the $Ni(OH)_2/NiOOH$ onset potential. The overall electrolysis reaction is given by Reaction 2.5.

The addition of nickel and other metals into nickel hydroxide has been shown to increase the electrode activity by altering the electronic structure and by expanding the electrochemically active surface area.[35,93,98,147,225,242–246] The inclusion of chromium oxide into nickel has been shown to depress the density of states at the Fermi level of the d-band of nickel, thereby weakening the Ni-O_{urea} bond and decreasing the energy for adsorption.[95] The inclusion of Mo into the nickel hydroxide films causes Ni to complete the $Ni(OH)_2/NiOOH$ transition at lower onset potentials.[98] The onset potential for UOR is also lowered from the addition of Mo into Ni, as UOR is dependent on the presence of NiOOH. Doping of Mo promotes coupling of the N—N bond on the intramolecular level as well as the fracture of the C=O in urea, promoting the selectivity of N_2 and CO_2 products.[99] Tafel slopes were lower on nickel iron hydroxide (57 mV dec^{-1}) than pure nickel (102 mV dec^{-1}), indicating that iron enhances the potential dependence of UOR.[93] The inclusion of manganese into the oxide film allows for active nickel centers to reach a 3+ oxidation state at lower potentials, thus lowering the potential needed to drive UOR.[247]

An electrochemically-based WAK relies on two major components - the dialyzer and the dialysate regenerator. The dialysate regenerator is comprised of a urea removal cell, where the urea is electrochemically removed with a catalyst in an electrolyzer-type configuration. Previous studies have computationally modeled dialyzers for use in traditional dialysis and electrolyzers for use in commercial applications.[248–250] A model combining the two process elements has not been previously seen before and is useful for determining operating parameters for a WAK. More importantly, the model is useful for finding pH of fluid downstream of the dialysate regenerator, as the production of CO_2 from Reac. 2.5 can affect the bicarbonate composition. Therefore, understanding urea electrooxidation on nickel-based catalysts is important for further development of the model, which is necessary to achieve a portable dialysis device.

This report combines incorporating electrochemical and model results for operation of an electrochemically-based WAK. Here, nickel-based electrocatalysts (Ni, NiMn, NiCr, NiMo, NiFe) were synthesized through a one-pot hydrothermal growth process. The electrochemical performance of each catalyst was investigated with cyclic voltammetry and staircase polarization techniques. Furthermore, the electrochemical performance of the catalysts were considered in a computationally-developed WAK model. The model was created to demonstrate the flowrates, urea concentrations, and pH of streams in contact with the dialyzer and the catalyst. Together, the catalysts and the model define and satisfy the criteria needed for development of a simplified dialysis device, setting the stage for future improvements.

7.2 Experimental

7.2.1 Electrochemical Cell

All electrochemical experiments were performed in a 150 mL three-electrode cell (Pine Research). Experiments were conducted in 0.5 M KOH with reagent grade concentrations of 0, 10, and 200 mM urea. The redox properties of nickel hydroxide have been seen to be affected by the presence of incidental iron (as low as 40 ppb) in the electrolyte. However, other groups have identified that nickel undergoes transformations with or without the presence of incidental iron in the electrolyte.[35,57,106] The concentration of iron was not monitored within this study, as there is assumed to be non-zero concentrations of iron in the dialysate in real-life applications.[251] A Pt coil (~ 5 cm^2) was used as the counter electrode, and a double-junction mercury oxide electrode (4.24 M KOH, $E^{\ominus}_{\mathrm{Hg/HgO}} = 0.098$ V, Pine Research) was used as the reference electrode. Since measurements were made in 0.5 M KOH, the reference electrode potential was adjusted for the liquid junction potential (E_{LJP}) of –25.1 mV between 4.24 M KOH and 0.5 M KOH calculated with the stationary Nernst-Planck equation using LJPcalc software (`https://swharden.com/LJPcalc`).[171] Voltages are reported with respect to the reversible hydrogen electrode (RHE), calculated using equation 4.1. Eq. 4.1 is simplified and is seen as:

$$E_{\mathrm{RHE}} = E_{\mathrm{Hg/HgO}} + (0.059)\,\mathrm{pH} + E^{\Theta}_{\mathrm{Hg/HgO}} - E_{\mathrm{LJP}} = E_{\mathrm{Hg/HgO}} + 0.931 \tag{7.1}$$

The nickel transition and urea oxidation reaction onset potentials within this study are similar to those found in other reports, suggesting that the reference electrode and liquid junction potential are acceptable.[43,106]

The electrochemical experiments were controlled by a Solartron 1287 potentiostat. Cyclic voltammetry (CV) and staircase polarization experiments were performed at 37 °C with and without urea. Cyclic voltammetry was performed within a potential window that encompasses the $Ni(OH)_2/NiOOH$ transition (Reaction 2.3) and oxygen evolution reactions. Cyclic potential sweeps from 0.90 to 1.60 V_{RHE} were conducted at 5 mV s^{-1}. The third CV scan was used for figures and analysis. Staircase potential step (polarization) experiments were conducted for steady-state analysis of UOR. For the staircase polarization experiments, the potential was stepped from 1.25 to 1.60 V_{RHE} in 10 mV increments at 20 min per step. Staircase polarization curves were generated by plotting the average of the last five minutes of current for a given step vs. the potential of that step.

7.2.2 Electrodes

Nickel foam (99.5 wt %, 95% porosity, Goodfellow) was laser cut to 1 cm^2 pieces and used as a substrate for hydrothermal growth. The nickel foam (NiF) was sequentially sonicated in deionized water (DI, Millipore-Q water system), ethanol (95 wt.%, Fisher-Scientific), and 3 M HCl (Macron Fine Chemicals) for 10 minutes each to remove any contaminants before being placed in the hydrothermal growth chamber. The percentage of metal grown on the working electrode was targeted to be 1 mol%, with the remaining as nickel. Metallic salts of 1.00 mg of $Cr(NO_3)_3 \cdot 9H_2O$ (99.9 wt.%, Acros Organics), 1.01 mg of $Fe(NO_3)_3 \cdot 9H_2O$ (99.95 wt.%, Aldrich), 0.39 mg of $KMnO_4$ (>99 wt.%, Fisher-Scientific), and 1.75 mg of $(NH_4)_6Mo_7O_{24} \cdot 4H_2O$ (99.97 wt.%, Aldrich) were added and mixed with 20 mL DI water in separate vials. Then, 72 mg $Ni(NO_3)_2 \cdot 6H_2O$ (99.9 wt.%, Acros Organics) and 150 mg urea (99.6 wt. %, Fisher-Scientific) were added and mixed into each vial. The solutions were individually transferred into a 25 mL Teflon-lined stainless-steel hydrothermal vessel. Four pieces of NiF were placed vertically into the solution in the vessel. The vessel was sealed and placed in a 105 °C oven for 12 hours. The vessel was cooled to room temperature before opening. The hydrothermally grown NiF pieces were sonicated sequentially in DI water and ethanol for 10 minutes each to remove loose particulates. Each electrode was imaged with a scanning electron microscope (SEM, ThermoFisher Scientific Apreo-Symmetry with Ultimax 100) equipped with an energy dispersive spectrometer (EDS). The mol % loading for each electrode was confirmed with elemental analysis by EDS.

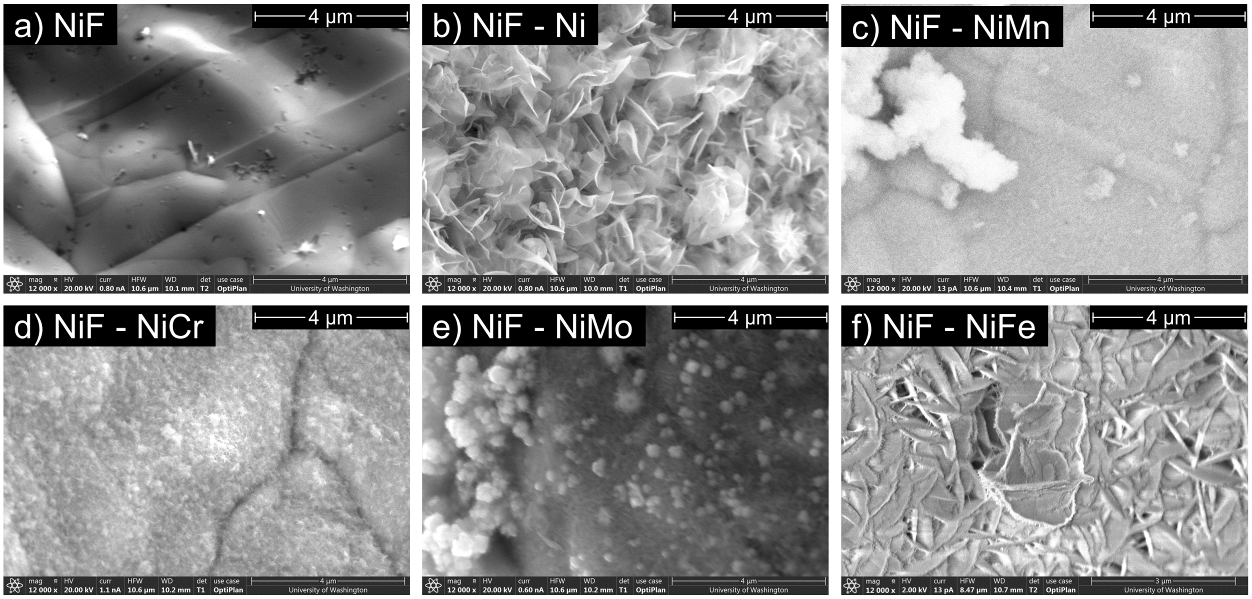

Fig. 7.1 Scanning electron microscopy images taken at 12,000x magnification of a) nickel foam (NiF) and metallic species b) Ni, c) NiMn, d) NiCr, e) NiMo, and f) NiFe grown on NiF prior to experimentation.

Table 7.1 Mole % composition of metal species (M) grown on nickel foam, ignoring oxygen content.

Ni(M)	Ni	M
Ni	100.00	0.00
NiMn	99.30	0.70
NiCr	99.30	0.70
NiMo	99.18	0.82
NiFe	99.56	0.44

7.3 Results

7.4 Results

7.4.1 SEM/EDS

Scanning electron microscopy images taken at 12,000x magnification for nickel-based electrodes used in this study are seen in Fig. 7.1. The NiF electrode showed a smooth surface, while grown species exhibit a change in surface morphology. NiF-Ni and NiF-NiFe growths form platelets that are similar to surfaces seen in literature (Fig. 7.1b, f).[43,252] NiF-NiMn and NiF-NiMo growths form large crystalline nodes (Fig. 7.1c, e). NiF-NiCr does not form large crystalline structures, but rather evenly coats the surface with a rough mossy texture (Fig. 7.1d). The compositions of the grown metallic species was confirmed by EDS and are seen in Table 7.1 and in elemental maps in Supplementary Information.

7.4.2 Nickel Transition And Oxygen Evolution

Cyclic voltammetry scans of 0, 10, and 200 mM urea in 0.5 M KOH for nickel foams are presented in Figure 7.2. Currents for the grown species exceed those for NiF for all cases. The urea-free nickel transition onset potential can be seen for all electrodes near 1.36 V_{RHE} on the forward scan, except for NiF-NiMn, which has the lowest onset of $\sim$1.33 V_{RHE}. The NiF electrode exhibits a narrow peak at 1.36 V (inset of Fig. 7.2 a) while the grown species

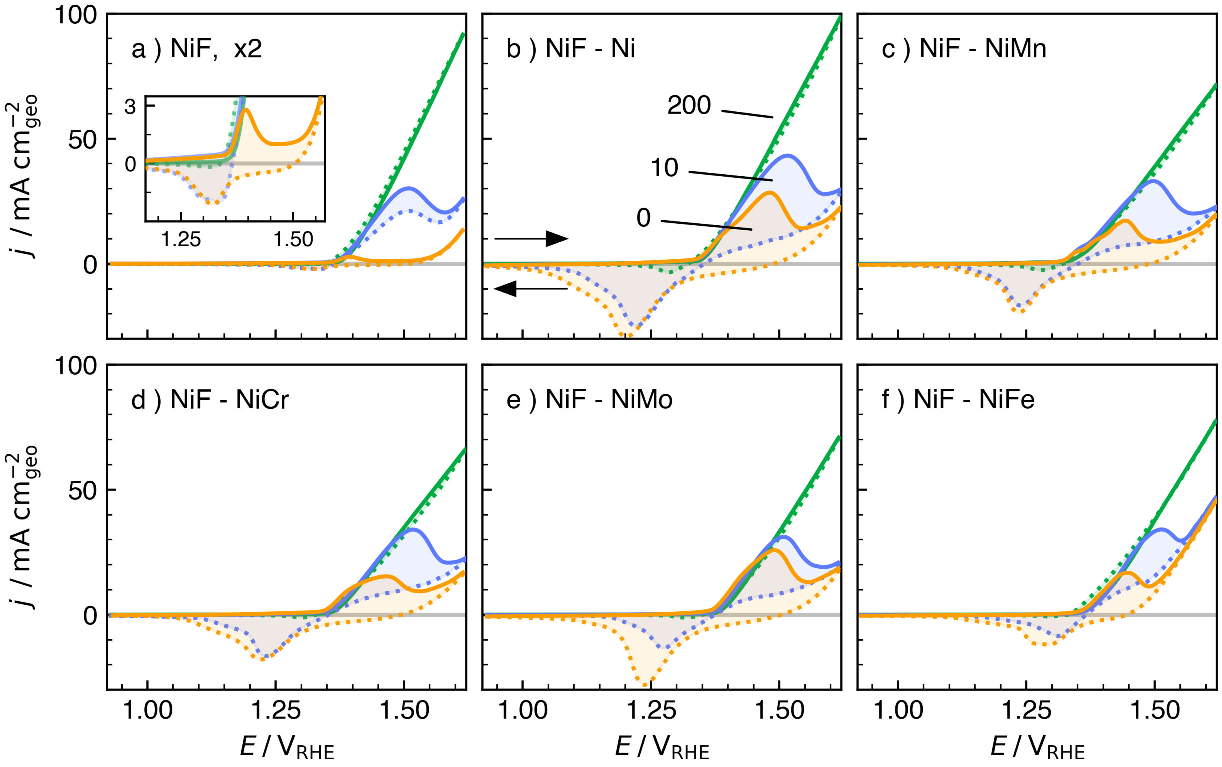

Fig. 7.2 Cyclic voltammetry scans (5 mV s^{-1}) of a) nickel foam (NiF) and metallic species b) Ni, c) NiMn, d) NiCr, e) NiMo, and f) NiFe grown on NiF for concentrations of 0, 10, and 200 mM urea in 0.5 M KOH at 37 °C. The solid line on the CV indicates the forward scan while the dotted line indicates the reverse scan. The current for NiF is scaled by 2 to include the curves on the same y-axis.

show a single, wide peak. At higher potentials, the current increases sharply due to the onset of oxygen evolution reaction (OER, ∼1.50 V$_{RHE}$). The grown species show an increase in OER current compared to NiF, with NiF-NiFe showing the largest OER current at 1.60 V$_{RHE}$.

The reverse sweep shows the reduction of NiOOH back to Ni(OH)$_2$. All grown species show a single reduction peak, but NiF-NiFe exhibits a plateau from 1.31–1.27 V$_{RHE}$ suggesting a second peak.

Staircase polarization curves (SPC) for 0, 10, and 200 mM urea for all electrodes are

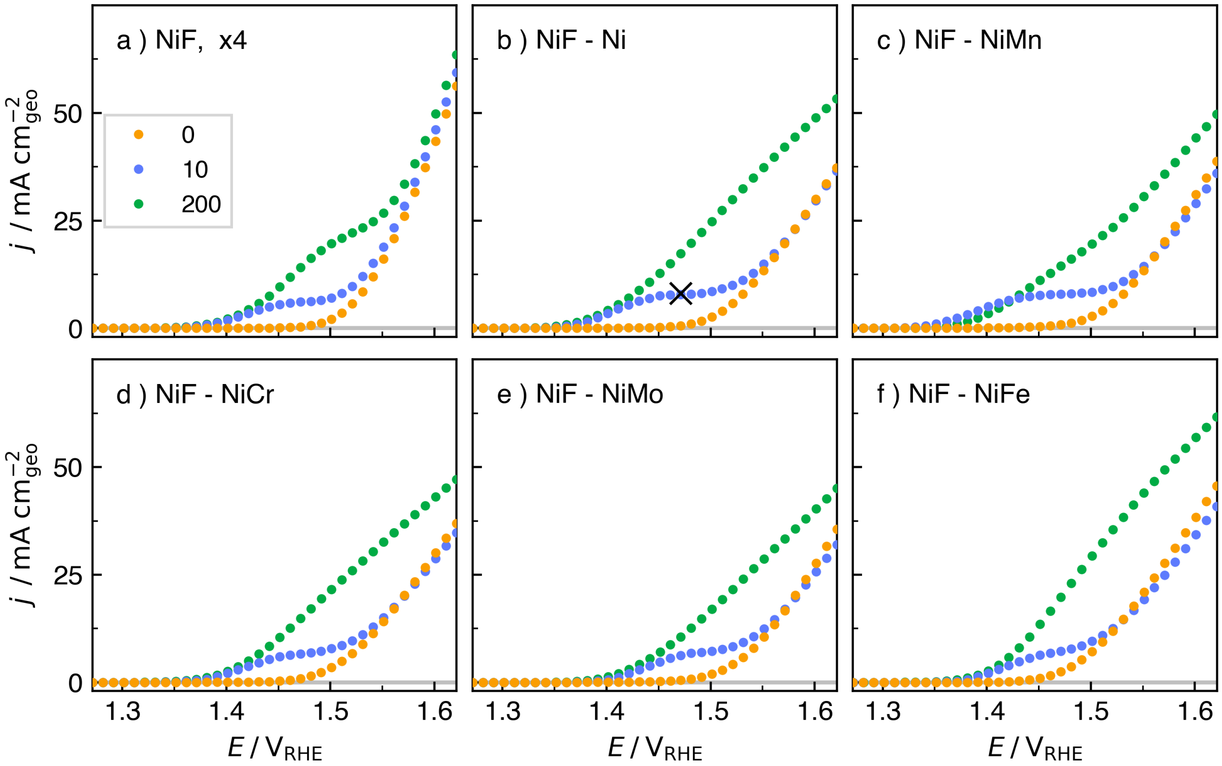

Fig. 7.3 Staircase polarization curves of a) nickel foam (NiF) and metallic species b) Ni, c) NiMn, d) NiCr, e) NiMo, and f) NiFe grown on NiF for concentrations of 0, 10, and 200 mM urea in 0.5 M KOH. The catalyst and potential shown in Figure 7.8 is designated by an 'X' for NiF-Ni at 1.45 V$_{\mathrm{RHE}}$, respectfully. The current for NiF is scaled by 4 to include the points on the same y-axis.

presented in Figure 7.3. The 0 mm plots for all electrodes show no current during potentials where Ni(OH)$_2$/NiOOH occurs, indicating that steady state was achieved. The current increases near 1.48 V$_{\mathrm{RHE}}$ as the potential is large enough to begin OER. At 1.63 V$_{\mathrm{RHE}}$, the rightmost point in the plots, all electrodes exhibit similar currents near 33 mA cm$^{-2}_{\mathrm{geo}}$, except NiF and NiF-NiFe. NiF-NiFe has the largest OER current compared to the other electrodes, in agreement with other studies of iron-containing electrodes that show improved oxygen evolution kinetics.[43,57,106,142,146]

7.4.3 Urea oxidation

Urea electrooxidation was performed at 10 mM urea to understand performance under dialysate-relevant solutions and in 200 mM urea to probe UOR kinetics. The 10 and 200 mM CV responses are seen in Fig. 7.2. For both 10 and 200 mM, the current is essentially zero from 0–1.36 V_{RHE} since UOR does not occur on $Ni(OH)_2$. Urea oxidation begins near the same potential as the $Ni(OH)_2$/NiOOH onset potential, as there is now NiOOH appearing on the surface. The 10 mM current continues to increase until a mass transfer limitation is reached, as seen by a peak in Fig. 7.2. The mass transfer limit is semi-consistent amongst the grown species. The 200 mM CV response is not impeded by a mass transfer limitation, however OER may be participating on the surface at potentials greater than 1.53 V_{RHE}.

The reverse scans exhibit similar behaviors for all electrodes in Fig. 7.2. The reduction peak is smaller with the addition of urea because urea consumes nickel sites by a catalyst regeneration mechanism, converting NiOOH back to $Ni(OH)_2$. Higher concentrations of urea cause the reduction peak to be small, as seen by the 10 and 200 mM curves in Fig. 7.2.

Staircase polarization curves for 10 and 200 mM urea for all electrodes are seen in Figure 7.3. The 10 mM curves start to plateau at 1.46 V_{RHE} for all cases due to the mass transfer limitation. The mass transfer limitation occurs at nearly the same current (~ 9 mA cm_{geo}^{-2}) for all grown species. For all cases, 0 and 10 mM currents at 1.60 V_{RHE} were similar, suggesting OER was the dominant reaction on the surface. The 200 mM responses, except NiF, all show an increase in current at OER-relevant potentials (> 1.48 V_{RHE}) beyond the 10 mM responses in the SPC. The currents for 0, 10, and 200 mM on NiF indicate that OER is dominant from 1.58–1.63 V_{RHE}.

7.4.4 Model

A simplified dialysis model was created and evaluated to gauge the viability of the synthesized catalysts for a WAK. The two main components, the dialyzer and the regenerator, were modeled with specifications applicable to a WAK:

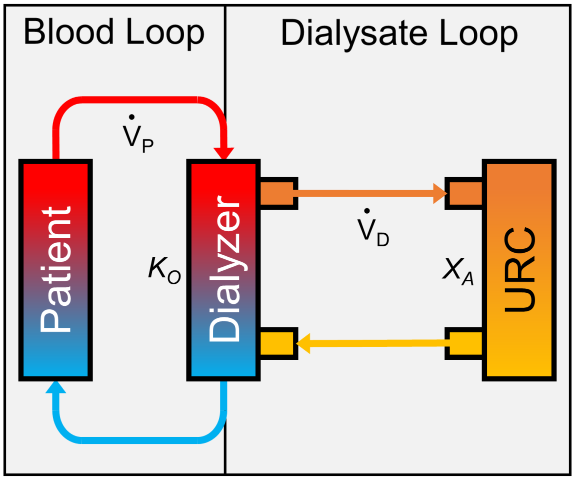

Fig. 7.4 Simplified model of a portable dialysis unit. Blood flows from the patient through a dialyzer, where the urea transfers to the dialysate and is removed by the urea removal cell (URC).

- Remove 30 g urea of during an 8 hour operation (3.75 g urea hr^{-1});
- Accommodate flow rates up to 300 mL/min from the dialyzer[253] and;
- Conduct hemodialysis without a continuous water source.

A diagram of the continuous dialysis unit is seen in Figure 7.4. Blood flows from the patient into the dialyzer, where urea crosses over from the blood loop into the dialysate loop due to a concentration gradient. The dialysate flows into the urea removal cell (URC) where urea is removed *via* Reac. 5.2. The dialysate leaves the URC and enters the dialyzer to receive more urea from blood.

The dialyzer is based on a hollow-fiber and tube mass exchanger. Blood flows through hollow fibers, where small solutes and ions can migrate to the dialysate by diffusion and convection.[254] Sherwood numbers of hollow-fiber dialyzers tend to be large to induce higher fluxes of uremic toxins and middle-molecular weight solutes.[255–257] Toxins other than urea are not included in the systems of equations, but can be added in the future. The dialyzer is designed for counter-current operation to maximize urea removal. The dialyzer was modeled with the mass transfer and mass balance, Eqs. 7.2 and 7.3, respectively:

$$N_u = K_O A \, \Delta C_{u,lm} \tag{7.2}$$

$$\dot{V}_{P,i} \, C_{u,P,i} - \dot{V}_{P,o} \, C_{u,P,o} \;\; = \;\; \dot{V}_{D,i} \, C_{u,D,i} - \dot{V}_{D,o} \, C_{u,D,o} \tag{7.3}$$

where N_u is the flux of urea through the dialyzer membrane, $K_O A$ is the mass transfer coefficient with area (units of mL min^{-1}), P is the patient side, D is the dialysate side, and $\dot{V}$ and C_u are volumetric flowrate and urea concentration, respectively, of inlets i and outlets o.

The anolyte chamber of the URC was modeled as a continuous stirred tank reactor. The URC extent of reaction was set as a design variable for calculation simplicity.[258–260] The extent of reaction was based on the urea electrooxidation half reaction in Reac. 5.2. The model uses the following equations to find the changes in molar flows through the URC:

$$\dot{n}_{N_2} = \dot{n}_{CO_2} = \dot{V}_{D,i} C_u X_A \tag{7.4}$$

$$\dot{n}_{H_2O,m} = 6 \, \eta \dot{V}_{D,i} C_u X_A \tag{7.5}$$

$$\dot{n}_{H_2O,g} = \frac{2 \, \dot{V}_{D,i} C_u X_A P_s}{P} \tag{7.6}$$

$$\dot{n}_{H_2O,l} = \dot{V}_{D,i} - \dot{n}_{H_2O,g} + \dot{n}_{H_2O,m} + 5 \, \dot{V}_{D,i} C_u X_A \tag{7.7}$$

$$\dot{n}_u = \dot{V}_{D,i} C_u (1 - X_A) \tag{7.8}$$

where $\dot{n}$ is the molar flow rate per respective species, $\dot{V}_{D,i}$ volumetric flowrate of fluid into the URC, C_u is the concentration of urea, X_A is extent of reaction,η is the osmotic drag coefficient through the membrane (m), P is the total pressure (760 torr), and P_s is the saturation pressure of water at 37°C. Water molecules are able to cross over from the cathode compartment to the anode compartment due to osmotic drag, which is proportionally related to the number of hydroxide ions generated from Reac. 5.2 and the osmotic drag coefficient.[261] The osmotic drag coefficient is constant for this study, but depends on reaction conditions and can be tuned accordingly for increased model accuracy.

7.4.5 Model Trends

A system of the combined dialyzer and URC was be modeled to cover a range of flow and urea concentration conditions. An array of K_OA (200 - 400 mL min^{-1}) and X_A (0.4 - 1) values was used to calculate flowrates, concentrations in and out of the dialyzer, and pH of dialysate after the URC, as seen in Figure 7.5. The model, for example, provided urea concentrations of 1.6 and 8.2 mM of dialysate entering and exiting the dialyzer at 160 mL min^{-1}, respectively, while showing that the pH drops from 7.4 to 7.1 for an X_A of 0.8 and a K_OA of 231 mL min^{-1} (Fig. 7.5, F3).

At a low extent of reaction, the URC is not able to remove enough urea to substantially lower the concentration entering the dialyzer, as seen by Fig. 7.5a. A low extent of reaction also requires a high mass flowrate of urea to enter the URC, thus requiring a high volumetric flowrate of dialysate through the dialyzer in order to remove 3.75 g urea hr^{-1}. A high extent of reaction lowers the urea concentration entering the dialyzer (with 0 mM at 100 % X_A), maximizing the flux of urea from blood across the dialyzer. A high extent of reaction consumes urea faster, thereby allowing for a low flowrate to be achieved. A larger extent of reaction also produces more CO_2, which reduces the solution pH, as seen in Fig. 7.5d. As CO_2 is produced on the anode, a fraction of CO_2 reacts with H_2O to form H_2CO_3, a weak acid that dissociates to form H^+ and HCO_3^-.[207]

Fresnius F3 and F4 dialyzers are included in Fig. 7.5 to show the performance of commonly used, commercially available products.[262–264] Larger mass transfer coefficients allow for more urea to move through the dialyzer membrane, as seen by the increase in concentration along the arrow in Fig. 7.5b. The Fresnius F4 has a higher K_OA value than the F3

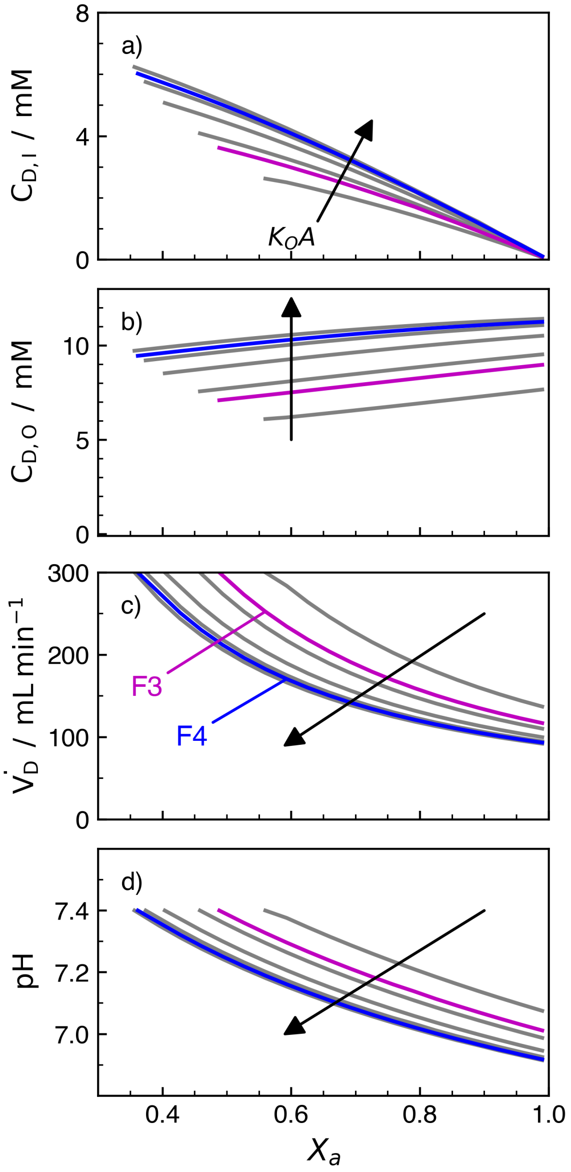

Fig. 7.5 Model output for: concentration of urea flowing a) in and b) out of the dialyzer, c) flowrate into the dialyzer, and d) pH of fluid flowing into the dialyzer. Arrows indicate an increase in mass transfer coefficient ($K_O A$). Fresnius F3 and F4 are commercially available dialyzers with mass transfer coefficients of 231 and 374 mL min^{-1}, respectively.[262–264]

($374 > 231$ mL min^{-1}), allowing for the system to operate with a lower extent of reaction.

7.5 Discussion

7.5.1 Electrochemical surface area

The electrochemical surface area (A_{ECSA}) of each electrocatalyst was determined by finding the number of sites participating in the $Ni(OH)_2$/NiOOH transition. The number of sites was calculated by integrating the reverse sweep where current was less than 0 mA. The A_{ECSA} was calculated by correlating the number of sites to the average cell density of the NiOOH plane by Equation 3.1.

Values for A_{ECSA} are presented in Figure 7.6. The grown species increased the physical surface area within the pores of NiF (seen in Fig. 7.1), allowing more active sites to participate in $Ni(OH)_2$/NiOOH and increasing ECSA. The ECSA of grown species were within an order of magnitude with each other. NiF-NiFe had a smaller ECSA than NiF-Ni, but had similar platelet structures (Fig. 7.1a,f). NiF-NiFe and NiF-NiCr had the similar ECSAs, despite different crystal morphologies.

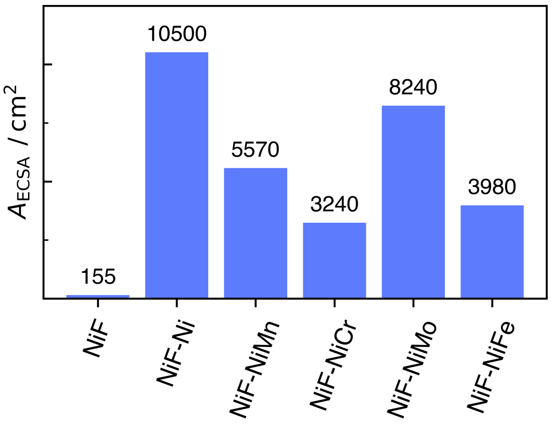

Fig. 7.6 Electrochemical surface area (A_{ECSA}) for nickel foam (NiF) and metallic species. The metallic species were grown on a NiF precursor *via* a hydrothermal method.

7.5.2 Turnover Frequency

The 10 and 200 mM urea staircase polarization curves were used to determine turnover frequencies (TOF) for a per-site kinetic analysis.The TOF was examined over a potential range of 1.30–1.45 V_{RHE} to avoid current associated with OER. The TOF is given by Eq. 3.9. The 10 and 200 mM TOFs for all electrodes are seen in Figure 7.7. Although the SPC data continues past 1.45 V_{RHE}, oxygen evolution becomes large and skews the conclusions drawn for UOR kinetics. The TOFs level off after ∼ 1.41 V_{RHE} as a mass transfer limitation is reached for 10mM urea, but otherwise follows the same trend as the 200 mM TOF.

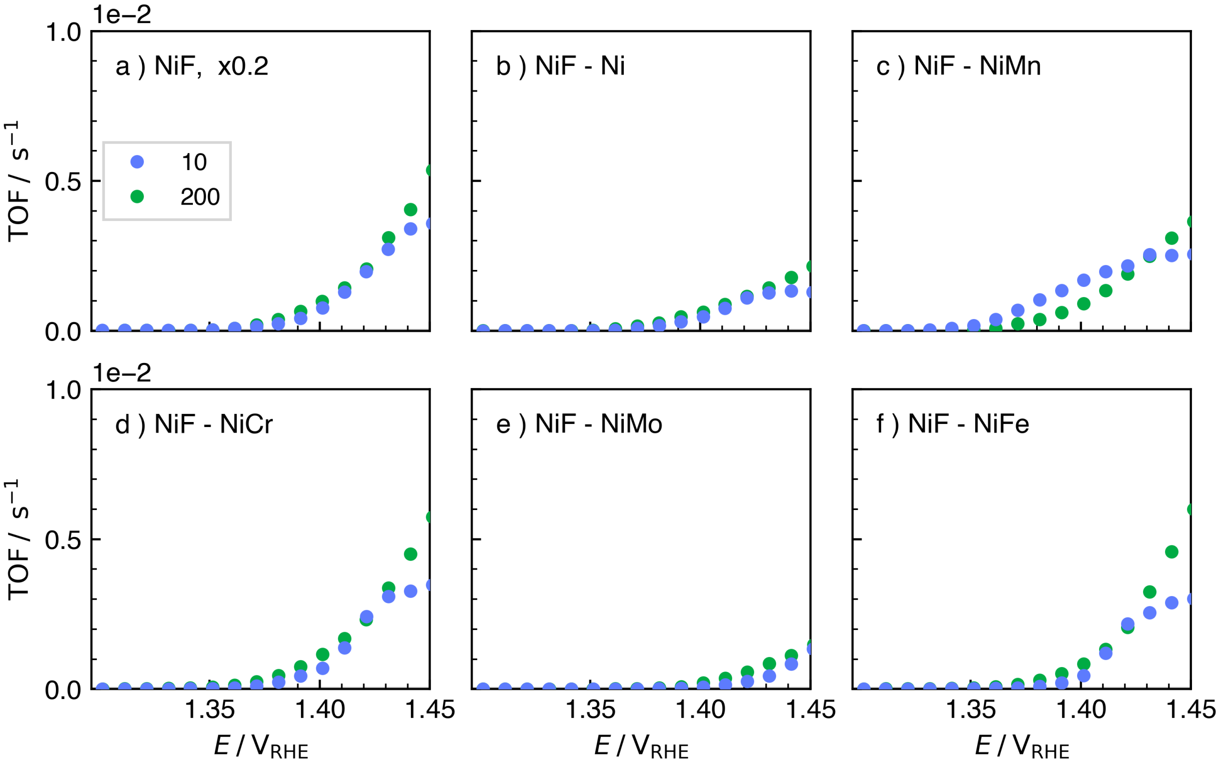

Fig. 7.7 Turnover Frequency (TOF) of a) nickel foam (NiF) and metallic species b) Ni, c) NiMn, d) NiCr, e) NiMo, and f) NiFe grown on NiF for concentrations of 0, 10, and 200 mM urea in 0.5 M KOH. The TOF for NiF is scaled by 0.2 to include the points on the same y-axis.

NiF-based grown species had UOR TOF values similar to electrodes seen in literature.[114,265,266] The hydrothermal growth increased the number of active sites from NiF, as seen by the A_{ECSA} in Fig. 7.6, but decreased the UOR kinetics of NiF based on the TOF analysis. Growing more sites allowed for more urea to oxidize, but at a slower rate per site.

7.5.3 Implementation

The synthesized electrodes provided values that, when combined with the results of the model, show operation parameters necessary for a simplified dialysis device. All electrodes with grown species electrodes exhibited similar currents towards UOR due to the mass transfer limitation between 1.40 and 1.45 V_{RHE}. The NiF-Ni catalyst was chosen to be paired with the model due to its single element composition.

Figure 7.8 shows the performance of a NiF-Ni electrode (operating at 7.64 mA cm^{-2} at 1.45 V_{RHE}, as seen in Fig. 7.3) with four different sizes of geometric area for a dialyzer flowrate of 200 mL min^{-1}. The curve represents the performance of a Fresnius F4 dialyzer (K_OA of 374 mL min^{-1}), where the shaded area shows the flowrates and extent of reaction of catalysts that remove $\geq$ 3.75 g urea hr^{-1}. Fig. 7.8I represents a current of 7.64 mA

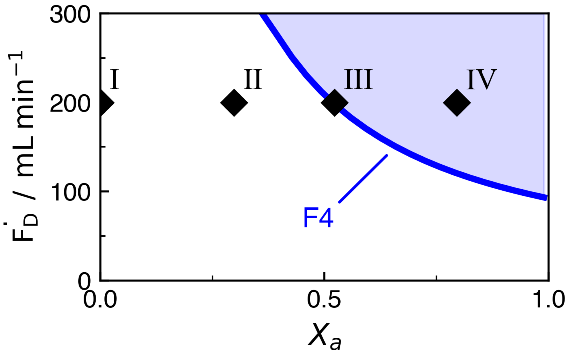

Fig. 7.8 Performance of NiF-Ni catalyst with 1 (I), 750 (II), 1314 (III), and 2000 (IV) cm^2 with a dialyzer flowrate of 200 mL min^{-1}. The line represents the model output for a Fresnius F4 dialyzer (K_OA: 374 mL min^{-1} 1.[262] Points in the shaded region are acceptable for use in the simplified dialysis device.

cm^{-2}, which is beneath the curve and is not usable in the WAK for any dialyzer flowrate. However, the geometric area of the catalyst can be expanded to increase the current supplied to the anode, increasing the rate of urea removal. Fig. 7.8III represents the lowest geometric area needed (1314 cm^2) to remove 3.75 g urea hr^{-1} at a 200 mL min^{-1} dialyzer flowrate. Fig. 7.8IV represents an area of 2000 cm^2, which obtains an extent of reaction higher than necessary for operation. However, these large, planar areas necessary for a URC may impinge on the portability of the system.

A rough estimate of URC size can be made on the basis of a total area of 2,000 cm_2, which allows for de-rated electrooxidation performance. For a single cell of 100 cm^2 and spacing between cells of 0.5 cm, the size of the electrolysis stack would be 10 x 10 x 10 cm^3 (1 liter). This estimate includes only the electrodes and flow field plates. A conservative estimate of ancillary hardware (compression plates, manifolds, tabulation, etc.) is a volume equal to that of the URC. This brings the total reactor volume to approximately 2 liters. This is a large volume for a portable dialysis device and clearly needs to be reduced. Because of the mass transfer limit of dilute urea solutions, further URC development should be focused on improving mass transfer.

7.6 Conclusion

Nickel-based catalysts were developed by a hydrothermal growth procedure to include Ni, NiMn, NiCr, NiMo, and NiFe deposited on nickel foam to improve the urea oxidation current density for application in a wearable artificial kidney. The grown species increase the electrochemically active surface area and roughness of the electrode. Although the electrochemically active surface area is increased, a mass transfer limitation is reached with 10 mM urea for all grown metallic electrodes. Urea oxidation kinetics were investigated using non-dialysate concentrations of urea (200 mM), as reaction was not limited by mass transfer. The grown electrodes had the highest currents during staircase polarization, but have some of the lowest values of TOF.

A simplified dialysis model was created to evaluate the viability of nickel-based catalysts by establishing necessary flowrates, urea concentrations, and pH of streams as a function of the dialyzer mass transfer coefficient and the URC extent of reaction. The performance of a NiF-Ni electrode was evaluated in the computational model of a simplified, continuous dialysis system. The minimum required area is 1,314 cm^2 to remove 3.75 g urea hr^{-1} for a Fresnius F4 dialyzer flowrate of 200 mL min^{-1}. Together, the model and the catalysts provided operating conditions of a simplified, continuous dialysis system, setting the stage for future improvements.

7.7 Acknowledgements

Part of this work was conducted at the Molecular Analysis Facility, a National Nanotechnology Coordinated Infrastructure (NNCI) site at the University of Washington, which is supported in part by funds from the National Science Foundation (awards NNCI-2025489, NNCI-1542101), the Molecular Engineering & Sciences Institute, and the Clean Energy Institute. The authors thank the members of Center for Dialysis Innovation for the shared knowledge of dialysis systems. The authors also thank Prof. Peter Strasser and Prof. Gregory Jerkiewicz for the shared knowledge of nickel hydroxide catalysts in electrochemical systems.

Chapter 8

CONCLUSIONS AND PERSPECTIVES

Conclusions

The primary objective of this work was to advance the current understand of nickel and nickel-based catalysts for the removal of urea from alkaline solutions. Motivated by the pollution of urea in waste streams, we used a range of electrochemical and non-electrochemical methods to characterize the nickel hydroxide surfaces to better understand the role of the hydroxide layer during oxygen evolution and urea oxidation.

8.0.1 Development of Nickel Phases For Studying Oxygen Evolution

In Chapter 4, selective cycling procedures were developed to target the formation of individual NiOOH phases. The resulting oxide structures underwent characterization using cyclic voltammetry and scanning electron microscopy, and their electrocatalytic properties were bench-marked using impedance spectroscopy, Tafel analysis, and overpotentials.

The switching potential was employed to control NiOOH formation, revealing that γ-NiOOH could be preferentially formed at higher potentials (1.64 V) due to oxygen evolution, while the more stable β-NiOOH phase formed at lower potentials (1.54 V). The $Ni(OH)_2$ facets were captured using SEM, and a clear increase in grain boundary density was observed for the γ-NiOOH–developed electrode. A kinetics analysis of the NiOOH phases indicated that the β-NiOOH phase was considerably more active towards the OER, evident through lower overpotentials and higher turnover frequencies. Additionally, the improved kinetics of the β-NiOOH phase persisted for an extended time period compared to the γ-NiOOH phase.

8.0.2 Development of Nickel Phases For Studying Urea Oxidation

In Chapter 5, The procedure for developing β-NiOOH and γ-NiOOH phases were applied to nickel foams to study the urea oxidation reaction with electrochemistry and mass spectrometry. These phases were maintained at potentials sufficient to induce urea oxidation and oxygen evolution, and the resulting gases were analyzed using mass spectrometry. These techniques allowed for the detection of changes in the catalyst surface during electrochemical cycling and the evaluation of selectivity in OER.

Notably, electrodes developed with urea, operating at similar switching potentials to those without urea, exhibited an increased activity for OER. This enhancement was discernible through alterations in cyclic voltammetry profiles and a heightened presence of the mass 28 peak in mass spectrometry analysis. It is essential to highlight that urea did not appear to influence the structure of the nickel surface during oxidation, but rather during reduction. In a system where urea oxidation consumed nickel sites during reduction, assuming an indirect mechanism, there was a positive shift in the onset potential towards values relevant to the β-$Ni(OH)_2$/β-NiOOH transition.

Purified electrolytes, when investigated, exhibited hysteresis in cyclic voltammetry at higher potentials, with a timescale shorter than that of staircase potential experiments. This hysteresis may stem from transitions between $Ni(OH)_2$/NiOOH at low potentials and NiOOH/NiO_2 at high potentials, where nickel can assume chemical states below the respective redox potential. The presence of distinct nickel states during electrochemical experiments complicates the analysis of whether the current drop at higher potentials is attributed to NiO_2 formation or a shift in the urea oxidation reaction mechanism.

8.0.3 Nickel-Chromium-Molybdenum Electrocatalysts

In Chapter 6, nickel-based alloys BC-1, C-276, and C-2000 were subjected to two distinct oxide growth procedures to show the UOR dependence on oxide layer. The mature oxide layers were found to be thicker and had a higher number of electrochemically active sites than initial oxide layers. This increased oxide layer thickness led to higher urea oxidation currents in respect to geometric electrode area. TOF ratio analysis revealed that, while the developed oxide layer significantly contributed to the increased number of electrochemically active sites, the UOR activity remained relatively constant on a per-site basis.

This study suggests that these alloys are well-suited for urea electrooxidation and merit further exploration in corrosive environments. Key findings from this research encompass the alloys' support for urea electrooxidation, the correlation of electrochemical surface area and roughness with the active area for urea oxidation, the predominance of the indirect mechanism in urea oxidation at potentials near the nickel transition, the shift in the rate-determining step with higher potentials dependent on alloy composition, and the similarity in urea oxidation turnover frequency among site-normalized oxide layers.

8.0.4 Urea Electrooxidation for Simplified Dialysis Device with Nickel-Metal Foam

In Chapter 7, nickel-based catalysts, such as Ni, NiMn, NiCr, NiMo, and NiFe, were synthesized using a hydrothermal growth and applied to nickel foam method to improve the urea oxidation current density. The grown electrodes exhibited the highest current densities during polarization curves but displayed relatively lower currents per site, as indicated by TOF measurements.

To evaluate the capabilities of nickel-based catalysts, a simplified dialysis model was constructed to determine the necessary flow rates, urea concentrations, and pH levels in the streams. The computational model, featuring a NiF-Ni electrode, assessed the performance within a simplified, continuous dialysis system, concluding that a minimum area of 1,314 cm^2 is essential to remove 3.75 g of urea per hour with a Fresnius F4 dialyzer operating at a flow rate of 200 mL per minute. This model, with the developed catalysts, helps to establish the operational parameters for a simplified, continuous dialysis system, providing a framework for potential future improvements.

Perspectives

8.0.5 Nickel-based Alloys

In this work, nickel-chromium-molybdenum were seen to oxidize urea at higher current densities than pure nickel. The addition of Cr and Mo have been seen to also increase the corrosion resistance of the oxide layer, granting use in corrosive environments. The field of urea oxidation would benefit from studies showing the combined urea oxidation and corrosive properties of these materials, especially in studies with differing pH, corrosive electrolytes (such as chloride), and other organic molecules (such as methanol and formaldehyde).

8.0.6 Iron-free Urea Oxidation

Recent literature has identified the affect incidental iron within the nickel oxide layer on the oxygen evolution reaction. Although addressed in this study, the effect of iron on the urea oxidation reaction is not well known. In an iron-free electrolyte, the current density was seen to drop at higher potentials and was attributed to a change in urea oxidation mechanism. The product distribution of urea oxidation has not been identified within iron-free systems, leading to a gap of knowledge of UOR on pure-nickel catalysts.

BIBLIOGRAPHY

1. Fowler, D., Coyle, M., Skiba, U., Sutton, M. A., Cape, J. N., Reis, S., Sheppard, L. J., Jenkins, A., Grizzetti, B., Galloway, J. N., Vitousek, P., Leach, A., Bouwman, A. F., Butterbach-Bahl, K., Dentener, F., Stevenson, D., Amann, M. & Voss, M. The global nitrogen cycle in the twenty-first century. *Philosophical Transactions of the Royal Society B: Biological Sciences* **368,** 20130164. doi:`10.1098/rstb.2013.0164` (1621 July 2013).
2. *Clean Energy for America Act. S.1298 117th Congress (2021-2022)*
3. Park, B. D. & Causin, V. Crystallinity and domain size of cured urea-formaldehyde resin adhesives with different formaldehyde/urea mole ratios. *European Polymer Journal* **49,** 532–537. doi:`10.1016/j.eurpolymj.2012.10.029` (2 Feb. 2013).
4. Ingoglia, F., Chong, J. L., Pasquali, M. & Longo, N. Creatine metabolism in patients with urea cycle disorders. *Molecular Genetics and Metabolism Reports* **29.** doi:`10.1016/j.ymgmr.2021.100791` (Dec. 2021).
5. Rossky, P. J. Protein denaturation by urea: Slash and bond. *Proceedings of the National Academy of Sciences* **105,** 16825–16826. doi:`10.1073/pnas.0809224105` (44 Nov. 2008).
6. Rollinson, A. N., Jones, J., Dupont, V. & Twigg, M. V. Urea as a hydrogen carrier: A perspective on its potential for safe, sustainable and long-term energy supply. *Energy and Environmental Science* **4,** 1216–1224. doi:`10.1039/c0ee00705f` (4 Apr. 2011).
7. Ivey, J. E., Wolny, J. L., Heil, C. A., Murasko, S. M., Brame, J. A. & Parks, A. A. Urea inputs drive picoplankton blooms in sarasota bay, florida, u.S.a. *Water (Switzerland)* **12.** doi:`10.3390/w12102755` (10 Oct. 2020).

8. Burrows, N. R., Koyama, A. & Pavkov, M. E. Reported Cases of End-Stage Kidney Disease — United States, 2000–2019. *MMWR. Morbidity and Mortality Weekly Report* **71,** 412–415. doi:`10.15585/mmwr.mm7111a3` (Mar. 2022).
9. Banach, M., Aronow, W. S., Serban, M. C., Rysz, J., Voroneanu, L. & Covic, A. Lipids, blood pressure and kidney update 2015. *Lipids in Health and Disease* **14.** doi:`10.1186/s12944-015-0169-0` (1 Dec. 2015).
10. Gura, V., Rivara, M. B., Bieber, S., Munshi, R., Smith, N. C., Linke, L., Kundzins, J., Beizai, M., Ezon, C., Kessler, L. & Himmelfarb, J. A wearable artificial kidney for patients with end-stage renal disease. *JCI Insight* **1.** doi:`10.1172/jci.insight.86397` (June 2016).
11. Mapes, D. L., Lopes, A. A., Satayathum, S., Mccullough, K. P., Goodkin, D. A., Locatelli, F., Fukuhara, S., Young, E. W., Kurokawa, K., Saito, A., Bommer, J., Wolfe, R. A., Held, P. J. & Port, F. K. Health-related quality of life as a predictor of mortality and hospitalization: The Dialysis Outcomes and Practice Patterns Study (DOPPS). *Kidney International* **64,** 339–349. doi:`10.1046/j.1523-1755.2003.00072.x` (July 2003).
12. Evans, R. W., Manninen, D. L., Garrison, L. P., Hart, L. G., Blagg, C. R., Gutman, R. A., Hull, A. R. & Lowrie, E. G. The Quality of Life of Patients with End-Stage Renal Disease. *New England Journal of Medicine* **312,** 553–559. doi:`10.1056/NEJM198502283120905` (Feb. 1985).
13. Chiu, Y.-W., Teitelbaum, I., Misra, M., de Leon, E. M., Adzize, T. & Mehrotra, R. Pill Burden, Adherence, Hyperphosphatemia, and Quality of Life in Maintenance Dialysis Patients. *Clinical Journal of the American Society of Nephrology* **4,** 1089–1096. doi:`10.2215/CJN.00290109` (June 2009).
14. Carpenter, K. & Stuve, E. M. Electrooxidation of urea and creatinine on nickel foam-based electrocatalysts. *Journal of Applied Electrochemistry* **51,** 945–957. doi:`10.1007/s10800-021-01545-1` (June 2021).

15. Locatelli, F., La Milia, V., Violo, L., Del Vecchio, L. & Di Filippo, S. Optimizing haemodialysate composition. *Clinical Kidney Journal* **8,** 580–589. doi:`10.1093/ckj/sfv057` (Oct. 2015).
16. Desai, N. Basics of base in hemodialysis solution: Dialysate buffer production, delivery and decontamination. *Indian Journal of Nephrology* **25,** 189. doi:`10.4103/0971-4065.147369` (2015).
17. Liu, C., Liu, F., Andersen, M. N., Wang, G., Wu, K., Zhao, Q. & Ye, Z. Domestic wastewater infiltration process in desert sandy soil and its irrigation prospect analysis. *Ecotoxicology and Environmental Safety* **208.** doi:`10.1016/j.ecoenv.2020.111419` (Jan. 2021).
18. Alexandrova, A. N. & Jorgensen, W. L. Why urea eliminates ammonia rather than hydrolyzes in aqueous solution. *Journal of Physical Chemistry B* **111,** 720–730. doi:`10.1021/jp066478s` (4 Feb. 2007).
19. Van Gelder, M. K., Jong, J. A., Folkertsma, L., Guo, Y., Blüchel, C., Verhaar, M. C., Odijk, M., Nostrum, C. F. V., Hennink, W. E. & Gerritsen, K. G. Urea removal strategies for dialysate regeneration in a wearable artificial kidney. *Biomaterials* **234,** 119735. doi:`10.1016/j.biomaterials.2019.119735` (Mar. 2020).
20. Wernert, V., Schäf, O., Ghobarkar, H. & Denoyel, R. Adsorption properties of zeolites for artificial kidney applications. *Microporous and Mesoporous Materials* **83,** 101–113. doi:`10.1016/j.micromeso.2005.03.018` (Sept. 2005).
21. Giordano, C., Esposito, R., Bello, P., Quarto, E. & Gonzalez, F. M. Cold Carbon Apparatus for Hemodialysis. *Journal of Dialysis* **1,** 165–179. doi:`10.3109/08860227609039143` (Jan. 1976).
22. Hu, G., Pojman, J. A., Scott, S. K., Wrobel, M. M. & Taylor, A. F. Base-Catalyzed Feedback in the Urea-Urease Reaction. *The Journal of Physical Chemistry B* **114,** 14059–14063. doi:`10.1021/jp106532d` (Nov. 2010).

23. Hameed, R. A. & Medany, S. S. NiO nanoparticles on graphene nanosheets at different calcination temperatures as effective electrocatalysts for urea electro-oxidation in alkaline medium. *Journal of Colloid and Interface Science* **508,** 291–302. doi:`10.1016/j.jcis.2017.08.048` (Dec. 2017).

24. Gheriany, I. E., Abdel-Aziz, M. H., El-Ashtoukhy, E.-S. Z. & Sedahmed, G. H. Electrochemical removal of urea from wastewater by anodic oxidation using a new cell design: An experimental and modeling study. *Process Safety and Environmental Protection* **159,** 133–145. doi:`10.1016/j.psep.2021.12.055` (Mar. 2022).

25. Putri, Y. M. T. A., Gunlazuardi, J., Yulizar, Y., Wibowo, R., Einaga, Y. & Ivandini, T. A. Recent progress in direct urea fuel cell. *Open Chemistry* **19,** 1116–1133. doi:`10.1515/chem-2021-0100` (1 Nov. 2021).

26. Nutting, J. E., Gerken, J. B., Stamoulis, A. G., Bruns, D. L. & Stahl, S. S. "How Should I Think about Voltage? What Is Overpotential?": Establishing an Organic Chemistry Intuition for Electrochemistry. *Journal of Organic Chemistry* **86,** 15875–15885. doi:`10.1021/acs.joc.1c01520` (22 Nov. 2021).

27. Lee, W. H., Han, M. H., Ko, Y. J., Min, B. K., Chae, K. H. & Oh, H. S. Electrode reconstruction strategy for oxygen evolution reaction: maintaining Fe-CoOOH phase with intermediate-spin state during electrolysis. *Nature Communications* **13.** doi:`10.1038/s41467-022-28260-5` (1 Dec. 2022).

28. Reier, T., Oezaslan, M. & Strasser, P. Electrocatalytic oxygen evolution reaction (OER) on Ru, Ir, and pt catalysts: A comparative study of nanoparticles and bulk materials. *ACS Catalysis* **2,** 1765–1772. doi:`10.1021/cs3003098` (Aug. 2012).

29. Seitz, L. C., Dickens, C. F., Nishio, K., Hikita, Y., Montoya, J., Doyle, A., Kirk, C., Vojvodic, A., Hwang, H. Y., Norskov, J. K. & Jaramillo, T. F. A highly active and stable IrO_x $SrIrO_3$ catalyst for the oxygen evolution reaction. *Science* **353,** 1011–1014. doi:`10.1126/science.aaf5050` (6303 Sept. 2016).

30. Climent, V., Rodes, A., Albalat, R., Claret, J., Feliu, J. M. & Aldaz, A. Urea adsorption on platinum single crystal stepped surfaces. *Langmuir* **17,** 8260–8269. doi:`10.1021/la011122n` (Dec. 2001).

31. Wang, X., Xi, S., Lee, W. S. V., Huang, P., Cui, P., Zhao, L., Hao, W., Zhao, X., Wang, Z., Wu, H., Wang, H., Diao, C., Borgna, A., Du, Y., Yu, Z. G., Pennycook, S. & Xue, J. Materializing efficient methanol oxidation via electron delocalization in nickel hydroxide nanoribbon. *Nature Communications* **11.** doi:`10.1038/s41467-020-18459-9` (1 Dec. 2020).

32. Van Drunen, J., Barbosa, A. F. & Tremiliosi-Filho, G. The Formation of Surface Oxides on Nickel in Oxalate-Containing Alkaline Media. *Electrocatalysis* **6,** 481–491. doi:`10.1007/s12678-015-0268-8` (5 Sept. 2015).

33. El-Shafei, A. A. Electrocatalytic oxidation of methanol at a nickel hydroxide/glassy carbon modified electrode in alkaline medium. *Journal of Electroanalytical Chemistry* **471,** 89–95 (1999).

34. Taraszewska, J. & Roslonek, G. Electrocatalytic oxidation of methanol on a glassy carbon electrode modified by nickel hydroxide formed by ex situ chemical precipitation. *Journal of Electroanalytical Chemistry* **364,** 209–213 (1994).

35. Dionigi, F., Zeng, Z., Sinev, I., Merzdorf, T., Deshpande, S., Lopez, M. B., Kunze, S., Zegkinoglou, I., Sarodnik, H., Fan, D., Bergmann, A., Drnec, J., de Araujo, J. F., Gliech, M., Teschner, D., Zhu, J., Li, W. X., Greeley, J., Cuenya, B. R. & Strasser, P. In-situ structure and catalytic mechanism of NiFe and CoFe layered double hydroxides during oxygen evolution. *Nature Communications* **11.** doi:`10.1038/s41467-020-16237-1` (1 Sept. 2020).

36. Fleischmann, M., Korinek, K. & Pletcher, D. The oxidation of organic compounds at a nickel anode in alkaline solution. *Journal of Electroanalytical Chemistry and Interfacial Electrochemistry* **31,** 39–49. doi:`10.1016/S0022-0728(71)80040-2` (1 June 1971).

37. Gerald, B. V. Electrolytic Pretreatment Unit Gaseous Effluent Conditioning (Aug. 1976).

38. Patzer, J. F., Yao, S. J., Woffson, S. K. & Ruppel-Kerr, R. 341-353 A section of. *Jr. Electroanai. Chem., and constituting* **22** (1989).

39. Cherevko, S., Zeradjanin, A. R., Keeley, G. P. & Mayrhofer, K. J. J. A Comparative Study on Gold and Platinum Dissolution in Acidic and Alkaline Media. *Journal of The Electrochemical Society* **161,** H822–H830. doi:`10.1149/2.0881412jes` (12 Sept. 2014).

40. Bagotzky, V., Khrushcheva, E., Tarasevich, M. & Shumilova, N. Corrosion of platinum catalyst in alkaline solutions. *Journal of Power Sources* **8,** 301–309. doi:`10.1016/0378-7753(82)80063-3` (2 Jan. 1982).

41. Yan, W., Wang, D. & Botte, G. G. Electrochemical decomposition of urea with Ni-based catalysts. *Applied Catalysis B: Environmental* **127,** 221–226. doi:`10.1016/j.apcatb.2012.08.022` (Oct. 2012).

42. Keller, R. W., Yao, S. J., Brown, J. M., Wolfson, S. K. & Zeller, M. V. Electrochemical removal of urea from physiological buffer as the basis for a regenerative dialysis system. *Journal of Electroanalytical Chemistry and Interfacial Electrochemistry* **116,** 469–485. doi:`10.1016/S0022-0728(80)80271-3` (Jan. 1980).

43. Xie, J., Liu, W., Lei, F., Zhang, X., Qu, H., Gao, L., Hao, P., Tang, B. & Xie, Y. Iron-Incorporated α-Ni(OH)$_2$ Hierarchical Nanosheet Arrays for Electrocatalytic Urea Oxidation. *Chemistry - A European Journal* **24,** 18408–18412. doi:`10.1002/chem.201803718` (Dec. 2018).

44. Xu, W., Wu, Z. & Tao, S. Urea-Based Fuel Cells and Electrocatalysts for Urea Oxidation. *Energy Technology* **4,** 1329–1337. doi:`10.1002/ente.201600185` (Nov. 2016).

45. Maddren, J. & Marschall, E. Predicting thermal contact resistance at cryogenic temperatures for spacecraft applications. *Journal of Spacecraft and Rockets* **32,** 469–474. doi:`10.2514/3.26639` (3 May 1995).

46. Kowalski, J., Licznerski, Ł., Supernak-Marczewska, M. & Emilianowicz, K. Influence of Process of Straightening Ship Hull Structure Made of 316L Stainless Steel on Corrosion Resistance and Mechanical Properties. *Polish Maritime Research* **27,** 103–111. doi:`10.2478/pomr-2020-0070` (4 Dec. 2020).

47. Cao, J. & Grenestedt, J. L. Design and testing of joints for composite sandwich/steel hybrid ship hulls. *Composites Part A: Applied Science and Manufacturing* **35,** 1091–1105. doi:`10.1016/j.compositesa.2004.02.010` (9 Sept. 2004).

48. Rowcliffe, A., Mansur, L., Hoelzer, D. & Nanstad, R. Perspectives on radiation effects in nickel-base alloys for applications in advanced reactors. *Journal of Nuclear Materials* **392,** 341–352. doi:`10.1016/j.jnucmat.2009.03.023` (2 July 2009).

49. Boggs, B. K., King, R. L. & Botte, G. G. Urea electrolysis: Direct hydrogen production from urine. *Chemical Communications,* 4859–4861. doi:`10.1039/b905974a` (2009).

50. Wang, D. & Botte, G. G. In Situ X-Ray Diffraction Study of Urea Electrolysis on Nickel Catalysts. *ECS Electrochemistry Letters* **3,** H29–H32. doi:`10.1149/2.0031409eel` (July 2014).

51. Guo, F., Ye, K., Du, M., Huang, X., Cheng, K., Wang, G. & Cao, D. Electrochemical impedance analysis of urea electro-oxidation mechanism on nickel catalyst in alkaline medium. *Electrochimica Acta* **210,** 474–482. doi:`10.1016/j.electacta.2016.05.149` (Aug. 2016).

52. Hopsort, G., Latapie, L., Groenen Serrano, K., Loubière, K. & Tzedakis, T. Indirect urea electrooxidation by nickel(III) in alkaline medium: From kinetic and mechanism to reactor modeling. *AIChE Journal.* doi:`10.1002/aic.18113` (May 2023).

53. Barnard, R., Randell, C. F. & Tye, F. L. Studies concerning charged nickel hydroxide electrodes I. Measurement of reversible potentials. *Journal of Applied Electrochemistry* **10,** 109–125. doi:`10.1007/BF00937345` (Jan. 1980).

54. Dionigi, F., Reier, T., Pawolek, Z., Gliech, M. & Strasser, P. Design Criteria, Operating Conditions, and Nickel-Iron Hydroxide Catalyst Materials for Selective Seawater Electrolysis. *ChemSusChem* **9,** 962–972. doi:`10.1002/cssc.201501581` (9 May 2016).

55. Dau, H., Limberg, C., Reier, T., Risch, M., Roggan, S. & Strasser, P. The Mechanism of Water Oxidation: From Electrolysis via Homogeneous to Biological Catalysis. *ChemCatChem* **2,** 724–761. doi:`10.1002/cctc.201000126` (July 2010).

56. Song, F., Busch, M. M., Lassalle-Kaiser, B., Hsu, C. S., Petkucheva, E., Bensimon, M., Chen, H. M., Corminboeuf, C. & Hu, X. An Unconventional Iron Nickel Catalyst for the Oxygen Evolution Reaction. *ACS Central Science* **5,** 558–568. doi:`10.1021/acscentsci.9b00053` (3 Mar. 2019).

57. Trotochaud, L., Young, S. L., Ranney, J. K. & Boettcher, S. W. Nickel–Iron Oxyhydroxide Oxygen-Evolution Electrocatalysts: The Role of Intentional and Incidental Iron Incorporation. *Journal of the American Chemical Society* **136,** 6744–6753. doi:`10.1021/ja502379c` (18 Sept. 2014).

58. Lyu, X., Li, J., Jafta, C. J., Bai, Y., Canales, C. P., Magnus, F., Ingason, Á. S. & Serov, A. Investigation of oxygen evolution reaction with Ni foam and stainless-steel mesh electrodes in alkaline seawater electrolysis. *Journal of Environmental Chemical Engineering* **10.** doi:`10.1016/j.jece.2022.108486` (5 Oct. 2022).

59. Li, J., Li, J., Liu, T., Chen, L., Li, Y., Wang, H., Chen, X., Gong, M., Liu, Z.-P. & Yang, X. Deciphering and Suppressing Over-Oxidized Nitrogen in Nickel-Catalyzed Urea Electrolysis. *Angewandte Chemie International Edition* **60,** 26656–26662. doi:`10.1002/anie.202107886` (51 Dec. 2021).

60. Density functional theory studies of transition metal carbides and nitrides as electrocatalysts. *Chemical Society Reviews* **50,** 12338–12376. doi:`10.1039/D1CS00590A` (22 2021).

61. Kryachko, E. S. & Ludeña, E. V. Density functional theory: Foundations reviewed. *Physics Reports* **544,** 123–239. doi:`10.1016/j.physrep.2014.06.002` (2 Nov. 2014).

62. Geerlings, P., Proft, F. D. & Langenaeker, W. Conceptual Density Functional Theory. *Chemical Reviews* **103,** 1793–1874. doi:`10.1021/cr990029p` (5 May 2003).

63. Li, Q., He, T., Jiang, X., Lei, Y., Liu, Q., Liu, C., Sun, Z., Chen, S. & Zhang, Y. Boosting oxygen evolution activity of nickel iron hydroxide by iron hydroxide colloidal particles. *Journal of Colloid and Interface Science* **606,** 518–525. doi:`10.1016/j.jcis.2021.08.037` (Jan. 2022).

64. Daramola, D. A., Singh, D. & Botte, G. G. Dissociation rates of urea in the presence of NiOOH catalyst: A DFT analysis. *Journal of Physical Chemistry A* **114,** 11513–11521. doi:`10.1021/jp105159t` (Nov. 2010).

65. Tatarchuk, S. W., Medvedev, J. J., Li, F., Tobolovskaya, Y. & Klinkova, A. Nickel-Catalyzed Urea Electrolysis: From Nitrite and Cyanate as Major Products to Nitrogen Evolution. *Angewandte Chemie International Edition* **61.** doi:`10.1002/anie.202209839` (Sept. 2022).

66. Chakrabarty, S., Offen-Polak, I., Burshtein, T. Y., Farber, E. M., Kornblum, L. & Eisenberg, D. Urea oxidation electrocatalysis on nickel hydroxide: the role of disorder. *Journal of Solid State Electrochemistry* **25,** 159–171. doi:`10.1007/s10008-020-04744-6` (1 Jan. 2021).

67. Iwamoto, M., Yoda, Y., Yamazoe, N. & Seiyama, T. Study of Metal Oxide Catalysts by Temperature Programmed Desorption. 4. Oxygen Adsorption on Various Metal Oxides. *The Journal of Physical Chemistry* **82.** doi:`https://doi.org/10.1021/j100513a006` (1978).

68. Coutanceau, C., Demarconnay, L., Lamy, C. & Léger, J. M. Development of electrocatalysts for solid alkaline fuel cell (SAFC). *Journal of Power Sources* **156,** 14–19. doi:`10.1016/j.jpowsour.2005.08.035` (1 SPEC. ISS. May 2006).

69. Van der Ven, A., Morgan, D., Meng, Y. S. & Ceder, G. Phase Stability of Nickel Hydroxides and Oxyhydroxides. *Journal of The Electrochemical Society* **153,** A210. doi:`10.1149/1.2138572` (2006).

70. H., e. a. B. Zur Kenntnis der Nickelhydroxidelektrode. II. Über die Oxydationsprodukte von Nickel(II)-hydroxiden. *Zeitschrift für anorganische und allgemeine Chemie* **366,** 1–21 (1-2 1950).

71. Hall, D. S., Lockwood, D. J., Bock, C. & MacDougall, B. R. Nickel hydroxides and related materials: A review of their structures, synthesis and properties. *Proceedings of the Royal Society A: Mathematical, Physical and Engineering Sciences* **471.** doi:`10.1098/rspa.2014.0792` (2174 Sept. 2015).

72. Yang, C.-C. Synthesis and characterization of active materials of Ni(OH)_2 powders. *International Journal of Hydrogen Energy* **27,** 1071–1081. doi:`10.1016/S0360-3199(02)00013-7` (Oct. 2002).

73. McEwen, R. S. Crystallographic studies on nickel hydroxide and the higher nickel oxides. *The Journal of Physical Chemistry* **75,** 1782–1789. doi:`10.1021/j100681a004` (12 Sept. 1971).

74. Visscher, W. & Barendrecht, E. The anodic oxidation of nickel in alkaline solution. *Electrochimica Acta* **25,** 651–655. doi:`10.1016/0013-4686(80)87072-1` (5 May 1980).

75. Oliva, P., Leonardi, J., Laurent, J., Delmas, C., Braconnier, J., Figlarz, M., Fievet, F. & Guibert, A. Review of the structure and the electrochemistry of nickel hydroxides and oxy-hydroxides. *Journal of Power Sources* **8,** 229–255. doi:`10.1016/0378-7753(82)80057-8` (Jan. 1982).

76. Alsabet, M., Grdeń, M. & Jerkiewicz, G. Electrochemical Growth of Surface Oxides on Nickel. Part 3: Formation of β-NiOOH in Relation to the Polarization Potential, Polarization Time, and Temperature. *Electrocatalysis* **6,** 60–71. doi:`10.1007/s12678-014-0214-1` (1 Sept. 2015).

77. Kinoshita, K. *Electrochemical oxygen technology* (John Wiley and Sons, 1992).

78. Lu, P. W. T. & Srinivasan, S. Electrochemical Ellipsometric Studies of Oxide Film Formed on Nickel during Oxygen Evolution. *Journal of The Electrochemical Society* **125,** 1416–1422. doi:`10.1149/1.2131689` (Sept. 1978).

79. Damjanovic, A. & Jovanovic, B. Anodic Oxide Films as Barriers to Charge Transfer in O_2 Evolution at Pt in Acid Solutions. *Journal of The Electrochemical Society* **123,** 374–381. doi:`10.1149/1.2132828` (Mar. 1976).

80. MacDonald, J. J. & Conway, B. E. The role of surface films in the kinetics of oxygen evolution at Pd + Au alloy electrodes. *Proceedings of the Royal Society of London. Series A. Mathematical and Physical Sciences* **269,** 419–440. doi:`10.1098/rspa.1962.0186` (Sept. 1962).

81. Surendranath, Y. & Nocera, D. G. Oxygen Evolution Reaction Chemistry of Oxide-Based Electrodes, 505–560. doi:`10.1002/9781118148235.ch9` (Dec. 2011).

82. Bediako, D. K., Lassalle-Kaiser, B., Surendranath, Y., Yano, J., Yachandra, V. K. & Nocera, D. G. Structure Activity Correlations in a Nickel Borate Oxygen Evolution Catalyst. *Journal of the American Chemical Society* **134,** 6801–6809. doi:`10.1021/ja301018q` (15 Sept. 2012).

83. Juodkazis, K., Juodkazytė, J., Vilkauskaitė, R. & Jasulaitienė, V. Nickel surface anodic oxidation and electrocatalysis of oxygen evolution. *Journal of Solid State Electrochemistry* **12,** 1469–1479. doi:`10.1007/s10008-007-0484-0` (Nov. 2008).

84. Desilvestro, J., Corrigan, D. A. & Weaver, M. J. Characterization of Redox States of Nickel Hydroxide Film Electrodes by In Situ Surface Raman Spectroscopy. *Journal of The Electrochemical Society* **135,** 885–892. doi:`10.1149/1.2095818` (4 Apr. 1988).

85. Swierk, J. R., Klaus, S., Trotochaud, L., Bell, A. T. & Tilley, T. D. Electrochemical Study of the Energetics of the Oxygen Evolution Reaction at Nickel Iron (Oxy)Hydroxide Catalysts. *The Journal of Physical Chemistry C* **119,** 19022–19029. doi:`10.1021/acs.jpcc.5b05861` (Aug. 2015).

86. Pissinis, D. E., Sereno, L. E. & Marioli, J. M. Utilization of Special Potential Scan Programs for Cyclic Voltammetric Development of Different Nickel Oxide-Hydroxide Species on Ni Based Electrodes. *Open Journal of Physical Chemistry* **02,** 23–33. doi:`10.4236/ojpc.2012.21004` (2012).

87. Dose, W. M., Morzy, J. K., Mahadevegowda, A., Ducati, C., Grey, C. P. & De Volder, M. F. L. The influence of electrochemical cycling protocols on capacity loss in nickel-rich lithium-ion batteries. *Journal of Materials Chemistry A* **9,** 23582–23596. doi:`10.1039/D1TA06324C` (2021).

88. Bode, H., Dehmelt, K. & Witte, J. Zur Kenntnis Der Nickelhydroxidelektrode I. Über Das Nickel (II)-Hydroxidhydrat. *Electrochimica Acta* **11,** 1079–1087. doi:`10.1016/0013-4686(66)80045-2` (8 Sept. 1966).

89. Yeo, B. S. & Bell, A. T. In Situ Raman Study of Nickel Oxide and Gold-Supported Nickel Oxide Catalysts for the Electrochemical Evolution of Oxygen. *The Journal of Physical Chemistry C* **116,** 8394–8400. doi:`10.1021/jp3007415` (15 Sept. 2012).

90. Singh, R. K., Subramanian, P. & Schechter, A. Enhanced Urea Activity of Oxidation on Nickel-Deposited Tin Dendrites. *ChemElectroChem* **4,** 1037–1043. doi:`10.1002/celc.201600862` (5 May 2017).

91. Corrigan, D. A. The Catalysis of the Oxygen Evolution Reaction by Iron Impurities in Thin Film Nickel Oxide Electrodes. *Journal of The Electrochemical Society* **134,** 377–384. doi:`10.1149/1.2100463` (2 Feb. 1987).

92. Spanos, I., Masa, J., Zeradjanin, A. & Schlögl, R. The Effect of Iron Impurities on Transition Metal Catalysts for the Oxygen Evolution Reaction in Alkaline Environment: Activity Mediators or Active Sites? *Catalysis Letters* **151,** 1843–1856. doi:`10.1007/s10562-020-03478-4` (7 July 2021).

93. Babar, P., Patil, K., Lee, D. M., Karade, V., Gour, K., Pawar, S. & Kim, J. H. Cost-effective and efficient water and urea oxidation catalysis using nickel-iron oxyhydroxide nanosheets synthesized by an ultrafast method. *Journal of Colloid and Interface Science* **584,** 760–769. doi:`10.1016/j.jcis.2020.09.108` (Feb. 2021).

94. Cwalina, K. L., Ha, H. M., Ott, N., Reinke, P., Birbilis, N. & Scully, J. R. In Operando Analysis of Passive Film Growth on Ni-Cr and Ni-Cr-Mo Alloys in Chloride Solutions. *Journal of The Electrochemical Society* **166,** C3241–C3253. doi:`10.1149/2.0261911jes` (2019).

95. Lu, S., Pan, J., Huang, A., Zhuang, L. & Lu, J. Alkaline polymer electrolyte fuel cells completely free from noble metal catalysts. doi:`10.1073/pnas.0810041106` (2008).

96. Shi, W., Sun, X., Ding, R., Ying, D., Huang, Y., Huang, Y., Tan, C., Jia, Z. & Liu, E. Trimetallic NiCoMo/graphene multifunctional electrocatalysts with moderate structural/electronic effects for highly efficient alkaline urea oxidation reaction. *Chemical Communications* **56,** 6503–6506. doi:`10.1039/d0cc02132f` (June 2020).

97. Yu, X. x. & Marks, L. D. Combining the physics of metal/oxide heterostructure, interface dipole, band bending, crystallography, and surface state to understand heterogeneity contrast in oxidation and corrosion. *Corrosion* **75,** 152–166. doi:`10.5006/2794` (Feb. 2019).

98. Yang, D., Yang, L., Zhong, L., Yu, X. & Feng, L. Urea electro-oxidation efficiently catalyzed by nickel-molybdenum oxide nanorods. *Electrochimica Acta* **295,** 524–531. doi:`10.1016/j.electacta.2018.10.190` (Sept. 2019).

99. Ge, J., Lai, Y., Guan, M., Xiao, Y., Kuang, J. & Yang, C. Nickel borate with a 3D hierarchical structure as a robust and efficient electrocatalyst for urea oxidation. *Environmental Science: Nano* **8,** 1326–1335. doi:`10.1039/d0en01247e` (5 May 2021).

100. Zhong, M., Li, W., Wang, C. & Lu, X. Synthesis of hierarchical nickel sulfide nanotubes for highly efficient electrocatalytic urea oxidation. *Applied Surface Science* **575.** doi:`10.1016/j.apsusc.2021.151708` (Feb. 2022).

101. Zhao, Q., Meng, C., Kong, D., Wang, Y., Hu, H., Chen, X., Han, Y., Chen, X., Zhou, Y., Lin, M. & Wu, M. In Situ Construction of Nickel Sulfide Nano-Heterostructures for Highly Efficient Overall Urea Electrolysis. *ACS Sustainable Chemistry and Engineering* **9,** 15582–15590. doi:`10.1021/acssuschemeng.1c05722` (46 Nov. 2021).

102. Ji, Z., Song, Y., Zhao, S., Li, Y., Liu, J. & Hu, W. Pathway Manipulation via Ni, Co, and v Ternary Synergism to Realize High Efficiency for Urea Electrocatalytic Oxidation. *ACS Catalysis* **12,** 569–579. doi:`10.1021/acscatal.1c05190` (1 Jan. 2022).

103. Xu, W., Zhang, H., Li, G. & Wu, Z. Nickel-cobalt bimetallic anode catalysts for direct urea fuel cell. *Scientific Reports* **4,** 5863. doi:`10.1038/srep05863` (1 Aug. 2014).

104. Zhang, J., Wang, T., Pohl, D., Rellinghaus, B., Dong, R., Liu, S., Zhuang, X. & Feng, X. Interface Engineering of MoS 2 /Ni 3 S 2 Heterostructures for Highly Enhanced Electrochemical Overall-Water-Splitting Activity. *Angewandte Chemie* **128,** 6814–6819. doi:`10.1002/ange.201602237` (23 June 2016).

105. Wu, M. S., Chen, F. Y., Lai, Y. H. & Sie, Y. J. Electrocatalytic oxidation of urea in alkaline solution using nickel/nickel oxide nanoparticles derived from nickel-organic

framework. *Electrochimica Acta* **258,** 167–174. doi:`10.1016/j.electacta.2017.10.113` (Dec. 2017).

106. Klaus, S., Cai, Y., Louie, M. W., Trotochaud, L. & Bell, A. T. Effects of Fe Electrolyte Impurities on Ni(OH) ₂ /NiOOH Structure and Oxygen Evolution Activity. *The Journal of Physical Chemistry C* **119,** 7243–7254. doi:`10.1021/acs.jpcc.5b00105` (13 Apr. 2015).

107. Son, Y. J., Kawashima, K., Wygant, B. R., Lam, C. H., Burrow, J. N., Celio, H., Dolocan, A., Ekerdt, J. G. & Mullins, C. B. Anodized Nickel Foam for Oxygen Evolution Reaction in Fe-Free and Unpurified Alkaline Electrolytes at High Current Densities. *ACS Nano* **15,** 3468–3480. doi:`10.1021/acsnano.0c10788` (2 Feb. 2021).

108. Márquez, R. A., Kawashima, K., Son, Y. J., Castelino, G., Miller, N., Smith, L. A., Chukwuneke, C. E. & Mullins, C. B. Getting the Basics Right: Preparing Alkaline Electrolytes for Electrochemical Applications. *ACS Energy Letters* **8,** 1141–1146. doi:`10.1021/acsenergylett.2c02847` (2 Feb. 2023).

109. Zemtsova, V. M., Oshchepkov, A. G. & Savinova, E. R. Unveiling the Role of Iron in the Nickel-Catalyzed Urea Oxidation Reaction. *ACS Catalysis* **13,** 13466–13473. doi:`10.1021/acscatal.3c03126` (20 Oct. 2023).

110. Hopsort, G., Carmo, D. P. D., Latapie, L., Loubière, K., Serrano, K. G. & Tzedakis, T. Progress toward a better understanding of the urea oxidation by electromediation of Ni(III)/Ni(II) system in alkaline media. *Electrochimica Acta* **442,** 141898. doi:`10.1016/j.electacta.2023.141898` (Feb. 2023).

111. Hopsort, G., Latapie, L., Serrano, K. G., Loubière, K. & Tzedakis, T. Indirect urea electrooxidation by nickel(III) in alkaline medium: From kinetic and mechanism to reactor modeling. *AIChE Journal.* doi:`10.1002/aic.18113` (May 2023).

112. Lukashuk, L., Yigit, N., Rameshan, R., Kolar, E., Teschner, D., Hävecker, M., Knop-Gericke, A., Schlögl, R., Föttinger, K. & Rupprechter, G. Operando Insights into CO

Oxidation on Cobalt Oxide Catalysts by NAP-XPS, FTIR, and XRD. *ACS Catalysis* **8,** 8630–8641. doi:`10.1021/acscatal.8b01237` (9 Sept. 2018).

113. Jiang, J., Sun, F., Zhou, S., Hu, W., Zhang, H., Dong, J., Jiang, Z., Zhao, J., Li, J., Yan, W. & Wang, M. Atomic-level insight into super-efficient electrocatalytic oxygen evolution on iron and vanadium co-doped nickel (oxy)hydroxide. *Nature Communications* **9.** doi:`10.1038/s41467-018-05341-y` (1 Dec. 2018).

114. Xu, Q., Yu, T., Chen, J., Qian, G., Song, H., Luo, L., Chen, Y., Liu, T., Wang, Y. & Yin, S. Coupling Interface Constructions of $FeNi_3$-MoO_2 Heterostructures for Efficient Urea Oxidation and Hydrogen Evolution Reaction. *ACS Applied Materials & Interfaces* **13,** 16355–16363. doi:`10.1021/acsami.1c01188` (Apr. 2021).

115. Olefjord, I., Brox, B. & Jelvestam, U. Surface Composition of Stainless Steels during Anodic Dissolution and Passivation Studied by ESCA. *Journal of The Electrochemical Society* **132,** 2854–2861. doi:`10.1149/1.2113683` (12 Dec. 1985).

116. Kovendhan, M., Kang, H., Youn, J. S., Cho, H. & Jeon, K. J. Alternative cost-effective electrodes for hydrogen production in saline water condition. *International Journal of Hydrogen Energy,* 5090–5098. doi:`10.1016/j.ijhydene.2018.08.038` (Feb. 2019).

117. Verma, J. & Taiwade, R. V. Effect of welding processes and conditions on the microstructure, mechanical properties and corrosion resistance of duplex stainless steel weldments—A review. *Journal of Manufacturing Processes* **25,** 134–152. doi:`10.1016/j.jmapro.2016.11.003` (Jan. 2017).

118. Jebaraj, A. V., Ajaykumar, L., Deepak, C. R. & Aditya, K. V. Weldability, machinability and surfacing of commercial duplex stainless steel AISI2205 for marine applications – A recent review. *Journal of Advanced Research* **8,** 183–199. doi:`10.1016/j.jare.2017.01.002` (3 May 2017).

119. Jacob, G. Prediction of solidification phases in Cr-Ni stainless steel alloys manufactured by laser based powder bed fusion process. doi:`10.6028/NIST.AMS.100-14` (Mar. 2018).

120. Liu, L., Zhou, Z. & Peng, C. Sonochemical intercalation synthesis of nano γ-nickel oxyhydroxide: Structure and electrochemical properties. *Electrochimica Acta* **54,** 434–441. doi:`10.1016/j.electacta.2008.07.055` (Dec. 2008).

121. Cossar, E., Houache, M. S., Zhang, Z. & Baranova, E. A. Comparison of electrochemical active surface area methods for various nickel nanostructures. *Journal of Electroanalytical Chemistry* **870,** 114246. doi:`10.1016/J.JELECHEM.2020.114246` (Aug. 2020).

122. Alévêque, O. & Levillain, E. A generalized lateral interactions function to fit voltammetric peaks of self-assembled monolayers. *Electrochemistry Communications* **67,** 73–79. doi:`10.1016/j.elecom.2016.04.003` (June 2016).

123. Doyle, R. L. & Lyons, M. E. G. An electrochemical impedance study of the oxygen evolution reaction at hydrous iron oxide in base. *Physical Chemistry Chemical Physics* **15,** 5224. doi:`10.1039/c3cp43464h` (2013).

124. Bard, A. J. & Faulkner, L. R. *Electrochemical Methods: Fundamentals and Applications* (Wiley, 2001).

125. Lazanas, A. C. & Prodromidis, M. I. Electrochemical Impedance Spectroscopy–A Tutorial. *ACS Measurement Science Au.* doi:`10.1021/acsmeasuresciau.2c00070` (Mar. 2023).

126. Danaee, I., Jafarian, M., Forouzandeh, F., Gobal, F. & Mahjani, M. G. Kinetic Interpretation of a Negative Time Constant Impedance of Glucose Electrooxidation. *The Journal of Physical Chemistry B* **112,** 15933–15940. doi:`10.1021/jp8069173` (Dec. 2008).

127. Danaee, I., Jafarian, M., Forouzandeh, F., Gobal, F. & Mahjani, M. Impedance spectroscopy analysis of glucose electro-oxidation on Ni-modified glassy carbon electrode. *Electrochimica Acta* **53,** 6602–6609. doi:`10.1016/j.electacta.2008.04.042` (Sept. 2008).

128. Murbach, M., Gerwe, B., Dawson-Elli, N. & Tsui, L.-k. impedance.py: A Python package for electrochemical impedance analysis. *Journal of Open Source Software* **5,** 2349. doi:`10.21105/joss.02349` (52 Aug. 2020).

129. Moya, A. Identification of characteristic time constants in the initial dynamic response of electric double layer capacitors from high-frequency electrochemical impedance. *Journal of Power Sources* **397,** 124–133. doi:`10.1016/j.jpowsour.2018.07.015` (Sept. 2018).

130. Orazem, M. E. & Tribollet, B. *Electrochemical Impedance Spectroscopy* 2nd ed., 768 (Standards Information Network, 2017).

131. Vernon-Parry, K. Scanning electron microscopy: an introduction. *III-Vs Review* **13,** 40–44. doi:`10.1016/S0961-1290(00)80006-X` (4 July 2000).

132. O'Hanlon, J. F. *A User's Guide to Vacuum Technology* doi:`10.1002/0471467162` (Wiley, June 2003).

133. Bridge, G., Bouzarovski, S., Bradshaw, M. & Eyre, N. Geographies of energy transition: Space, place and the low-carbon economy. *Energy Policy* **53,** 331–340. doi:`10.1016/j.enpol.2012.10.066` (Feb. 2013).

134. Liu, K.-H., Zhong, H.-X., Li, S.-J., Duan, Y.-X., Shi, M.-M., Zhang, X.-B., Yan, J.-M. & Jiang, Q. Advanced catalysts for sustainable hydrogen generation and storage via hydrogen evolution and carbon dioxide/nitrogen reduction reactions. *Progress in Materials Science* **92,** 64–111. doi:`10.1016/j.pmatsci.2017.09.001` (Mar. 2018).

135. Zhang, L.-N., Li, R., Zang, H.-Y., Tan, H.-Q., Kang, Z.-H., Wang, Y.-H. & Li, Y.-G. Advanced hydrogen evolution electrocatalysts promising sustainable hydrogen and chlor-alkali co-production. *Energy & Environmental Science* **14,** 6191–6210. doi:`10.1039/D1EE02798K` (2021).

136. Dutta, S., Han, H., Je, M., Choi, H., Kwon, J., Park, K., Indra, A., Kim, K. M., Paik, U. & Song, T. Chemical and structural engineering of transition metal boride towards excellent and sustainable hydrogen evolution reaction. *Nano Energy* **67,** 104245. doi:`10.1016/j.nanoen.2019.104245` (Jan. 2020).

137. Grimaud, A., Diaz-Morales, O., Han, B., Hong, W. T., Lee, Y.-L., Giordano, L., Stoerzinger, K. A., Koper, M. T. M. & Shao-Horn, Y. Activating lattice oxygen redox reactions in metal oxides to catalyse oxygen evolution. *Nature Chemistry* **9,** 457–465. doi:`10.1038/nchem.2695` (May 2017).

138. Song, J., Wei, C., Huang, Z.-F., Liu, C., Zeng, L., Wang, X. & Xu, Z. J. A review on fundamentals for designing oxygen evolution electrocatalysts. *Chemical Society Reviews* **49,** 2196–2214. doi:`10.1039/C9CS00607A` (2020).

139. Liu, W.-J., Xu, Z., Zhao, D., Pan, X.-Q., Li, H.-C., Hu, X., Fan, Z.-Y., Wang, W.-K., Zhao, G.-H., Jin, S., Huber, G. W. & Yu, H.-Q. Efficient electrochemical production of glucaric acid and H_2 via glucose electrolysis. *Nature Communications* **11,** 265. doi:`10.1038/s41467-019-14157-3` (Jan. 2020).

140. Mlinar, A. N., Keitz, B. K., Gygi, D., Bloch, E. D., Long, J. R. & Bell, A. T. Selective Propene Oligomerization with Nickel(II)-Based Metal–Organic Frameworks. *ACS Catalysis* **4,** 717–721. doi:`10.1021/cs401189a` (Mar. 2014).

141. Angeles-Olvera, Z., Crespo-Yapur, A., Rodríguez, O., Cholula-Díaz, J., Martínez, L. & Videa, M. Nickel-Based Electrocatalysts for Water Electrolysis. *Energies* **15,** 1609. doi:`10.3390/en15051609` (Feb. 2022).

142. McCrory, C. C. L., Jung, S., Peters, J. C. & Jaramillo, T. F. Benchmarking Heterogeneous Electrocatalysts for the Oxygen Evolution Reaction. *Journal of the American Chemical Society* **135,** 16977–16987. doi:`10.1021/ja407115p` (Nov. 2013).

143. Ng, J. W. D., García-Melchor, M., Bajdich, M., Chakthranont, P., Kirk, C., Vojvodic, A. & Jaramillo, T. F. Gold-supported cerium-doped NiO_x catalysts for water oxidation. *Nature Energy* **1,** 16053. doi:`10.1038/nenergy.2016.53` (Apr. 2016).

144. Chen, Z., Cai, L., Yang, X., Kronawitter, C., Guo, L., Shen, S. & Koel, B. E. Reversible Structural Evolution of $NiCoO_xH_y$ during the Oxygen Evolution Reaction and Identification of the Catalytically Active Phase. *ACS Catalysis* **8,** 1238–1247. doi:`10.1021/acscatal.7b03191` (Feb. 2018).

145. Ali-Löytty, H., Louie, M. W., Singh, M. R., Li, L., Sanchez Casalongue, H. G., Ogasawara, H., Crumlin, E. J., Liu, Z., Bell, A. T., Nilsson, A. & Friebel, D. Ambient-Pressure XPS Study of a Ni–Fe Electrocatalyst for the Oxygen Evolution Reaction. *The Journal of Physical Chemistry C* **120,** 2247–2253. doi:`10.1021/acs.jpcc.5b10931` (Feb. 2016).

146. Chakthranont, P., Kibsgaard, J., Gallo, A., Park, J., Mitani, M., Sokaras, D., Kroll, T., Sinclair, R., Mogensen, M. B. & Jaramillo, T. F. Effects of Gold Substrates on the Intrinsic and Extrinsic Activity of High-Loading Nickel-Based Oxyhydroxide Oxygen Evolution Catalysts. *ACS Catalysis* **7,** 5399–5409. doi:`10.1021/acscatal.7b01070` (Aug. 2017).

147. Steimecke, M., Seiffarth, G. & Bron, M. In Situ Characterization of Ni and Ni/Fe Thin Film Electrodes for Oxygen Evolution in Alkaline Media by a Raman-Coupled Scanning Electrochemical Microscope Setup. *Analytical Chemistry* **89,** 10679–10686. doi:`10.1021/acs.analchem.7b01060` (Oct. 2017).

148. Ferreira, E. B. & Jerkiewicz, G. On the Electrochemical Reduction of β-Ni(OH)2 to Metallic Nickel. *Electrocatalysis* **12,** 199–209. doi:`10.1007/s12678-021-00643-0` (2 Mar. 2021).

149. Hahn, F., Floner, D., Beden, B. & Lamy, C. In situ investigation of the behaviour of a nickel electrode in alkaline solution by uv-vis and ir reflectance spectroscopies. *Electrochimica Acta* **32,** 1631–1636. doi:`10.1016/0013-4686(87)90016-8` (11 Nov. 1987).

150. Lyons, M. E. G., Russell, L., O'brien, M., Doyle, R. L., Godwin, I. & Brandon, M. P. *Redox Switching and Oxygen Evolution at Hydrous Oxyhydroxide Modified Nickel Electrodes in Aqueous Alkaline Solution: Effect of Hydrous Oxide Thickness and Base Concentration* 2012.

151. Burke, L. & Twomey, T. Influence of ph on the redox behaviour of hydrous nickel oxide. *Journal of Electroanalytical Chemistry and Interfacial Electrochemistry* **134,** 353–362. doi:`10.1016/0022-0728(82)80013-2` (2 Apr. 1982).

152. Kim, B., Kabiraz, M. K., Lee, J., Choi, C., Baik, H., Jung, Y., Oh, H.-S., Choi, S.-I. & Lee, K. Vertical-crystalline Fe-doped β-Ni oxyhydroxides for highly active and stable oxygen evolution reaction. *Matter* **4,** 3585–3604. doi:`10.1016/j.matt.2021.09.003` (Nov. 2021).

153. Görlin, M., Chernev, P., Ferreira de Araújo, J., Reier, T., Dresp, S., Paul, B., Krähnert, R., Dau, H. & Strasser, P. Oxygen Evolution Reaction Dynamics, Faradaic Charge Efficiency, and the Active Metal Redox States of Ni–Fe Oxide Water Splitting Electrocatalysts. *Journal of the American Chemical Society* **138,** 5603–5614. doi:`10.1021/jacs.6b00332` (May 2016).

154. Singh, D. Characteristics and Effects of γ-NiOOH on Cell Performance and a Method to Quantify It in Nickel Electrodes. *Journal of The Electrochemical Society* **145,** 116–120. doi:`10.1149/1.1838222` (1 Jan. 1998).

155. Godwin, I. & Lyons, M. Enhanced oxygen evolution at hydrous nickel oxide electrodes via electrochemical ageing in alkaline solution. *Electrochemistry Communications* **32,** 39–42. doi:`10.1016/j.elecom.2013.03.040` (July 2013).

156. Rajan, A. G., Martirez, J. M. P. & Carter, E. A. Facet-Independent Oxygen Evolution Activity of Pure β-NiOOH: Different Chemistries Leading to Similar Overpotentials. *Journal of the American Chemical Society* **142,** 3600–3612. doi:`10.1021/jacs.9b13708` (7 Feb. 2020).

157. Li, L.-F., Li, Y.-F. & Liu, Z.-P. Oxygen Evolution Activity on NiOOH Catalysts: Four-Coordinated Ni Cation as the Active Site and the Hydroperoxide Mechanism. *ACS Catalysis* **10,** 2581–2590. doi:`10.1021/acscatal.9b04975` (4 Feb. 2020).

158. Peng, W., Deshmukh, A., Chen, N., Lv, Z., Zhao, S., Li, J., Yan, B., Gao, X., Shang, L., Gong, Y., Wu, L., Chen, M., Zhang, T. & Gou, H. Deciphering the Dynamic Structure Evolution of Fe- and Ni-Codoped CoS ₂ for Enhanced Water Oxidation. *ACS Catalysis* **12,** 3743–3751. doi:`10.1021/acscatal.2c00328` (7 Apr. 2022).

159. Diaz-Morales, O., Ferrus-Suspedra, D. & Koper, M. T. M. The importance of nickel oxyhydroxide deprotonation on its activity towards electrochemical water oxidation. *Chemical Science* **7,** 2639–2645. doi:`10.1039/C5SC04486C` (4 2016).

160. Vedharathinam, V. & Botte, G. G. Understanding the electro-catalytic oxidation mechanism of urea on nickel electrodes in alkaline medium. *Electrochimica Acta* **81,** 292–300. doi:`10.1016/j.electacta.2012.07.007` (Oct. 2012).

161. Jeon, M. K. & McGinn, P. J. Composition dependence of ternary Pt–Ni–Cr catalyst activity for the methanol electro-oxidation reaction. *Journal of Power Sources* **194,** 737–745. doi:`10.1016/j.jpowsour.2009.06.019` (2 Dec. 2009).

162. Candelaria, S. L., Bedford, N. M., Woehl, T. J., Rentz, N. S., Showalter, A. R., Pylypenko, S., Bunker, B. A., Lee, S., Reinhart, B., Ren, Y., Ertem, S. P., Coughlin, E. B., Sather, N. A., Horan, J. L., Herring, A. M. & Greenlee, L. F. Multi-Component Fe–Ni Hydroxide Nanocatalyst for Oxygen Evolution and Methanol Oxidation Reactions under Alkaline Conditions. *ACS Catalysis* **7,** 365–379. doi:`10.1021/acscatal.6b02552` (1 Jan. 2017).

163. Houache, M. S., Cossar, E., Ntais, S. & Baranova, E. A. Electrochemical modification of nickel surfaces for efficient glycerol electrooxidation. *Journal of Power Sources* **375,** 310–319. doi:`10.1016/j.jpowsour.2017.08.089` (Jan. 2018).

164. Pissinis, D., Sereno, L. & Marioli, J. Characterization of glucose electro-oxidation at Ni and Ni–Cr alloy electrodes. *Journal of Electroanalytical Chemistry* **694,** 23–29. doi:`10.1016/j.jelechem.2013.01.040` (Apr. 2013).

165. Gu, Y., Yang, H., Li, B. & An, Y. A ternary nanocatalyst of Ni/Cr/Co oxides with high activity and stability for alkaline glucose electrooxidation. *Electrochimica Acta* **192,** 296–302. doi:`10.1016/j.electacta.2016.01.186` (Feb. 2016).

166. Urbańczyk, E., Sowa, M. & Simka, W. Urea removal from aqueous solutions—a review. *Journal of Applied Electrochemistry* **46,** 1011–1029. doi:`10.1007/s10800-016-0993-6` (Oct. 2016).

167. Schranck, A., Marks, R., Yates, E. & Doudrick, K. Effect of Urine Compounds on the Electrochemical Oxidation of Urea Using a Nickel Cobaltite Catalyst: An Electroanalytical and Spectroscopic Investigation. *Environmental Science & Technology* **52,** 8638–8648. doi:`10.1021/acs.est.8b01743` (15 Aug. 2018).

168. Singh, R. K. & Schechter, A. Electrochemical investigation of urea oxidation reaction on β Ni(OH)2 and Ni/Ni(OH)2. *Electrochimica Acta* **278,** 405–411. doi:`10.1016/j.electacta.2018.05.049` (July 2018).

169. Barakat, N., Abdelkareem, M. A. & Abdelghani, E. Influence of Sn Content, Nanostructural Morphology, and Synthesis Temperature on the Electrochemical Active Area of Ni-Sn/C Nanocomposite: Verification of Methanol and Urea Electrooxidation. *Catalysts* **9,** 330. doi:`10.3390/catal9040330` (4 Apr. 2019).

170. Abdelkareem, M. A., Sayed, E. T., Mohamed, H. O., Obaid, M., Rezk, H. & Chae, K.-J. Nonprecious anodic catalysts for low-molecular-hydrocarbon fuel cells: Theoret-

ical consideration and current progress. *Progress in Energy and Combustion Science* **77,** 100805. doi:`10.1016/j.pecs.2019.100805` (Mar. 2020).

171. Marino, M., Misuri, L. & Brogioli, D. A new open source software for the calculation of the liquid junction potential between two solutions according to the stationary Nernst-Planck equation. doi:`10.48550/arXiv.1403.3640` (Mar. 2014).

172. Kawashima, K., Márquez, R. A., Son, Y. J., Guo, C., Vaidyula, R. R., Smith, L. A., Chukwuneke, C. E. & Mullins, C. B. Accurate Potentials of Hg/HgO Electrodes: Practical Parameters for Reporting Alkaline Water Electrolysis Overpotentials. *ACS Catalysis* **13,** 1893–1898. doi:`10.1021/acscatal.2c05655` (3 Feb. 2023).

173. Luba, M., Mikołajczyk, T., Kuczyński, M., Pierożyński, B. & Kowalski, I. M. Enhancing the Effectiveness of Oxygen Evolution Reaction by Electrodeposition of Transition Metal Nanoparticles on Nickel Foam Material. *Catalysts* **11,** 468. doi:`10.3390/catal11040468` (4 Apr. 2021).

174. Garcia, A. C., Touzalin, T., Nieuwland, C., Perini, N. & Koper, M. T. M. Enhancement of Oxygen Evolution Activity of Nickel Oxyhydroxide by Electrolyte Alkali Cations. *Angewandte Chemie International Edition* **58,** 12999–13003. doi:`10.1002/anie.201905501` (37 Sept. 2019).

175. Dionigi, F., Zhu, J., Zeng, Z., Merzdorf, T., Sarodnik, H., Gliech, M., Pan, L., Li, W. X., Greeley, J. & Strasser, P. Intrinsic Electrocatalytic Activity for Oxygen Evolution of Crystalline 3d-Transition Metal Layered Double Hydroxides. *Angewandte Chemie International Edition* **60,** 14446–14457. doi:`10.1002/anie.202100631` (26 Sept. 2021).

176. Lee, S. B., Yoon, D. Y., Hwang, N. M. & Henry, M. F. Grain boundary faceting and abnormal grain growth in nickel. *Metallurgical and Materials Transactions A* **31,** 985–994. doi:`10.1007/s11661-000-0040-3` (Mar. 2000).

177. Randle, V. & Horton, D. Grain growth phenomena in nickel. *Scripta Metallurgica et Materialia* **31,** 891–895. doi:`10.1016/0956-716X(94)90498-7` (Oct. 1994).

178. Alsabet, M., Grden, M. & Jerkiewicz, G. Electrochemical Growth of Surface Oxides on Nickel. Part 1: Formation of α-Ni(OH)$_2$ in Relation to the Polarization Potential, Polarization Time, and Temperature. *Electrocatalysis* **2,** 317–330. doi:`10.1007/s12678-011-0067-9` (Dec. 2011).

179. Esau, D., Schuett, F. M., Varvaris, K. L., Björk, J., Jacob, T. & Jerkiewicz, G. Controlled-Atmosphere Flame Fusion Growth of Nickel Poly-oriented Spherical Single Crystals—Unraveling Decades of Impossibility. *Electrocatalysis* **11,** 1–13. doi:`10.1007/s12678-019-00575-w` (Jan. 2020).

180. MacDougall, B. & Cohen, M. Anodic Oxidation of Nickel in Neutral Sulfate Solution. *Journal of The Electrochemical Society* **121,** 1152. doi:`10.1149/1.2402003` (1974).

181. Streinz, C. C., Hartman, A. P., Motupally, S. & Weidner, J. W. The Effect of Current and Nickel Nitrate Concentration on the Deposition of Nickel Hydroxide Films. *Journal of The Electrochemical Society* **142,** 1084–1089. doi:`10.1149/1.2044134` (Apr. 1995).

182. Delmas, C., Faure, C. & Borthomieu, Y. The effect of cobalt on the chemical and electrochemical behaviour of the nickel hydroxide electrode. *Materials Science and Engineering: B* **13,** 89–96. doi:`10.1016/0921-5107(92)90147-2` (Mar. 1992).

183. Pandya, K. I., O'Grady, W. E., Corrigan, D. A., McBreen, J. & Hoffman, R. W. Extended X-Ray Absorption Fine Structure Investigations Of Nickel Hydroxides. *The Journal of Physical Chemistry* **94,** 21–26. doi:`10.1021/j100364a005` (Jan. 1990).

184. Lian, K. K., Kirk, D. W. & Thorpe, S. J. Investigation of a "Two State" Tafel Phenomenon for the Oxygen Evolution Reaction on an Amorphous Ni-Co Alloy. *Journal of The Electrochemical Society* **142,** 3704–3712. doi:`10.1149/1.2048402` (Nov. 1995).

185. Arulmozhi, N., Esau, D., Lamsal, R. P., Beauchemin, D. & Jerkiewicz, G. Structural Transformation of Monocrystalline Platinum Electrodes upon Electro-oxidation and Electro-dissolution. *ACS Catalysis* **8,** 6426–6439. doi:`10.1021/acscatal.8b00319` (July 2018).

186. Jacobse, L., Vonk, V., McCrum, I. T., Seitz, C., Koper, M. T., Rost, M. J. & Stierle, A. Electrochemical oxidation of Pt(111) beyond the place-exchange model. *Electrochimica Acta* **407,** 139881. doi:`10.1016/j.electacta.2022.139881` (Mar. 2022).

187. Lyons, M. & Brandon, M. The Oxygen Evolution Reaction on Passive Oxide Covered Transition Metal Electrodes in Aqueous Alkaline Solution. Part 1-Nickel. *Int. J. Electrochem. Sci. International Journal* **3,** 1386–1424 (Mar. 2008).

188. Shinagawa, T., Garcia-Esparza, A. T. & Takanabe, K. Insight on Tafel slopes from a microkinetic analysis of aqueous electrocatalysis for energy conversion. *Scientific Reports* **5.** doi:`https://doi.org/10.1038/srep13801` (Sept. 2015).

189. McCrory, C. C. L., Jung, S., Ferrer, I. M., Chatman, S. M., Peters, J. C. & Jaramillo, T. F. Benchmarking Hydrogen Evolving Reaction and Oxygen Evolving Reaction Electrocatalysts for Solar Water Splitting Devices. *Journal of the American Chemical Society* **137,** 4347–4357. doi:`10.1021/ja510442p` (Apr. 2015).

190. Chulkin, P. & Data, P. Electrochemical Impedance Spectroscopy as a Tool for Electrochemical Rate Constant Estimation. *Journal of Visualized Experiments.* doi:`10.3791/56611` (Oct. 2018).

191. Anantharaj, S., Karthik, P. E. & Noda, S. The Significance of Properly Reporting Turnover Frequency in Electrocatalysis Research. *Angewandte Chemie International Edition* **60,** 23051–23067. doi:`10.1002/anie.202110352` (Oct. 2021).

192. Lin, Z., Bu, P., Xiao, Y., Gao, Q. & Diao, P. β- and γ-NiFeOOH electrocatalysts for an efficient oxygen evolution reaction: an electrochemical activation energy aspect.

Journal of Materials Chemistry A **10,** 20847–20855. doi:`10.1039/D2TA04688A` (39 2022).

193. Straumal, B. B., Kogtenkova, O. A., Gornakova, A. S., Sursaeva, V. G. & Baretzky, B. Review: grain boundary faceting–roughening phenomena. *Journal of Materials Science* **51,** 382–404. doi:`10.1007/s10853-015-9341-1` (Jan. 2016).

194. Huang, L.-F., Hutchison, M. J., Santucci, R. J., Scully, J. R. & Rondinelli, J. M. Improved Electrochemical Phase Diagrams from Theory and Experiment: The Ni–Water System and Its Complex Compounds. *The Journal of Physical Chemistry C* **121,** 9782–9789. doi:`10.1021/acs.jpcc.7b02771` (May 2017).

195. Köster, K., Wendt, H., Gallus, J., Krisam, G. & Lehmann, H. D. Regeneration of Hemofiltrate by Anodic Oxidation of Urea. *Artificial Organs* **7,** 163–168. doi:`10.1111/j.1525-1594.1983.tb04182.x` (May 1983).

196. King, R. L. & Botte, G. G. Investigation of multi-metal catalysts for stable hydrogen production via urea electrolysis. *Journal of Power Sources* **196,** 9579–9584. doi:`10.1016/j.jpowsour.2011.06.079` (Nov. 2011).

197. Yang, S. B., Tsai, Y. C. & Wu, M. S. Honeycomb-like copper/cuprous oxide with supported nickel hydroxide layer as an electrode material for electrochemical oxidation of urea. *Journal of Alloys and Compounds* **836,** 155533. doi:`10.1016/J.JALLCOM.2020.155533` (Sept. 2020).

198. Klapper, H. S., Zadorozne, N. S. & Rebak, R. B. Localized Corrosion Characteristics of Nickel Alloys: A Review. *Acta Metallurgica Sinica (English Letters)* **30,** 296–305. doi:`10.1007/s40195-017-0553-z` (Apr. 2017).

199. Guo, S., Xu, D., Jiang, G. & Kuang, W. Corrosion behavior and mechanism of Ni-based alloys Hastelloy C2000 and Inconel 740 in chloride-containing supercritical water oxidation. *Journal of Alloys and Compounds* **907,** 164452. doi:`10.1016/j.jallcom.2022.164452` (June 2022).

200. Gietzelt, T., Walter, M., Toth, V., Messerschmidt, F. & Dahm, R. Highly Molybdenum-Alloyed Materials Hastelloy BC-1 (2.4708) and B3 (2.4600): Diffusion Bonding Experiments and Evaluation of both Mechanical Behavior and Corrosion Resistance in Hot 70% Sulfuric Acid. *Metals* **10,** 376. doi:`10.3390/met10030376` (Mar. 2020).

201. Al-Malahy, K. S. & Hodgkiess, T. Comparative studies of the seawater corrosion behaviour of a range of materials. *Desalination* **158,** 35–42. doi:`10.1016/S0011-9164(03)00430-2` (Aug. 2003).

202. Xue, S., Liang, Y., Hou, S., Zhang, Y. & Jiang, H. Alpha-Nickel Hydroxide Coating of Metallic Nickel for Enhanced Alkaline Hydrogen Evolution. *ChemSusChem* **15.** doi:`10.1002/cssc.202201072` (18 Sept. 2022).

203. Radha, A. V., Weiß, S., Sanjuán, I., Ertl, M., Andronescu, C. & Breu, J. The Effect of Interlayer Anion Grafting on Water Oxidation Electrocatalysis: A Comparative Study of Ni- and Co-Based Brucite-Type Layered Hydroxides, Layered Double Hydroxides and Hydroxynitrate Salts. *Chemistry – A European Journal* **27,** 16930–16937. doi:`10.1002/chem.202100452` (68 Dec. 2021).

204. Barakat, N. A., Yassin, M. A., Al-Mubaddel, F. S. & Amen, M. T. New electrooxidation characteristic for Ni-based electrodes for wide application in methanol fuel cells. *Applied Catalysis A: General* **555,** 148–154. doi:`10.1016/j.apcata.2018.02.016` (Apr. 2018).

205. Hall, D. S., Bock, C. & MacDougall, B. R. An Oxalate Method for Measuring the Surface Area of Nickel Electrodes. *Journal of The Electrochemical Society* **161,** H787–H795. doi:`10.1149/2.0711412jes` (12 2014).

206. Dionigi, F., Weber, C. C., Primbs, M., Gocyla, M., Bonastre, A. M., Spöri, C., Schmies, H., Hornberger, E., Kühl, S., Drnec, J., Heggen, M., Sharman, J., Dunin-Borkowski, R. E. & Strasser, P. Controlling Near-Surface Ni Composition in Octahedral PtNi(Mo)

Nanoparticles by Mo Doping for a Highly Active Oxygen Reduction Reaction Catalyst. *Nano Letters* **19,** 6876–6885. doi:`10.1021/acs.nanolett.9b02116` (10 Oct. 2019).

207. Wang, X.-x., Fu, H., Du, D.-m., Zhou, Z.-y., Zhang, A.-g., Su, C.-f. & Ma, K.-s. The comparison of pKa determination between carbonic acid and formic acid and its application to prediction of the hydration numbers. *Chemical Physics Letters* **460,** 339–342. doi:`10.1016/j.cplett.2008.05.074` (July 2008).

208. Mohammadian, E., Hadavimoghaddam, F., Kheirollahi, M., Jafari, M., Chenlu, X. & Liu, B. Probing Solubility and pH of CO2 in aqueous solutions: Implications for CO2 injection into oceans. *Journal of CO2 Utilization* **71,** 102463. doi:`10.1016/j.jcou.2023.102463` (May 2023).

209. Simpraga, R. & Conway, B. Irreversibility in formation of nominal monolayer and sub-monolayer levels of surface oxide attained at Fe at low temperatures. *Journal of Electroanalytical Chemistry and Interfacial Electrochemistry* **313,** 161–179. doi:`10.1016/0022-0728(91)85178-R` (1-2 Sept. 1991).

210. Alsabet, M., Grden, M. & Jerkiewicz, G. Electrochemical Growth of Surface Oxides on Nickel. Part 2: Formation of β-Ni(OH)2 and NiO in Relation to the Polarization Potential, Polarization Time, and Temperature. *Electrocatalysis* **5,** 136–147. doi:`10.1007/s12678-013-0172-z` (2 Apr. 2014).

211. Hall, D. S., Bock, C. & MacDougall, B. R. Surface Layers in Alkaline Media: Nickel Hydrides on Metallic Nickel Electrodes. *ECS Transactions* **50,** 165–179. doi:`10.1149/05031.0165ecst` (31 May 2013).

212. Miao, Y., Ouyang, L., Zhou, S., Xu, L., Yang, Z., Xiao, M. & Ouyang, R. Electrocatalysis and electroanalysis of nickel, its oxides, hydroxides and oxyhydroxides toward small molecules. *Biosensors and Bioelectronics* **53,** 428–439. doi:`10.1016/j.bios.2013.10.008` (Mar. 2014).

213. Kashale, A. A., Ghule, A. V. & Chen, I.-W. P. Active Edge Site Exposed β-Ni(OH) ₂ Nanosheets on Stainless Steel Mesh as a Versatile Electrocatalyst for the Oxidation of Urea, Hydrazine, and Water. *ChemCatChem* **13,** 1165–1174. doi:10.1002/cctc.202001528 (4 Feb. 2021).

214. Marioli, J. M. & Sereno, L. E. The potentiodynamic behavior of nickel-chromium (80:20) alloy electrodes in 0.10 N sodium hydroxide. *Electrochimica Acta* **40,** 983–989. doi:10.1016/0013-4686(94)00362-5 (8 June 1995).

215. Kim, M.-S. & Kim, K.-B. A Study on the Phase Transformation of Electrochemically Precipitated Nickel Hydroxides Using an Electrochemical Quartz Crystal Microbalance. *Journal of The Electrochemical Society* **145,** 507–511. doi:10.1149/1.1838294 (2 Feb. 1998).

216. Peng, J., Lin, L., Chen, X., Wan, R., Fu, L., Shan, A. & Chen, L. Fabrication of electrocatalytic anode by surface treatment of 4J40 INVAR alloy for feasible water splitting. *International Journal of Hydrogen Energy* **48,** 8909–8920. doi:10.1016/j.ijhydene.2022.12.066 (24 Mar. 2023).

217. Sing, R., Pandey, J. & Anitha, K. Preparation of electrodeposited thin films of nickel-iron alloys on mild steel for alkaline water electrolysis. Part I: studies on oxygen evolution. *International Journal of Hydrogen Energy* **18,** 467–473. doi:10.1016/0360-3199(93)90002-R (6 June 1993).

218. Potvin, E. & Brossard, L. Electrocatalytic activity of Ni-Fe anodes for alkaline water electrolysis. *Materials Chemistry and Physics* **31,** 311–318. doi:10.1016/0254-0584(92)90192-B (4 June 1992).

219. Louie, M. W. & Bell, A. T. An Investigation of Thin-Film Ni–Fe Oxide Catalysts for the Electrochemical Evolution of Oxygen. *Journal of the American Chemical Society* **135,** 12329–12337. doi:10.1021/ja405351s (33 Aug. 2013).

220. Wang, P., Bai, X., Jin, H., Gao, X., Davey, K., Zheng, Y., Jiao, Y. & Qiao, S.-Z. Directed Urea-to-Nitrite Electrooxidation via Tuning Intermediate Adsorption on Co, Ge Co-Doped Ni Sites. *Advanced Functional Materials* **33.** doi:`10.1002/adfm.202300687` (25 June 2023).

221. Voorhoeve, R. J. H., Trimble, L. E. & Freed, D. J. Synthesis of Ammonium Cyanate and Urea by Reduction of Nitric Oxide on Platinum, Rhodium, and Ruthenium Catalysts. *Science* **200,** 759–761. doi:`10.1126/science.200.4343.759` (May 1978).

222. Petrii, O. A. & Ya Vassina, S. Adsorption of urea on platinum at low positive potentials: the time dependence and unexpectedly strong effect on the oxidation of unicarbon particles. *Z Electroanal. Chem* **349,** 197–209. doi:`10.1016/0022-0728(93)80173-F` (1993).

223. Mishra, A., Ramamurthy, S., Biesinger, M. & Shoesmith, D. The activation/depassivation of nickel–chromium–molybdenum alloys in bicarbonate solution: Part I. *Electrochimica Acta* **100,** 118–124. doi:`10.1016/j.electacta.2013.03.161` (June 2013).

224. Henderson, J., Ebrahimi, N., Dehnavi, V., Guo, M., Shoesmith, D. & Noël, J. The role of internal cathodic support during the crevice corrosion of Ni-Cr-Mo alloys. *Electrochimica Acta* **283,** 1600–1608. doi:`10.1016/j.electacta.2018.07.048` (Sept. 2018).

225. Wang, J., Mo, F., Fei, J., Ling, W., Cui, M., Lei, H., Jiang, L. & Huang, Y. Insights into the synergistic effect between nickel and molybdenum for catalyzing urea electrooxidation. *Carbon Neutralization* **1,** 267–276. doi:`10.1002/cnl2.27` (Dec. 2022).

226. Wester, M., Simonis, F., Lachkar, N., Wodzig, W. K., Meuwissen, F. J., Kooman, J. P., Boer, W. H., Joles, J. A. & Gerritsen, K. G. Removal of Urea in a Wearable Dialysis Device: A Reappraisal of Electro-Oxidation. *Artificial Organs* **38,** 998–1006. doi:`10.1111/aor.12309` (Dec. 2014).

227. Wester, M., van Gelder, M. K., Joles, J. A., Simonis, F., Hazenbrink, D. H. M., van Berkel, T. W. M., Vaessen, K. R. D., Boer, W. H., Verhaar, M. C. & Gerritsen, K. G. F. Removal of urea by electro-oxidation in a miniature dialysis device: a study in awake goats. *American Journal of Physiology-Renal Physiology* **315,** F1385–F1397. doi:`10.1152/ajprenal.00094.2018` (Nov. 2018).

228. Groth, T., Stegmayr, B. G., Ash, S. R., Kuchinka, J., Wieringa, F. P., Fissell, W. H. & Roy, S. Wearable and implantable artificial kidney devices for end-stage kidney disease treatment: Current status and review. *Artificial Organs* **47,** 649–666. doi:`10.1111/aor.14396` (Apr. 2023).

229. Hoenich, N. A. & Ronco, C. Haemodialysis Fluid: Composition and Clinical Importance. *Blood Purification* **25,** 62–68. doi:`10.1159/000096400` (2007).

230. Volkovich, V. A., Ivanov, A. B., Kamalov, R. V., Maltsev, D. S., Vasin, B. D. & Griffiths, T. R. Electrode and Redox Potentials of Molybdenum and Stability of Molybdenum Chloro-Species in Alkali Chloride Melts. *Journal of The Electrochemical Society* **164,** H5336–H5344. doi:`10.1149/2.0511708jes` (8 July 2017).

231. Safeer N. K., M., Alex, C., Jana, R., Datta, A. & John, N. S. Remarkable CO_x tolerance of Ni^{3+} active species in a Ni_2O_3 catalyst for sustained electrochemical urea oxidation. *Journal of Materials Chemistry A* **10,** 4209–4221. doi:`10.1039/D1TA05753G` (2022).

232. Alex, C., Shukla, G. & John, N. S. Introduction of surface defects in NiO with effective removal of adsorbed catalyst poisons for improved electrochemical urea oxidation. *Electrochimica Acta* **385,** 138425. doi:`10.1016/j.electacta.2021.138425` (July 2021).

233. Kerner, Z. & Pajkossy, T. On the origin of capacitance dispersion of rough electrodes. *Electrochimica Acta* **46,** 207–211. doi:`10.1016/S0013-4686(00)00574-0` (Nov. 2000).

234. Lozano-Castelló, D., Cazorla-Amorós, D., Linares-Solano, A., Shiraishi, S., Kurihara, H. & Oya, A. Influence of pore structure and surface chemistry on electric double layer

capacitance in non-aqueous electrolyte. *Carbon* **41,** 1765–1775. doi:`10.1016/S0008-6223(03)00141-6` (2003).

235. Magnani, S. & Atti, M. Uremic Toxins and Blood Purification: A Review of Current Evidence and Future Perspectives. *Toxins* **13,** 246. doi:`10.3390/toxins13040246` (Mar. 2021).

236. Van Gelder, M. K., Jong, J. A., Folkertsma, L., Guo, Y., Blüchel, C., Verhaar, M. C., Odijk, M., Van Nostrum, C. F., Hennink, W. E. & Gerritsen, K. G. Urea removal strategies for dialysate regeneration in a wearable artificial kidney. *Biomaterials* **234,** 119735. doi:`10.1016/j.biomaterials.2019.119735` (Mar. 2020).

237. Grinval'd, V. M., Leshchinskii, G. M., Rodin, V. V., Strelkov, S. I. & Yakovleva, A. A. Development and Testing of a Unit for Electrochemical Oxidation of Products of Hemodialysis. *Biomedical Engineering* **37,** 67–72. doi:`10.1023/A:1024727513884` (2003).

238. Hintzen, K., Stiller, S., Brunner, H., Rautenbach, R. & Mann, H. Electrodialysis and Reverse Osmosis as a Regeneration System for Hemofiltrate. *Artificial Organs* **7,** 169–175. doi:`10.1111/j.1525-1594.1983.tb04183.x` (May 1983).

239. Fels, M. Recycle of dialysate from the artificial kidney by electrochemical degradatian of waste metabolites: Small-scale laboratory investigations. *Medical & Biological Engineering & Computing* **16,** 25–30. doi:`10.1007/BF02442928` (Jan. 1978).

240. Fels, M. Recycle of dialysate from the artificial kidney by electrochemical degradation of waste metabolites: Continuous reactor investigations. *Medical & Biological Engineering & Computing* **20,** 257–263. doi:`10.1007/BF02442789` (May 1982).

241. Neth, M. R., Love, J. S., Horowitz, B. Z., Shertz, M. D., Sahni, R. & Daya, M. R. Fatal Sodium Nitrite Poisoning: Key Considerations for Prehospital Providers. *Prehospital Emergency Care* **25,** 844–850. doi:`10.1080/10903127.2020.1838009` (Nov. 2021).

242. Conrad, H., Corbett, J. & Golden, T. D. Electrochemical Deposition of γ-Phase Zinc-Nickel Alloys from Alkaline Solution. *ECS Transactions* **33,** 85–95. doi:`10.1149/1.3566091` (Mar. 2011).

243. Goswami, A., Ghosh, D., Pradhan, D. & Biradha, K. In Situ Grown Mn(II) MOF upon Nickel Foam Acts as a Robust Self-Supporting Bifunctional Electrode for Overall Water Splitting: A Bimetallic Synergistic Collaboration Strategy. *ACS Applied Materials & Interfaces* **14,** 29722–29734. doi:`10.1021/acsami.2c04304` (July 2022).

244. Xu, D., Stevens, M. B., Rui, Y., DeLuca, G., Boettcher, S. W., Reichmanis, E., Li, Y., Zhang, Q. & Wang, H. The role of Cr doping in Ni Fe oxide/(oxy)hydroxide electrocatalysts for oxygen evolution. *Electrochimica Acta* **265,** 10–18. doi:`10.1016/j.electacta.2018.01.143` (Mar. 2018).

245. Feng, K., Tian, J., Guo, M., Wang, Y., Wang, S., Wu, Z., Zhang, J., He, L. & Yan, B. Experimentally unveiling the origin of tunable selectivity for CO_2 hydrogenation over Ni-based catalysts. *Applied Catalysis B: Environmental* **292,** 120191. doi:`10.1016/j.apcatb.2021.120191` (Sept. 2021).

246. Yan, X., Zhang, W.-D., Xu, H., Xiang, L., Liu, J., Yang, J., Zhu, H. & Gu, Z.-G. Hierarchical NiCr hydroxide nanospheres with tunable domain boundaries for highly efficient urea electro-oxidation. *Electrochimica Acta* **388,** 138633. doi:`10.1016/j.electacta.2021.138633` (Aug. 2021).

247. Periyasamy, S., Subramanian, P., Levi, E., Aurbach, D., Gedanken, A. & Schechter, A. Exceptionally Active and Stable Spinel Nickel Manganese Oxide Electrocatalysts for Urea Oxidation Reaction. *ACS Applied Materials & Interfaces* **8,** 12176–12185. doi:`10.1021/acsami.6b02491` (19 May 2016).

248. Annan, K. Mathematical modeling of the dynamic exchange of solutes during bicarbonate dialysis. *Mathematical and Computer Modelling* **55,** 1691–1704. doi:`10.1016/j.mcm.2011.11.013` (5-6 Mar. 2012).

249. Yaqoob, T., Ahsan, M., Farrukh, S. & Ahmad, I. Design and Development of a Computational Tool for a Dialyzer by Using Computational Fluid Dynamic (CFD) Model. *Membranes* **11,** 916. doi:`10.3390/membranes11120916` (12 Nov. 2021).

250. Gheriany, I. E., Abdel-Aziz, M. H., El-Ashtoukhy, E.-S. Z. & Sedahmed, G. H. Electrochemical removal of urea from wastewater by anodic oxidation using a new cell design: An experimental and modeling study. *Process Safety and Environmental Protection* **159,** 133–145. doi:`10.1016/j.psep.2021.12.055` (Mar. 2022).

251. Macdougall, I. C. Supplemental iron via dialysate: a novel mode of delivery for hemodialysis patients. *Kidney International* **88,** 946–949. doi:`10.1038/ki.2015.260` (5 Nov. 2015).

252. Tang, Y., Liu, Y., Yu, S., Zhao, Y., Mu, S. & Gao, F. Hydrothermal synthesis of a flower-like nano-nickel hydroxide for high performance supercapacitors. *Electrochimica Acta* **123,** 158–166. doi:`10.1016/j.electacta.2013.12.187` (Mar. 2014).

253. Ouseph, R. & Ward, R. A. Increasing Dialysate Flow Rate Increases Dialyzer Urea Mass Transfer-Area Coefficients During Clinical Use. *American Journal of Kidney Diseases* **37,** 316–320. doi:`10.1053/ajkd.2001.21296` (Feb. 2001).

254. Gostoli, C. & Gatta, A. Mass transfer in a hollow fiber dialyzer. *Journal of Membrane Science* **6,** 133–148. doi:`10.1016/S0376-7388(00)82156-0` (Jan. 1980).

255. Locatelli, F., Altieri, P., Andrulli, S., Bolasco, P., Sau, G., Pedrini, L. A., Basile, C., David, S., Feriani, M., Montagna, G., Di Iorio, B. R., Memoli, B., Cravero, R., Battaglia, G. & Zoccali, C. Hemofiltration and Hemodiafiltration Reduce Intradialytic Hypotension in ESRD. *Journal of the American Society of Nephrology* **21,** 1798–1807. doi:`10.1681/ASN.2010030280` (Oct. 2010).

256. Kirsch, A. H., Lyko, R., Nilsson, L.-G., Beck, W., Amdahl, M., Lechner, P., Schneider, A., Wanner, C., Rosenkranz, A. R. & Krieter, D. H. Performance of hemodialysis

with novel medium cut-off dialyzers. *Nephrology Dialysis Transplantation,* gfw310. doi:`10.1093/ndt/gfw310` (Sept. 2016).

257. Leypoldt, J. K., Cheung, A. K., Agodoa, L. Y., Daugirdas, J. T., Greene, T., Keshaviah, P. R. & Beck, G. J. Hemodialyzer mass transfer-area coefficients for urea increase at high dialysate flow rates. *Kidney International* **51,** 2013–2017. doi:`10.1038/ki.1997.274` (June 1997).

258. Benziger, J., Chia, E., Karnas, E., Moxley, J., Teuscher, C. & Kevrekidis, I. G. The stirred tank reactor polymer electrolyte membrane fuel cell. *AIChE Journal* **50,** 1889–1900. doi:`10.1002/aic.10158` (Aug. 2004).

259. Small, L. J., Pratt, H. D. & Anderson, T. M. Crossover in Membranes for Aqueous Soluble Organic Redox Flow Batteries. *Journal of The Electrochemical Society* **166,** A2536–A2542. doi:`10.1149/2.0681912jes` (July 2019).

260. Rommerskirchen, A., Roth, H., Linnartz, C. J., Egidi, F., Kneppeck, C., Roghmans, F. & Wessling, M. Mitigating Water Crossover by Crosslinked Coating of Cation-Exchange Membranes for Brine Concentration. *Advanced Materials Technologies* **6,** 2100202. doi:`10.1002/admt.202100202` (Oct. 2021).

261. Eriksson, B., Grimler, H., Carlson, A., Ekström, H., Wreland Lindström, R., Lindbergh, G. & Lagergren, C. Quantifying water transport in anion exchange membrane fuel cells. *International Journal of Hydrogen Energy* **44,** 4930–4939. doi:`10.1016/j.ijhydene.2018.12.185` (Feb. 2019).

262. Goldstein, S. L., Allsteadt, A., Beck, W. & Nilsson, L.-G. Evaluation of the Polyflux® 6H Dialyzer in Pediatric Patients Receiving Maintenance Hemodialysis. *The International Journal of Artificial Organs* **30,** 321–324. doi:`10.1177/039139880703000407` (Apr. 2007).

263. Al-Biltagi, M., Tolba, O. A., ElHafez, M. A. A., Abo-Elezz, A. A. E., EL Kady, E. K. & Hazza, S. M. E.-d. Oxidative stress and cardiac dysfunction in children with

chronic renal failure on regular hemodialysis. *Pediatric Nephrology* **31,** 1329–1339. doi:`10.1007/s00467-016-3314-8` (Aug. 2016).

264. Soo, E. & Schaefer, F. in *Handbook of Dialysis Therapy* 948–954 (Elsevier, 2017). doi:`10.1016/B978-0-323-39154-2.00082-5`.

265. Jadhav, R. G. & Das, A. K. Pulse electrodeposited, morphology controlled organic–inorganic nanohybrids as bifunctional electrocatalysts for urea oxidation. *Nanoscale* **12,** 23596–23606. doi:`10.1039/D0NR07236B` (2020).

266. Anuratha, K. S., Rinawati, M., Wu, T.-H., Yeh, M.-H. & Lin, J.-Y. Recent Development of Nickel-Based Electrocatalysts for Urea Electrolysis in Alkaline Solution. *Nanomaterials* **12,** 2970. doi:`10.3390/nano12172970` (Aug. 2022).

Chapter 9

APPENDIX A: PROCEDURES

9.1 Polishing Procedure

Table 9.1 Planar Nickel Polishing Procedure

Surface [Wheel Type]	Abrasive [Grit type]	Speed [RPM]	Rotation [Direction]	Time [Min: Sec]
Carbimet	240 grit SiC water cooled	150	Against Spin	2:00
Carbimet	600 grit SiC water cooled	150	Against Spin	1:00
UltrPad	9 µm MetaDi Supreme Diamond	150	Against Spin	1:00
UltraPad	3 µm MetaDi Supreme Diamond	150	Against Spin	1:00
TriDent	1 µm MetaDi Supreme Diamond	150	Against Spin	1:00

9.2 Iron Purification Procedure

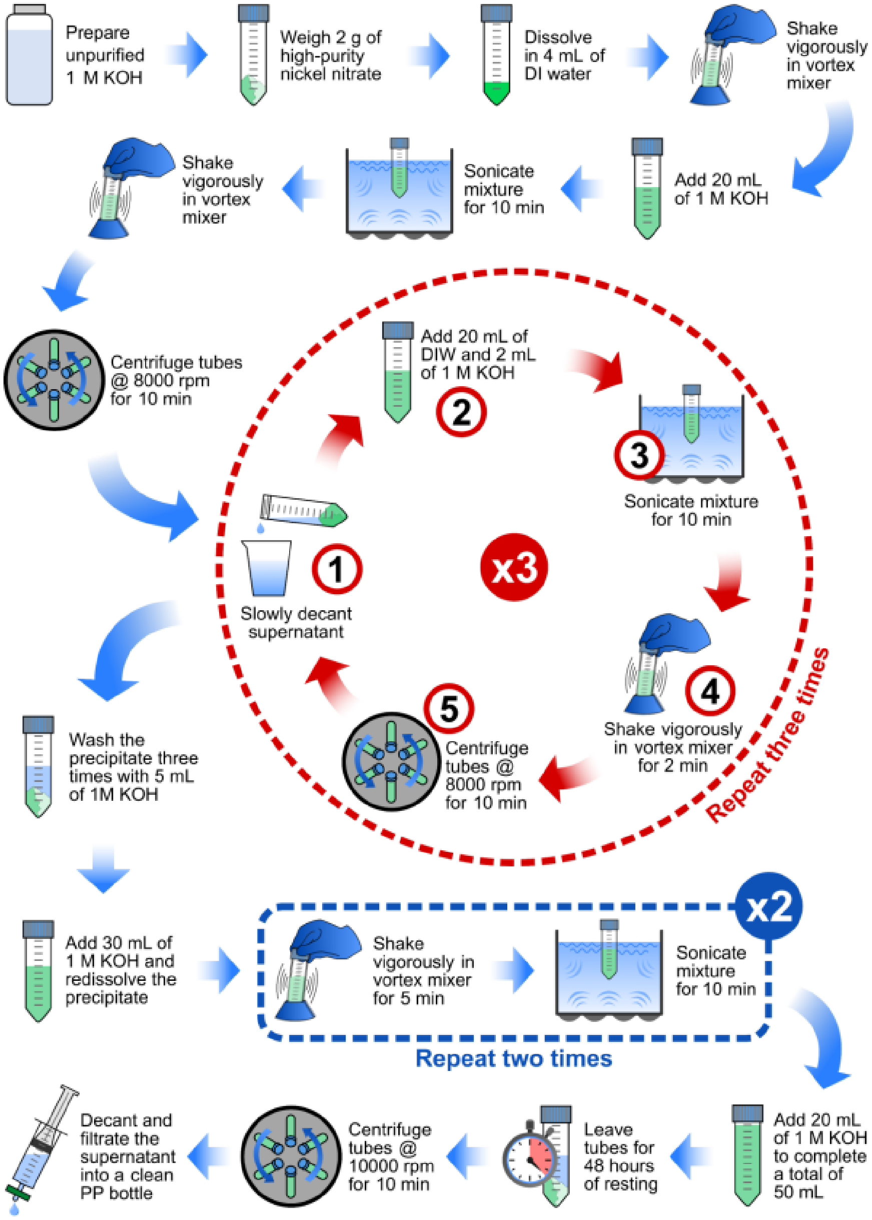

Fig. 9.1 Suggested workflow for alkaline electrolyte purification. Reprinted with permission from Márquez *et al.*[108] Copyright 2023 American Chemical Society.

9.3 Reference Electrode Calibration Procedure

To calibrate the reference electrode, two platinum wires were used as the working (anode) and counter (cathode) electrodes. A linear sweep voltammogram was conducted with ± 50 mV above and below the expected reversible hydrogen electrode for the respective electrolyte. For example, a Hg/HgO reference electrode was calibrated in a 0.5 M KOH solution, where the expected potential is 0.931 V_{RHE} using Eq. 4.1. The LSV is seen below, where the current crossed over at 0.915 V. The reference electrode measurements are then adjusted to include the 0.016 V difference.

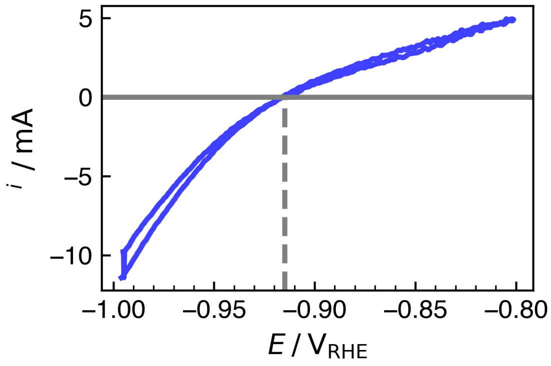

Fig. 9.2 Reference electrode calibration curve conducted at 1 mV s^{-1}.

9.4 Chemical Inventory

Table 9.2 Product specifications of KOH pellets used to make 0.5 M KOH electrolyte. Product obtained from Fisher Scientific LOT 221848.

Chemical	Amount
Assay	85.0% Minimum
Calcium (Ca)	0.005% Maximum
Chloride	0.01% Maximum
Heavy Metals by ICP-OES	0.001% Maximum
Iron (Fe)	0.001% Maximum
Magnesium (Mg)	0.002 % Maximum
Nickel (Ni)	0.001% Maximum
Nitrogen Compounds	0.001% Maximum
Phosphate (PO_4)	5 PPM Maximum
Potassium Carbonate	2.0% Maximum
Sodium (Na)	0.05% Maximum
Sulfate (SO_4)	0.003% Maximum

Table 9.3 Product specifications of urea pellets used to make 0.2 M urea electrolyte. Product obtained from Fisher Scientific LOT 191287.

Chemical	Amount
Assay	99.6%
Chloride	< 5 PPM
Ignition Residue	< 0.003%
Heavy Metals by ICP-OES	0.001% Maximum
Iron (Fe)	0.001% Maximum
Sulfate (SO_4)	0.001% Maximum

Table 9.4 Product specifications of H_2SO_4 used for glass cleaning. Product obtained from Mallinckrodt Chemicals LOT K02037.

Chemical	Amount
Assay	95.0% Minimum
Chloride	0.2 PPM Maximum
Nitrate	0.5 PPM Maximum
Ammonium	2 PPM Maximum
Permanganate	1 PPM Maximum
Heavy Metals	5 PPM Maximum
Arsenic	0.01 PPM Maximum
Boron	0.01 PPM Maximum
Iron	0.2 PPM Maximum

9.5 Electron Bombardment Apparatus

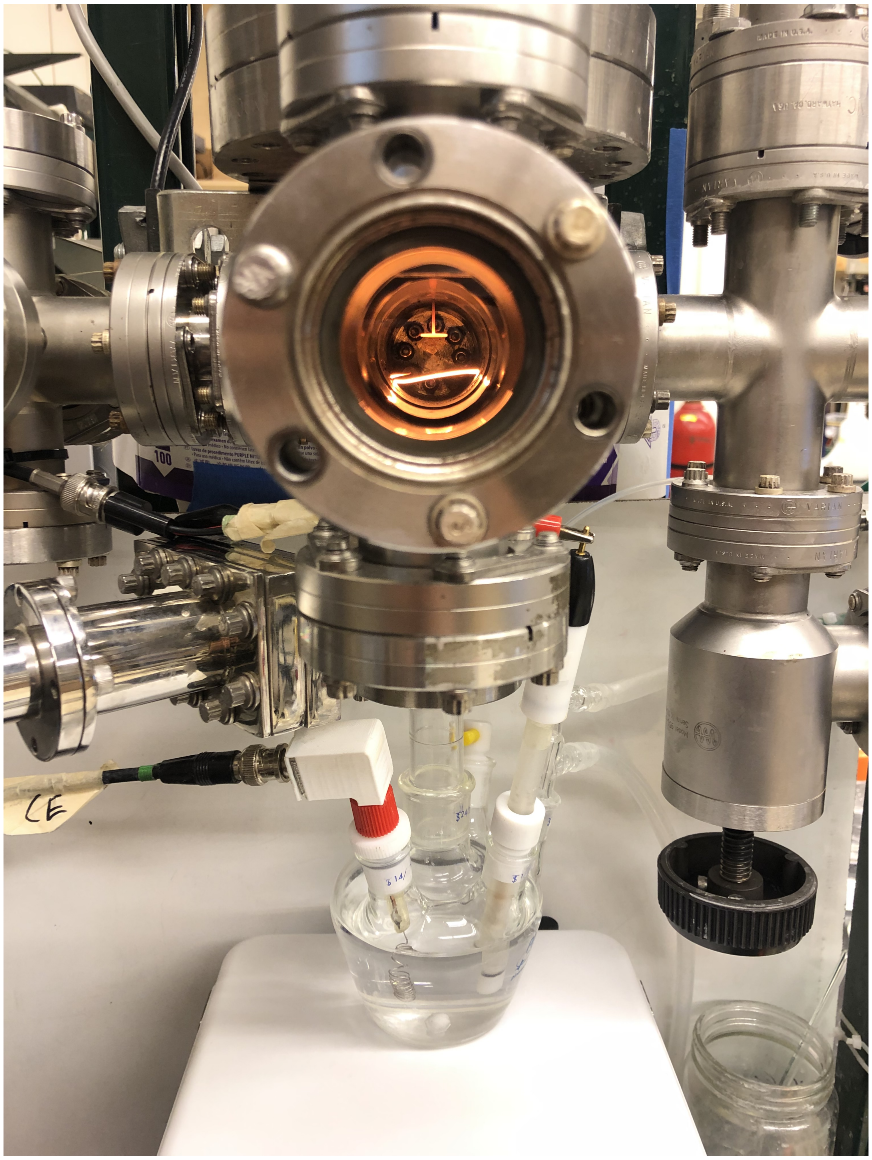

1. Vacuum Handling

1.1. Overview

This section incorporates the operation and components associated with vacuum technologies implemented into the system. The melting chamber was designed to be switched from atmospheric pressure to high vacuum pressure via a coupled vacuum and gas handling systems. The turbomolecular pump is to be left on indefinitely, as continuous operation at low speed greatly extends the lifetime of the pump.

1.2. Diagram

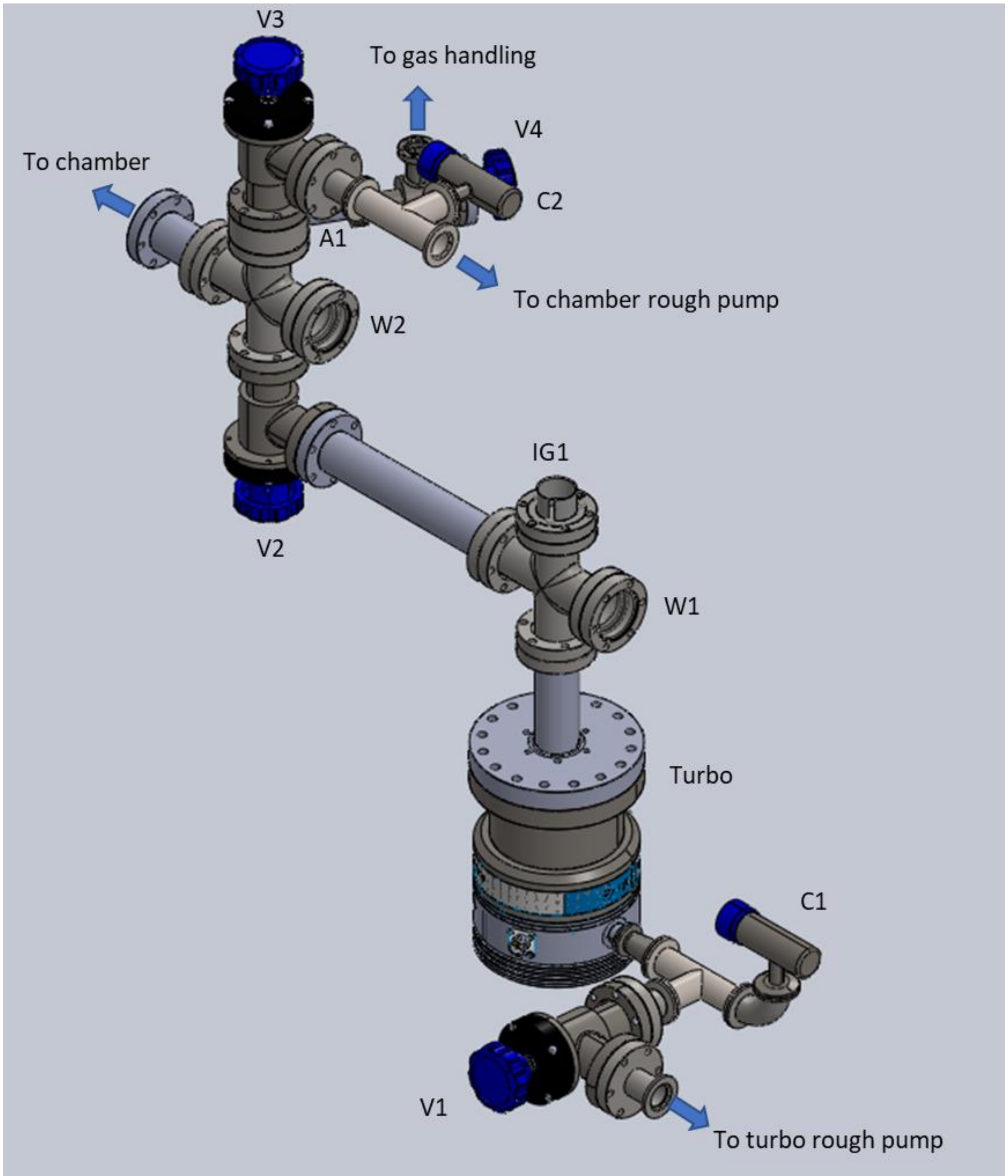

Figure 2

1.3. Parts List

Item	**Name**
Granville Phillips 275 Convectron Gauge	C1
Granville Phillips 275 Convectron Gauge	C2
CF 2.75 in. Manual Bellows Angle HV Valve	V1
CF 2.75 in. Manual Bellows Angle HV Valve	V2
CF 2.75 in. Manual Bellows Angle HV Valve	V3
CF 1.33 in. HV Manual Angle Vacuum Valve	V4
CF 2.75 in. Window	W1
CF 2.75 in. Window	W2
Nude ion gauge	IG1
1.33CF to 2.75CF Sideported Flange	A1
Varian 150HT turbomolecular pump	Turbo
CF 6 in. to CF 2.75 in. Transducer	
CF 2.75 in. 4-way valve	
CF 2.75 in. to CF 2.75 in. 3 in. pipe	
KF25 3-way cross	
KF25 3-way cross	
KF16 to KF25 transducer	
CF2.75 in. to K25 transducer	
CF2.75 in. to K25 transducer	
CF2.75 in. to K25 transducer	

1.4. Operation

1.4.1. Startup

1.4.1.1. The turbo pump is off and has spun down for least 30 minutes
1.4.1.2. Close valves V2, V3, and V4
1.4.1.3. Close valve V8 (not seen in Figure 2, but seen in Figure 4)
1.4.1.4. Turn on turbo rough pump
1.4.1.5. Once the pressure reading on C1 has reached < 1 torr, turn on the turbo pump.
1.4.1.6. The turbo will reduce the pressure the components leading to V2. Once completely spun up (41KRPM on the turbo controller), turn on the ion gauge via on the 307 Vacuum Gauge controller. A pressure reading of < 5E-4 torr. Shut down turbo immediately if the pressure is greater than 5E-3 torr.
1.4.1.7. Open Valve V8

1.4.2. Pumping Down The Melt Chamber

1.4.2.1. Check to see if valves V2, V3, V4, and V5 are closed. (V5 seen in Figure 4)
1.4.2.2. Open valve V3.
1.4.2.3. Turn on chamber rough pump
1.4.2.4. Once the pressure reading on C2 has reached < 1 torr, close V3.
1.4.2.5. Turn off chamber rough pump
1.4.2.6. Turn off the ion gauge via on the 307 Vacuum Gauge controller
1.4.2.7. Slowly open valve V2
1.4.2.8. Once the pressure reading on C1 has reached < 1E-2 torr, turn on ion gauge.
1.4.2.9. A pressure reading of < 5E-4 torr should appear.

1.5. Maintenance

  1.5.1. Every 6-12 months the oil in roughing pumps must be changed out

  1.5.2. Every month the ion gauge must be degassed for accurate readings

1.6. Common problems and Tips

  1.6.1. No reading on C1 or C2:

  - Connections to C1 and C2 are a little finnicky at times. Slightly end the pins inwards on the convectrons to form a better electrical connection

  1.6.2. Higher than usual pressure reading on C1 and/or C2

  - Replace pump oil
  - Re-grease the O-rings on KF flanges

  1.6.3. No reading on IG1

  - Replace filament

2. Melting Chamber

2.1. Overview

This 4-way cross holds the heating and melting of nickel wire into a nickel single crystal. This apparatus used electron bombardment. A tungsten filament is heated in vacuum to give off electrons. These electrons travel to the nickel wire, which is under high voltage. The current of these electrons heat the wire. E-beam was chosen over a hydrogen torch for better control of an oxide environment.

2.2. Diagram

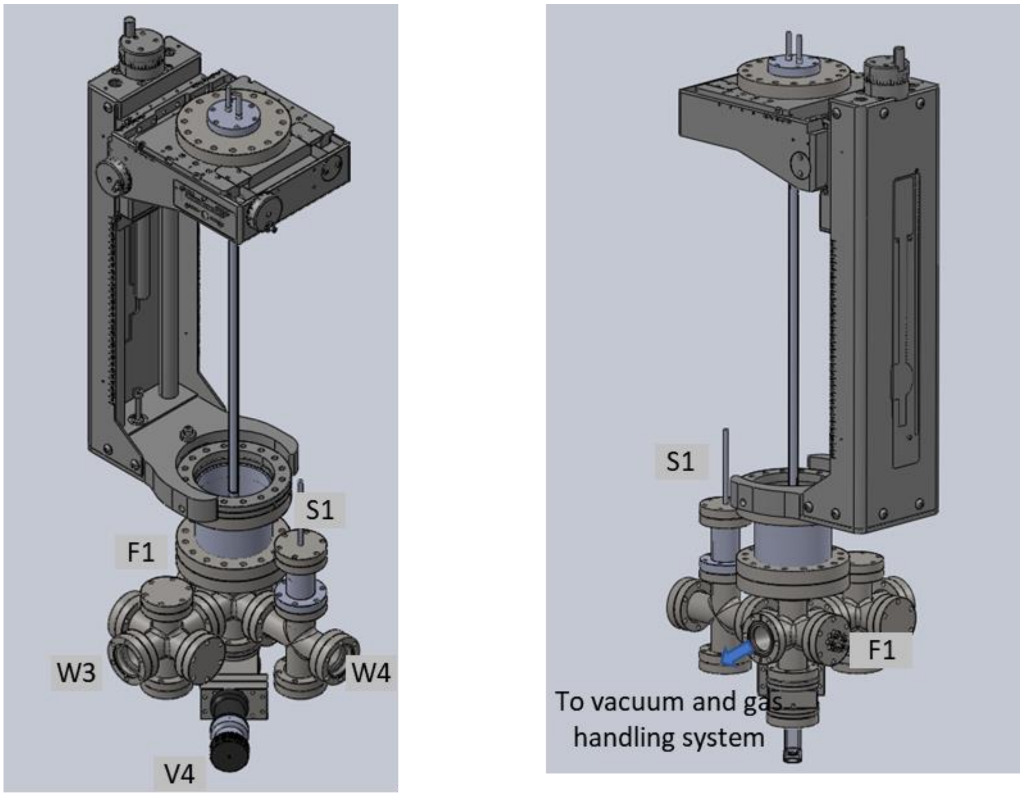

Figure 3: front and back view

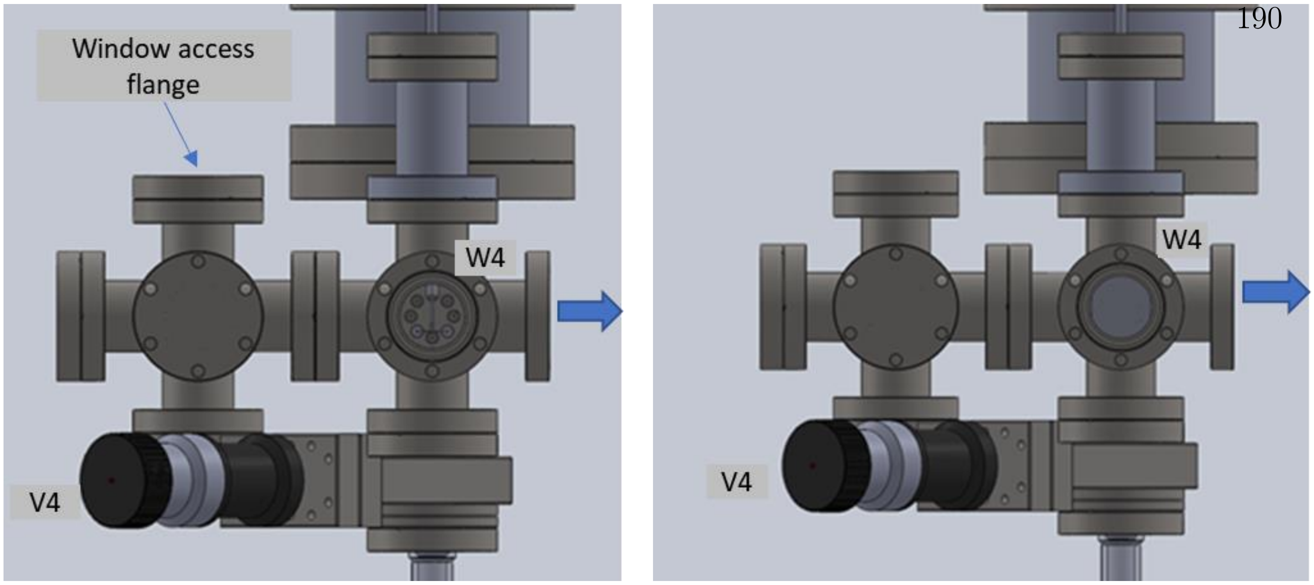

Figure 4. Open and closed shutter

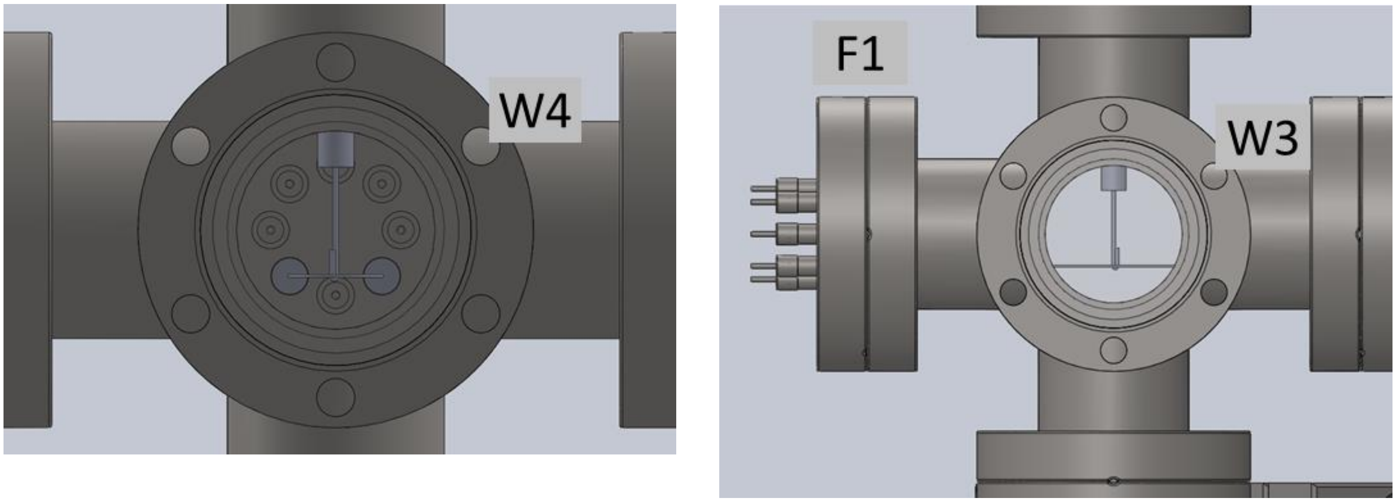

Figure 5. Shutter view and camera view

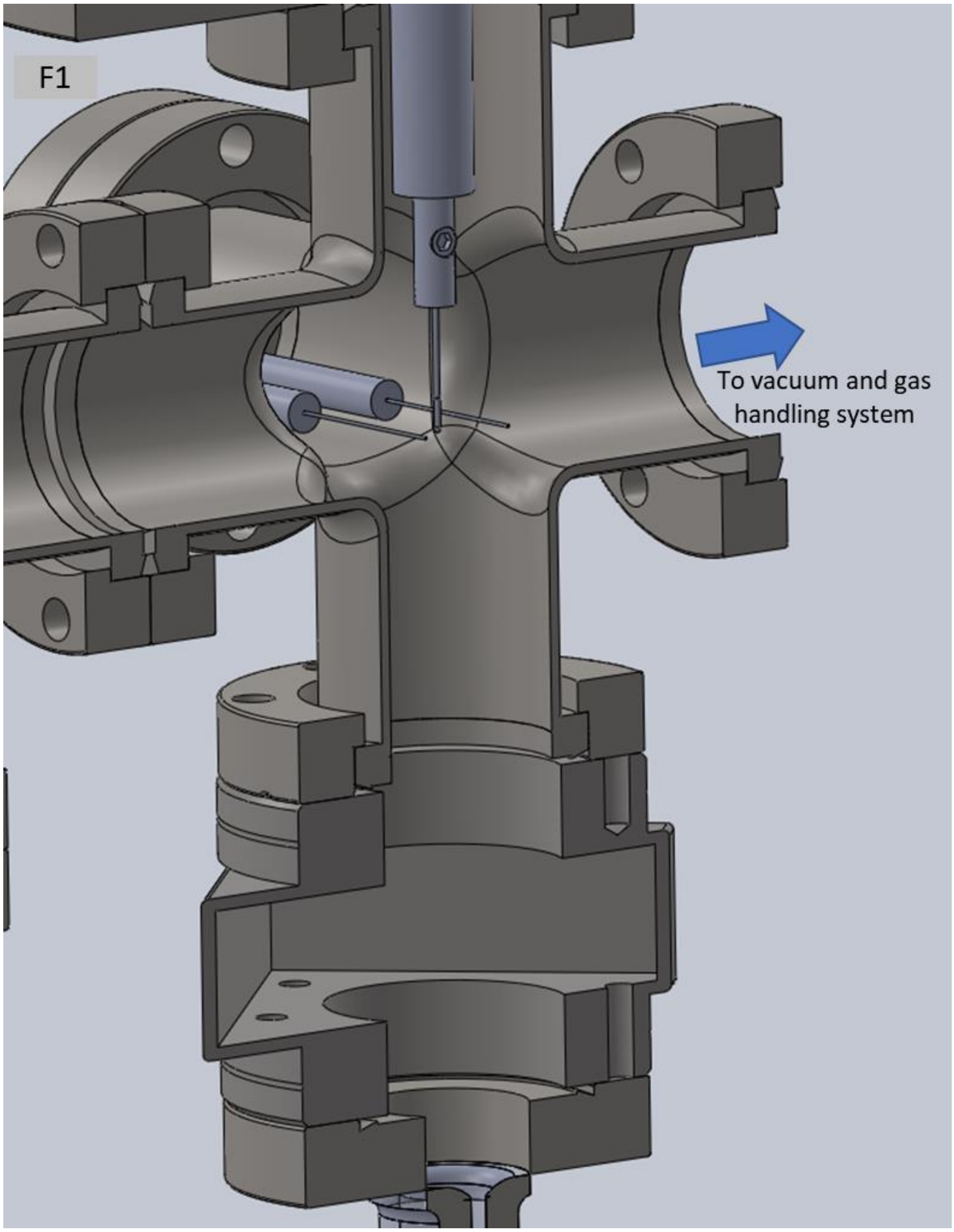

Figure 6: Cut view of melting chamber

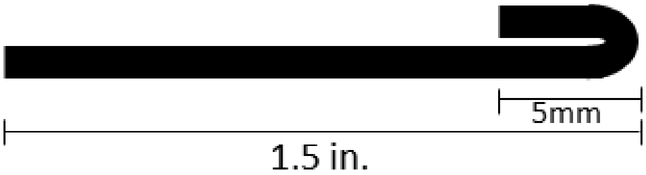

Figure 7: wire cutting dimensions

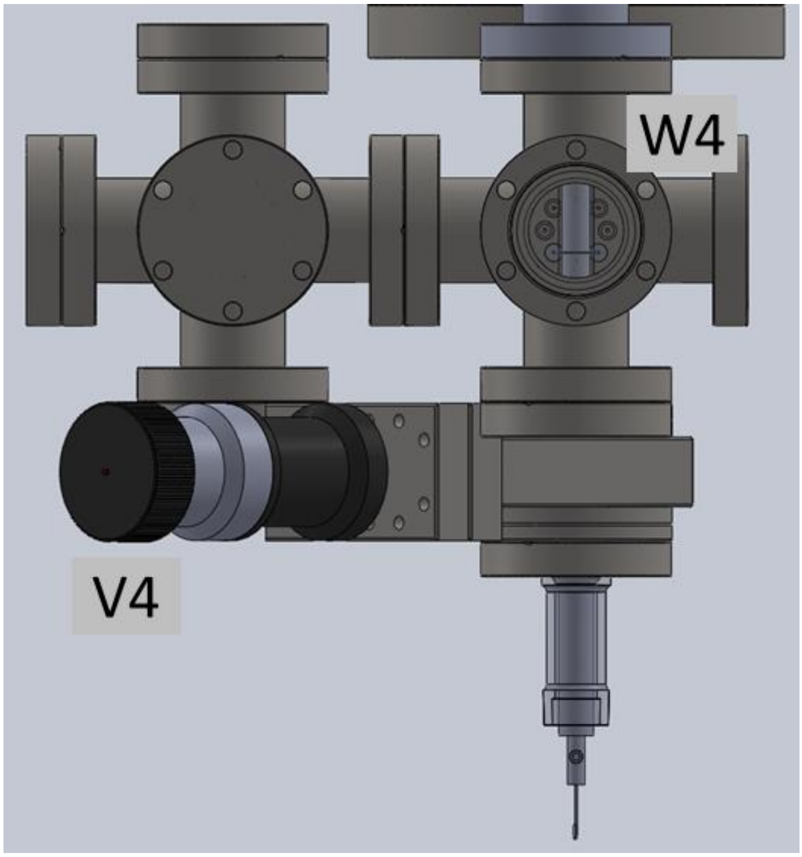

Figure 8: Lowered sample rod position

Figure 9: Control unit for arm and filament

2.3. Parts list

Item	Name
Filament flange	F1
Shutter	S1
Camera window	W3
Shutter window	W4
Gate valve	V4
12 inch travel manipulator arm	
Ceramic insulated flange	
2.75 in. CF to 6 in. Flange	
Melting chamber 6-way cross	
Glass holding 6-way cross	
2.75 in. CF to 24/25 glass port	
6 in. CF to 6 in. CF spacer	
Stainless steel rod	
Insulating glass for stainless steel rod	
8/32 set screw	
Nickel sample holding rod	
Nickel wire	
Stainless steel filament holders	
0.02 in. tungsten wire (filament)	
Viton and copper CF gaskets	

2.4. Operations

2.4.1. Crystal Preparation

2.4.1.1. Locate stock wire of 1mm diameter thick 4N nickel wire purity (should be in box)
2.4.1.2. Straighten a 6-inch portion of the wire
2.4.1.3. Bend 5 mm of and wire back on itself to forma hook, like in Figure 7
2.4.1.4. Cut the wire at 1.5 inches from the end
2.4.1.5. Repeat as many times as necessary (I do 4 at a time)
2.4.1.6. Sonicate cut pieces in acetone for 1 hour

2.4.2. Crystal Mounting and Positioning

2.4.2.1. Remove the three-electrode cell from glass connection
2.4.2.2. Look at Figure 9. Click the bottom right switch labeled “P” to on. This enables the motorized unit.
2.4.2.3. Move the dial labeled “R” in the dotted zone. Click the bottom left switch labeled “R” on. This enables the motorized unit for moving up and down.
2.4.2.4. Turn the knob counter-clockwise. This will lower the rod. The more counter-clockwise you turn it, the faster it moves.
2.4.2.5. Lower the sample rod until the 8-32 set screw is below the glass port as seen in Figure 8
2.4.2.6. Loosen the set screw via hex key and remove previous sample. The heating process causes the screws to expand, so don’t be afraid to apply a little pressure to turn the screw.
2.4.2.7. Wearing gloves, insert the new sample from the bottom.
2.4.2.8. Tighten set screw. Not too tight.
2.4.2.9. Turn the knob clockwise. This will raise the rod.

2.4.2.10. Raise the rod until the bottom of the sample is in line with the filament as seen in Figure 5.

2.4.2.11. Move the knob back into the dotted region. Do not move the knob. Do not turn off the switches.

2.4.3. Mirror Cleaning

2.4.3.1. Vent the system properly. See section 3.4.2

2.4.3.2. There is a mirror located a 4-way cross that needs to be cleaned EVERY TIME YOU MELT A CRYSTAL.

2.4.3.3. Open the window access flange seen in Figure 4.

2.4.3.4. Remove the flange

2.4.3.5. Use a pair of tweezers and grab two holes of the aluminum window holder. Lift the window out.

2.4.3.6. There is a piece of a brass ferrule sandwiching the glass to the aluminum. Do not remove. If it falls out, replace it.

2.4.3.7. You will notice a circle that looks like a mirror. We need to remove that so the camera can see the crystal properly.

2.4.3.8. Place the glass window into a beaker of nitric acid. A concentration of 3 parts water to 1-part nitric acid will suffice. DO NOT put the aluminum in the acid

2.4.3.9. Wait until the nickel has dissolved off.

2.4.3.10. Wipe the glass with water

2.4.3.11. Wipe the glass with acetone

2.4.3.12. Air dry

2.4.3.13. Place mirror into the system. There is another aluminum holding block at the bottom of the 6-way cross. Line it up.

2.4.3.14. Verify placement by opening any the camera application (look up camera in the windows search bar). Rotate the aluminum holder with tweezers until the image is clear.

2.4.3.15. Bolt in the window access flange.

2.4.4. Crystal Melting

2.4.4.1. Pump down system. Instructions seen in section 1.4.2

2.4.4.2. Open the shutter in Figure 4

2.4.4.3. Once the ion gauge is turned on, flip the switch on the white box to “5” in Figure 9. This applies current to a relay, turning on the filament. A bright light will appear in window W4.

2.4.4.4. Close the shutter.

2.4.4.5. Turn off the switch by placing it to the center position.

2.4.4.6. Unhook the sample rod electrical connection. It is a coaxial cable.

2.4.4.7. Hook the sample rod coaxial connection to the HV coaxial connection.

2.4.4.8. Turn on the high voltage power supply. Do not touch any of the dials. I found the perfect settings.

2.4.4.9. Go to the desktop → Beanstalk Scripts. Open the python script labeled “Melter.py”. This script uses image recognition to track the growth of the nickel single crystal. Hit run.

2.4.4.10. Click the switch right to the “A” position.

2.4.4.11. A window called “Circles” will appear in a few seconds. Three lines along with the sample wire will appear on this window. The yellow line is the required growth limit. The purple line is the maximum growth limit. The blue line is the exceeded growth limit. The software will locate the bead via a circle identifier. If the circle passes yellow, the crystal is acceptable to use. If the circle is past purple it is ideal. If it passes blue, the system will shut down to prevent the metal from falling. The system will shut down automatically if the center of the crystal is higher than the purple line or if process exceeds three hours.

- 2.4.4.12. There is a widget I added that will text you when the process is done. Look up twilio if you are interested
- 2.4.4.13. There is a setting for slow cooling. True allows the system to cool down over a course of 5 minutes. False allows the system to shut down immediately
- 2.4.4.14. Once the crystal has melted, turn off the high voltage power supply.
- 2.4.4.15. Click the switch back to the center position in Figure 9.

.

2.4.5.Crystal Reheating.

- 2.4.5.1. Raise the crystal to the center of the filament flange above the tungsten filament.
- 2.4.5.2. Hook the sample rod coaxial connection to the HV coaxial connection.
- 2.4.5.3. Turn on the high voltage power supply. Do not touch any of the dials. I found the perfect settings.
- 2.4.5.4. Go to the desktop → Beanstalk Scripts. Open the python script labeled "Heater.py". This script uses a 93% duty cycle to heat the crystal, but not melt it. Hit run.
- 2.4.5.5. Click the switch right to the "A" position.
- 2.4.5.6. Wait until heating is completed. Currently the heating time is 30 minutes
- 2.4.5.7. Turn off the high voltage power supply.
- 2.4.5.8. Click the switch back to the center position in Figure 9.
- 2.4.5.9. Heated crystal is ready.

2.5. Maintenance

2.5.1. Remember to clean the glass window in section 2.4.3

2.5.2. Tungsten filament can be removed by opening the filament flange, undoing the set screws, and taking out the broken filament. Cut an 11cm length of 0.02 in. tungsten wire, bend into place, and tighten the set screws to insert the filament.

2.6. Common Problems and Tips

2.6.1. There is no filament

- 2.6.1.1. Someone turned on the transformer (either ran the Melter.py or Heater.py scripts or flipped the switch to "5" while in atmosphere). Replace the filament mentioned in 2.5.2

2.6.2. There is no current flowing in the HV power supply

- 2.6.2.1. Check the coaxial connection
- 2.6.2.2. Make sure the system is under vacuum.
- 2.6.2.3. Check to see if the filament is on

2.6.3.Current is high but the bead is not glowing

- 2.6.3.1. Make sure you are operating in high vacuum, not low vacuum. AKA check to see if your turbo is pumping. Valve V3 needs to be closed.

2.6.4.The bead is not centered

- 2.6.4.1. Don't worry. The XY coordinates are set for the 3-electrode cell.

2.6.5. The script does not see a ball, but I can on the screen

- 2.6.5.1. The window was not cleaned. Clean the window.

- 2.6.6. There is a lot of reflection coming off from behind the crystal, looking through the camera port
  - 2.6.6.1. Remove window W2. Throw away the aluminum foil and replace with new foil

- 2.6.7. I forgot to close the shutter. Now the window is a mirror
  - 2.6.7.1. The mirror is the result of nickel become a gas and depositing on a “cold” surface. You may notice flakes of foil on the walls of the melt chamber as well.
  - 2.6.7.2. Take off the respective window. Clean with nitric acid with a cotton swab. Do not let the acid touch the sides of the window. This mess up the glass-metal seal.

3. Gas Handling

3.1. Overview

The gas manifold in Figure 10 is responsible for venting the turbo, venting the heating chamber, clearing out headspace, and sparging the solution in the electrochemical cell. The purpose of this system is to prevent oxygen from entering the system.

3.2. Diagram

Figure 10

3.3. Parts list

Item	Name
Nupro Needle Valve – Argon melt chamber	V6
Nupro Needle Valve – Argon headspace and sparge	V7
Nupro Needle Valve – Argon turbo vent	V8
Nupro Needle Valve – Argon headspace	V9
Nupro Needle Valve – Argon sparge	V10
Nupro Needle Valve – Hydrogen on/off	V11
Nupro Needle Valve – Hydrogen sparge on/off	V12
Nupro Needle Valve – Hydrogen Sparge setting	V13
Nupro Needle Valve – Hydrogen melt chamber	V14
3 – way VCR	
3 – way VCR	
3 – way VCR	
3 – way VCR	
4 – way VCR	
A lot of VCR gaskets	
A lot of male-male VCR fittings	
A lot of female-female VCR fittings	
A lot of male-female VCR fittings	
Hydrogen flame arrestor	

3.4. Operations

3.4.1. Venting Turbo

3.4.1.1. If the turbo ever needs to be shut down, make sure valve V8 is open.

3.4.2. Venting Melt Chamber

3.4.2.1. Valves V6 and V14 have been set to have a 4:1 flow of Argon:Hydrogen
3.4.2.2. Close valve V2
3.4.2.3. Open valve V4
3.4.2.4. Watch as the bellows starts to expand slightly. Shut V4 when bellows starts to bend/buckle

3.4.3. Venting Headspace and Sparging

3.4.3.1. Valves V9 and V12 have been preset to flow hydrogen and argon at a desired flowrate.
3.4.3.2. Open V7 to start the flow of argon to the headspace below the gate valve
3.4.3.3. Open V13 to sparge hydrogen into solution
3.4.3.4. Open V10 to sparge argon into solution

3.5. Maintenance

3.5.1. Remember to replace gas tanks when the run low

3.6. Common Problems and Tips

3.6.1. Don’t touch valves V5, V9, V12, and V14

- They’ve been preset. Matter of fact I should remove the turn heads.

4. Electrochemical Chamber

4.1. Diagram

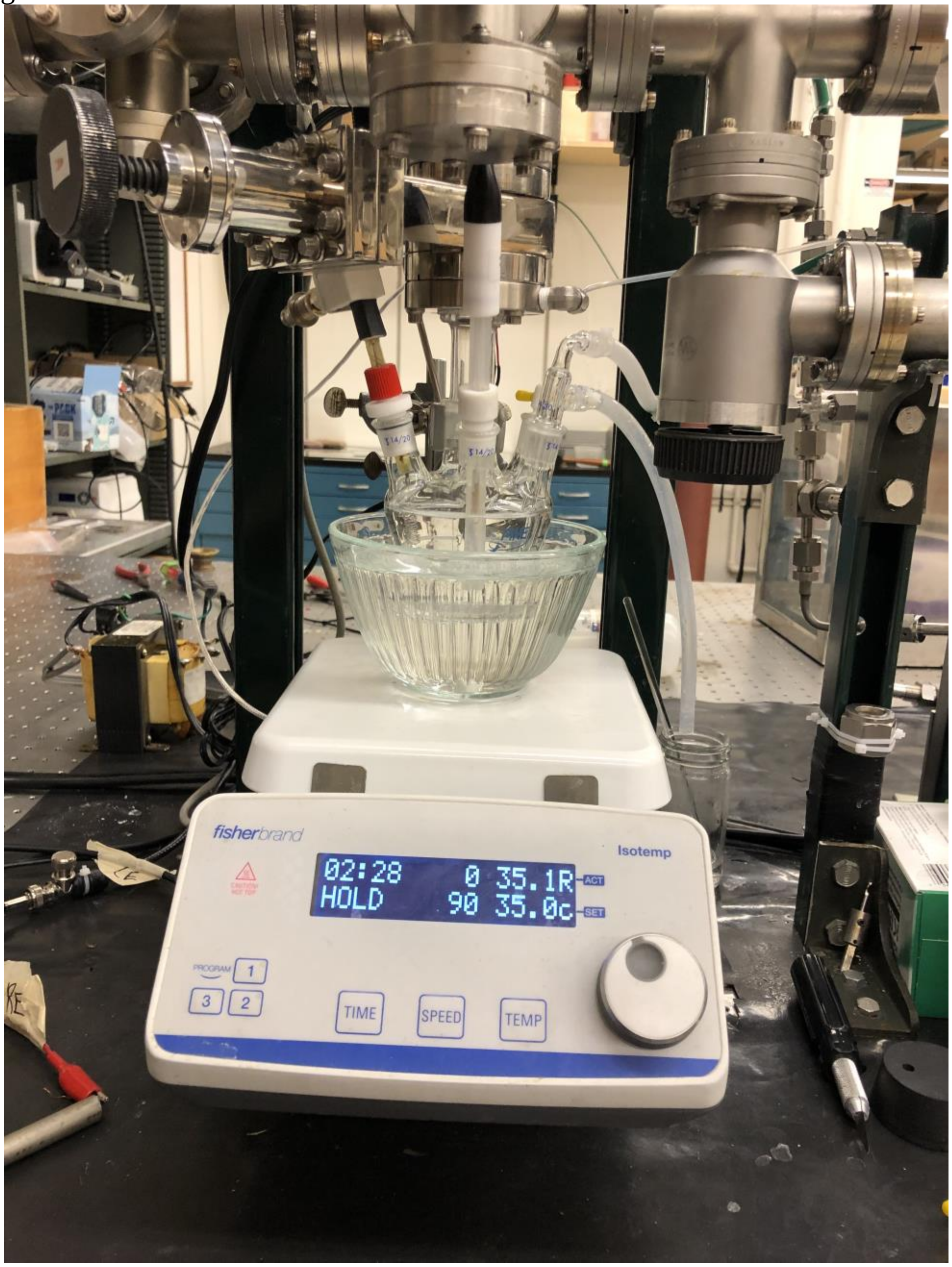

Figure 11

4.2. Parts list

Item	Name
Pine three-electrode cell	
Platinum counter electrode	
Hg/HgO reference electrode	
Gas sparge	
Clamps	
Hot plate	
Vertical jack	

4.3. Operations

4.3.1. Making the Solution

4.3.1.1. The volume of liquid is 175mL so the crystal can reach the water
4.3.1.2. Add 175mL of liquid into the 3-electrode cell
4.3.1.3. Add the necessary solutes
4.3.1.4. Mix

4.3.2. Removing the Cell

4.3.2.1. Lift the crystal out of solution and above the class connection. Refer to section 2.4.2
4.3.2.2. Lower the hotplate completely via the twisting the knob on the jack
4.3.2.3. Hold the cell with one hand
4.3.2.4. Untwist the clamp holding the 24/25 connection
4.3.2.5. Remove the cell from the apparatus

4.3.3.Attaching the Cell

4.3.3.1. Lower the hotplate completely via the twisting the knob on the jack
4.3.3.2. Hold the cell with one hand
4.3.3.3. Attach the 24/25 glass joint to the respective glass joint
4.3.3.4. Position and twist the clamp to the 24/25 connection
4.3.3.5. Raise the jack to wanted position
4.3.3.6. Insert reference, counter, and sparger.

4.3.4. Purging the cell

4.3.4.1. Open valve V7. This will flow argon into the headspace above the cell
4.3.4.2. Make sure there is water in the pre-sparge beaker. Valves V10 and V13 feed directly into this beaker.
4.3.4.3. Open valve V10. This will sparge argon
4.3.4.4. Open valve V13. This will sparge hydrogen

4.3.5.Heating the Cell

4.3.5.1. Make sure the thermocouple is submerged
4.3.5.2. Click the “Temp” button and turn the dial to the desired temperature. Click the “Temp” button again.
4.3.5.3. Click the “speed” button and turn the dial to the desired stir bar rotation speed. Click the “speed” button again.
4.3.5.4. Press the dial to start the heating process

4.3.6. Taking Electrochemical Measurements

4.3.6.1. Vent the chamber in accordance to section 3.4.2
4.3.6.2. Open valve V4 completely.

4.3.6.3. Go to the desktop → Beanstalk Scripts and open hghgo - poscc v1 - solartron1287.cpw
4.3.6.4. This script has an experiment labeled “-1 seed.cor” This experiment will start the cyclic voltammetry when the circuit is completed. Run the list of experiments with “-1 seed.cor” as the first experiment.
4.3.6.5. Lower the bead into solution. Refer to section 2.4.2
4.3.6.6. Stop when the crystal makes contact

4.4. Maintenance
  4.4.1. No real maintenance here. Take care of the reference electrode. Wear gloves

4.5. Common Problems and Tips
  4.5.1. Learn electrochemistry. Read Bard and Faulkner

9.5.1 Synthesizing Nickel Single Crystals Script

The electron bombardment apparatus was fitted with a camera to monitor the state of the electrode throughout the heating process. The camera allowed for image analysis to be conducted during heating, thus allowing for accurate control of size of the nickel single crystal. The image analysis software is seen below with the necessary functions and packages. Software for heating the electrode without the image processing code is used to heat the electrode for a set amount of time.

[ ]:

```
import os
import time
import cv2 as cv
import pyfirmata
import numpy as np
import soundfile as sf
import sounddevice as sd
from datetime import datetime



videoCapture = cv.VideoCapture(0,cv.CAP_DSHOW)

board = pyfirmata.Arduino('COM4')
board.digital[10].write(1)

Slow_cooling = True

xcenter = int(1280/2)
```

```
ycenter = int(1024/2)
videoCapture.set(cv.CAP_PROP_FRAME_WIDTH, xcenter*2)
videoCapture.set(cv.CAP_PROP_FRAME_HEIGHT, ycenter*2)



def line_splitter(frame, x1,x2,y1,y2, color,line_thickness, num_lines):

    x_dat = np.linspace(x1,x2,num_lines)
    y_dat = np.linspace(y1,y2,num_lines)



    for i in range(0,len(x_dat)-1,2):
        cv.line(frame, (int(x_dat[i]), int(y_dat[i])), (int(x_dat[i+1]),␣
 ↪int(y_dat[i+1])), color, thickness=line_thickness)

prevCircle = None
dist = lambda x1,y1,x2,y2: (x1-x2)**2 + (y1-y2)**2

sharpen_filter = np.array([[0, -1, 0], [-1, 5, -1], [0, -1, 0]])

xdis = 150
ydis = 300
new_w = 500
new_h =  500

y_lowy = ycenter - ydis
y_highy = ycenter + ydis - 200
```

```
x_lowy = xcenter - xdis+75
x_highy = xcenter + xdis



fourcc = cv.VideoWriter_fourcc(*'XVID')
result = cv.VideoWriter('Q://Shared drives//NSF-DFG Urea//Operations//
 ↪Single Crystal//Output//' +  now.strftime("Melted at %H..%M on %d.%m.
 ↪%Y")+ '.avi', fourcc, 20, (int(x_highy - x_lowy),int(y_highy - y_lowy)))



low_limit = 0
high_limit = 0
higher_limit = 0

timeout = 60*3 # minutes

timeout = timeout*60 # [seconds]
timeout_start = time.time()
time_switch = 0
timer_checker = time.time()
while time.time() < timeout_start + timeout:
    ret, frame = videoCapture.read()
    frame  = frame[y_lowy:y_highy, x_lowy:x_highy]
    if not ret: break

    grayFrame = cv.cvtColor(frame, cv.COLOR_BGR2GRAY)
```

```
    blurFrame = grayFrame

    circles = cv.HoughCircles(blurFrame,cv.HOUGH_GRADIENT,1.2,1,
                              param1 = 100, param2 = 40,  minRadius =␣
↪1,maxRadius = 15)
    offset = 15


    ylim = 200 + offset # bottom line
    ylim2 = 175 + offset
    ylim3 = 162 + offset # top line
    filament_line = 230 + offset
    center_off = 100
    center = 50


    if circles is not None:
        cricles = np.uint16(np.around(circles))
        chosen = None
        for i in circles[0,:]:
            if chosen is None: chosen = i
            if prevCircle is not None:
                if dist(chosen[0],chosen[1],prevCircle[0],prevCircle[1])␣
↪<= dist(i[0],i[1],prevCircle[0],prevCircle[1]):
                    chosen = i
```

```
        if int(chosen[1]) < ylim   and int(chosen[1]) > ylim3 - 5 and␣
↪int(chosen[0]) > center_off - center and int(chosen[0]) < center_off +␣
↪center:
            low_limit = low_limit + 1
            cv.circle(frame,␣
↪(int(chosen[0]),int(chosen[1])),1,(0,100,100),1)
            cv.circle(frame,␣
↪(int(chosen[0]),int(chosen[1])),int(chosen[2]) + 3,(255,0,0),2)

            prevCircle = chosen
            if int(chosen[1]) < ylim2 and int(chosen[1]) > ylim3:


                if high_limit > 10:

                    if Slow_cooling == True:
                        print('Limit Reached, Starting slow cooling')

                    if Slow_cooling == False:
                        print('Limit Reached, Shutting Down')

                    board.digital[10].write(0)
                    time_switch = 1
                    break
            high_limit = high_limit + 1

            if int(chosen[1]) < ylim3:
```

```
                higher_limit = higher_limit + 1

            if int(chosen[1]) > ylim2 or int(chosen[1]) < ylim3:
                high_limit = 0

    line_thickness = 2
    num_lines = 20
    line_splitter(frame, center_off - center,center_off +␣
↪center,ylim,ylim, (0, 255, 255),line_thickness, num_lines = 25)
    line_splitter(frame, center_off - center,center_off +␣
↪center,ylim2,ylim2, (255, 0, 255),line_thickness, num_lines = 25)
    line_splitter(frame, center_off - center,center_off +␣
↪center,ylim3,ylim3, (255, 255, ),line_thickness, num_lines = 25)



    line_splitter(frame, center_off - center,center_off -␣
↪center,ylim,filament_line , (0, 0, 0),2, num_lines = 25)
    result.write(frame)
    cv.imshow("circles",frame)

    if cv.waitKey(1) & 0xff == ord('q'):
        texting = False
        break

if time_switch == 0:
    print('Took too long. Shutting down for safety.')
```

```
if low_limit > 20 and higher_limit <=5:
    print('Crystal is usable.')

if higher_limit >=5:
    print('Melted too far. Crystal is unusable.')



timer = 0.1
duty = 1
duty_2 = 0.5
rate = 0.0005

while Slow_cooling == True:
    ret, frame = videoCapture.read()

    frame  = frame[ycenter - ydis:ycenter + ydis - 200, xcenter - xdis+75:
 ↪xcenter + xdis]
    board.digital[10].write(1)
    time.sleep(timer*(duty)*2)
    board.digital[10].write(0)
    time.sleep(timer*(1 - duty)*2)
    duty = np.round(duty-rate,4)

    cv.imshow("circles",frame)
    result.write(frame)
    if duty < duty_2:
        print("Slow cooling completed")
```

```
        break

    if cv.waitKey(1) & 0xff == ord('q'): break

board.digital[10].write(0)

videoCapture.release()
result.release()
cv.destroyAllWindows()

# datetime object containing current date and time


# dd/mm/YY H:M:S
dt_string = now.strftime("at %H:%M on %d.%m.%Y ")



print(("Melting Finished " + dt_string))
```

9.6 Scripts

9.6.1 Data Import

The software used for conducting several hundred cyclic voltammetry, potentiostatic holds, and electrochemical impedance spectrometry experiments is Corrware© and is publicly available by Scribner. The data files outputted by this software have the '.cor' extension, which is an ASCII text encoded format and can be imported into Python.

[ ]:

```
def data_importer_hold(directory):


filepathh = directory

mylines = []


with open (filepathh, 'r') as myfile:


    for myline in myfile:

        mylines.append(myline)


data = mylines[93:]

data_2 = np.zeros([np.shape(data)[0],3])

for j in range(0,np.shape(data)[0]):

    data_2[j] = np.array(list(map(float, data[j].split())))

cv_current = data_2[:,1]


return data_2[:,0],cv_current,data_2[:,2]
```

9.6.2 Dialysis Model

The functions and code necessary to run the model in Chapter 7 are presented here.

[ ]:

```
######## Calculates stuff for CSTR of alkaline fuel cell
def CSTR(conversion, flow_in ,urea_concentration ):
    #Required amperage for 15g/Day Urea

    #specs
    MW_U = 60.06; #g/mol
    MW_W = 18.016; #g/mol
    Conc = urea_concentration/1000 #Molar
    row_tot = 1.0*1000
    psat_w = 47.1 #torr
    p_tot = 750.062; #torr
    beta = 3

    J = flow_in*Conc*conversion #mol/min

    #### In
    Anode_in_urea = flow_in*Conc #mol/min
    Anode_in_water = (row_tot/MW_W/Conc)*J/conversion #mol/min

    #### Out
    membrane_out_h2o = 6*beta*J #mol/min
    Anode_out_N2 = J #mol/min
    Anode_out_CO2 = J #mol/min
    Anode_out_h20_g = psat_w/(p_tot-psat_w)*2*J #mol/min
    Anode_out_h20_l = Anode_in_water + 5*J - Anode_out_N2 +␣
 ↪membrane_out_h2o #mol/min
```

```
    Anode_out_h20_l = Anode_in_water + 5*J - Anode_out_h20_g +␣
 ↪membrane_out_h2o #mol/min
    Anode_out_u = (1-conversion)*Anode_in_urea #mol/min

    #### Overall
    liq_out = (Anode_out_h20_l)/55.5 #mL/min
    Anode_u_conc = (Anode_out_u/liq_out)*1000 # mMolar
    grams_converted = (Anode_in_urea - Anode_out_u )*MW_U*24*60/1000
    output = [liq_out,  Anode_u_conc,  grams_converted,Anode_out_CO2]
    return output

######### Area finder for mass transfer column
def A_finder(cd_i,k_log):

    A_dialyser = 1
    cp_i = 12
    cp_o = 12
    def equations(p):
        cd_o = p
        return ( k_log*A_dialyser *    ((cp_o - cd_i  ) - (cp_i - cd_o ))/
 ↪(np.log(((cp_o - cd_i ))/(cp_i - cd_o ))) - 15)
    x =  fsolve(equations, (11.9999))

    return(x)
```

[ ]:

```
# Allocation
A = np.zeros(2)
```

```
B = np.zeros(2)
C = np.ones(2)
D = np.zeros(2)
E = np.zeros(2)

# Seeding Parameters
A[0] = 50 #mL/min
B[0] = 50  #mL/min
C[0] = A[0] + B[0]  #mL/min
D[0] = C[0]  #mL/min
E[0] = D[0] - B[0]  #mL/min

primed = 8 #mMolar Urea

A[1] = primed #mMolar
B[1] = primed #mMolar
C[1] = (A[0]*A[1] + B[0]*B[1])/ C[0] #mMolar
D[1] = primed #mMolar
E[1] = primed #mMolar
A_test_i = 1
A_test_f = 0
########### TUNABLE PARAMETERS ###########

cap = 300 # mL/min
crit = 90 # urea removal per day
```

```python
k_mass_transfer_coeff = list(np.linspace(2,4,5)) + [2.314,3.73] # Assumed A = 1 cm^2, these values are for units of K_o of mL/min. Convert to cm/min by mutiply by 100, which is relevant to life
conversion = np.linspace(0.03,0.99,30)

##########################################
yplot_1 = np.zeros((len(k_mass_transfer_coeff),len(conversion)))
yplot_2 = np.zeros((len(k_mass_transfer_coeff),len(conversion)))
yplot_3 = np.zeros((len(k_mass_transfer_coeff),len(conversion)))
yplot_4 = np.zeros((len(k_mass_transfer_coeff),len(conversion)))
yplot_5 = np.zeros((len(k_mass_transfer_coeff),len(conversion)))
yplot_7 = np.zeros((len(k_mass_transfer_coeff),len(conversion)))
yplot_8 = np.zeros((len(k_mass_transfer_coeff),len(conversion)))
pH = np.zeros((len(k_mass_transfer_coeff),len(conversion)))

y = symbols('y')
ka = 10**(-6.1)
kw = 10**(-7.4)
ksp = 2.7*10**(-3)

H2O_conc = 55.5 #Mol/L


timeout = 3
timeout_start1 = time.time()
timeout_start2 = time.time()
log = []
```

```
printer = False

for j in trange(0,len(k_mass_transfer_coeff)):

    for k in range(0,len(conversion)):
        A_test_i = 1
        A_test_f = 0
        check = 0

        timeout_start1 = time.time()
        while np.abs(A_test_i-A_test_f) > 0.001:
            if time.time() > timeout_start1 + timeout:
                log.append('timeout1 at k = ' +␣
 ↪str(k_mass_transfer_coeff[j]) + ', x = ' + str(conversion[k]))
                check = 1
                break


            A_test_i = A[0]
            p = 0
            while True:
                B[0] = p*2
                C[0] =  A[0] + B[0]
                D[0] = C[0]
                E[0] = D[0] - B[0]
                A[1] = A_finder(B[1],k_mass_transfer_coeff[j])
```

```
A[0] =  crit*1000*1000/60.06/A[1]/1440/conversion[k]
if A[0] >= cap:
    A[0] = cap

B[1] = primed
C[1] = (A[0]*A[1] + B[0]*B[1])/ C[0]
D[1] = 8
E[1] = 8

Con_test_begin = 1
Con_test_end = 0
timeout_start2 = time.time()
while Con_test_begin - Con_test_end > 0.001:
    if time.time() > timeout_start2 + timeout:
            log.append('timeout2')
            break
    Con_test_begin = B[1]
    reactor_out = CSTR(conversion[k],C[0],C[1] )
    D[0] =  reactor_out[0]
    E[0] =  A[0]
    D[1] = reactor_out[1]
    B[1] = D[1]
    C[1] = (A[0]*A[1] + B[0]*B[1])/ C[0]
    E[1] = D[1]
    Con_test_end = B[1]

p = p + 1
```

```
                if reactor_out[2] > crit:
                    if B[0] <= 3:
                        B[0] = 0
                        D[0] =  reactor_out[0]
                        E[0] =  A[0]

                        D[1] = reactor_out[1]
                        B[1] = D[1]
                        C[1] = (A[0]*A[1] + B[0]*B[1])/ C[0]
                        E[1] = D[1]
                    break
            A_test_f = A[0]
        yplot_1[j,k] = A[0] # Flow of dialyzer out
        yplot_2[j,k] = A[1] # Concentraiton of dialyzer out
        yplot_3[j,k] = B[0] # Flow of recycle
        yplot_4[j,k] = E[1] # Concentraiton of dialyzer in
        yplot_5[j,k] = C[1] # conc in urc
        yplot_7[j,k] = C[0] # flow in urc
        yplot_8[j,k] = reactor_out[3] # CO2 flow

        H2O = yplot_1[j,:][k] #mol/min
        H2O = H2O/H2O_conc #mL/min
        CO2 = yplot_8[j,:][k]/H2O/1000 #mol/mL
        z = ((kw + y)*(y) + ka*y)/ka
        expr = z/((CO2-z)*(H2O_conc/1000-z)) - ksp
        sol = solve(expr)
        val = -math.log10(float(sol[2]))
```

```
        pH[j,k] = val

        if check == 1:
            yplot_1[j,k] = None # Flow of dialyzer out
            yplot_2[j,k] = None # Concentraiton of dialyzer out
            yplot_3[j,k] = None # Flow of recycle
            yplot_4[j,k] = None # Concentraiton of dialyzer in
            yplot_5[j,k] = None # conc in urc
            yplot_7[j,k] = None # flow out CO2
            yplot_8[j,k] = None # pH
            pH[j,k] = None

        if np.round(conversion[k]%0.1,2)%0.1 == 0 and printer == True:

            print('Conversion: %.2f' % conversion[k])
            print('Urea converted in 24 hours: %.2f g' % (reactor_out[2])␣
↪)
            Data = [A,B,C,D,E]
            Table_print(Data)
            print('\n')

display(log)
```

9.6.3 General Lateral Interactions

The reduction peaks of cyclic voltammetry were fitted using the General Lateral Interactions (GLI) fitting function. The initial guesses for the fitting are permutated to increase the accuracy of the fit.

[ ]:

```
def GLI_4_fit(xdata,ydata,bounds):
    B_guesses = [-1.2,1.2]
    gamma_guesses = [1E-9]
    Ep1g = 0.44
    Ep2g = 0.35
    Ep3g = 0.27
    Ep4g = 0.49
    guess_list = perms2(B_guesses,gamma_guesses,Ep1g,Ep2g,Ep3g,Ep4g)

    # Fitting
    r_sq_list = []
    coef_list = []
    for guess in range(4):
        coeff, var_matrix = curve_fit(GLI4,xdata,ydata,
                                      p0=guess_list[guess],
                                      maxfev=None,
                                      bounds=bounds,
                                      ftol=1E-12,
                                      xtol=1E-12,
                                      gtol=1E-12)
        i_fit = [GLI4(xx, *tuple(coeff)) for xx in xdata]
        residuals = ydata - GLI4(xdata, *coeff)
        ss_res = np.sum(residuals**2)
        ss_tot = np.sum((ydata-np.mean(ydata))**2)
        r_squared = 1 - (ss_res / ss_tot)
        r_sq_list.append(r_squared)
        coef_list.append(coeff)
```

```
    r_sq_fit = max(r_sq_list)
    coeff_fit = coef_list[r_sq_list.index(r_sq_fit)]
    param_list = []
    for i in range(4):
        param_list.append(coeff_fit[(i)*3:(i+1)*3])
    ip_list = []
    for i,param in enumerate(param_list):
        ip_list.append((n**2)*(F**2)*A*v/R/T*param[2]/(4-2*param[1]))


    return param_list, coeff_fit,r_sq_fit
```

[ ]:

```
##### Guesses permutations
def perms2(B_list,G_list,Ep1g,Ep2g,Ep3g,Ep4g):
    guess_list = []
    for B in B_list:
        for G in G_list:
            guess1 = [Ep1g,B,G] # Includes initial guess for Ep1
            for B in B_list:
                for G in G_list:
                    guess2 = [Ep2g,B,G] # Includes initial guess for Ep2
                    for B in B_list:
                        for G in G_list:
                            guess3 = [Ep3g,B,G] # Includes initial guess␣
 ↪for Ep3
                            for B in B_list:
                                for G in G_list:
```

```
                                    guess4 = [Ep4g,B,G] # Includes␣
↪initial guess for Ep4
                                    guess = guess1+guess2+guess3+guess4
                                    guess_list.append(guess)
    return guess_list
```